NUREG/CR-6132
ORNL/TM-12498

Biaxial Loading and Shallow-Flaw Effects on Crack-Tip Constraint and Fracture Toughness

Prepared by
B. R. Bass, J. W. Bryson, T. J. Theiss, M. C. Rao

Oak Ridge National Laboratory

Prepared for
U.S. Nuclear Regulatory Commission

NUREG/CR-6132
ORNL/TM-12498
RF

Biaxial Loading and Shallow-Flaw Effects on Crack-Tip Constraint and Fracture Toughness

Manuscript Completed: November 1993
Date Published: January 1994

Prepared by
B. R. Bass, J. W. Bryson, T. J. Theiss, M. C. Rao

Oak Ridge National Laboratory
Managed by Martin Marietta Energy Systems, Inc.

Oak Ridge National Laboratory
Oak Ridge, TN 37831-6285

Prepared for
Division of Engineering
Office of Nuclear Regulatory Research
U.S. Nuclear Regulatory Commission
Washington, DC 20555-0001
NRC FIN B0119
Under Contract No. DE-AC05-84OR21400

Abstract

A program to develop and evaluate fracture methodologies for the assessment of crack-tip constraint effects on fracture toughness of reactor pressure vessel (RPV) steels has been initiated in the Heavy-Section Steel Technology (HSST) Program. Crack-tip constraint is an issue that significantly impacts fracture mechanics technologies employed in safety assessment procedures for commercially licensed nuclear RPVs. A validated technology that incorporates constraint effects is essential to the transfer of fracture toughness data from, for example, miniature fracture toughness surveillance specimens to RPVs. The focus of studies described herein is on the evaluation of two stressed-based methodologies for quantifying crack-tip constraint (i.e., J-Q theory and a micromechanical scaling model based on critical stressed volumes) through applications to experimental and fractographic data. Data were utilized from single-edge notch bend (SENB) specimens and HSST-developed cruciform beam specimens that were tested in HSST shallow-crack and biaxial testing programs. Shallow-crack effects and far-field tensile out-of-plane biaxial loading have been identified as constraint issues that influence both fracture toughness and the extent of the toughness scatter band.

Results from applications indicate that both the J-Q methodology and the micromechanical scaling model can be used successfully to interpret experimental data from the shallow- and deep-crack SENB specimen tests. When applied to the uniaxially and biaxially loaded cruciform specimens, the two methodologies showed some promising features, but also raised several questions concerning the interpretation of constraint conditions in the specimen based on near-tip stress fields. Fractographic data taken from the fracture surfaces of the SENB and cruciform specimens are used to assess the relevance of stress-based fracture characterizations to conditions at cleavage initiation sites. Comparisons of initiation sites with near-tip stress fields from the SENB shallow-crack specimens tend to support a fracture criterion based on critical stress; however, those utilizing data from the cruciform specimens are ambiguous and require further study. Crack-tip constraint analyses of the shallow-crack cruciform specimen subjected to uniaxial or biaxial loading conditions are shown to represent a significant challenge for these methodologies. Unresolved issues identified from these analyses require resolution as part of a validation process for biaxial loading applications. This report is designated as HSST Report No. 142.

Contents

Page

Abstract iii

List of Figures vii

List of Tables xi

Acknowledgments xiii

1 Introduction 1

2 Biaxial and Shallow-Crack Testing Programs 5

2.1 Summary of Shallow-Crack Testing Program 5
2.2 Biaxial Testing Program 5
2.2.1 Cruciform Bend Specimen 5
2.2.2 Test Matrix 8
2.2.3 Experimental Results and Interpretation 8

3 Constraint Analyses 13

3.1 Finite-Element Analysis of Cruciform Specimen 13
3.2 Stress Triaxiality (J-Q) Method 20

3.2.1 Application of J-Q Method to Shallow-Crack Specimens 20
3.2.2 Application of J-Q Method to Cruciform Specimens 21

3.3 Fracture Toughness Scaling Model (Dodds-Anderson) 29

3.3.1 Application of Scaling Model to Shallow-Crack Data 29
3.3.2 Application of Scaling Model to Cruciform Beam Data 33

3.4 Discussion of Crack-Tip Analyses 35

4 Fractography and Fracture Characterization Issues 39

4.1 Fractographic Examinations 39
4.2 Cleavage Initiation Sites and Stress-Based Fracture Characterization 39
4.3 3-D Interpretation of Toughness 43

5 Summary and Conclusions 47

References 51

Appendix A: Small-Scale Yielding Solution 53

Appendix B: Finite Strain Calculations 55

List of Figures

Figure		Page
1.1	Vessel wall biaxial far-field stresses during PTS transient with one component aligned parallel to front of longitudinal crack	1
1.2	Toughness (K_{Jc}) data vs normalized temperature for shallow- and deep-crack specimens with shallow- and deep-crack lower-bound curves	2
2.1	Cruciform bend specimen used in HSST biaxial testing program: (a) dimensions of cruciform specimen and (b) detail of crack plane	6
2.2	Slot configurations used in analyses of the cruciform bend specimen: (*a*) uniform slots on test section boundary, (*b*) outer slots extended inward by 8.9 mm across test section boundary, (*c*) center slot contracted away by 5.1 mm from test section boundary, (*d*) a superposition of configurations (*b*) and (*c*)	7
2.3	Biaxial and uniaxial shallow-crack toughness data as function of normalized temperature	10
2.4	Uniaxial and biaxial toughness data as function of crack depth at $T - RT_{NDT} = -10°C$	10
2.5	Toughness data for deep- and shallow-crack specimens as function of load ratio at $T - RT_{NDT} = -10°C$	11
3.1	Definition of coordinate system and locations of interest for interpretation of finite-element results from analysis of HSST cruciform bend specimen	13
3.2	(*a*) Finite-element model for local crack-tip analyses of cruciform bend specimen, (*b*) test section region of finite-element model for cruciform bend specimen, (*c*) highly refined crack-tip region of finite-element model for cruciform bend specimen, and (*d*) finite-element model with expanded region of refinement near the crack tip for analysis of uniaxially loaded cruciform specimen	14
3.3	Material representation for A 533 B steel at $T = -46°C$	16
3.4	Comparison of calculated and measured LLD for cruciform bend specimens	17
3.5	Comparison of calculated and measured CMOD for cruciform bend specimens	17
3.6	Applied J at X = 0 mm, uniaxial and biaxial 0.6:1 loading	18
3.7	Applied J at X = 26 mm, uniaxial and biaxial 0.6:1 loading	18
3.8	Variation of K_J along crack front, biaxial 0.6:1 loading	19
3.9	Variation of normalized K_J along crack front for both uniaxial and biaxial 0.6:1 loading at low load and at load near failure	19
3.10	Distributions of opening-mode stress component for SENB specimen with a/W = 0.1 as function of applied load up to crack initiation	20
3.11	Normalized opening-mode stress ahead of crack tip, X = 0 mm, uniaxial loading	21
3.12	Normalized opening-mode stress ahead of crack tip, X = 0 mm, biaxial 0.6:1 loading	22
3.13	Variation of Q with normalized distance ahead of the crack tip, X = 0 mm, uniaxial loading	22

3.14 Variation of Q with normalized distance ahead of the crack tip, X = 0 mm, biaxial 0.6:1 loading 23

3.15 J-Q trajectories at X = 0 mm for a normalized distance $r\sigma_0/J = 2$ 23

3.16 J-Q trajectories at X = 0 mm for a normalized distance $r\sigma_0/J = 3$ 24

3.17 J-Q trajectories at X = 0 mm for a normalized distance $r\sigma_0/J = 4$ 24

3.18 J-Q trajectories at X = 0 mm for a normalized distance $r\sigma_0/J = 5$ 25

3.19 J-Q trajectories at X = 26 mm for a normalized distance $r\sigma_0/J = 2$ 25

3.20 J-Q trajectories at X = 26 mm for a normalized distance $r\sigma_0/J = 3$ 26

3.21 J-Q trajectories at X = 26 mm for a normalized distance $r\sigma_0/J = 4$ 26

3.22 J-Q trajectories at X = 26 mm for a normalized distance $r\sigma_0/J = 5$ 27

3.23 J-Q failure locus for A 533 grade B class 1 steel at $T - RT_{NDT} = -10°C$ 27

3.24 HSST shallow-crack fracture toughness results as function of normalized temperature $T - RT_{NDT}$ 30

3.25 Toughness data at $T - RT_{NDT} = -25$ to $-10°C$ as function of crack depth 30

3.26 SSY toughness (K_o) results as function of normalized temperature 32

3.27 K_o data at $T - RT_{NDT} = -25$ to $-10°C$ as function of crack depth 33

3.28 Determination of finite-body to SSY toughness ratio from stresses ahead of crack tip 34

3.29 Finite-body to SSY toughness ratio as a function of normalized distance ahead of crack tip 35

3.30 Opening-mode stresses ahead of crack tip for the SSY solution and uniaxial and biaxial cruciform specimens at critical values of J 36

3.31 Q-stress ahead of crack tip at critical values of J for uniaxial and biaxial cruciform specimens 37

4.1 Schematic defining fractographic variables 41

4.2 (*a*) Distributions of opening-mode stress component for SENB specimen with a/W = 0.1 as function of applied load up to crack initiation; (*b*) distribution of opening-mode stress component for biaxial shallow-crack cruciform specimen; (*c*) toughness vs normalized distance to initiation site for shallow- and deep-crack SENB specimens; and (*d*) toughness vs normalized distance to initiation site for uniaxial and biaxial shallow-crack cruciform specimens 42

4.3 Crack-driving force through-thickness for BB-4 and -5 43

4.4 3-D toughness results as function of load ratio for data at $RT_{NDT} = -10°C$ 45

A.1 (*a*) Finite-element model employed to obtain SSY reference solution; (*b*) crack-tip region of SSY finite-element model 53

A.2 SSY plane strain reference fields for cruciform bend specimen 54

B.1 Comparison of calculated (finite strain) and measured LLD for cruciform bend specimens 55

B.2 Comparison of calculated (finite strain) and measured CMOD for cruciform bend specimens 56

B.3 Applied J at specimen midplane (X = 0 mm) (finite strain) 56

B.4 Normalized opening-mode stress ahead of crack tip, X = 0 mm, uniaxial loading (finite strain) 57

B.5 Normalized opening-mode stress ahead of crack tip, X = 0 mm, biaxial 0.6:1 loading (finite strain) 57

B.6 Variation of Q with normalized distance ahead of crack tip, X = 0 mm, uniaxial loading (finite strain) 58

B.7 Variation of Q with normalized distance ahead of crack tip, X = 0 mm, biaxial 0.6:1 loading (finite strain) 58

B.8 J-Q trajectories at X = 0 mm for normalized distance $r\sigma_0/J = 2$ (finite strain) 59

B.9 J-Q trajectories at X = 0 mm for normalized distance $r\sigma_0/J = 3$ (finite strain) 59

B.10 J-Q trajectories at X = 0 mm for normalized distance $r\sigma_0/J = 4$ (finite strain) 60

B.11 J-Q trajectories at X = 0 mm for normalized distance $r\sigma_0/J = 5$ (finite strain) 60

List of Tables

Table		Page
2.1	Test matrix for development phase of biaxial testing program	8
2.2	Summary of results of the development phase of the biaxial testing program	9
3.1	Results of scaling model applied to shallow-crack data	31
3.2	Scaling model results at distances ahead of crack tip for the uniaxial and biaxial cruciform specimens	34
3.3	SSY toughness results for the uniaxial and biaxial cruciform specimens	36
4.1	Summary of fractographic information	40
4.2	3-D interpretation of toughness	44

Acknowledgments

The authors would like to acknowledge the valuable discussions with Professor Robert H. Dodds, Jr., University of Illinois, concerning interpretations of analytical results presented in this report. We also acknowledge the contributions of Professor Stanley T. Rolfe of the University of Kansas, W. E. Pennell, D. E. McCabe, and J. A. Keeney of ORNL in reviewing this manuscript.

1 Introduction

Postulated pressurized-thermal-shock (PTS) accident conditions remain an important safety assessment issue in the licensing of commercial nuclear reactor pressure vessels (RPVs), especially in the case of aging nuclear plants. The development of technology required for an accurate safety assessment of RPVs under PTS conditions is a focal point of the U.S. Nuclear Regulatory Commission (NRC)-funded Heavy-Section Steel Technology (HSST) Program. Currently, the HSST Program is seeking an improved understanding of several issues that could significantly impact the fracture mechanics technologies employed in these safety-assessment procedures. One important area of research is that of crack-tip constraint, a topic that encompasses a number of factors relating to the material fracture resistance, as well as to the transfer of fracture toughness data from small-scale specimens (i.e., surveillance specimens) to large-scale structures. Factors affecting crack-tip constraint include structural and crack geometry, loading conditions, and material properties. Within these categories, far-field, tensile out-of-plane biaxial loading conditions, and shallow-surface crack effects have been identified as issues that could significantly impact RPV safety assessments. Crack-tip constraint effects of shallow cracks and biaxial loading influence both the fracture toughness and the width of the fracture toughness scatter band (described in this report). These influences can have a substantial impact on the outcome of probabilistic PTS analyses and assessments of startup/cooldown transients for aging nuclear plants.

This report provides an overview of ongoing HSST Program research aimed at evaluating the effects of biaxial loading conditions and shallow-crack geometries on constraint conditions. A validated technology that incorporates these constraint effects is essential to the transfer of fracture toughness data to RPVs from, for example, miniature fracture toughness surveillance specimens. Consequently, development and evaluation of fracture methodologies for the quantitative assessment of crack-tip constraint effects on fracture toughness represent a major element of this research.

The motivation for the HSST biaxial fracture toughness testing program[1] stems from several observations. First, startup/cooldown and PTS transients produce biaxial stress fields in an RPV wall with a significant positive out-of-plane stress aligned parallel to postulated surface cracks oriented in either the longitudinal or the circumferential direction (Fig. 1.1). Second, current RPV assessments are based on data generated from specimens that were loaded under uniaxial conditions. Furthermore, experimental evidence (see Ref. 1) of the influence of biaxial loading on fracture toughness, although scarce and difficult to interpret, indicates a decrease in toughness associated with biaxial loading. Consequently, a testing program was begun within the HSST Program to examine the influence of biaxial loads on shallow-flaw specimens under conditions prototypic of RPV service conditions.

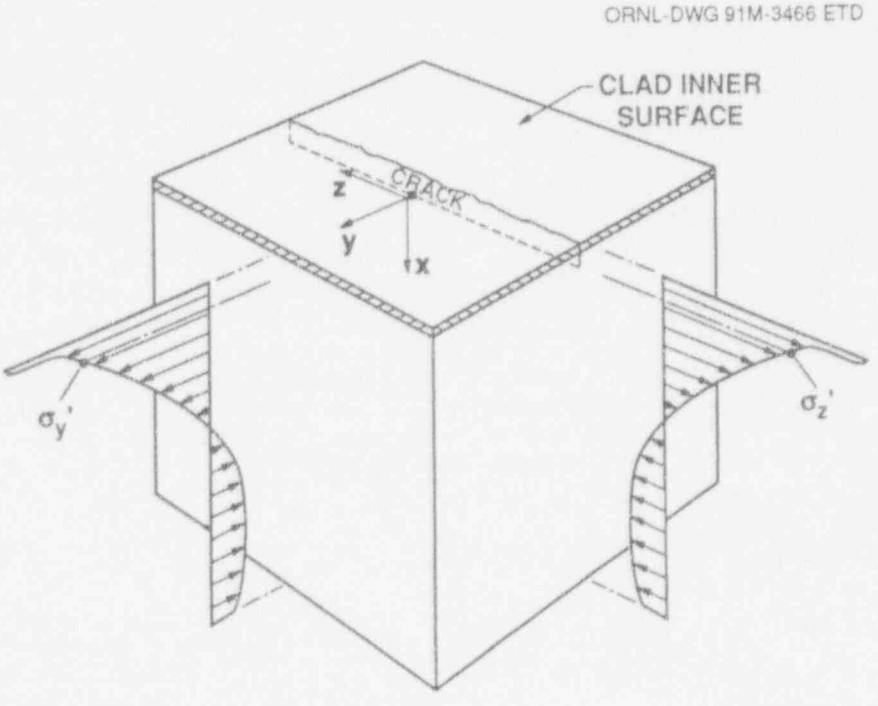

Figure 1.1 Vessel wall biaxial far-field stresses during PTS transient with one component aligned parallel to front of longitudinal crack

Introduction

Shallow-flaw specimens were used in the biaxial testing program for several reasons. First, the probability of failure of an RPV in a PTS analysis is dominated by initiations that originate from shallow flaws (<25 mm).[2–4] Second, recent testing[5] has shown an increase in the fracture toughness of specimens with shallow flaws compared to deep-flaw specimens (see Fig. 1.2 taken from Ref. 1).

In Fig. 1.2, the increase in toughness for shallow-crack beams is quantified in terms of a temperature shift. The shallow-crack lower-bound curve for essentially one crack depth was estimated by using the deep-crack lower-bound curve shifted to lower temperatures by T_S = 35 K (63°R). This temperature shift, which is crack-depth dependent, could be greater for shallower cracks that are also important in RPV analysis. The shifted lower-bound curve fits the shallow-crack data well at all test temperatures. However, any increase in crack-tip constraint resulting from tensile out-of-plane biaxial stresses would act in opposition to the in-plane constraint relaxation demonstrated by the uniaxial shallow-crack data. Potentially, this could lead to a reverse temperature shift (T_B in Fig. 1.2) of the lower-bound toughness curve that offsets the uniaxial "shallow-crack" effect by an undetermined amount. The existence and magnitude of a temperature shift due to biaxial stress effects must be determined from data generated in the transition region of the fracture toughness curve.

Current pressure vessel fracture prevention technology relies on the use of fracture-correlation parameter (K) to characterize both the applied load and the resistance of material to crack initiation. Shortcomings of these conventional one-parameter, fracture-correlation methods, which impact issues associated with the transferability of small-specimen (i.e., surveillance-sized) toughness data to large-scale RPV applications, are being addressed through evaluation of various dual-parameter fracture methodologies. These dual-parameter formulations[6–11] show promise as practical means for introducing the effect of crack-tip constraint into RPV safety assessments.

The existing methodologies being investigated within the HSST Program include stress-based fracture characterizations (i.e., J-Q methodology of O'Dowd and Shih[6–8,11] combined with Ritchie-Knott-Rice (RKR) fracture criteria[12] and the Dodds-Anderson constraint correction technique[9–11]) and stress-strain-based characterizations (i.e., plane strain fracture ductility techniques of Clausing,[13] Barsom,[14] Merkle,[15] and other researchers). Determinations are being made concerning the bounds of

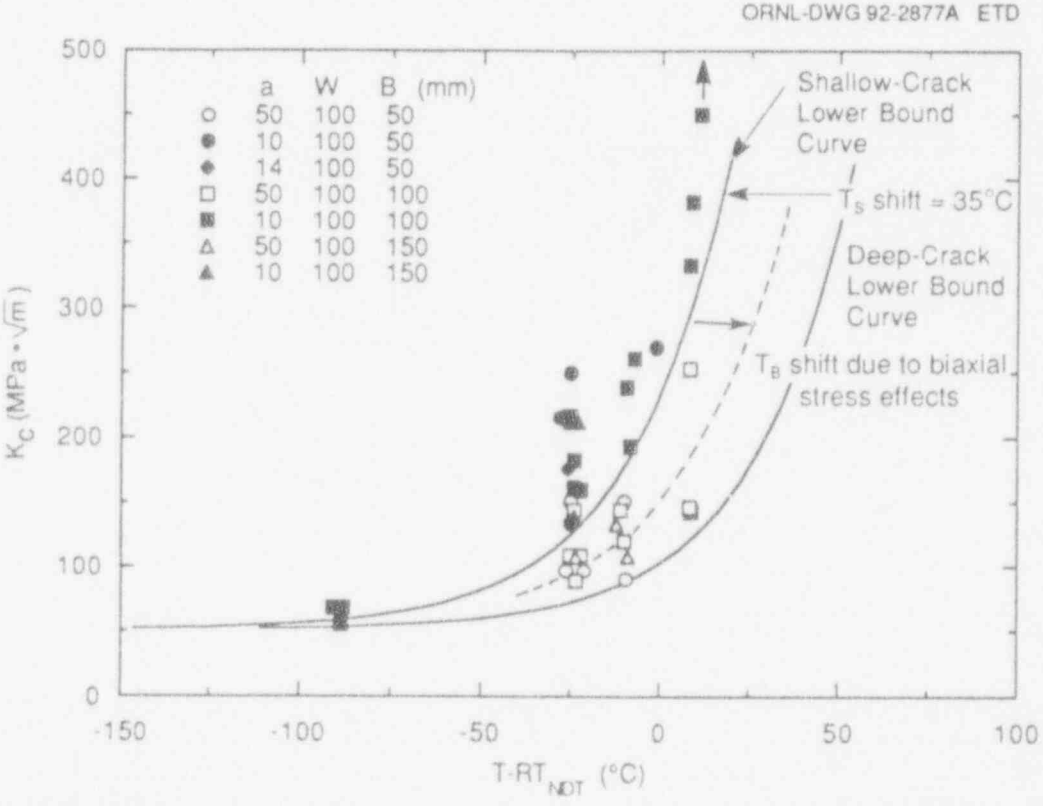

Figure 1.2 Toughness (K_{Jc}) data vs normalized temperature for shallow- and deep-crack specimens with shallow- and deep-crack lower-bound curves

applicability of the existing constraint effects correlation methodologies (i.e., how effective are they in matching existing data?). If the existing methodologies are found to be deficient, determinations will be made concerning whether or not they can be modified to make them work. If necessary, alternative constraint methodologies will be developed and validated.

The following chapters describe applications of the stress-based constraint characterizations developed by O'Dowd and Shih[6–8,11] and by Dodds and Anderson[9–11] to experimental and fractographic data obtained from conventional single-edge notch bend (SENB)[5] and cruciform beam[1] specimens tested in the HSST Program. Chapter 2 provides summaries of the HSST testing programs[1,5] that utilized conventional shallow- and deep-crack SENB specimens and cruciform specimens tested under uniaxial and biaxial loading, respectively. Chapter 3 describes the effect of loading conditions (biaxial vs uniaxial) on crack-tip stress triaxiality in the cruciform beam specimen, based on applications of J-Q methodology. Also, results from applications of the Dodds-Anderson (D-A) fracture toughness scaling model to data from both conventional SENB and cruciform beam specimens are presented. Fractographic data taken from the fracture surfaces of the beam specimens are described in Chap. 4; also, some fracture characterization issues arising from comparison of analysis predictions with fractographic data are discussed. Finally, a summary and interim conclusions are provided in Chap. 5.

2 Biaxial and Shallow-Crack Testing Programs

2.1 Summary of Shallow-Crack Testing Program

The HSST Shallow-Crack Fracture Toughness Testing Program has been ongoing since FY 1990, producing data by testing 100-mm-deep SENB specimens. Results from the testing portion of the program have been reported previously.[5] A summary of the findings from the shallow-crack fracture toughness testing program are included here for completeness.

1. Thirty-eight relatively large (W ~ 100 mm deep) laboratory beam specimens were tested to compare the behavior of specimens with shallow flaws to that of specimens with deep flaws.

2. The results showed conclusively that shallow-flaw beam specimens of A 533 B material have a significant increase in crack-tip-opening displacement (CTOD) or J_c toughness (~150%) and K_{Jc} toughness (~60%) over deep-crack specimens in the transition region of the toughness curve. All specimens were 100 mm deep (W). Shallow-crack beams had crack depths ranging from 9 to 14 mm (a/W ~ 0.1 to 0.14), while deep-crack beams had 50-mm-deep cracks (a/W ~ 0.5).

3. There is little or no difference in toughness between deep- and shallow-flaw specimens on the lower shelf where linear-elastic conditions exist.

4. Varying the beam thickness from 50 to 150 mm had little or no influence on the toughness in both the shallow- and deep-crack specimens in spite of the fact that the American Society for Testing and Materials (ASTM) E-399 requirement for valid plane strain results were not met. This observation suggests that plane strain behavior for steels of this strength level differ from ASTM E399.

5. In the transition region of the fracture toughness curve, the increase in shallow-flaw toughness compared with deep-flaw toughness appears to be well characterized by a temperature shift of about 35°C. This temperature shift, which is crack-depth dependent, could be greater for shallower cracks that are also important in RPV safety assessments.

6. Posttest 2-D plane strain analyses were performed on both shallow- and deep-flaw specimens. The analytical J-integral results were consistent with experimental J-integral results, confirming the validity of the J-estimation schemes used and the effect of flaw depth on fracture toughness.

7. The two-parameter J-Q analysis methodology was used as a means of quantifying the effect of flaw depth on constraint and fracture toughness. Analysis results appear to support the utility of the J-Q concept and interpretation method to characterize the crack-tip fields up to the onset of crack initiation in specimens with either deep or shallow flaws. At J-critical (onset of cleavage initiation) for the deep-flawed specimens, the Q-stress was about zero, indicating small-scale yielding (SSY) conditions. At J-critical for the shallow-flawed specimens, the Q-stress was about –0.7. This negative Q-stress indicates a significant loss of constraint.

8. The observation that the two-parameter J-Q approach correlated with the loss of constraint with decreasing crack depth indicates that a J-Q analysis of actual reactor vessels may give more accurate failure predictions than current analyses.

Results (figures, tables, etc.) from the shallow-crack program have been combined with the biaxial testing program results[1] and are presented as necessary. Fracture toughness determinations are based on the use of the area under the load vs the crack-mouth-opening-displacement (CMOD) curve method described in Ref. 1.

2.2 Biaxial Testing Program

Results of the development phase of the Oak Ridge National Laboratory (ORNL)/HSST biaxial testing program were reported previously in Ref. 1. A description of the cruciform bend specimen and a summary of results from the program are included here for completeness.

2.2.1 Cruciform Bend Specimen

The configuration of the cruciform bend specimen used in the testing program is depicted in Fig. 2.1. The specimen has a cruciform-shaped geometry with a cross section with dimensions of 91 × 102 mm and a straight through-crack of uniform depth of 10 mm in the test section. The total length of this specimen in the longitudinal or transverse direction, including the test section and the loading arms, is 610 mm. Three slots are machined into each arm to minimize diffusion of the load around the test section

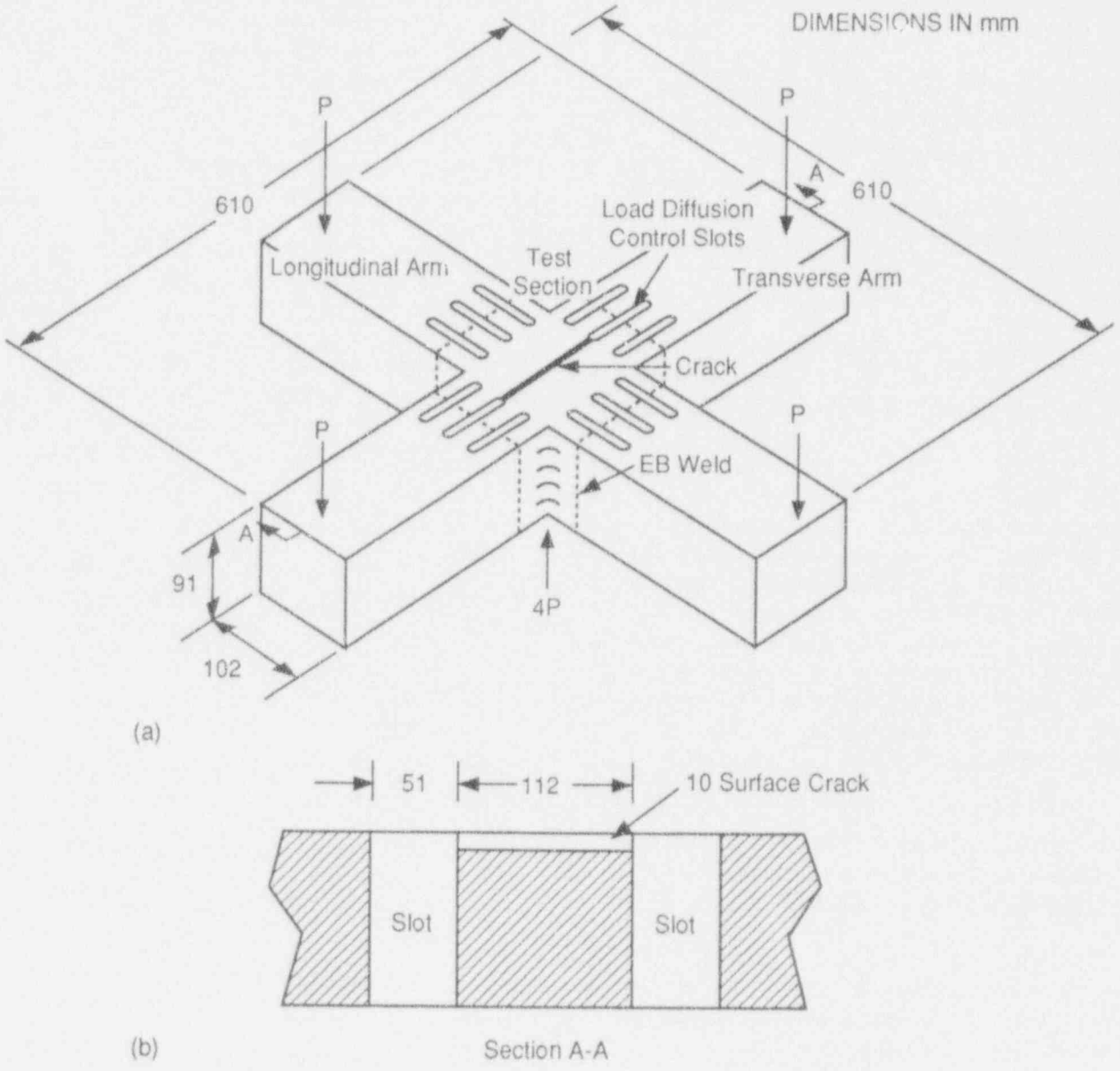

Figure 2.1 Cruciform bend specimen used in HSST biaxial testing program: (a) dimensions of cruciform specimen and (b) detail of crack plane

containing the through-crack. The crack is cut between two opposite central load diffusion control slots to produce a two-dimensional (2-D) shallow crack with no singularity on the surface. Figure 2.1(*b*) shows the profile of the crack and the intersection of the crack and the central slot.

The test section of the specimen is fabricated from A 533 grade B class 1 steel plate previously employed in the HSST wide-plate[16,17] and shallow-crack[5] testing programs. The specimen is notched and precracked after the two longitudinal arms are electron-beam (EB) welded to the test section. EB welding is employed to ensure minimal distortion in the specimen and a relatively small heat-affected zone. The distance from the weld to the crack is sufficiently large that residual stresses at the crack tip are low. Following precracking, a machining operation is performed to remove an embrittled layer of material thickness (~0.38 mm) at the root of each central load-diffusion control slot where it intersects the crack. The embrittled layers are introduced into the specimen by an electro-discharge machining process used to cut the slots. Then the transverse arms are EB welded to the specimen.

Instrumentation is placed on the specimen to monitor CMOD, load-line displacement (LLD), surface strain, and temperature at various locations. A special load reaction system has been constructed for applying bending loads (P) to the arms of the specimen in a statically determinant manner. Loading is applied at midspan to the specimen using a square, flat seat having rounded edges and the same planar dimensions as the test section. The test section bends into two orthogonal surfaces that contact the seat along the outer edges, resulting in eight-point bending (or four-point bending for the uniaxial case). Additional details concerning instrumentation and the specially designed loading system for the cruciform specimen are given in Ref. 18.

An important element in the design of the cruciform specimen concerns the optimal positioning of the center load-diffusion control slots to minimize peak K_I values and stress concentrations at the end of the crack. Results from 2-D and three-dimensional (3-D) finite-element analyses (described in Ref. 1) indicate that locating the center and outer load-diffusion control slots at different distances from the specimen midplane can be effective in controlling these peak K_I values. Figure 2.2 illustrates different slot configurations that were analyzed to demonstrate the techniques. In Fig. 2.2(*a*), the edge of the center slot is positioned at the boundary of the specimen test section. In Fig. 2.2(*b*), the outer slot extends inward across the test section boundary for a distance of 8.9 mm and toward the specimen centerline. Figure 2.2(*c*) shows a configuration from which the center slot is located away from the test section boundary a distance of 5.1 mm and away from the specimen centerline. The slot configuration of Fig. 2.2(*d*) represents a superposition of the shift in the outboard slots of Fig. 2.2(*b*) and of the center slot in Fig. 2.2(*c*), which yields a cumulative slot differential of 14 mm. The common factor of configurations (*b*)–(*d*) in Fig. 2.2 is that the outer slots project farther in toward the specimen centerline than does the center slot. Slot configuration (*d*) essentially eliminates stress concentrations that are present at the ends of the crack in configuration (*c*). Results for contours of von Mises effective stress (see Ref. 1) indicate a similar reduction in stress peaks at the end of the crack for configuration (*d*) when compared to configuration (*c*).

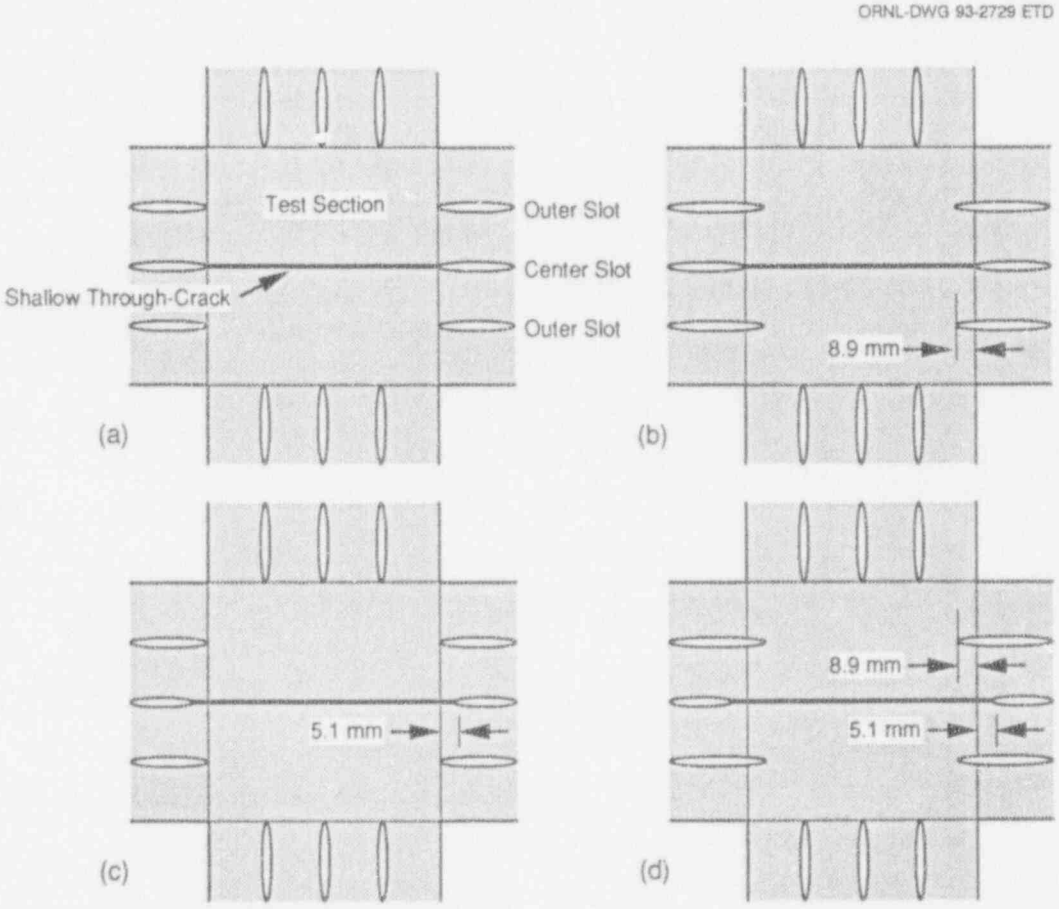

Figure 2.2 Slot configurations used in analyses of the cruciform bend specimen: (*a*) uniform slots on test section boundary, (*b*) outer slots extended inward by 8.9 mm across test section boundary, (*c*) center slot contracted away by 5.1 mm from test section boundary, (*d*) a superposition of configurations (*b*) and (*c*)

2.2.2 Test Matrix

The HSST Program assigned five cruciform specimens to the initial development phase of the biaxial testing program. These "development" specimens were used to evaluate the performance of the test specimen, test fixture, and procedures and to develop a test specimen geometry suitable for the generation of biaxial fracture toughness data.

Three specimen configurations having slot geometries shown in Fig. 2.2(*b*)–(*d*) were tested. As indicated in the summary of the test matrix shown in Table 2.1, configurations (*c*) and (*d*) represented two specimens each. In addition, to ensure that initiation did not occur at the crack-slot intersection of configuration (*d*), each corner of the crack was blunted with a slitting saw.

Table 2.1 Test matrix for development phase of biaxial testing program

Specimen No.	Test section configuration	Load ratio
BB-1	*b*	0.6:1
BB-2	*c*	0:1
BB-3	*c*	0.6:1
BB-4	*d*	0.6:1
BB-5	*d*	0.6:1

Of the five development specimens, four were tested under biaxial loading, and one was tested under uniaxial loading. All biaxially loaded cruciform specimens were tested with a transverse-to-longitudinal load ratio of 0.6:1, as described in Ref. 1. The uniaxially loaded cruciform specimen allows comparison with previous uniaxial shallow-crack specimens under identical test conditions (crack depth, temperature, etc.). Testing cruciform specimens in both uniaxial and biaxial loading configurations will allow toughness values to be measured with only one test condition changed, namely, the out-of-plane loading.

Test conditions were selected to facilitate comparison of data from the cruciform specimens with previous HSST shallow-crack data tested under uniaxial conditions.[5] Several of the uniaxial shallow-crack tests were conducted at $T - RT_{NDT} = -10°C$, which is in the transition region of the deep-crack toughness curve for A 533 B steel. The A 533 B steel used for the test section material in these tests has an RT_{NDT} of –35°C. Therefore the test temperature for the cruciform specimen tests was set at –45°C. The cruciform specimens were 91 mm deep with a crack depth of 10 mm. The beam width (W) and crack depth (a) of the cruciform specimen are approximately the same as for the HSST shallow-crack beams.

2.2.3 Experimental Results and Interpretation

The conditions of each specimen at failure, test temperature, and specimen geometry are tabulated in Table 2.2 (from Ref. 1). Also included in the table are the plastic component of the area under each P vs LLD curve (defined as U_{pl}) and P vs CMOD curve (defined as A_{pl}). Table 2.2 also lists the estimated toughness values for the tests with the parameters used to estimate the toughness. The load indicated in the table refers to the longitudinal load, that is, the total load (as measured by the load cell) divided by 1.6 for the biaxial tests. The results indicated in Table 2.2 reveal consistent, repeatable mechanical responses for the five tests.

The test results indicate that the critical load for each specimen was similar but that in the uniaxial test (BB-2) the specimen was able to withstand substantially more (≈60%) deflection (LLD or CMOD) than the biaxial tests (BB-1, -4, and -5). (Strains imposed in these tests were substantially higher than any that would be produced in an RPV either from normal or accident loading; this is a consequence of testing in the transition region of the toughness curve.) In addition, the plastic "work" at the crack tip as defined by either U_{pl} or A_{pl} in the three biaxial tests was about one-third of the corresponding uniaxial value of U_{pl} or A_{pl}. Furthermore, the critical displacements (LLD or CMOD) and work performed (U_{pl} or A_{pl}) were consistent for the three interpretable biaxial test results. These results indicate a pronounced reduction in the ductility of the material at fracture (as measured by critical displacement or work) due to biaxial loading.

Toughness data for the biaxial and uniaxial cruciform specimens were calculated using the techniques described in Ref. 1. The critical J-integral values were converted to critical elastic-plastic, stress-intensity factors K_{Jc} using the plane strain formulation.* The data necessary to estimate J and the resulting toughness values are tabulated in

*Some adjustment of the relationship between J and K may be appropriate for the positive out-of-plane strain condition generated in the biaxially loaded cruciform specimen. The form of this adjustment (if any) has not yet been investigated; however, future plans call for it to be a subject of study within the HSST Program. In this report, the plane strain conversion from J to K is employed as a matter of convention for comparison with existing data. Experimental and analytical results described herein for toughness values and crack-driving forces are generated in terms of J and consequently are unaffected by the conversion from J to K.

Table 2.2 Summary of results of the development phase of the biaxial testing program

	BB-1	BB-2	BB-3	BB-4	BB-5	Average SENB data (for comparison)
Load ratio	0.6:1	0:1	0.6:1	0.6:1	0.6:1	
Geometry						
B, mm	102	111	112	111	111	101
W, mm	91	91	91	91	91	102
a, mm	11.1	10.6	8.8	10.1	10.0	10.7
Temperature, °C	–45	–41	–47	–46	–44	–23[a]
Failure conditions			[b]			
P, kN	784	784		818	751	763
LLD, mm	4.20	8.51		5.10	5.08	4.06
CMOD, mm	0.47	0.82		0.47	0.51	0.65
U_{pl}, kN-mm	958	4110		1523	1501	1163
A_{pl}, kN-mm	168	455		181	206	329
η-factors			[b]			
η_{pl}^{ℓ}	0.195	0.117		0.189	0.190	1.15
η_{pl}^{c}	3.53	2.76		3.55	3.61	3.48
Fracture toughness			[b]			
Elastic component						
J_{el}, kN/m	66.7	67.4		72.6	61.2	67
K_I, MPa $\sqrt{m}$	120	120		125	115	122
P vs CMOD						
J_{pl}, kN/m	73.3	141		71.8	82.8	125
Total J, kN/m	140	209		144	144	192
K_{Jc}, MPa $\sqrt{m}$	175	214		178	178	206
P vs LLD						
J_{pl}	23.1	54.1		32.1	31.7	145
Total J	89.7	122		105	92.9	212
K_{Jc}	140	163		151	143	216

[a] RT_{NDT} for this material is –15°C, so $T - RT_{NDT}$ for these tests is the same.
[b] Not reported due to initiation in the corner.

Table 2.2. The P vs CMOD method is considered the more sensitive of the techniques examined for determining fracture toughness shallow-flaw specimens and is the primary method used for the cruciform specimen analysis.

Toughness results for the SENB and cruciform specimens expressed in terms of K_{Jc} are shown in Figs. 2.3–2.5 (taken from Ref. 1). Figure 2.3 shows the deep- and shallow-crack uniaxial toughness data as a function of normalized temperature. The data at $T - RT_{NDT} = -10°C$ are plotted as a function of crack depth in Fig. 2.4 and as a function of load ratio in Fig. 2.5. Examination of the data in Figs. 2.3–2.5 and Table 2.2 reveals several important points. First, biaxial loading appears to reduce the fracture toughness compared with either the uniaxial cruciform value from test BB-2 or the SENB data. The average of the biaxial toughness is ≈20% less than the uniaxial cruciform value and ≈18% less than the average of the uniaxial SENB and cruciform results.* Second, the uniaxial cruciform value is consistent with the SENB toughness results; this tends to validate the use of the cruciform specimen for uniaxial data generation. Third, the scatter band of the biaxial data may

*Conventional laboratory specimens have an essentially uniform crack-driving force through the thickness. Thus, toughness interpretations are based on a 2-D calculation without regard to the location of initiation sites along the crack front. The variation in crack-driving force through the thickness of the cruciform is substantially greater than that of conventional specimens. This variation, combined with fractography data on location of initiation sites, provides a basis for 3-D interpretations of fracture toughness described in Chap. 4. This 3-D interpretation tends to lower the toughness value determined from the specimen.

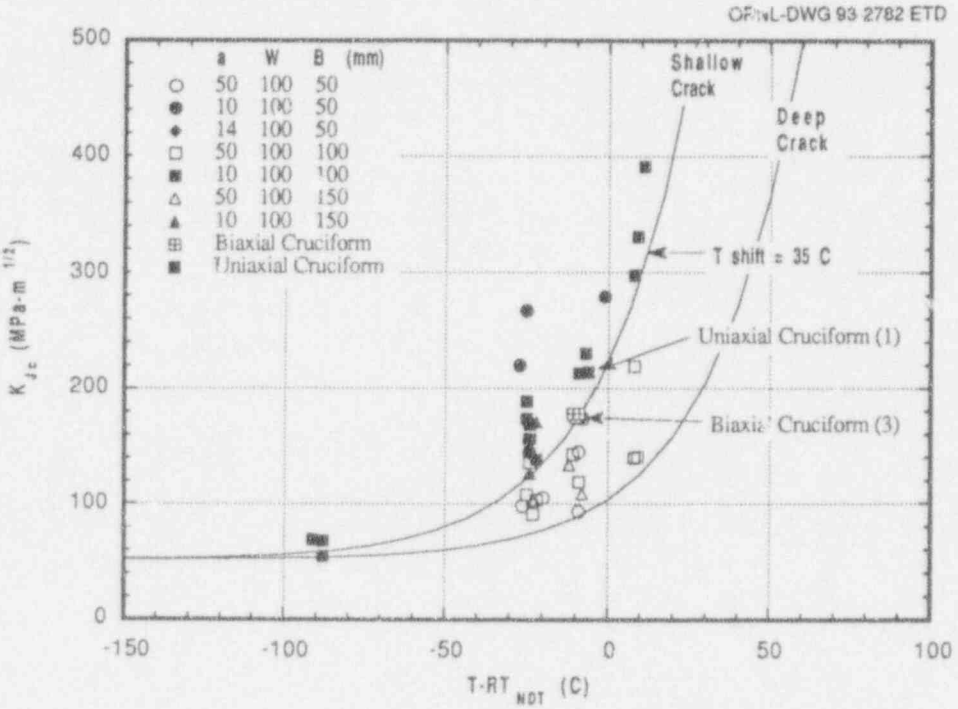

Figure 2.3 Biaxial and uniaxial shallow-crack toughness data as function of normalized temperature

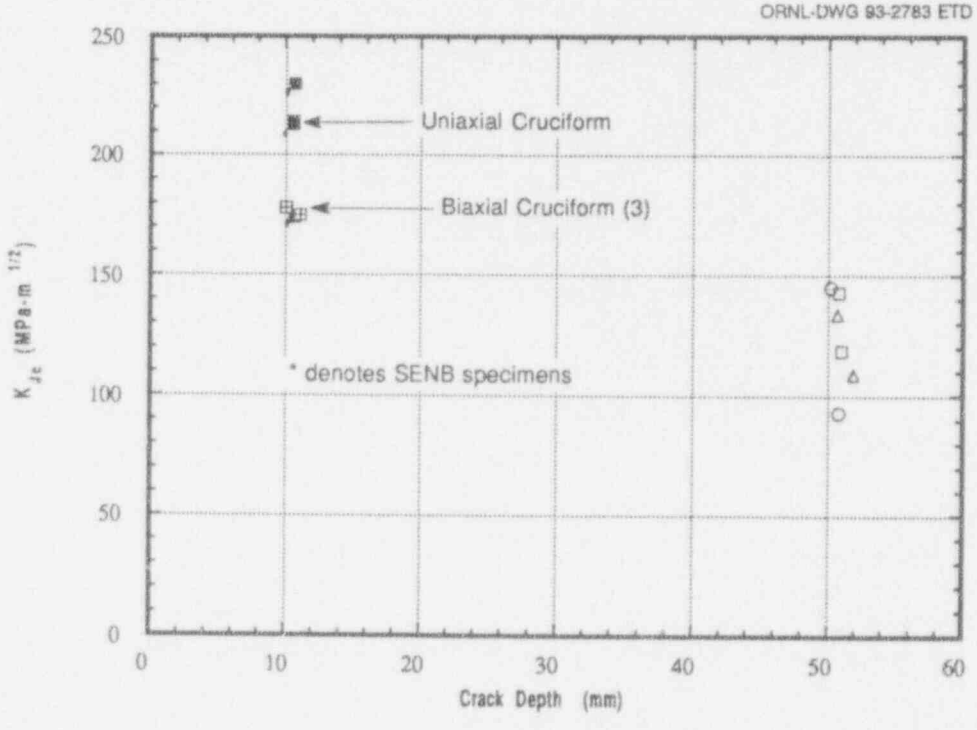

Figure 2.4 Uniaxial and biaxial toughness data as function of crack depth at $T - RT_{NDT} = -10°C$

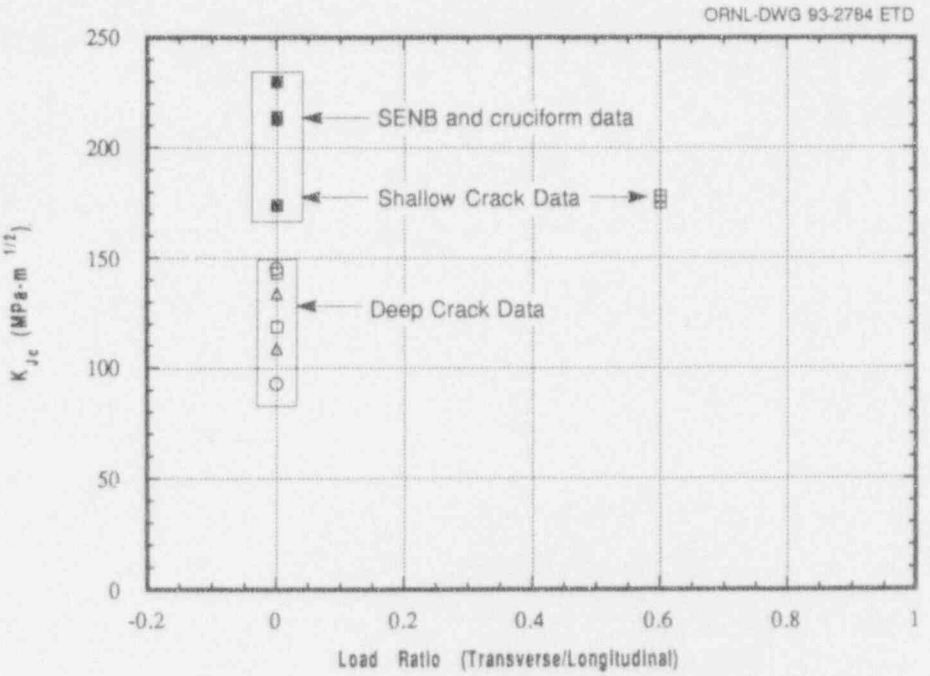

Figure 2.5 Toughness data for deep- and shallow-crack specimens as function of load ratio at $T - RT_{NDT} = -10°C$

be less than that associated with the uniaxial, shallow-crack data. An increase in toughness and scatter is associated with loss of constraint in laboratory specimens. Results presented in Fig. 2.4 indicate that biaxially loaded cruciform specimens yield results with reduced scatter. The trends in the biaxial and uniaxial cruciform data described here are tentative results based on very limited data. Additional data are required to substantiate these trends and to provide better quantification of the effect of biaxial loading on fracture toughness. Nonetheless these initial results strongly suggest that an improved understanding of the shallow-flaw and biaxial loading effects would significantly impact the fracture mechanics technologies employed in reactor vessel failure predictions.

3 Constraint Analyses

3.1 Finite-Element Analysis of Cruciform Specimen

Three-dimensional elastic-plastic, finite-element analyses were performed on the cruciform specimen depicted in Fig. 2.1. Local crack-tip stress fields obtained from these analyses are used in applications of stress-based constraint characterization models. The one-fourth section of the cruciform specimen depicted schematically in Fig. 3.1 is represented in the 3-D finite-element model of Fig. 3.2. The model consists of 18,650 nodes and 3,890 twenty-node isoparametric brick elements. Collapsed-prism elements arranged in a focused or centered fan configuration at the crack tip are used to produce a 1/r strain singularity appropriate for inelastic analysis. Reduced integration was employed to eliminate shear locking in the elements. The cruciform specimen is assumed to be supported on a rigid plate under the test section [i.e., the area defined by (-51 mm $\le Z \le 0$, $0 \le X \le 51$ mm) in Fig. 3.1] and loaded by uniformly applied forces at the ends of the longitudinal/transverse arms (i.e., locations C and D in Fig. 3.1) to produce the uniaxial or biaxial bending conditions. The rigid support plate is incorporated into the finite-element model of Fig. 3.2 using a contact element option in the ABAQUS (Ref. 19) finite-element program.

The full geometry of the load-diffusion control slots is represented in the finite-element model [Fig. 3.2(*b*)]. The slot geometry incorporated in the model is represented by the configuration of Fig. 2.2(*d*), which was used for test specimens BB-4 and -5. The same finite-element model was used for analysis of specimen BB-2, although the latter employed a different slot configuration [Fig. 2.2(*c*)]. The model also incorporated a highly refined mesh in the crack-tip region [Fig. 3.2(*c*)] to provide resolution of stress fields over the normalized distance $2 \le r\sigma_0/J \le 5$ in front of the crack.

The outermost semicircular ring of nodes in the mesh of Fig. 3.2(*c*) has a radius of 2 mm. This radius was extended to 4 mm in a second finite-element model developed for analysis of the BB-2 test [Fig. 3.2(*d*)]. The relatively

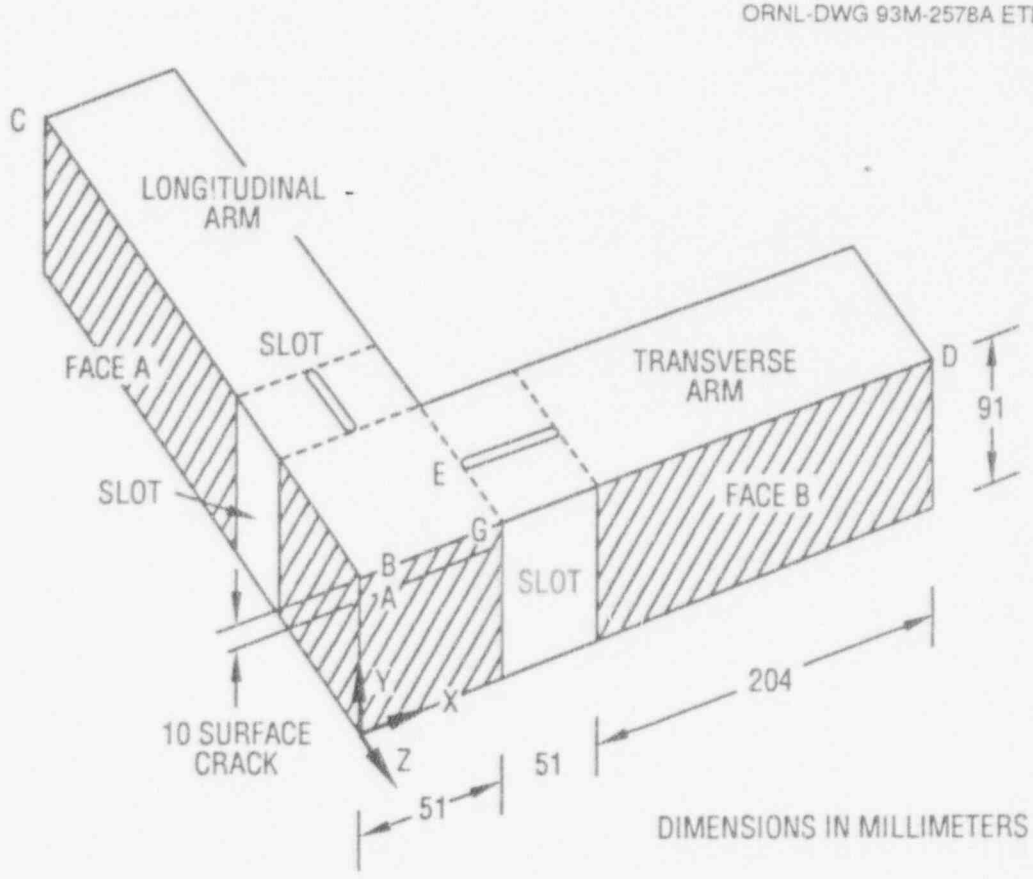

Figure 3.1 Definition of coordinate system and locations of interest for interpretation of finite-element results from analysis of HSST cruciform bend specimen

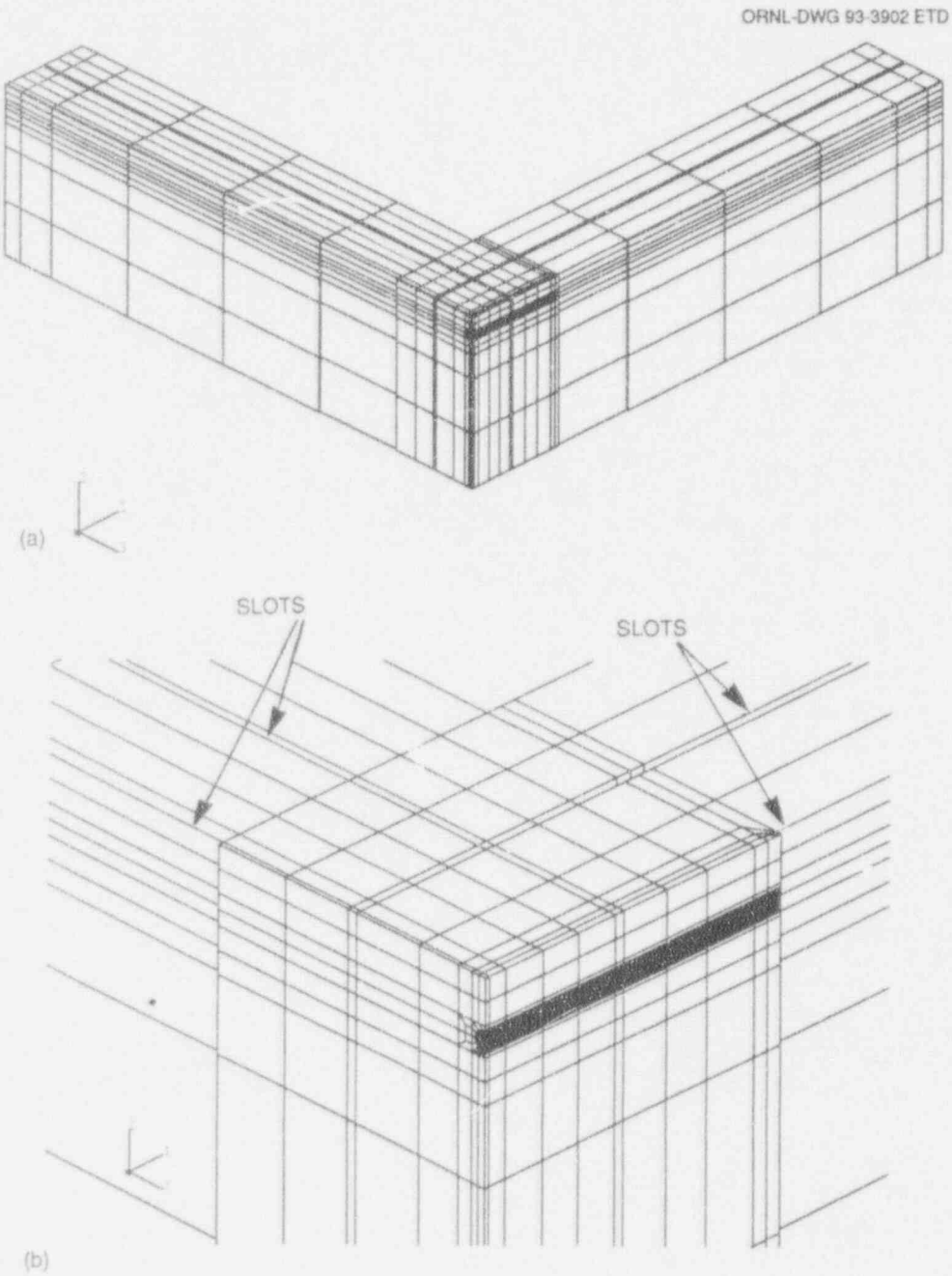

Figure 3.2 (*a*) **Finite-element model for local crack-tip analyses of cruciform bend specimen,** (*b*) **test section region of finite-element model for cruciform bend specimen,** (*c*) **highly refined crack-tip region of finite-element model for cruciform bend specimen, and** (*d*) **finite-element model with expanded region of refinement near the crack tip for analysis of uniaxially loaded cruciform specimen**

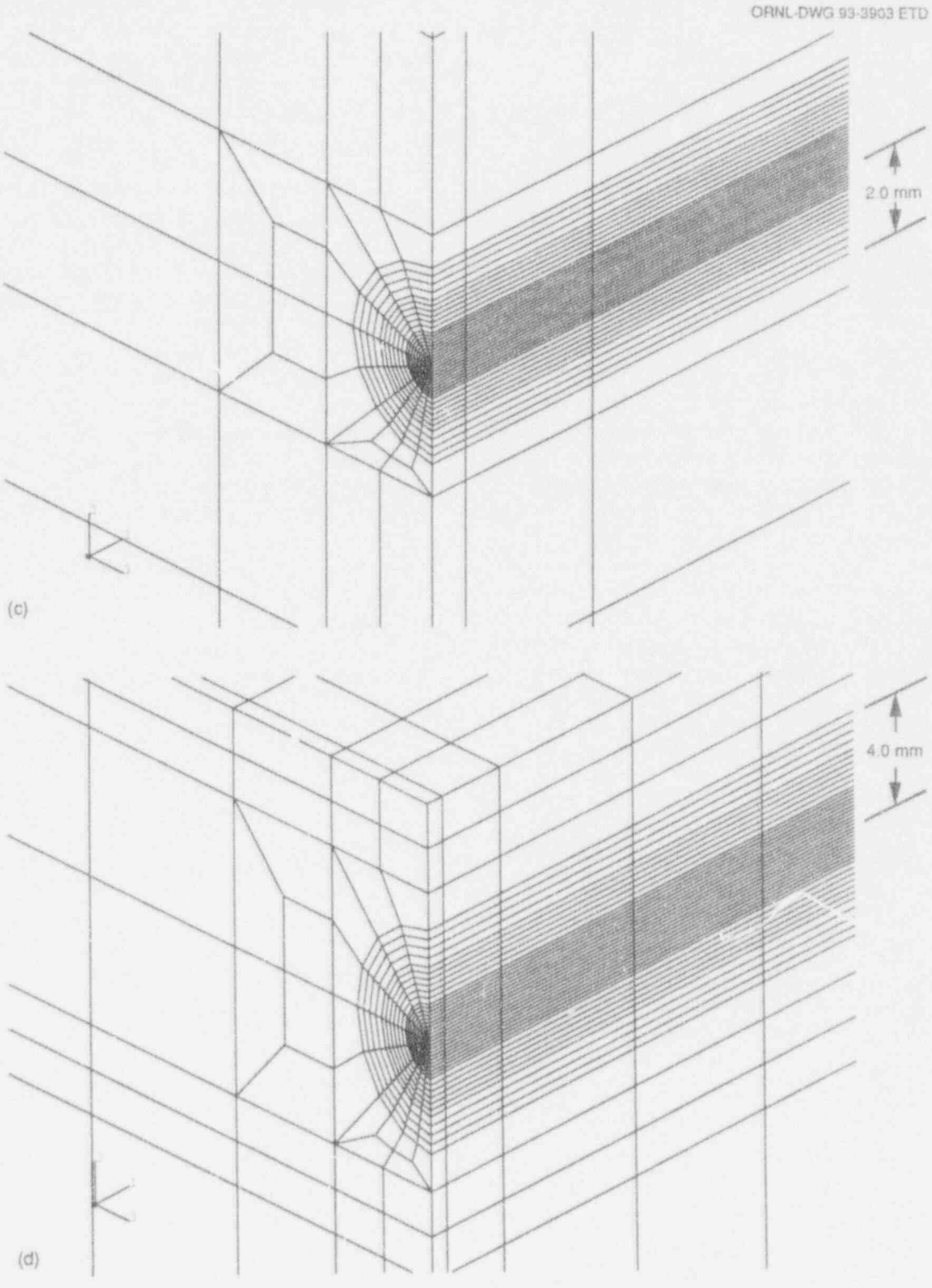

Figure 3.2 (continued)

higher failure load (measured in terms of J) of the latter test required an expanded region of refinement to resolve the stress at a normalized distance of $r\sigma_0/J = 5$.

The material properties used for all calculations presented herein include Young's modulus E = 205,170 MPa, Poisson's ratio ν = 0.25, and the piecewise linear stress strain curve depicted in Fig. 3.3. The curve in Fig. 3.3 represents a modification of material data for A 533 grade B class 1 steel taken from Ref. 17. The modification consists of an adjustment of the yield stress to produce better agreement with load vs CMOD data from the biaxial tests (described below).

Results from small-strain analyses of tests BB-2 (uniaxially loaded specimen) and BB-4 and -5 (biaxially loaded specimens) are compared with measured data in Figs. 3.4 and 3.5. Because geometry and test conditions were essentially the same for BB-4 and -5, only one computation was performed for the biaxial loading case. The longitudinal-to-transverse load ratio and the load to failure for each test are given in Table 2.2. In Fig. 3.4, the calculated longitudinal load vs LLD curves (measured at point C in Fig. 3.1) are compared with measured data from each of the three tests (BB-2, -4, and -5). Comparisons of calculated and measured longitudinal load vs CMOD for the same tests are given in Fig. 3.5. Both Figs. 3.4 and 3.5 show good agreement between the computed and measured load vs deflection curves for the BB-2 test. Minor differences between the CMOD curves in Fig. 3.5 for BB-2 may be partly due to differences in the slot configurations in the model and in the BB-2 test specimen. The load vs deflection curves for specimens BB-4 and -5 are within the data scatter for the two tests.

The applied J vs longitudinal load at two positions along the crack front, X = 0 and 26 mm (measured from the midplane), are given in Figs. 3.6 and 3.7 for the uniaxial and biaxial loading cases, respectively. These results illustrate the lower J-value computed for the biaxially loaded specimen at failure as compared to the uniaxial case. Figure 3.8 depicts the variation of K_J along the crack front as a function of the applied loading for the biaxially loaded specimen. As the failure load is approached in Fig. 3.8, the crack-driving force remains relatively uniform across the middle half of the crack front but decreases dramatically toward the ends of the crack. The slot configuration was designed to obtain this behavior to minimize the potential for crack initiation at the ends of the slots. In Fig. 3.9, the variations of K_J (normalized by the midplane value) along the crack front at low load and at load near failure are compared for the uniaxial and biaxial (0.6:1) loading cases. The differential placement of the outboard load-diffusion control slots (Fig. 2.2) effectively shields the end of the crack from effects of stress concentration and development of general yielding.

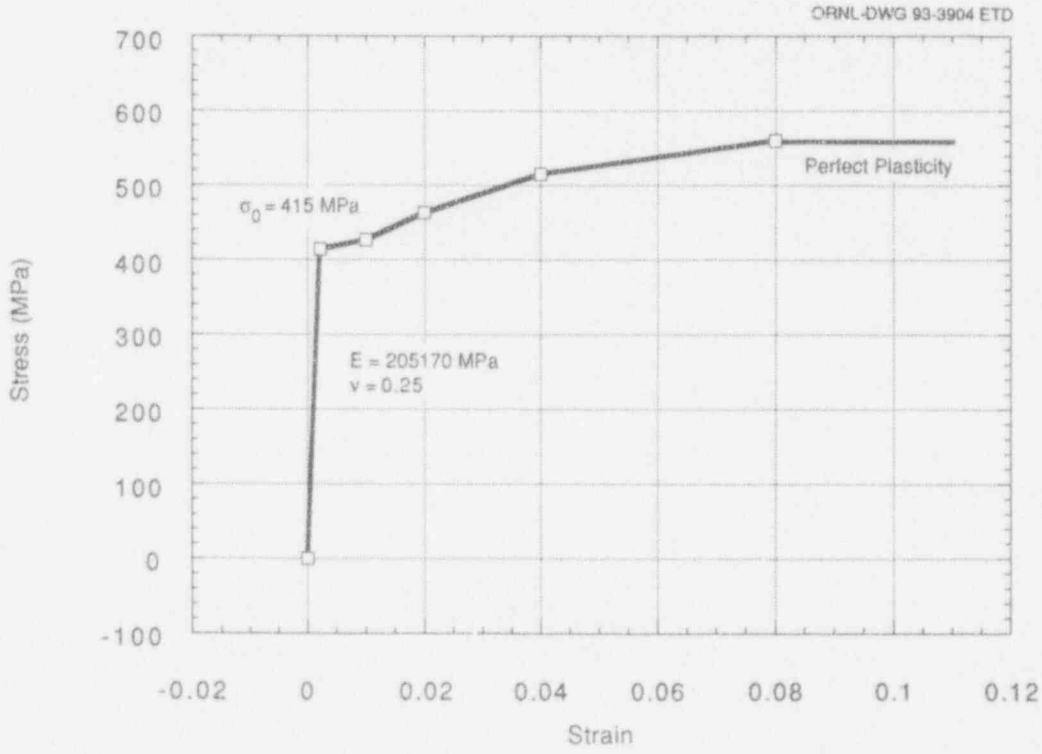

Figure 3.3 Material representation for A 533 B steel at T = –46°C

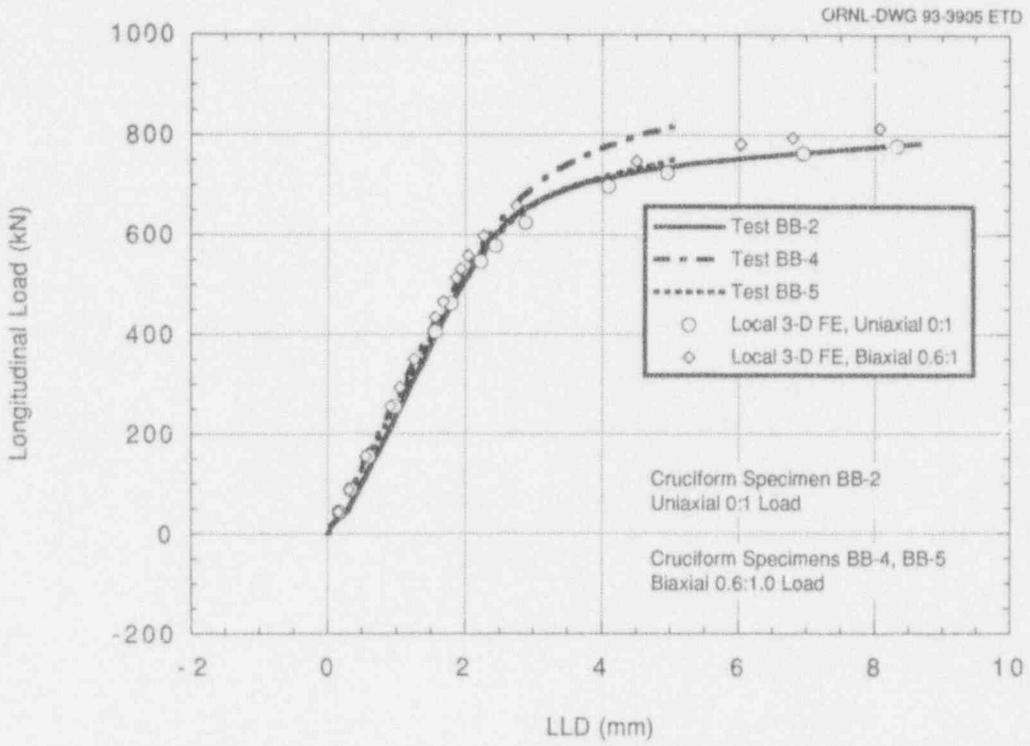

Figure 3.4 Comparison of calculated and measured LLD for cruciform bend specimens

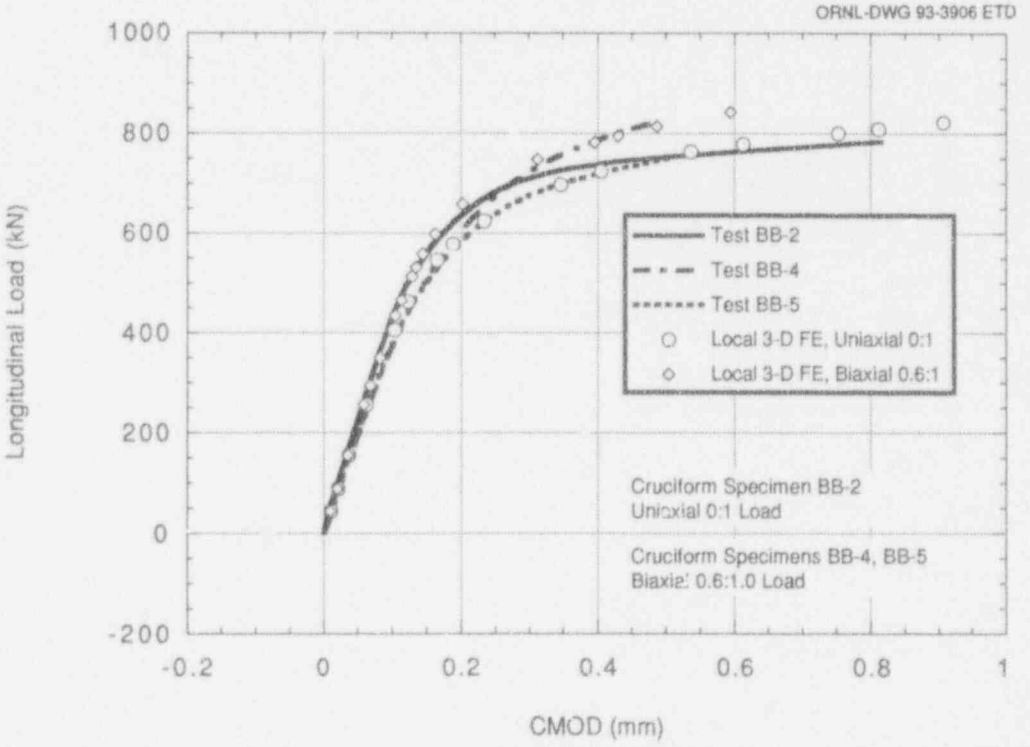

Figure 3.5 Comparison of calculated and measured CMOD for cruciform bend specimens

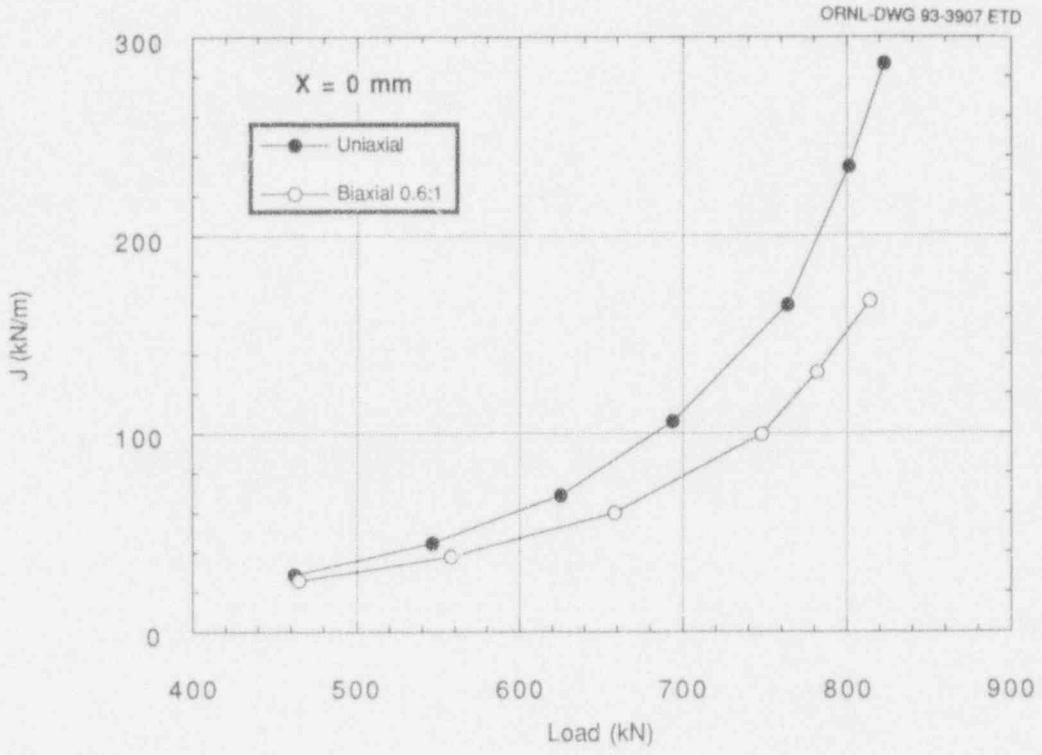

Figure 3.6 Applied J at X = 0 mm, uniaxial and biaxial 0.6:1 loading

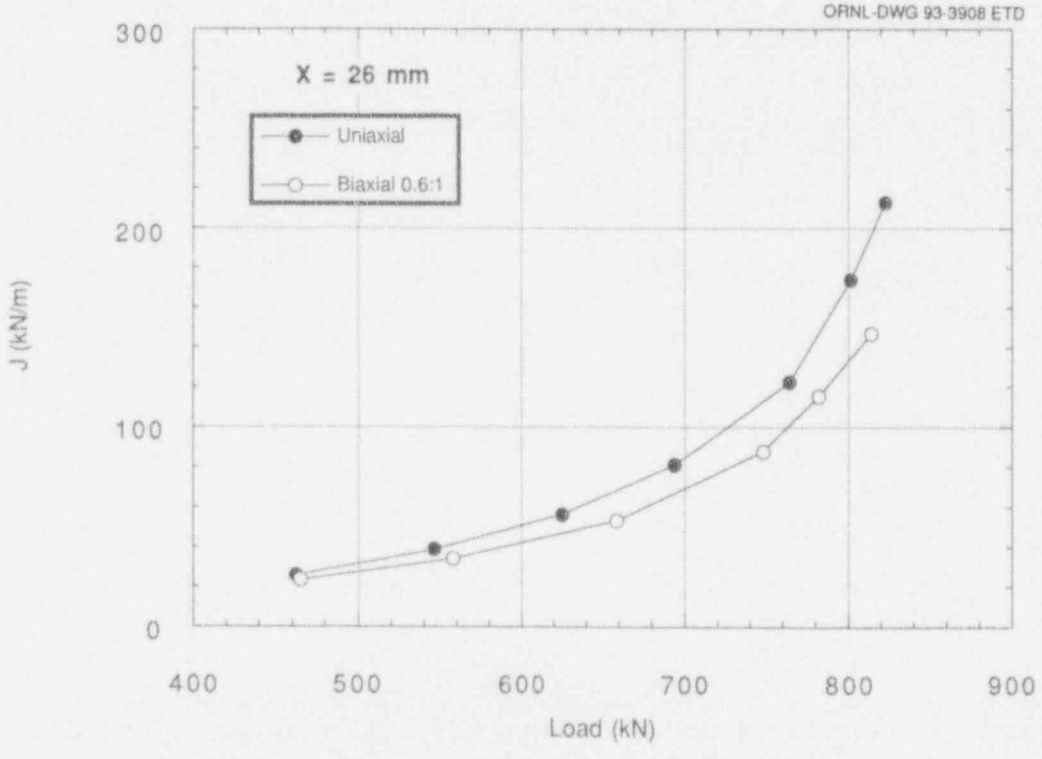

Figure 3.7 Applied J at X = 26 mm, uniaxial and biaxial 0.6:1 loading

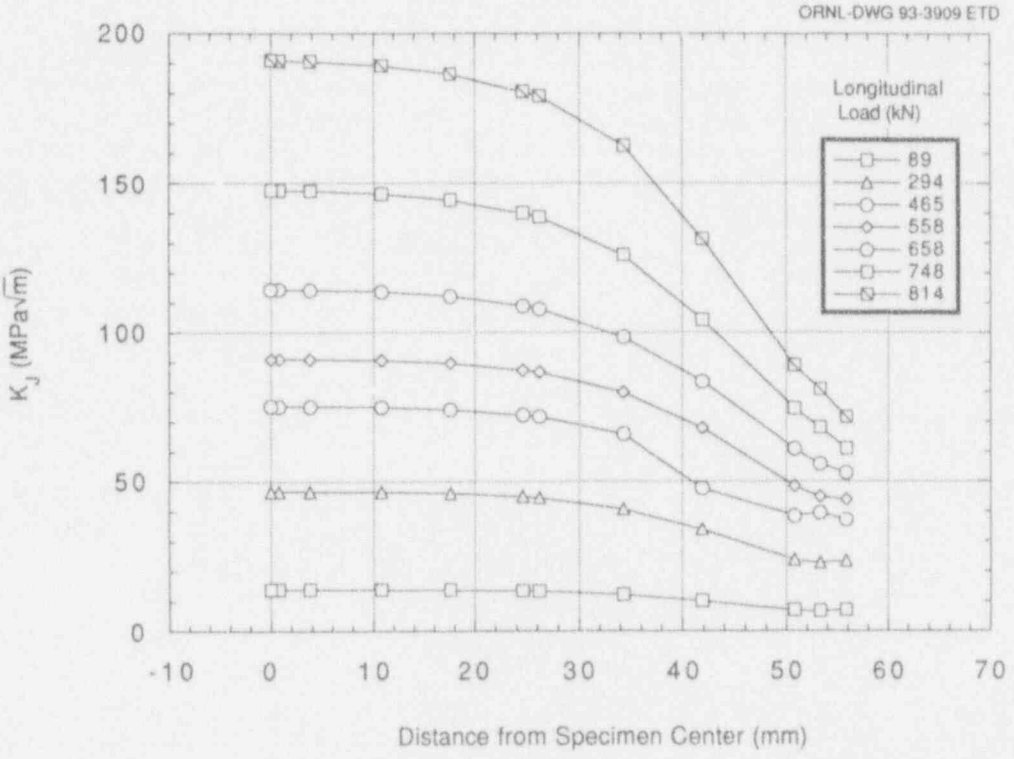

Figure 3.8 Variation of K_J along crack front, biaxial 0.6:1 loading

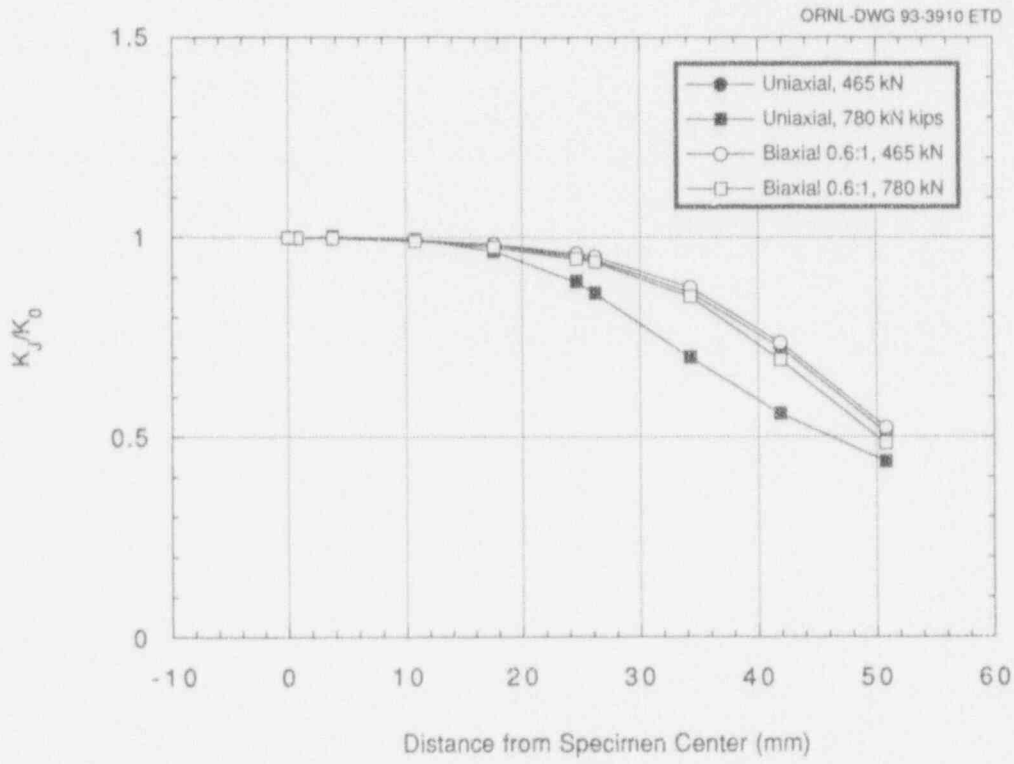

Figure 3.9 Variation of normalized K_J along crack front for both uniaxial and biaxial 0.6:1 loading at low load and at load near failure

3.2 Stress Triaxiality (J-Q) Method

One of the methods used to assess the effects of shallow-crack depths and biaxial loading on crack-tip stress triaxiality is the J-Q methodology. The J-Q method was applied to the shallow- and deep-crack SENB specimens previously.[5] The J-Q method applied to the uniaxial and biaxial cruciform specimen is based on analyses described in the previous section. Results of the J-Q analyses from both test series are presented in this chapter.

The definition of Q-stress employed here is given by O'Dowd and Shih[8] in the form

$$Q(\tilde{r}) = \frac{\sigma_{\theta\theta}(\tilde{r}) - [\sigma_{\theta\theta}(\tilde{r})]_{SSY}}{\sigma_0} , \qquad (1)$$

where $\tilde{r} = r/(J/\sigma_0)$ is a normalized distance measured in the crack plane ahead of the crack tip ($\theta = 0$); the r, θ polar coordinate system is centered at the crack tip such that $\theta = 0$ corresponds to the crack plane ahead of the tip. In Eq. (1), the Q-stress measures the departure of the opening-mode stress $\sigma_{\theta\theta}$ from the reference plane strain SSY solution, normalized by the yield stress σ_0.

Using a modified boundary layer (MBL) formulation, O'Dowd and Shih[8] determined that the Q-stress characterizes the magnitude of a spatially uniform (approximately) hydrostatic stress state in a forward sector ($|\theta| \le \pi/2$ and $1 \le \tilde{r} \le 5$) of the crack-tip region. The Q-stress, although found to be essentially independent of $\tilde{r}$, was formally defined at $\tilde{r} = 2$, which falls just outside the finite strain blunting zone. For conditions ahead of the crack that do not conform to a spatially uniform hydrostatic stress field, O'Dowd and Shih[8] introduced Eq. (1) to emphasize the explicit dependence of Q upon distance $\tilde{r}$. The latter definition of Q-stress is convenient for applications presented herein due to the spatial dependence of Q determined for certain loading conditions applied to the cruciform specimen. Additional information concerning SSY solutions to be used in Eq. (1) are given in Appendix A.

3.2.1 Application of J-Q Method to Shallow-Crack Specimens

The J-Q method was applied to a select number of shallow- and deep-crack SENB specimens as described previously.[5] The Q-stress at failure for the deep-crack specimens was found to be negligible, indicating that these specimens failed under essentially SSY conditions. The shallow-crack specimens, however, were found to have a Q-stress of about –0.7 at failure, which represents a significant loss of constraint. The opening-mode stresses ahead of the crack tip for the shallow-crack specimens, shown in Fig. 3.10 from Ref. 5, exhibited a uniform deviation from the SSY solution over a distance of $2 \le \tilde{r} \le 10$ (i.e., spatially uniform). The Q-stress was determined for these specimens

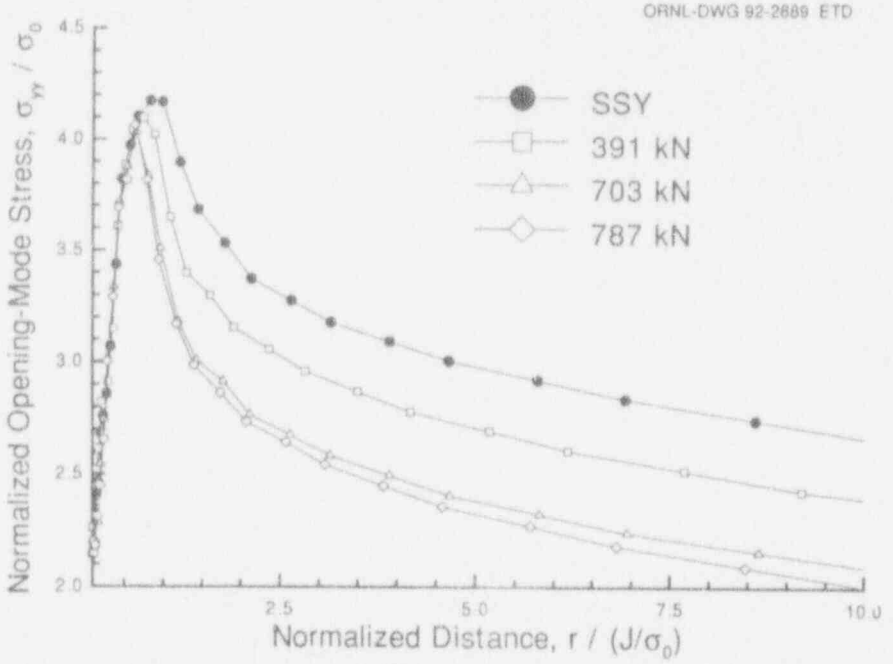

Figure 3.10 Distributions of opening-mode stress component for SENB specimen with a/W = 0.1 as function of applied load up to crack initiation

only at $\tilde{r} = 2$. These specimens were used to construct a preliminary J-Q toughness locus that could be then applied to RPV analyses.

The J-Q method was used to analyze the HSST wide-plate tests,[16,17] which also had relatively shallow cracks (a/W ~ 0.2) and exhibited a significant toughness increase. While the J-Q analysis revealed a loss of constraint associated with the wide-plate tests, the J-Q locus for these tests was not in agreement with the J-Q locus for the limited shallow-crack tests.[20] This discrepancy between the shallow-crack and wide-plate J-Q analysis is currently being investigated by reanalyzing both specimen types.* This reanalysis has generated a J-Q failure locus based on most of the shallow-crack data and several of the wide-plate results. A preliminary J-Q locus taken from this upcoming report will be presented in the next section with the cruciform data added.

3.2.2 Application of the J-Q Method to Cruciform Specimens

The J-Q constraint analyses reported in this section are based on small strain finite-element formulations. In Appendix B of this report, the crack-tip constraint analyses described in this section are reported using a finite strain finite-element formulation. Again, interpretations of biaxial loading effects on stress triaxiality are unchanged from the small strain formulation. This agreement between the finite strain and small strain solutions supports conclusions in Ref. 8 that small strain formulations for J-Q analyses are generally acceptable.

Trends in the response of near-tip stress triaxiality to uniaxial and biaxial loading conditions can be interpreted from Figs. 3.11–3.23. Values of Q-stress are determined from Eq. (1) and from the distributions given in Figs. 3.11 and 3.12 of opening-mode stress in the crack plane ahead of the tip as a function of applied load for the uniaxial and biaxial specimens, respectively. The SSY distribution is taken from a boundary layer solution described in Appendix A. For the uniaxial case (Fig. 3.11), the stress distribution continues to decrease with increasing applied load, reflecting a progressive loss of stress triaxiality associated with shallow cracks in bending. In Fig. 3.12, the decrease in stress for the biaxial case relative to the SSY solution saturates as the failure load is approached, resulting in near identical stress conditions ahead of the crack for several load steps.

The variation of Q with $\tilde{r}$ as a function of applied load over the annulus $2 \le \tilde{r} \le 5$ for the uniaxial and biaxial

*R. H. Dodds, Jr., "Constraint Analysis of the Shallow-Crack and Wide-Plate Test Results," to be issued as a NUREG under subcontract to the HSST Program.

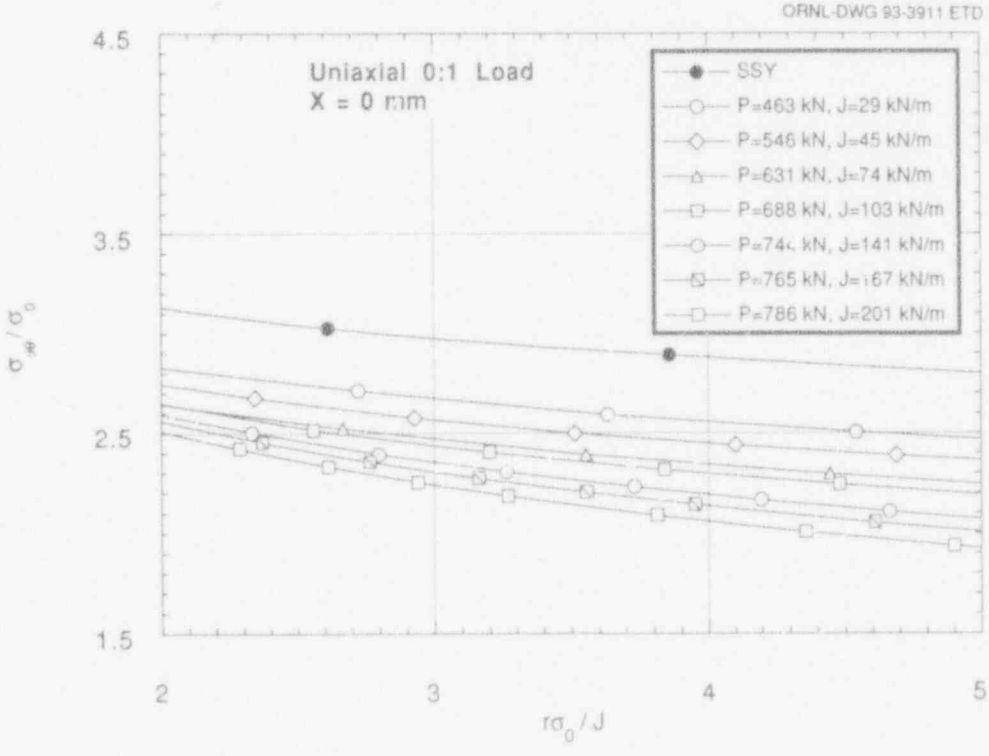

Figure 3.11 Normalized opening-mode stress ahead of crack tip, X = 0 mm, uniaxial loading

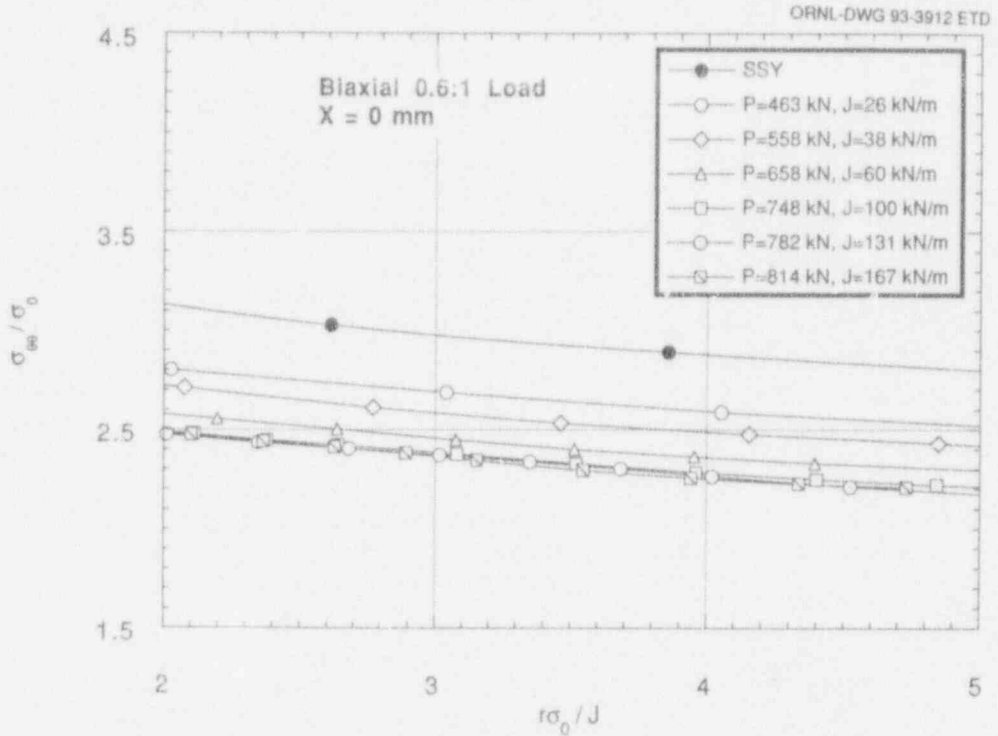

Figure 3.12 Normalized opening-mode stress ahead of crack tip, X = 0 mm, biaxial 0.6:1 loading

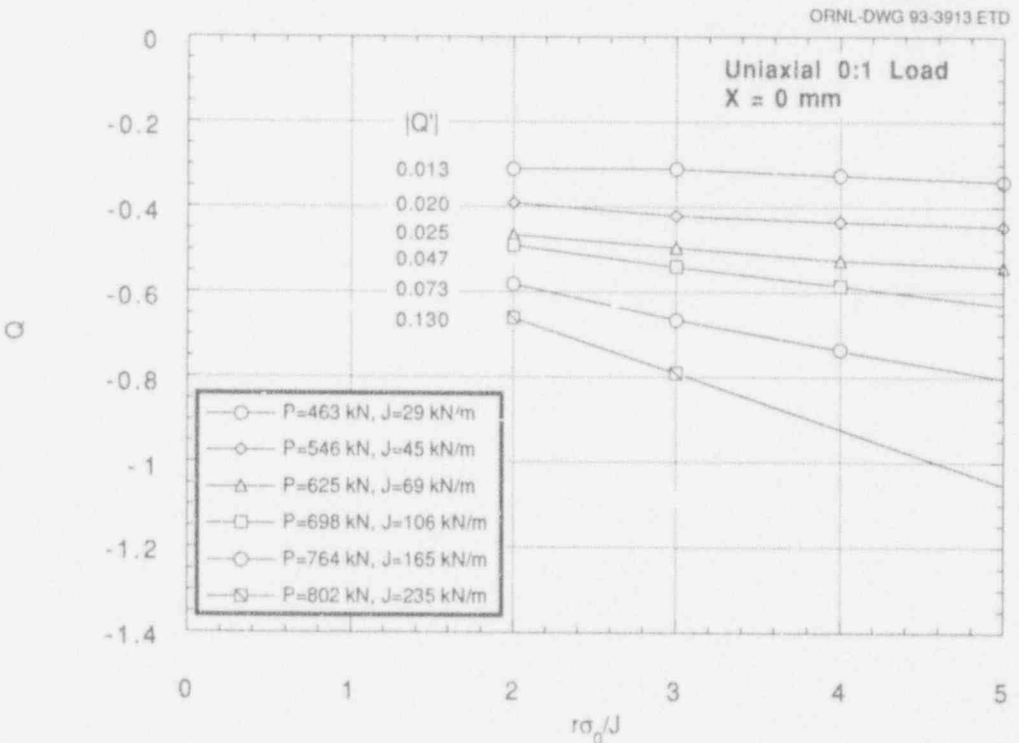

Figure 3.13 Variation of Q with normalized distance ahead of the crack tip, X = 0 mm, uniaxial loading

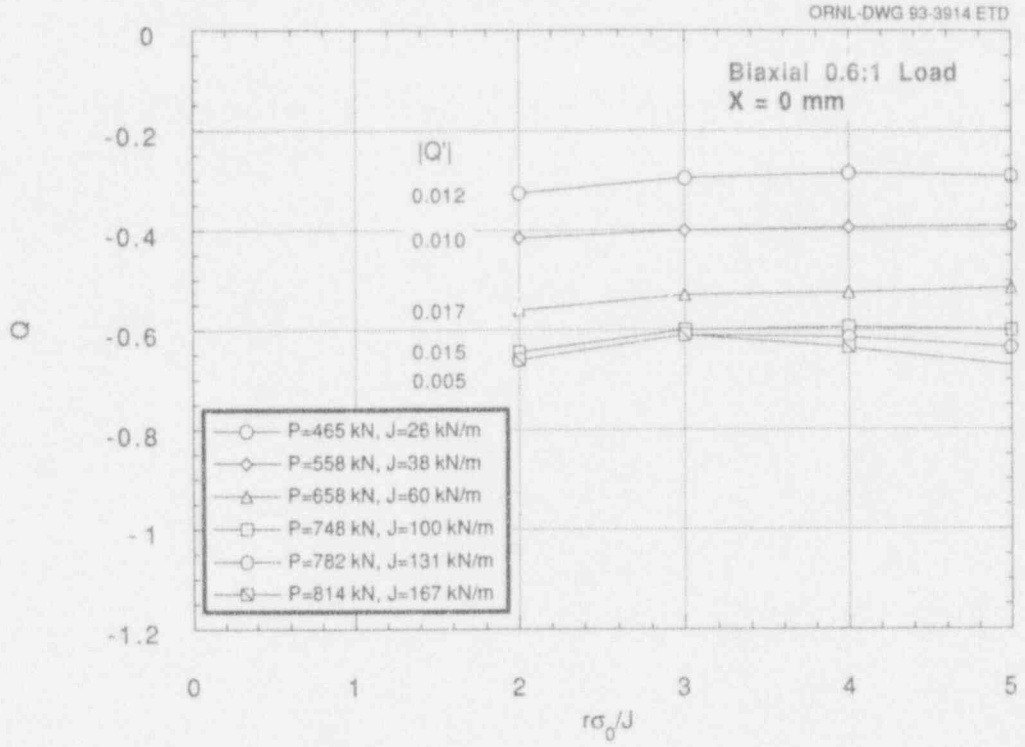

Figure 3.14 Variation of Q with normalized distance ahead of the crack tip, X = 0 mm, biaxial 0.6:1 loading

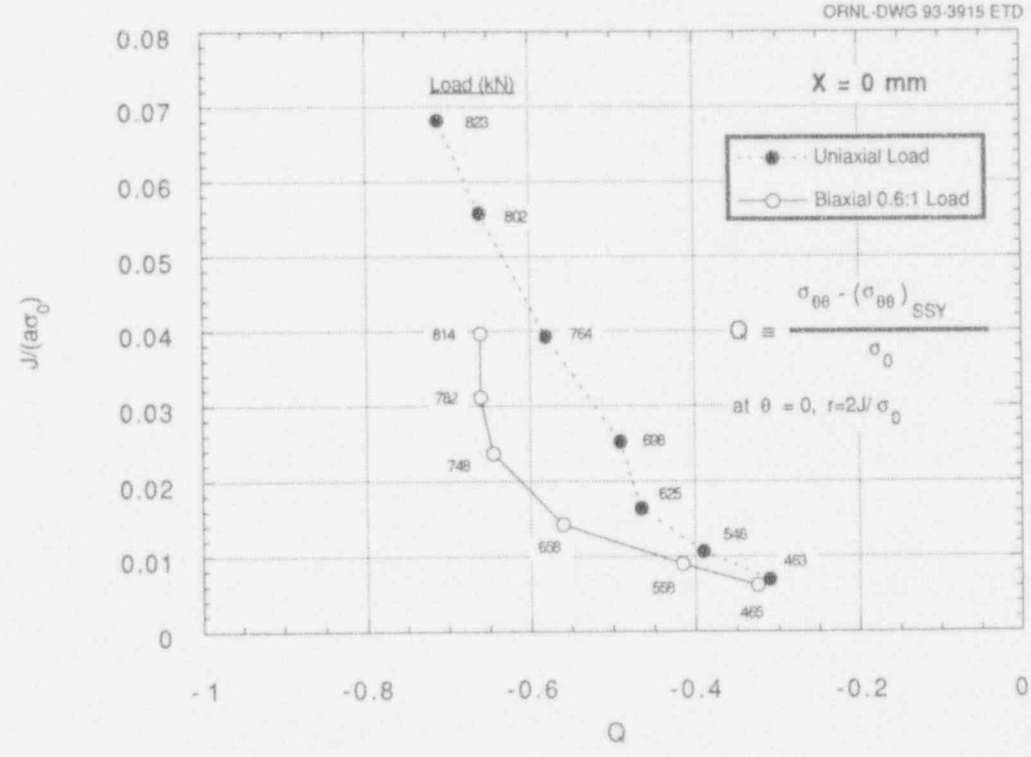

Figure 3.15 J-Q trajectories at X = 0 mm for a normalized distance $r\sigma_0/J = 2$

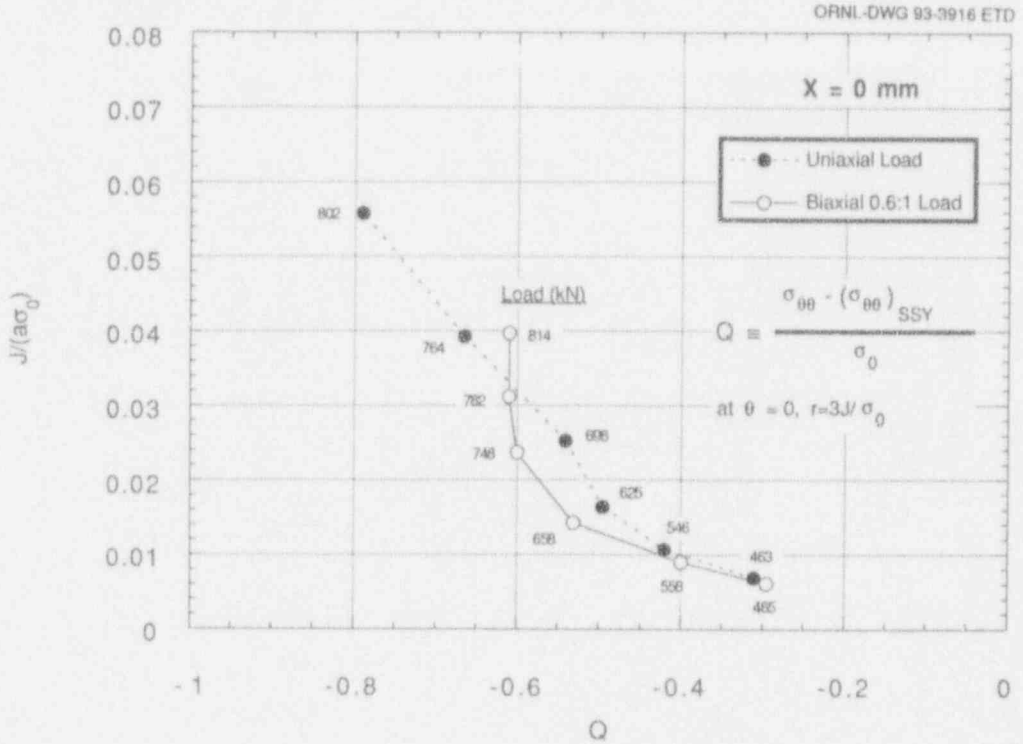

Figure 3.16 J-Q trajectories at X = 0 mm for a normalized distance $r\sigma_0/J = 3$

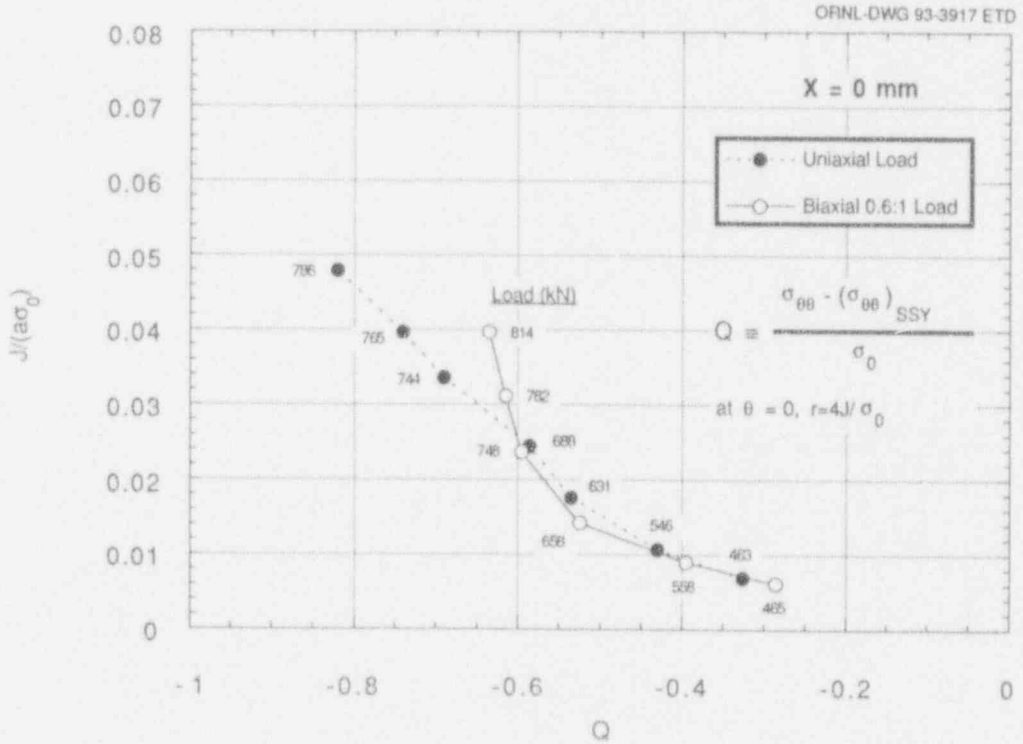

Figure 3.17 J-Q trajectories at X = 0 mm for a normalized distance $r\sigma_0/J = 4$

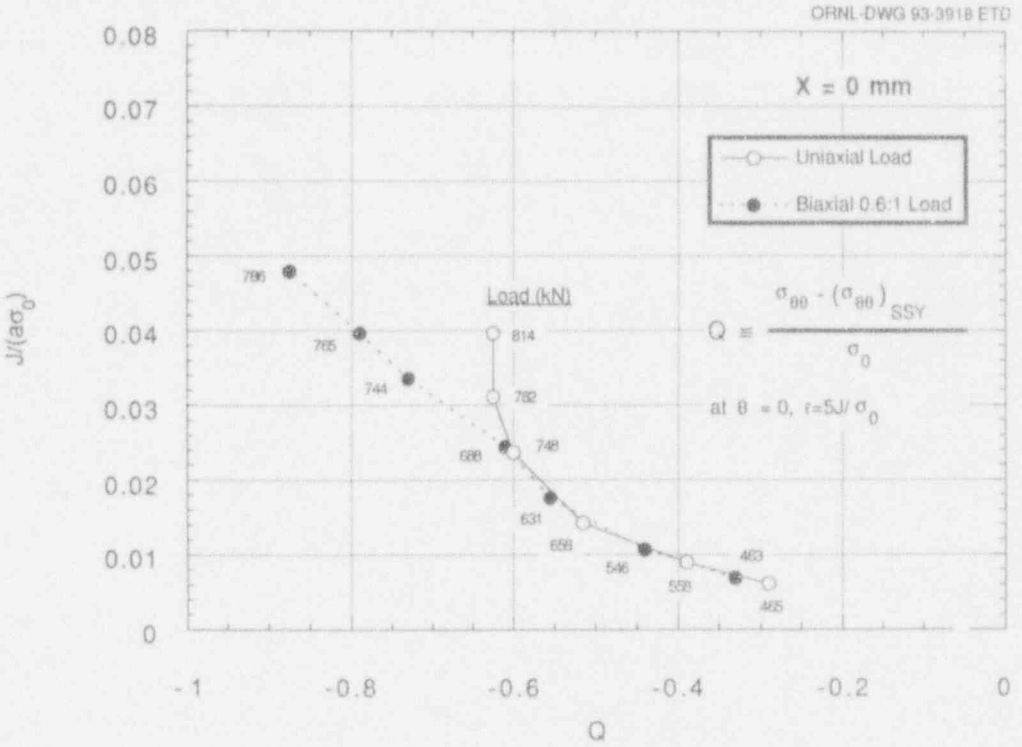

Figure 3.18 J-Q trajectories at X = 0 mm for a normalized distance $r\sigma_0/J = 5$

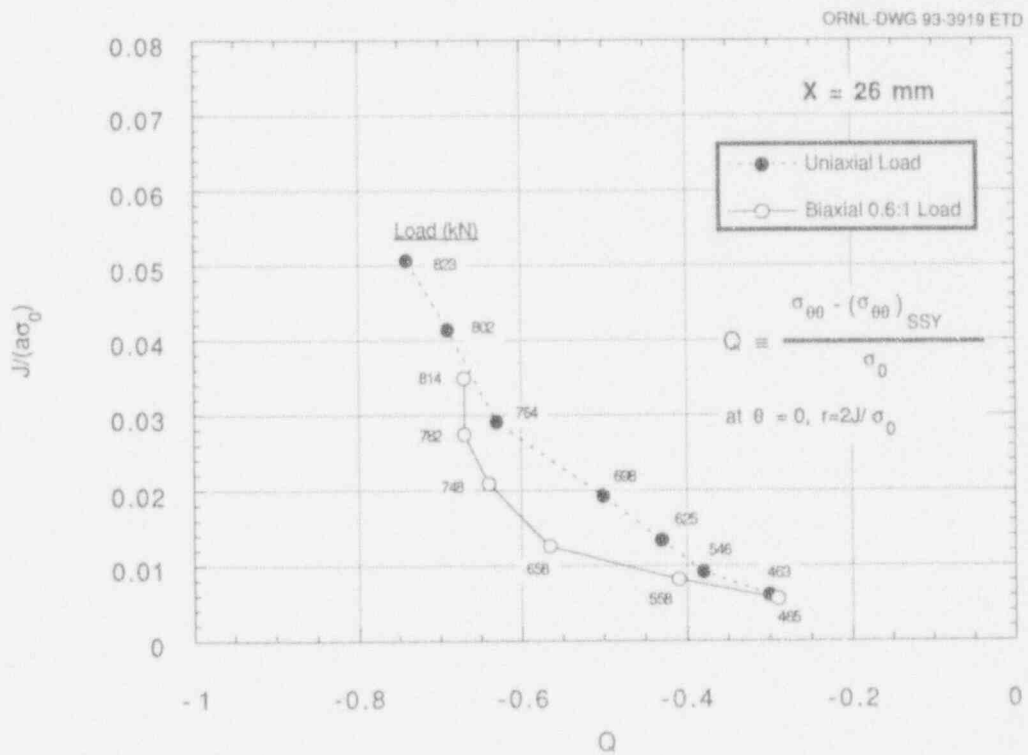

Figure 3.19 J-Q trajectories at X = 26 mm for a normalized distance $r\sigma_0/J = 2$

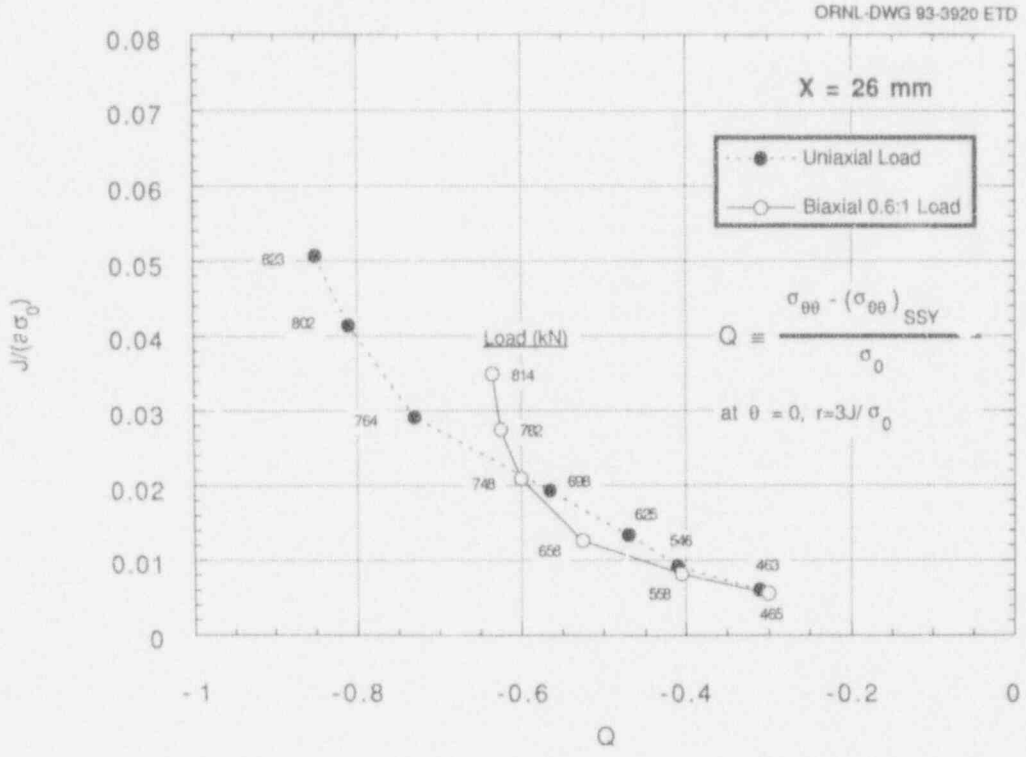

Figure 3.20 J-Q trajectories at X = 26 mm for a normalized distance $r\sigma_0/J = 3$

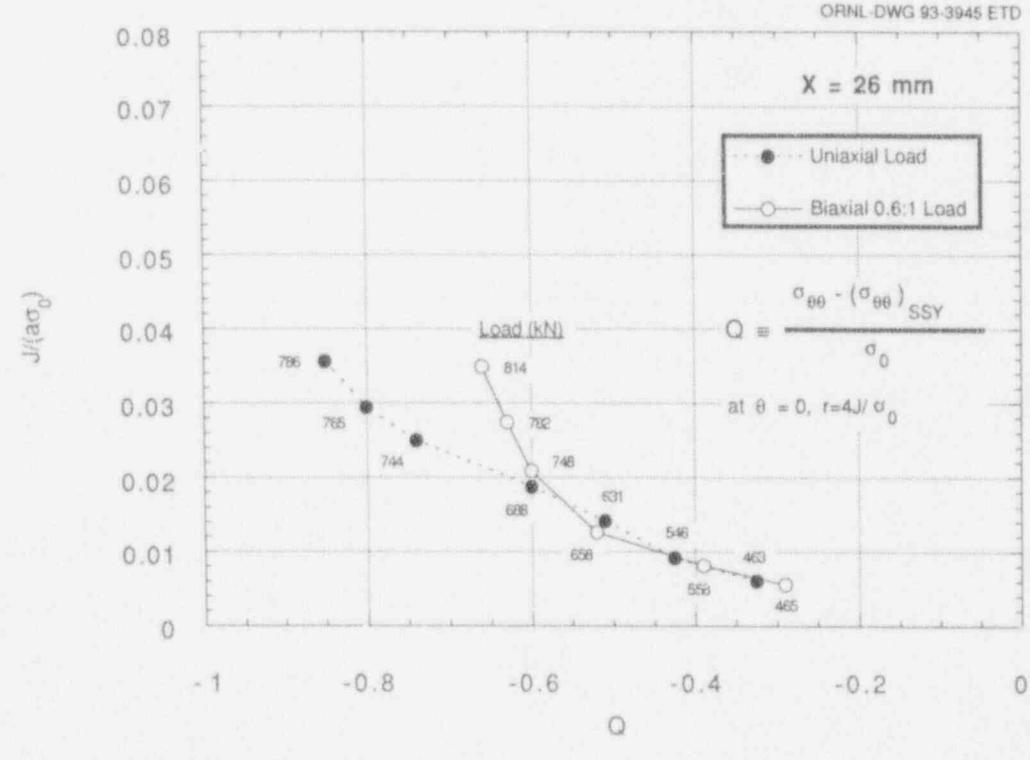

Figure 3.21 J-Q trajectories at X = 26 mm for a normalized distance $r\sigma_0/J = 4$

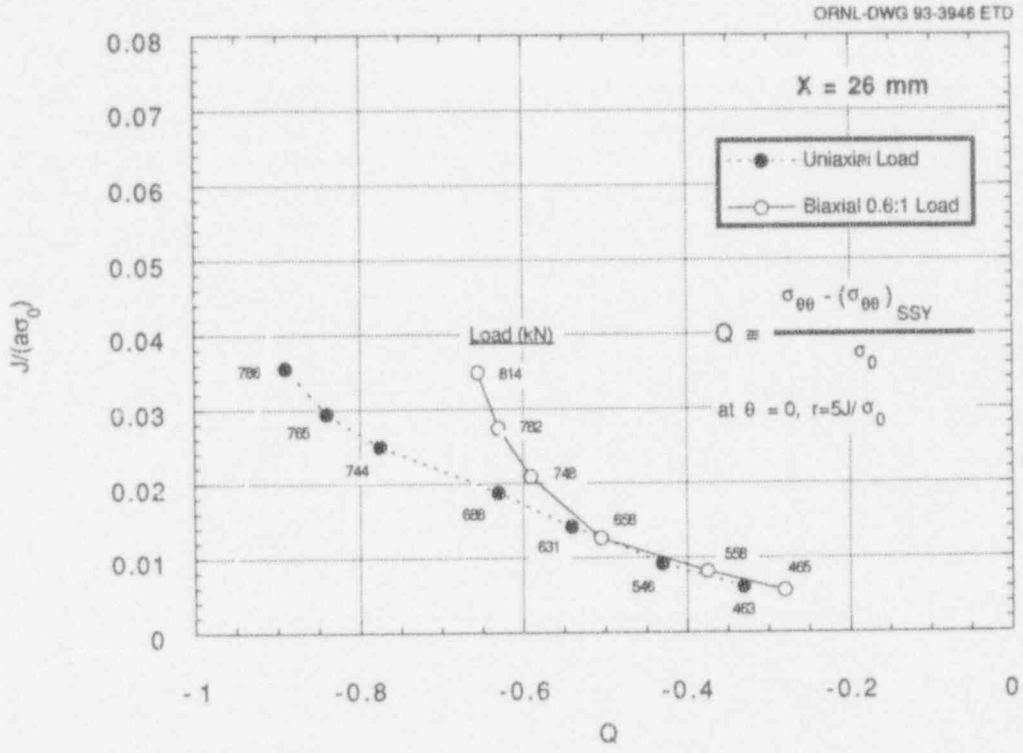

Figure 3.22 J-Q trajectories at X = 26 mm for a normalized distance $r\sigma_0/J = 5$

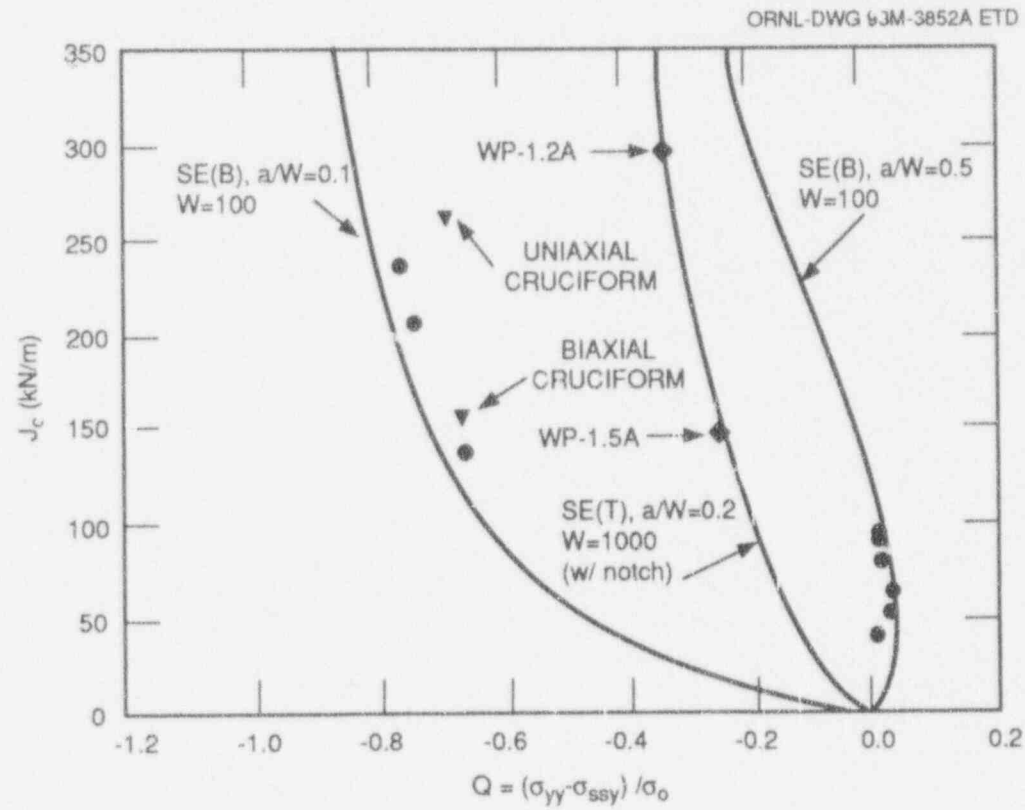

Figure 3.23 J-Q failure locus for A 533 grade B class 1 steel at $T - RT_{NDT} = -10°C$

loading cases is shown in Figs. 3.13 and 3.14, respectively. In Fig. 3.13, the Q-stress steadily decreases as the applied load is increased and as general yielding develops in the uniaxially loaded specimen. Also, the Q-stress exhibits a dependence on radial distance with increasing load, an effect previously observed in Fig. 3.11. The bending field imposed on the beam by the applied loads progressively impinges on the near crack-tip field within the region defined by $\tilde{r} \leq 5$, producing an essentially linear dependence of Q upon $\tilde{r}$ at higher J values.

To quantify changes in the stress triaxiality from a spatially uniform hydrostatic field ahead of the crack, O'Dowd and Shih[8] defined the mean gradient of Q over the annulus $1 \leq \tilde{r} \leq 5$:

$$Q' = \frac{Q(\tilde{r} = 5) - Q(\tilde{r} = 1)}{4} \quad . \qquad (2)$$

The criterion of $|Q'| < 0.1$ was proposed by O'Dowd and Shih[8] as an indication that the Q-stress field is essentially constant over the annulus $1 < \tilde{r} < 5$. The Q' function was used in Ref. 8 to assess the dependence of Q upon $\tilde{r}$ in analyses of three-point bend bar specimens for a range of crack depths. Values of $|Q'| > 0.1$ were computed at higher loads for deep-crack geometries in these analyses, reflecting the interaction of far-field bending stresses with the near-tip field. (This spatial dependence of Q-stresses was not evident in the HSST shallow-crack SENB analyses of Fig. 3.10.)

Previous discussion of Fig. 3.13 noted that the far-field bending stresses impact stress fields on the annulus $2 < \tilde{r} < 5$ at higher values of uniaxial loading applied to the cruciform specimen. For this specimen, Fig. 3.13 indicates that the criterion $|Q'| < 0.1$ is not satisfied on the annulus $2 < \tilde{r} < 5$ as failure load is approached. The Q' criterion based on a maximum of 0.1 appears to permit a large variation in Q-stress over the crack-tip annulus. In this case, the variation in Q over the crack-tip annulus is greater than the difference between calculated Q-stress values for uniform and biaxial loading cases. Thus, it remains difficult to support the quantification of crack-tip constraint based on stress conditions in this annulus that are so heavily influenced by the far-field stresses. Consequently, application of the Q-stress methodology under conditions represented by the uniaxially loaded specimen at failure appears to be problematic. Further discussion of this issue is provided in subsequent sections in the context of J-Q trajectories and fractographic data concerning cleavage initiation sites.

The effect on variation of Q-stress vs $\tilde{r}$ due to addition of the out-of-plane bending load is illustrated by results from the biaxial case given in Fig. 3.14. For this case, Q varies negligibly with $\tilde{r}$ (i.e., $|Q'| \sim 0.01$) over the annulus $2 \leq \tilde{r} \leq 5$ for the full range of loading. The Q-stress steadily decreases to a value of –0.6, where it remains (approximately) constant until failure conditions are reached. This value of Q-stress agrees well with the Q-stress determined at failure for the shallow-crack SENB specimens. Comparison of these results with the uniaxial case in Fig. 3.13 indicates that biaxial loading produces a higher stress triaxiality (as quantified by Q) at failure conditions and a hydrostatic stress field that is more spatially uniform over the annulus $2 \leq \tilde{r} \leq 5$. The interaction of the local stress field and the far-field bending stresses in the uniaxially and biaxially loaded cruciform specimens is discussed further in Sect. 3.4.

The evolution of the J-Q loading path at the midplane of the cruciform specimen for the uniaxial and biaxial loading cases is depicted in Figs. 3.15–3.18. The Q-stress is evaluated at distances ahead of the crack given by $\tilde{r} = 2$, 3, 4, and 5 in Figs. 3.15–3.18, respectively. The J-Q loading path for the biaxial case is essentially the same at $\tilde{r} = 3$, 4, and 5. The Q-stress reaches a constant value of approximately –0.6 as the loading path turns sharply upward and failure conditions are approached. For the uniaxial case, the J-Q path is sensitive to the choice of $\tilde{r}$ (i.e., Q becomes more negative with increasing $\tilde{r}$), as would be expected from results shown previously in Fig. 3.13. Response of the cruciform specimen in terms of measured P, LLD, and CMOD data (Figs. 3.4 and 3.5) indicated no significant biaxial loading effects for contained yielding conditions. Similar behavior between the uniaxial and biaxial cases for the J-Q trajectory is demonstrated only for values of $\tilde{r} \geq 4$. For this case, the uniaxial J-Q loading path follows the biaxial path up to a value of $J/(a\sigma_0) = 0.24$ (which corresponds to J ~ 100 kN/m or $K_J \sim 150$ MPa$\sqrt{m}$) and then diverges from the biaxial case as yielding increases in the specimens. In Fig. 3.18, the uniaxial and biaxial paths diverge at a Q-stress value of –0.6, a condition that represents substantial loss of triaxiality.

Several observations can be made concerning the J-Q trajectories computed at selected locations ahead of the crack tip in Figs. 3.15–3.18. Given the similarity of the uniaxial and biaxial P-CMOD responses at low loads, the expectation is that the J-Q trajectories for the uniaxial and biaxial specimens would exhibit similar behavior. Figure 3.15 depicts the J-Q trajectories computed at $\tilde{r} = 2$, that is, at the location formally defining the Q-stress. The trajectory for the uniaxial case exhibits a significantly higher constraint condition (i.e., higher Q-stress) than the biaxial case for almost the entire loading path. This analytical result is at odds with experimental results that imply the biaxially loaded specimen is the more highly constrained specimen.

At failure conditions, however, the uniaxial Q-stress is slightly more negative than the biaxial Q-stress, which is consistent with expected behavior. With increasing distance from the crack tip, the J-Q trajectory for the uniaxial case translates in the direction of decreasing triaxiality (i.e., more negative Q-stress values). For points in that portion of the annulus defined by $\tilde{r} \geq 4$, the uniaxial and biaxial trajectories are very similar for $Q > -0.6$ (see Figs. 3.17 and 3.18). However, there is no rationale for quantifying constraint at distances relatively far removed from the crack tip in an annulus where far-field stresses have a strong influence as in the uniaxial case. Fractographic examination of the test specimens (described in Chap. 4) showed no evidence of cleavage initiation sites in the annulus under consideration. Therefore, the cruciform specimens will be interpreted in terms of J-Q trajectories defined at $\tilde{r} = 2$, despite the previously observed inconsistencies between the uniaxial and biaxial trajectories at lower load.

Corresponding results for the J-Q loading paths for the uniaxial and biaxial cruciform specimen computed at a point on the crack front located 26 mm from the midplane are given in Figs. 3.19–3.22. These results show stress triaxiality effects similar to those determined for the midplane of the specimen. In Fig. 3.22, the J-Q trajectories for the uniaxial and biaxial loading cases diverge at $Q \sim -0.5$, which is somewhat higher than the corresponding midplane value of –0.6 (see Fig. 3.18)

A J-Q failure locus for A 533 grade B class 1 steel at one temperature is schematically constructed in Fig. 3.23. This failure locus utilizes J-Q trajectories from analyses of shallow- and deep-crack SENB and HSST wide-plate data performed by Dodds.* The estimated J-Q toughness values for the uniaxially and biaxially loaded cruciform specimen at $\tilde{r} = 2$ are also included. Figure 3.23 depicts the scatter for a toughness locus corresponding to these J-Q trajectories. The toughness locus implies that reduced stress triaxiality (as reflected in more negative values of Q) is associated with increases both in apparent fracture toughness and in data scatter. The trajectories for the cruciform specimens fall well within the scatter of the failure locus. Also, the tendency for the biaxially loaded specimen trajectory to saturate at a higher stress triaxiality (i.e., less negative Q-stress) and turn abruptly upward suggest that biaxial loading could produce less data scatter in shallow-crack geometries than the uniaxial case.

3.3 Fracture Toughness Scaling Model (Dodds-Anderson)

The Dodds-Anderson (or D-A) scaling model[10] analyzes constraint conditions by determining the area (or volume when considering a 3-D geometry) within a particular stress contour for a finite-body geometry and scaling that area (or volume) with an equivalent SSY solution. The SSY state is then considered to yield true fracture toughness results completely independent of specimen size or loading and is comparable to a specimen of infinite size. The scaling model has been successfully applied to fracture toughness results exhibiting either a loss of in-plane constraint (i.e., shallow cracks) or out-of-plane constraint (i.e., thickness effects).[10] The scaling model assumes that the volume of critically stressed material surrounding the crack tip is the same in different specimens with different constraint conditions. As a result, the SSY critical fracture toughness can be determined in a high-constraint geometry and then applied to a low-constraint geometry or vice versa.

3.3.1 Application of Scaling Model to Shallow-Crack Data

The D-A scaling model has been used to investigate both in-plane and out-of-plane constraint loss in the HSST shallow- and deep-crack test results. The in-plane investigation is reported herein; the application of the model to out-of-plane constraint or thickness effects is the subject of a separate report.† The scaling model was applied to the shallow-crack data using information available in the literature[21] without the need of additional crack-tip analysis.

The fracture toughness data from the HSST shallow-crack program are shown in Fig. 3.24 as a function of normalized temperature ($T - RT_{NDT}$). The shallow-crack toughness increase can be quantified by a temperature shift of ~35°C. The data within the box at a normalized temperature range of approximately –10°C to –25°C in Fig. 3.24 are replotted in Fig. 3.25 as a function of crack depth. As expected in a low-constraint geometry, Fig. 3.25 shows both an increase in the fracture toughness values and data scatter from the shallow-crack specimens when compared with the deep-crack specimens. Figures 3.24 and 3.23 are complementary, both indicating an increase in toughness and data scatter with decreased constraint. The regression analysis shown in Fig. 3.25 indicates a mean shallow-crack

*R. H. Dodds, Jr., "Constraint Analysis of the Shallow-Crack and Wide-Plate Test Results," to be issued as a NUREG under subcontract to the HSST Program.

†T. J. Theiss and S. K. Iskander, *Constraint and Statistical Analyses of Transition Range A533 B Toughness Data*, USNRC Report NUREG/CR-6106 (ORNL/TM-12467), to be published.

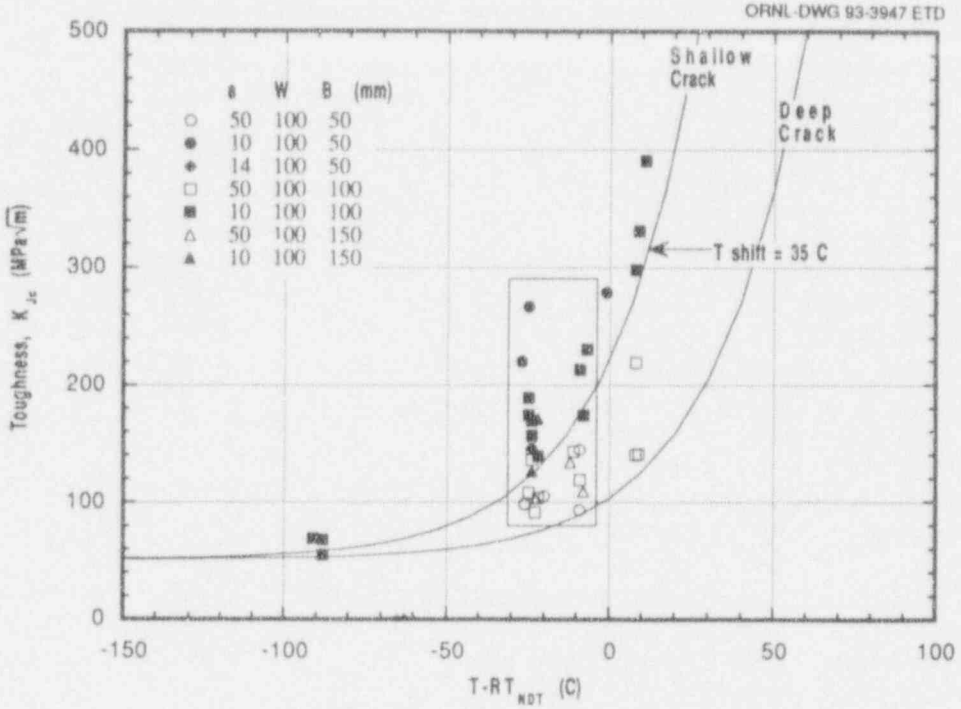

Figure 3.24 HSST shallow-crack fracture toughness results as function of normalized temperature T – RT_{NDT}

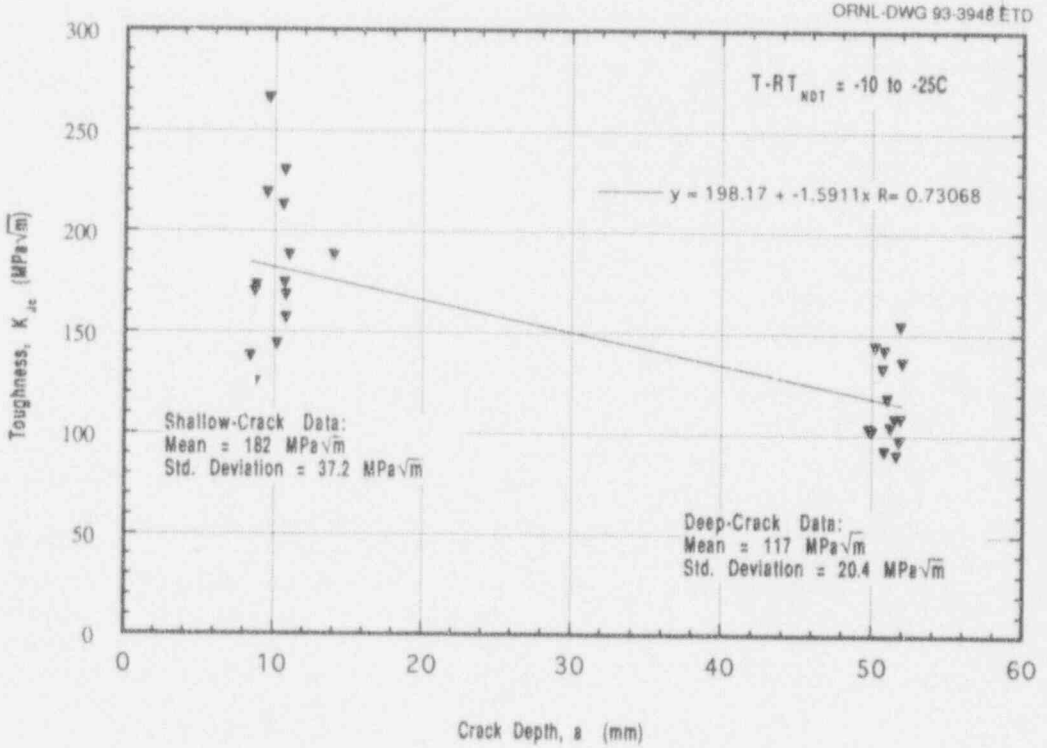

Figure 3.25 Toughness data at T – RT_{NDT} = –25 to –10°C as function of crack depth

toughness value of about 1.6 times the deep-crack toughness as previously reported.[5]

The following criteria developed by Dodds and Anderson[10] indicate dimensions in deep-crack (a/W > 0.5) specimens necessary for SSY:

$$a, b, B \geq 200\, J_c/\sigma_f \ , \qquad (3)$$

where a is the crack depth, b is the remaining ligament, B is the specimen thickness, J_c is the cleavage J-integral toughness, and σ_f is the flow stress of the material. Specimens not meeting the criteria are expected to exhibit a toughness increase due to the loss of out-of-plane constraint. The ratio $a\sigma_f/J_c$ was determined for each specimen and is listed in Table 3.1. As expected, the ratio exceeds 200 for most of the deep-crack specimens and is considerably less than 200 for the shallow-crack specimens.

Using the D-A[10] analysis results, Wallin[21] has quantified in-plane constraint loss by the following equation:

Table 3.1 Results of scaling model applied to shallow-crack data

HSST beam	$T - RT_{NDT}$ (°C)	a (mm)	K_{Jc} (MPa$\sqrt{m}$)	$a/(J/\sigma_f)$	J_{FB}/J_o	K_o (MPa$\sqrt{m}$)
3	–1	10.0	279	13	6.33	111
4	–26	51.8	98	579	1.03	96
5	–20	51.2	105	490	1.04	103
6	–24	51.9	155	230	1.10	147
7	–24	10.2	145	51	1.80	108
8	–25	9.6	267	14	5.58	113
9	–27	9.5	220	21	3.71	114
10	–25	14.0	189	42	2.05	132
11	–22	8.4	139	46	1.94	100
12	–22	49.8	103	494	1.04	101
13	–25	8.8	174	31	2.60	108
14	–22	8.7	171	31	2.56	107
15	–24	8.7	126	58	1.67	97
16	–23	50.0	103	501	1.04	101
12A	–9	51.0	119	369	1.05	116
13A	–11	50.8	143	255	1.09	137
14A1	–9	50.2	145	244	1.09	138
14A2	–9	50.8	93	601	1.03	91
15A	–12	50.7	134	289	1.07	129
16A	–8	51.9	109	445	1.04	107
17	9	52.6	141	254	1.09	135
18	–9	10.6	213	23	3.37	116
20	11	10.8	391	7	13.68	106
21	–8	10.7	174	35	2.34	114
22	8	10.9	298	12	6.93	113
24	8	52.0	219	105	1.30	192
25	–24	52.0	136	290	1.07	131
26	–25	11.0	189	32	2.51	119
27	–7	10.7	230	20	3.92	116
28	9	10.3	331	9	9.54	107
31	–25	51.5	108	455	1.04	106
32	–88	11.1	68	327	1.06	66
33	–88	10.7	55	499	1.04	54
34	–91	10.4	69	307	1.07	67
35	8	51.7	140	255	1.09	134
36	–23	51.6	91	645	1.02	90
37	–24	10.8	169	39	2.16	115
38	–24	10.8	157	45	1.95	112

$$J_{FB}/J_o = 1 + 176\,(J_{FB}/a\sigma_0)^{1.37}\ , \qquad (4)$$

where J_o is the SSY or reference value of J, and J_{FB} is the value of J in the finite body geometry. Equation (4) is applicable to materials with a Ramberg–Osgood hardening exponent of ~10, such as A 533 B steel. It is recommended in Ref. 10 that results from the above equation not be used in situations in which $J/J_o > 4$. The SSY value (J_o) was computed from Eq. (4) for each specimen tested as a part of the HSST Shallow-Crack Program. The results are listed in Table 3.1 as J_{FB}/J_o and K_o. The plane-strain elastic modulus was used to convert from J to K. The K_o results are shown in Fig. 3.26 as a function of normalized temperature. The K_o results show no toughness increase associated with the shallow-flaw specimens. As shown in Fig. 3.26, several of the shallow-crack K_o data are below the corresponding deep-crack K_o data at higher temperatures. These specimens exhibited a J_{FB}/J_o adjustment >4 and do not represent the SSY toughness value.

The K_o values as a function of crack depth in the transition region (i.e., the data subset in Fig. 3.26 within the box) are shown in Fig. 3.27. The data in Fig. 3.27 correspond to the uncorrected data in Fig. 3.25. As indicated in Fig. 3.27, the K_o results are reduced to a toughness level independent of the crack depth of the specimens. Comparing Figs. 3.25 and 3.27, the deep-crack data in Fig. 3.27 experience little to no reduction to their K_o values, while the shallow-crack data are reduced substantially to almost exactly the same toughness level. The regression analysis shown in Fig. 3.27 confirms that the K_o data are independent of crack depth. The mean and standard deviation of the shallow- and deep-crack data are included on Fig. 3.27 as well. The mean values are almost identical at 112 MPa$\sqrt{m}$ for the shallow-crack K_o data and 114 MPa$\sqrt{m}$ for the deep-crack K_o data. The shallow-crack K_o also exhibit substantially less scatter than the original shallow-crack data in Fig. 3.25. The standard deviation of the original shallow-crack K_{Jc} data was 37.2 MPa$\sqrt{m}$; the shallow-crack K_o data had a deviation of only 8.1 MPa$\sqrt{m}$. All of the data in Fig. 3.27 met the criteria of $J_{FB}/J_o \le 4$ except one specimen that had a J_{FB}/J_o ratio of ~5.6. The average J_{FB}/J_o ratio for the shallow-crack specimens in Fig. 3.27 was 2.73; the average deep-crack specimen J_{FB}/J_o value was 1.05.

Several conclusions can be drawn from the application of the D-A scaling model to the HSST shallow-crack data. First, the scaling model works very well with the shallow-crack data. The model adjusts both shallow- and deep-crack data to the SSY toughness value. In addition, the scatter in the corrected toughness data was also reduced by the application of the scaling model to the original shallow-crack toughness results. Furthermore, the scaling model is very simple to use in this application. The analysis of the data using the scaling model required no additional crack-tip analysis. The constraint corrections were based on specimen geometry and cleavage toughness results. It appears likely that J_c predictions for shallow-crack geometries could be made from K_o data obtained from deep-crack specimens.

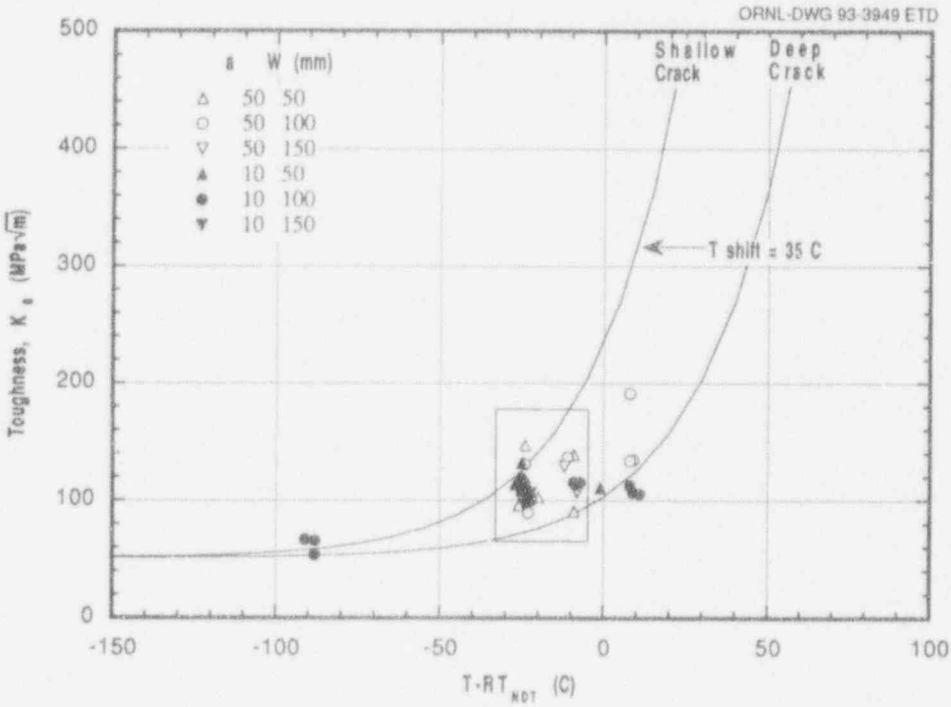

Figure 3.26 SSY toughness (K_o) results as function of normalized temperature

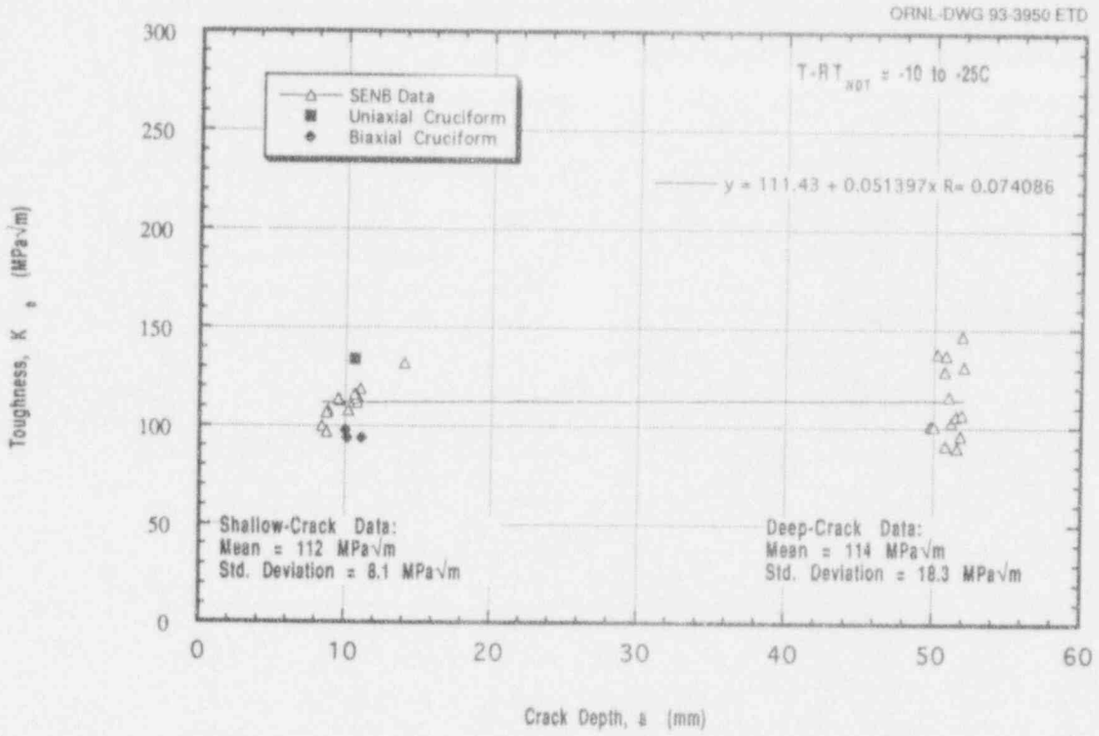

Figure 3.27 K_0 data at $T - RT_{NDT} = -25$ to $-10°C$ as function of crack depth

3.3.2 Application of Scaling Model to Cruciform Beam Data

Dodds et al.[11] have also developed a methodology for performing constraint adjustments of fracture toughness data from test specimens that utilize a J-Q description of the crack-tip stress fields. This methodology has the advantage of being computationally simpler to apply than the stressed-volume technique for constraint correction previously introduced by Dodds and Anderson.[10] Applications of this simplified approach to data from the uniaxially and biaxially loaded cruciform specimens, which draw upon the J-Q analyses of the previous section, are presented herein.

The modified D-A scaling procedure, like the scaling model previously described, determines the ratio of finite-body toughness to SSY toughness (i.e., J_{FB}/J_0). The modified D-A scaling procedure is based on the observation[11] that even under different constraint conditions the shape of the principal stress contour ahead of the crack tip remains the same, with only the size varying. This relationship is maintained until deformation becomes excessive. Critically stressed areas ahead of the crack can be related to critical distances ahead of the crack, which allows the use of the near-tip stress field to determine J_{FB}/J_0. Figure 3.28 shows the stresses ahead of the crack tip for the SSY solution and the cruciform specimen under uniaxial and biaxial loading. The uniaxial and biaxial stresses are at (or near) the critical value of J. This allows the determination of the constraint conditions (and J_0 toughness) in these specimens at failure (i.e., critical SSY toughness, J_0). The three biaxial specimens yielded toughness values sufficiently close such that only one J value for these specimens is necessary.

Two different methods of applying the D-A scaling procedure were used for these results.* Both methods begin with the ratio of the distance ahead of the crack tip, $\tilde{r}$, for the finite-body and SSY solutions to determine the J_{FB}/J_0 ratio. Both methods begin the construction with an $\tilde{r}$ value of about 2. The first method holds the finite-body stress constant at $\tilde{r} = 2$ and determines the distance ahead of the crack tip in the SSY solution that corresponds to that stress (see Fig. 3.28). The second method begins with the SSY stress at $\tilde{r} = 2$ and finds the distance corresponding to that stress in the finite-body solution(s). Both of these methods are outlined in Fig. 3.28. The first method begins with the finite-body stress at $\tilde{r} = 2$ or $r = 2J_{FB}/\sigma_0$. The distance in the SSY solution that yields the same critical stress is $\tilde{r} = 11.63$ or $r = 11.63\ J_0/\sigma_0$. Because the critical distances are assumed equal, $J_{FB}/J_0 = 11.63/2.0$ or 5.82. The second method yields a J_{FB}/J_0 of 2.0/0.621 = 3.22.

*Private conversation with R. H. Dodds, Jr., Sept. 28, 1993.

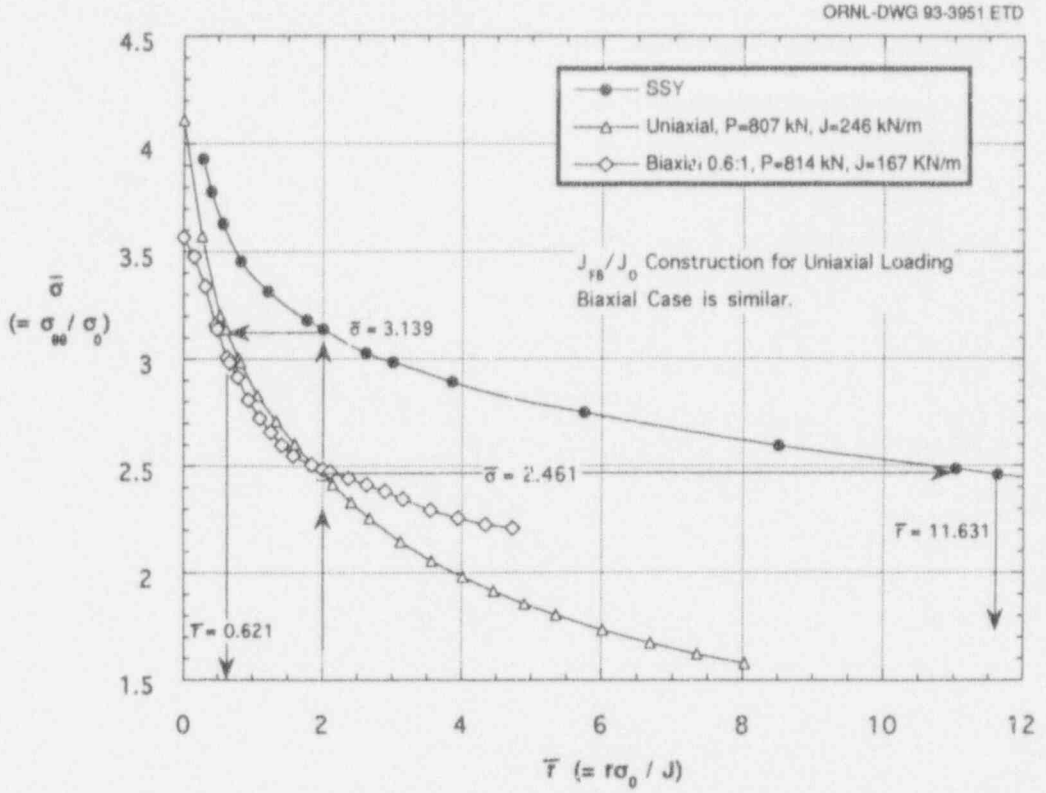

Figure 3.28 Determination of finite-body to SSY toughness ratio from stresses ahead of crack tip

The two methods of applying the D-A scaling model just described yield J_{FB}/J_o ratios that are quite different. Theoretically, as discussed in Ref. 11, both methods should yield identical results. One reason for this problem is that these are numerical approximations to the stresses near the crack tip, which always contain some error. The SSY stress solution tends to flatten as distance from the crack tip increases, which could exaggerate the error in J_{FB}/J_o with increasing distance from the crack tip. Furthermore, the first D-A scaling method used distances greater than $\bar{r}$ = 10, which is typically far beyond the process zone for cleavage fracture. (Additional information on the location of the cleavage origin site ahead of the crack tip will be covered in Chap. 4.) For the two reasons just outlined, the second D-A scaling procedure that uses smaller distances ahead of the crack tip is the preferred method in this investigation and will be used to interpret the results.

The J_{FB}/J_o results using the D-A scaling procedure for the uniaxial and biaxial cruciform specimens at $\bar{r}$ = 1.5 to 4 are included in Table 3.2. These results are plotted as a function of distance ahead of the crack tip in Fig. 3.29. Examination of these results leads to several observations. First, the J ratios (and subsequently J_o) vary as a function of distance ahead of the crack tip. For the uniaxial cruciform, the J_{FB}/J_o ratio increases from ~3 at $\bar{r}$ = 1.5 to ~4 at $\bar{r}$ = 4. The biaxial cruciform shows a similar increase in

Table 3.2 Scaling model results at distances ahead of crack tip for the uniaxial and biaxial cruciform specimens (at critical load)

$\bar{r}$	σ_{SSY}/σ_o	$\bar{r}_{FB}$	J_{FB}/J_o
	Uniaxial loading		
1.5	3.248	0.502	2.99
2.0	3.139	0.621	3.22
2.5	3.048	0.744	3.36
3.0	2.986	0.831	3.61
3.5	2.931	0.916	3.82
4.0	2.881	0.994	4.02
	Biaxial loading		
1.5	3.248	0.394	3.81
2.0	3.139	0.493	4.06
2.5	3.048	0.589	4.24
3.0	2.986	0.669	4.48
3.5	2.931	0.765	4.58
4.0	2.881	0.842	4.75

J_{FB}/J_o with distance ahead of the crack tip. In Ref. 11, the calculation of J_o is considered valid when values determined at $\bar{r}$ = 1.5 and at $\bar{r}$ = 4 differ by <10%. The variation in J_{FB}/J_o (and subsequently J_o) shown in Fig. 3.29 is about 25% over this range for both the uniaxial and biaxial

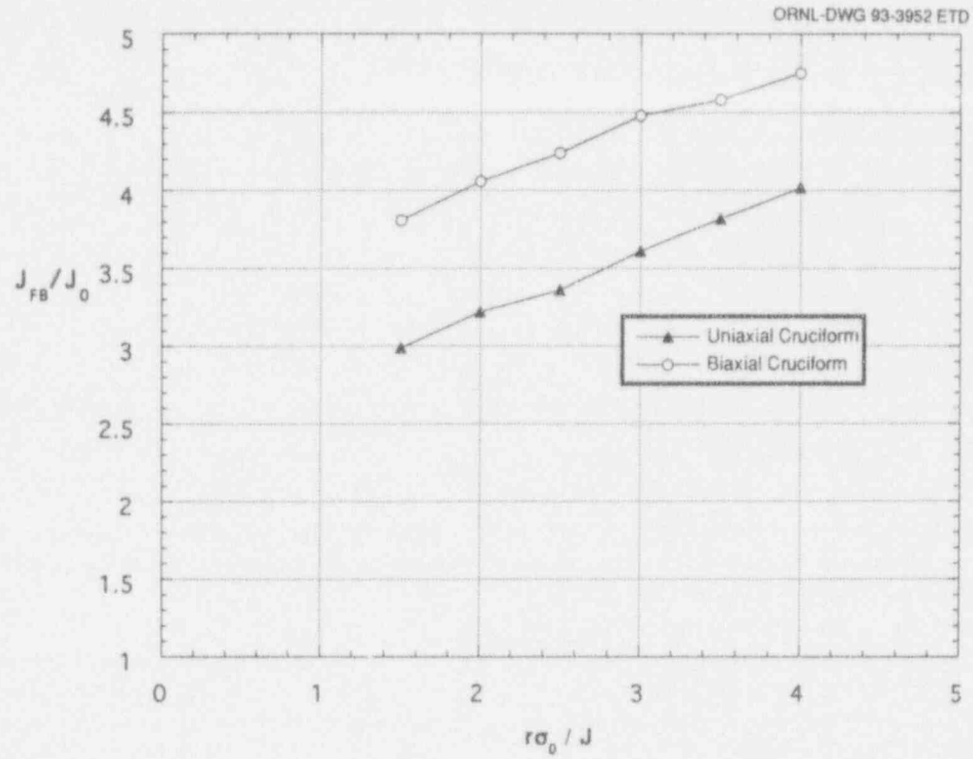

Figure 3.29 Finite-body to SSY toughness ratio as a function of normalized distance ahead of crack tip

cases. The D-A scaling model results do not, therefore, meet the criteria established in Ref. 11.

There are two potential explanations for J_0 varying by more than the accepted criteria of 10%. The first is the nature of the cruciform specimen itself, which possesses 3-D stress fields that vary through the thickness (see Fig. 3.8). The D-A scaling model allows the use of critically stressed areas ahead of the crack, assuming a relatively constant field through a specimen thickness. The second explanation is the assumption that the stressed areas in these cases are similarly shaped, allowing the comparison of distances ahead of the crack rather than areas. This assumption could lead to variations in J_0 that might not exist had the D-A scaling model used contour areas.

Figure 3.29 indicates that the range of J_{FB}/J_0 ratios for the uniaxial cruciform is consistent with previous J_{FB}/J_0 values for the shallow-crack SENB specimens. The uniaxial cruciform yields values of J_{FB}/J_0 between 3 and 4; the shallow-crack SENB specimens yielded J_{FB}/J_0 ratios ranging from 1.8 to 5.6, averaging ~2.7. Finally, as shown in Fig. 3.29, the biaxial J_{FB}/J_0 ratio is ~25% greater than the uniaxial J-ratio. This implies greater constraint loss for the biaxial specimen than the uniaxial specimen, a result which is inconsistent with the experimental toughness results. However, these ratios have been determined for a very limited number of tests. Additional tests will be necessary to determine if these trends continue.

The J_0 values were calculated for the uniaxial and biaxial cruciform tests for comparison with SENB J_0 values using the analytically based J_{FB} values and the J_{FB}/J_0 ratios determined at $\tilde{r} = 2$. The ratio at $\tilde{r} = 2$ was chosen because the Q-stress is typically determined at that location and the biaxial and uniaxial stresses ahead of the crack tip are almost identical at that location (see Fig. 3.28). The J_0 and K_0 values for the four cruciform tests are shown in Table 3.3 along with the upper and lower SSY toughness results from the shallow- and deep-crack SENB tests; K_0 values are also included in Fig. 3.27. As indicated in Table 3.3, all of the cruciform SSY toughness values are within the range of SSY data from the SENB specimens. The J_0 values from the biaxial cruciform are near the lower limit of the SENB J_0 range; the uniaxial J_0 value was nearer the upper limit. Additional data are necessary to determine the full range of SSY toughness values under uniaxial and biaxial loading.

3.4 Discussion of Crack-Tip Analyses

The J-Q method and D-A scaling model have been applied to the shallow- and deep-crack SENB tests and the uniaxial and biaxial cruciform tests. Data sets used in these applications are generated from tests of specimen geometries that

Table 3.3 SSY toughness results for the uniaxial and biaxial cruciform specimens

Specimen No.	Loading configuration	J_{FB} (kN/m)	J_o (kN/m)	K_{FB} (MPa$\sqrt{m}$)	K_o (MPa$\sqrt{m}$)
BB-1	0.6:1	160	39.4	190	94
BB-2	0:1	257	79.8	241	134
BB-4	0.6:1	160	39.4	190	94
BB-5	0.6:1	174	42.9	198	98

Notes: J_{FB}/J_o ratio at $\tilde{r} = 2$ was used.
Plane strain relationship between J and K was used.
SENB (shallow- and deep-crack) SSY data were J_o = 35.9–95.8 kN/m or K_o = 90–147 MPa$\sqrt{m}$.

provide a contrast in analytical modeling requirements. The SENB specimen is modeled in terms of a 2-D plane strain formulation, while the cruciform specimen exhibits a fully 3-D character that must be considered. Analysis results indicate that both methodologies can be used successfully to interpret experimental results from the deep- and shallow-crack SENB specimen tests. Applications of the two methodologies to the cruciform specimen each showed promising features, but they also raised several issues concerning constraint analysis based on near-tip stress fields. These issues have been identified and discussed in the preceding sections. Some additional observations of the limitations of the two methods applied to the cruciform specimen are presented herein.

Figure 3.30 shows the stresses ahead of the crack tip for the SSY solution and the uniaxial and biaxial cruciform specimens at the critical value of J. (Figure 3.30 is identical to Fig. 3.28 except for the distance scale and the construction of J_{FB}/J_o.) Because both the J-Q method and the scaling model are based on the stresses ahead of the crack tip, observations about Fig. 3.30 are germane to both techniques. First, the coincidence of the critical crack-tip

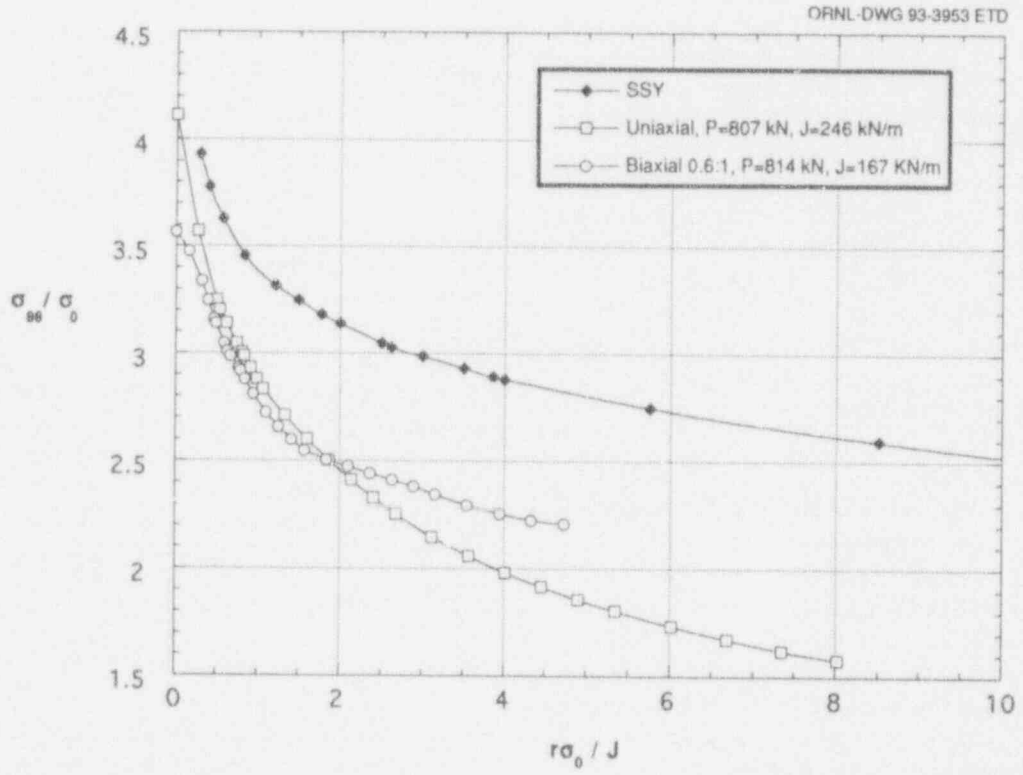

Figure 3.30 Opening-mode stresses ahead of crack tip for the SSY solution and uniaxial and biaxial cruciform specimens at critical values of J

stresses near the crack tip ($\tilde{r} \leq 2$) is encouraging and indicates the potential applicability of these methods to the uniaxial and biaxial cruciform specimens. Furthermore, both the uniaxial and biaxial stresses deviate significantly from the SSY solution, indicating that the J-integral alone cannot characterize the crack-tip stresses. The crack-tip stresses for the uniaxial and biaxial cruciform specimens begin to diverge at $\tilde{r} = 2$, which reflects that the far-field bending stresses are beginning to impinge on the crack-tip stresses in the uniaxial case. In other words, at distances very near the crack tip, ($\tilde{r} \leq 2$), the stresses are dominated by the crack-tip singularity. At distances satisfying $\tilde{r} > 2$, however, the stresses tend to be influenced by the far-field bending stress, resulting in a divergence of the uniaxial and biaxial stresses. Physically, $\tilde{r} \geq 2$ represents a distance ahead of the crack tip of 1.2 and 0.8 mm for the uniaxial and biaxial cruciform specimens, respectively. These distances are well within the corresponding plastic zone radius that is conservatively estimated, from the plane strain relation,[22] to be 14 and 9.6 mm for the uniaxial and biaxial case at failure, respectively. In reality, both the uniaxial and biaxial specimens have reached a condition of uncontained yielding at the point of failure.

The difference between the SSY stresses and the uniaxial and biaxial stresses (i.e., the Q-stress) ahead of the crack tip is shown in Fig. 3.31. The Q-stress for the uniaxial specimen is not constant within the range of $\tilde{r} = 1.5$ to 5 because of the interaction of the bending stresses with the crack-tip singular stresses. In fact, the uniaxial stresses in Fig. 3.30 between $\tilde{r} = 6$ and 8 appear to be controlled by the far-field bending stress, resulting in a near linear stress distribution. If the identical load were applied to the specimen in a tensile manner rather than through bending loads, the Q-stress for the uniaxial specimen is expected to be more uniform than shown in Fig. 3.31. It is anticipated, however, that the bending stress field will influence the uniaxial and biaxial specimens less as the specimen size increases and/or the load at failure decreases.

In contrast with the uniaxial specimen, the biaxial Q-stress shown in Fig. 3.31 is relatively constant over the distances shown. In fact, the biaxial Q-stress at failure agrees well with the shallow-crack Q-stress determined from the SENB specimens.[5] The reason for the constant biaxial Q-stress appears to be due to offsetting effects. First, the bending stress tends to drive the Q-stress more negative with distance from the crack tip as in the uniaxial case. The offsetting effect is the out-of-plane biaxial load itself. The addition of the out-of-plane stress increases the hydrostatic stress, which in turn increases the opening-mode stress. The offsetting nature of the bending stress and the out-of-plane stress cannot be generalized, however, for other biaxially loaded specimens.

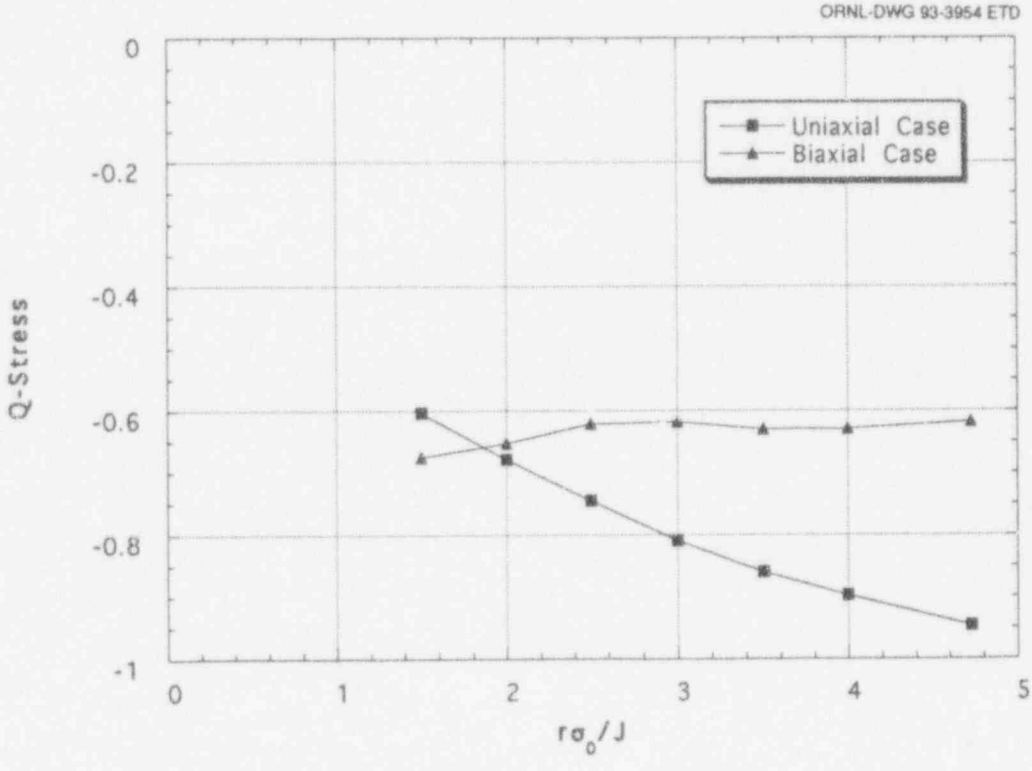

Figure 3.31 Q-stress ahead of crack tip at critical values of J for uniaxial and biaxial cruciform specimens

Constraint

The application of crack-tip analysis to a shallow-crack cruciform specimen under biaxial loading such as described in this chapter represents a significant challenge for these techniques. Differences in constraint conditions due to a biaxial load are difficult to quantify because of the absence of an appropriate distance parameter. Out-of-plane constraint (i.e., thickness effects) can be quantified in terms of the specimen thickness B. In-plane constraint loss is similarly related to a shallow-crack depth, a or a/W. Biaxial loading, however, which impacts the crack-tip stresses substantially, has no appropriate length scale or distance parameter to which the constraint condition can be related. Another way of considering the influence of biaxial loading is that the out-of-plane stress appears to make the specimen behave as a larger uniaxial specimen.

The final impact of out-of-plane biaxial loading is not fully known at this time. It is known, however, that biaxial loading does impact the conditions at the crack tip in a significant manner under conditions of uncontained yielding. Preliminary estimates from Ref. 23 indicated that under contained yielding, changes in initiation toughness due to biaxial effects would not exceed a few percent. Biaxial effects were exhibited in the cruciform specimen at conditions beyond contained yielding. The analyses confirm previously described experimental trends. As shown in Fig. 3.30, uniaxial and biaxial near-tip stresses ($\tilde{r} \leq 2$) are coincident at failure loads. The applied load at which failure occurred in the uniaxial and biaxial specimens is almost identical; however, the critical value of toughness (J in Fig. 3.30) is quite different. Biaxial loading further alters the way that applied load on a cracked specimen is related to the crack-driving force. Biaxial loading also substantially reduces the ductility of a specimen. Additional crack-tip analysis and additional biaxial tests are necessary before the impact of the biaxial loads on the fracture resistance of an RPV is understood.

4 Fractography and Fracture Characterization Issues

4.1 Fractographic Examinations

Fractographic examinations were conducted on the cruciform specimens and several of the shallow- and deep-crack specimens to examine the fracture modes, cleavage origins, and other characteristic surface features. The examinations included optical and scanning electron microscopy (SEM) observations as well as measurement of several key parameters. Previous fractographic results[1] have focused on the measurement of the fractographic data and a description of the general features of the fracture surface of the specimen(s). This section includes fractographic information reported previously on the cruciform specimens and describes additional fractographic information on these specimens, including the data from additional shallow- and deep-crack beams for comparison. This section also combines pertinent fractographic, analytical, and experimental results from these specimens and provides an interpretation (or reinterpretation) of analytical or experimental results in light of existing fractographic information.

The fractographic information obtained thus far from the cruciform, shallow- and deep-crack specimens is listed in Table 4.1. The information is generally consistent among the different specimen types or loading conditions. Specific details concerning the measurement methods used to compile Table 4.1 are found in Ref. 1. In addition to the fractographic information, Table 4.1 contains a comparison of fractographic and experimental estimates of CTOD for several deep- and shallow-crack specimens. The experimental estimate of CTOD is detailed in Ref. 5. The fractographic estimate of CTOD is calculated using the crack-tip blunting measurement (see Fig. 4.1) assuming an opening angle of 45° [i.e., CTOD = (2) (sin 45) (blunting)]. Recent fractographic measurements indicate that the opening angle (θ in Fig. 4.1) seems to vary with fracture toughness but averages about 45°. Future plans include the measurement of the crack-opening angle in different specimens and correlation of the angle with fracture toughness or other parameters. Toughness values shown in Table 4.1 are all based on the area under the P-CMOD curve method described in Chap. 2.

Several observations can be made relative to the information in Table 4.1. Additional data, however, are necessary before these observations can be deemed conclusive. The fractographic data show remarkable similarity in the measurements in all specimens with both ductile crack extension (Δa) and cleavage origin distances (X) falling within a narrow range. This is partially explained by the narrow range of toughness values. The data also show a consistent correlation between toughness and $\Delta a + X$ values. Next, the estimates of CTOD determined using the crack-tip blunting show good agreement with the experimental estimates of CTOD. This agreement tends to validate the techniques used in these evaluations and provides an independent verification of previously reported CTOD values.

Examining the ductile crack extension (Δa) and distance to the cleavage origin (X) reveals that shallow-flaw specimens often show less ductile crack extension (Δa) and cleavage origin distances (X) than deep-crack specimens at comparable toughness levels. Additional deep-crack toughness data are necessary, however, to determine if this trend is a function of crack depth or toughness. Finally, the cleavage origin distances (X) tend to be smaller in the specimens tested under 0.6:1 biaxial loading than in the uniaxial specimens. Again, additional data are required to confirm this trend.

4.2 Cleavage Initiation Sites and Stress-Based Fracture Characterization

Measured data in Table 4.1 are being used to assess the relevance of stress-based fracture characterizations to conditions at cleavage initiation sites in SENB and cruciform beam test specimens. (Previous studies that seek to interpret fracture toughness results through fractographic observations include those of Heerens et al.[24]) The important elements of this study can be summarized through reference to Fig. 4.2. Figure 4.2(*a*) and (*b*) depicts normalized opening-mode, near-crack-tip stress distributions from finite-strain analyses of SENB and biaxially loaded cruciform specimens; the stress distributions are plotted vs normalized distance in front of the crack tip. The finite-strain SSY solutions are shown for reference. In Fig. 4.2(*c*) and (*d*), normalized distances $[(X + \Delta a)\sigma_0/J]$ to cleavage initiation sites are plotted for SENB and cruciform bend test specimens. Values for the distance $X + \Delta a$, measured from the tip of the fatigue precrack to the cleavage initiation site, are taken from Table 4.1.

The central issue here concerns the location of a preponderance of the cleavage initiation sites relative to that region in front of the crack tip where increasing applied J implies increasing opening-mode stress. In Fig. 4.2(*a*), an effect of progressive loss of stress triaxiality is to shift the stress peak to the left (i.e., toward the crack tip) relative to the SSY stress peak. Given these conditions, the following question is posed: Do the measured cleavage initiation sites tend to fall in a region of the computed stress field where opening-mode stress is increasing with increasing applied J, that is, in Region A of Fig 4.2(*a*) to the right of the stress

Table 4.1 Summary of fractographic information

Specimen No.	Specimen type	Flaw depth	K_{Jc} (MPa$\sqrt{m}$)	T – RT_{NDT} (°C)	Distance to origin, X (μm)	Ductile crack extension, Δa (μm)	Distance from fatigue precrack to initiation location, Δa + X (μm)	Blunting (μm)	Fractographic CTOD (μm)	Experimental CTOD (μm)
11	SENB	Shallow	139	–22	74–150[a]	63	138–213	80	136	196
12	SENB	Deep	103	–22	75–120[a]	24	99–144	70	119	61
38	SENB	Shallow	157	–24	200	74	274	108	184	206
31	SENB	Deep	108	–25	70	11	81	88	150	63
22	SENB	Shallow	298	8	350	535	885	628	1069	942
24	SENB	Deep	219	8	550–950[a]	342	892–1292	324	551	367
27	SENB	Shallow	230	–7	220	270	490	290	494	559
28	SENB	Shallow	331	9	750	750	1500	*c*		
BB-1	Cruciform	Shallow	175	–10	90–125[a]	64	154–189	*c*		
BB-2	Cruciform	Shallow	214	–4	50–100[a]	77	127–177	*c*		
BB-3	Cruciform	Shallow	*c*	–12	*b*	45	*b*	*c*		
BB-4	Cruciform	Shallow	178	–11	140	83	223	*c*		
BB-5	Cruciform	Shaliow	178	–9	90	87	177	*c*		

[a]Location of origin unclear.

[b]Origin in corner.

[c]Not measured.

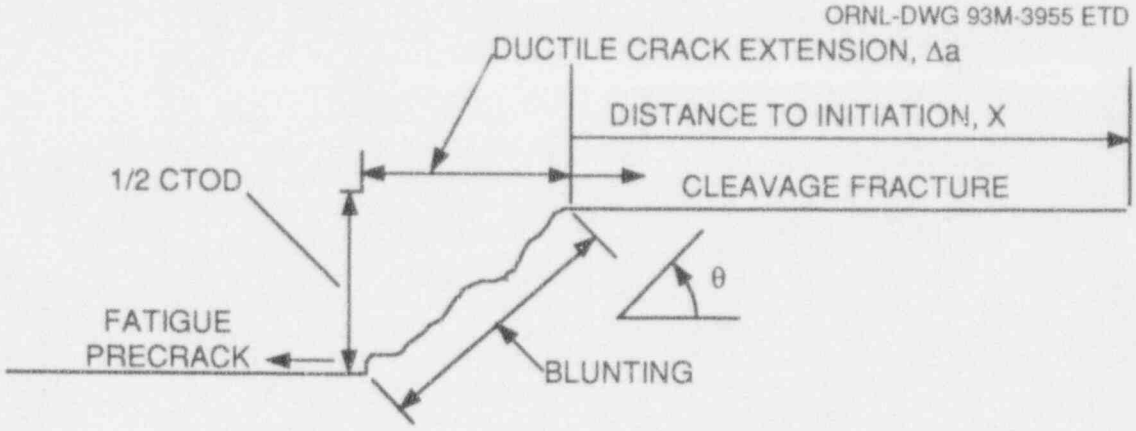

Figure 4.1 Schematic defining fractographic variables

peak? (Material points to the left of the stress peak experience a stress field that decreases in magnitude with increasing J). The expectation* is that a cleavage initiation event governed by a stress-based criterion will occur in a rising near-tip stress field under increasing applied load.

Results depicted in Fig. 4.2 permit comparisons of normalized distances from the crack tip to opening-mode stress peaks at failure and to measured cleavage initiation sites. For the SENB shallow-crack specimens, the initiation sites appear to fall in the region experiencing a rising stress field, that is, to the right of the stress peak in Fig. 4.2(*a*). The cruciform specimens present a contrasting result, with the sites located in a falling stress field with increasing J, that is, to the left of the stress peak in Fig. 4.2(*b*). Thus, fractographic data from the SENB shallow-crack specimens [Fig. 4.2(*c*)] tend to support the expectation for a critical stress-based fracture criterion discussed above, while data from the cruciform specimens [Fig. 4.2(*d*)] require further study for reasons discussed below.

Results of this comparison between locations of the stress peak and the cleavage initiation sites for the cruciform specimens must be evaluated in the context of several factors. The fractographic data in Table 4.1 reflect that the process leading to cleavage fracture involves ductile extension of the crack tip before unstable cleavage. The finite-element models employed in analyses of the specimens in Table 4.1 do not incorporate the micromechanical processes that lead to generation of new fracture surfaces before the onset of cleavage instability. The 3-D finite-element model of the cruciform specimen described herein utilizes centered-fan crack-tip elements that allow a simplified blunting and translation of the tip without considering the complexities of the actual process. Inclusion of model refinements associated with these crack-tip processes can potentially influence the near-crack-tip stress fields and, consequently, interpretations of any comparisons between analytical predictions and measured fractographic data.

The opening-mode stress distributions in Fig. 4.2(*a*) and (*b*) are plotted vs normalized distance from the crack tip based on the initial undeformed configuration of the model. Of necessity, measurements taken on the fracture surfaces and compiled in Table 4.1 are given in terms of deformed points in the broken specimen. To compensate for these differences, adjustments of the material reference configuration have been proposed for the analytical and experimental plots of Fig. 4.2. One option is to plot the opening-mode stress distribution in terms of the deformed coordinates of the finite-element model and compare this directly with distance X measured from the tip of the blunted crack to the cleavage initiation site.

The proposed adjustment for results given in Fig. 4.2 is based partly on a hypothesis describing micromechanical processes leading to cleavage fracture in the test specimens of Table 4.1. Studies to effectively validate such adjustments or hypotheses have been initiated but not completed. Motivation for such adjustments is derived primarily from recognized limitations of the analytical models in representing the micromechanics of fracture processes. It* has been proposed that development and application of a micromechanical model based on void formation and strain softening concepts (e.g., see Ref. 25) could potentially resolve issues related to representation of crack-tip stress fields.

*W. E. Pennell et al., Martin Marietta Energy Systems, Inc., Oak Ridge Natl. Lab., "Biaxial Loading and Shallow-Flaw Effects on Crack-Tip Constraint and Fracture-Toughness," presented at the Twenty-First Water Reactor Safety Information Meeting, Bethesda, Md., Oct. 25, 1993.

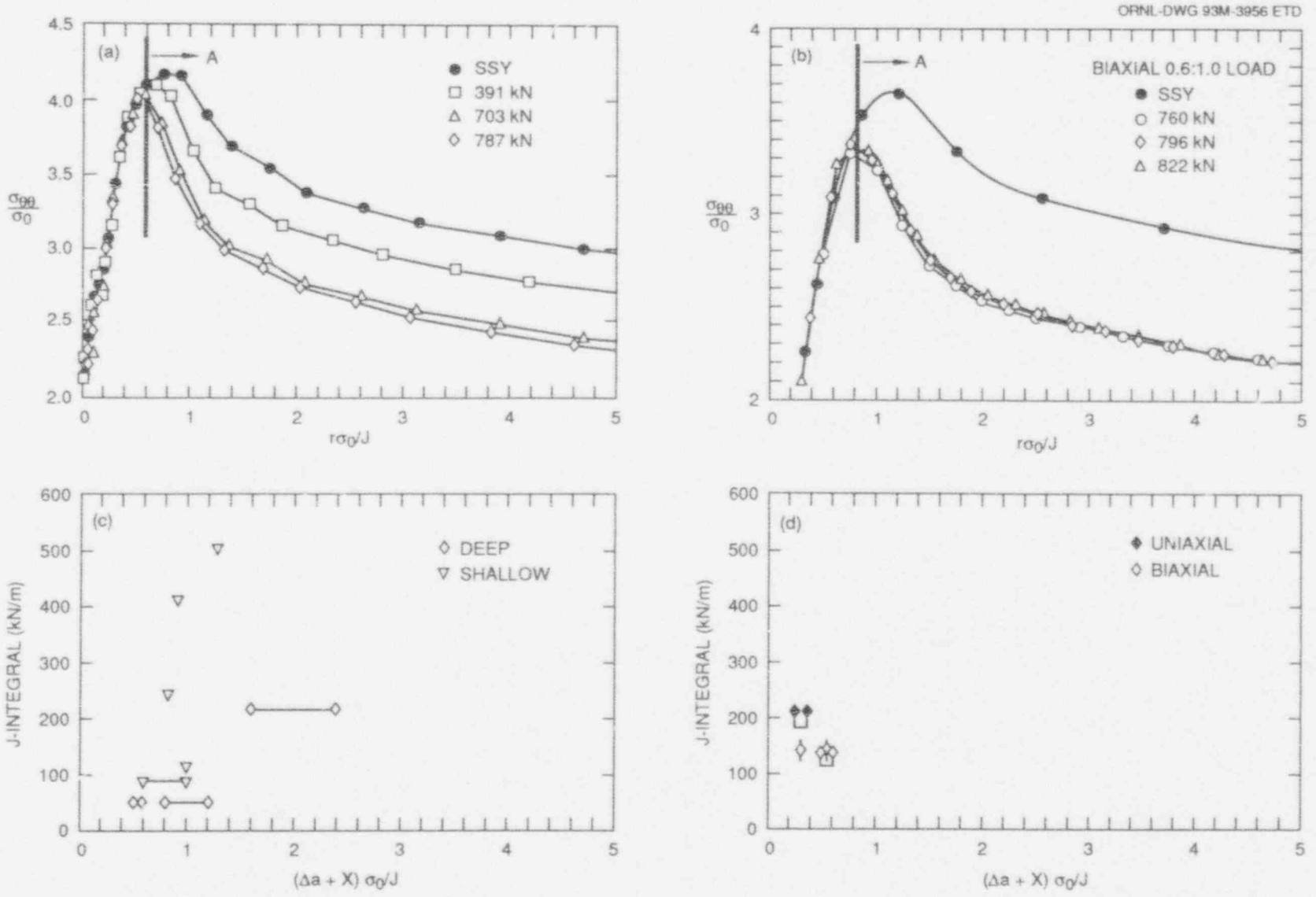

Figure 4.2 (*a*) **Distributions of opening-mode stress component for SENB specimen with a/W = 0.1 as function of applied load up to crack initiation; (*b*) distribution of opening-mode stress component for biaxial shallow-crack cruciform specimen; (*c*) toughness vs normalized distance to initiation site for shallow- and deep-crack SENB specimens; and (*d*) toughness vs normalized distance to initiation site for uniaxial and biaxial shallow-crack cruciform specimens**

4.3 3-D Interpretation of Toughness

One of the functional criteria of a satisfactory biaxial cruciform specimen design was that "the crack-driving forces be relatively uniform over a substantial portion of the crack distance with no significant edge effects."[1] The criteria were satisfied for the initial phase of the biaxial testing program by showing that the cruciform specimen did not have a propensity for crack initiation at the intersection of the diffusion slots and the crack tip. One specimen (BB-3) did initiate at the corner, and as a consequence the toughness result was considered suspect and was not determined. Due to the concern over edge effects in the cruciform specimens, the initiation site location along the crack front for all of the cruciform specimens and for several of the shallow- and deep-crack beam specimens was measured.

Conventionally, the position of the initiation site within the thickness of the specimen is not important because of the consistency of crack-driving force through the specimen thickness. For example, analysis of a 4T compact-tension specimen reveals that at the limit of plane strain validity determined by ASTM E399, the crack-driving force is within 5% of the centerline value over the central 90% of the specimen thickness.* Obviously, as the load level increases into the elastic-plastic domain, thickness variation in the crack-driving force will take place. The point remains, however, that conventional specimens have fairly uniform crack-driving forces over their thickness, making the toughness interpretation a 2-D calculation without regard to the actual location of the initiation site along the crack front.

As discussed previously in this report and in Ref. 1, the variation of crack-driving forces through the thickness of the cruciform specimen is greater than that for conventional specimens. In fact, through-thickness variation is estimated to be as large as the toughness difference between biaxial and uniaxial loading conditions being determined in these studies. These observations have led to consideration of initiation site locations along the crack front and to the 3-D interpretation of fracture toughness described herein.

All experimental measurements used to measure fracture toughness are taken at the specimen centerline, and additional measurements through thickness are impractical. Analytical results provide the best estimate of the variation of the crack-driving force and, subsequently, 3-D toughness values. The calculated variation of crack-driving forces through the thickness for specimens BB-4 and -5 is shown in Fig. 4.3 along with the location of the initiation sites for these two tests. As shown in Fig. 4.3, specimen

*D. K. M. Shum, "Preliminary Investigation on the Inclusion of Warm Prestress Effects in Fracture-Margin Assessment of Reactor Pressure Vessels," NUREG/CR-5946 (ORNL/TM-12236), to be issued.

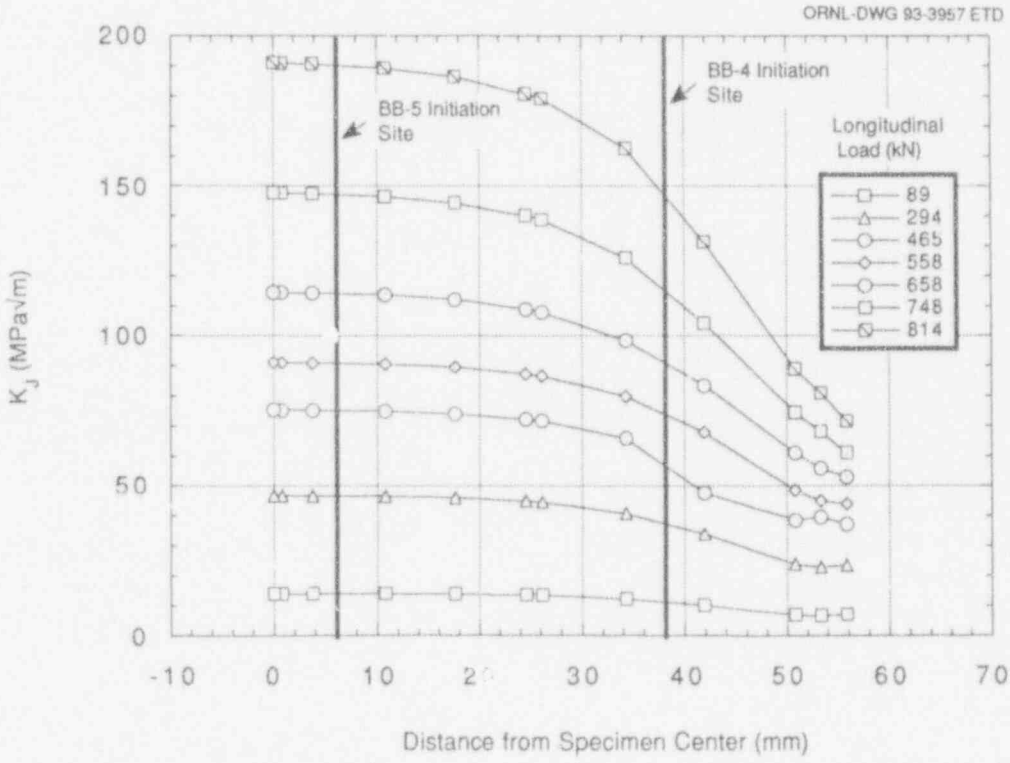

Figure 4.3 Crack-driving force through-thickness for BB-4 and -5

BB-5 initiated sufficiently close to the specimen centerline that the 3-D toughness value is the same as 2-D toughness value. Specimen BB-4 initiated about 38 mm from the centerline. The crack-driving force at this position is ~20% less than at the center. The 3-D toughness values are computed by decreasing the 2-D toughness values as determined analytically from the variation of crack-driving force at the center and the position of crack initiation.

The 3-D toughness values were determined for all the cruciform specimens (except BB-3) and the shallow- and deep-crack SENB specimens tested at the same normalized temperature ($T - RT_{NDT} = -10°C$). The 3-D toughness data for these specimens and the information needed to compute the 3-D toughness, such as initiation location and analytical ratio of 3-D/2-D toughness values, are included in Table 4.2. Table 4.2 indicates that few of the specimens initiated directly at the specimen center or close to the edge. Most specimens initiated at about the 1/4 t location through the specimen thickness. As expected, the 3-D toughness values for the deep-crack specimens are indistinguishable from the 2-D values. The shallow-crack specimens, however, exhibit a small increase in toughness at the 1/4 t location over the centerline value. The cruciform specimens BB-1, -2, and -4 show a reduction in toughness of about 20 to 25%. The toughness for specimen BB-5 remains unchanged. The 3-D toughness results for all specimens tested at $T - RT_{NDT} = -10°C$ are plotted as a function of load ratio in Fig. 4.4. The comparable 2-D toughness plot is shown in Fig. 2.5. A comparison of Figs. 4.4 and 2.5 indicates that both interpretations of toughness are reasonable. The uniaxial cruciform specimen (BB-2) has a 2-D toughness toward the mean of the shallow-crack specimens but a 3-D toughness near the lower bound of the shallow-crack beam data. The average of biaxial cruciform data is decreased about 15% from 177 to 149 MPa$\sqrt{m}$ by considering the initiation site location. The scatter of the biaxial data is increased when the 3-D toughness interpretation is considered. The primary observation, however, that biaxial loading reduces some but not all of the shallow-crack toughness increase appears accurate for both toughness interpretations.

The 3-D interpretation of toughness is not being recommended or proposed for all testing applications. The analytical and fractographic effort to interpret the 3-D toughness is not justified for most specimens. The cruciform specimen tests are sufficiently unconventional and novel to warrant this type of treatment. These results should be considered tentative because the entire concept of considering the initiation point in toughness determinations is new and not well understood.

Table 4.2 3-D interpretation of toughness

Specimen	B (mm)	Initiation location	% t (1/4 t . . .)	Ratio of 3-D K_J to 2-D K_J	2-D K_{Jc} (MPa$\sqrt{m}$)	3-D K_{Jc} (MPa$\sqrt{m}$)
Deep-crack beams at $T - RT_{NDT} = -10°C$ [CE material]						
12A	100	31 mm from edge	0.31	1	119	119
13A	100	12 mm from edge ?	0.12	0.95	143	136
14A1	50	15 mm from edge	0.30	1	145	145
14A1	50	Center ?	0.50	1	93	93
15A	150	Center ?	0.50	1	134	134
16A	150	Center ?	0.50	1	109	109
Shallow-crack beams at $T - RT_{NDT} = -10°C$ [13B material]						
18	100	12 mm from edge	0.12	1.06	213	226
21	100	29 mm from edge	0.29	1.03	174	179
27	100	26 mm from edge	0.26	1.03	230	237
Shallow-crack cruciforms at $T - RT_{NDT} = -10°C$ [CE material]						
BB-1	100	2.5 mm from edge	0.03	0.76	175	133
BB-2	110	20 mm from edge	0.18	0.82	214	175
BB-3	110	Corner	0.00	N/A	N/A	N/A
BB-4	110	18 mm from edge	0.16	0.76	178	135
BB-5	110	50 mm from edge	0.45	1	178	178

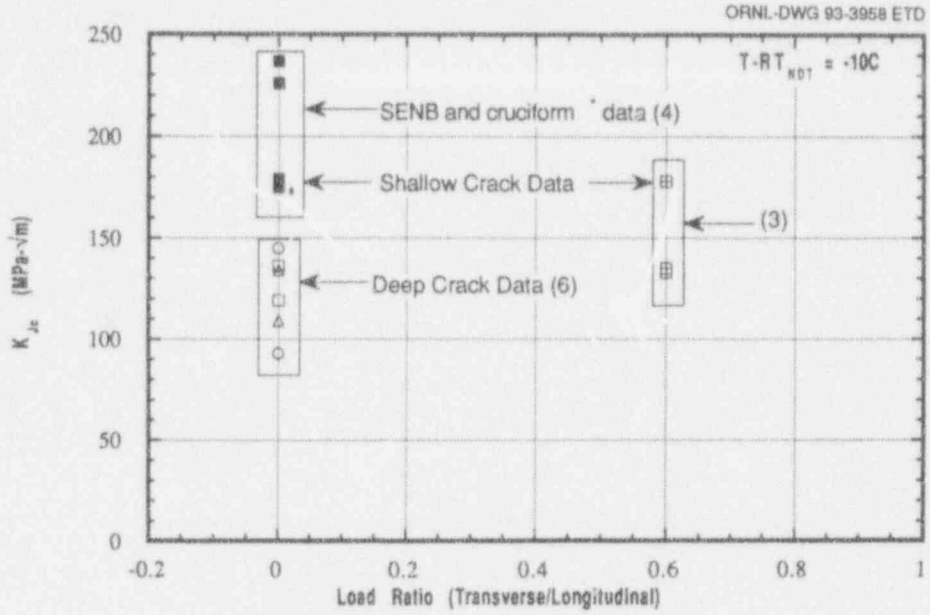

Figure 4.4 3-D toughness results as function of load ratio for data at RT_{NDT} = –10°C

5 Summary and Conclusions

Crack-tip constraint is an issue that significantly impacts fracture mechanics technologies employed in failure predictions for commercially licensed nuclear RPVs. A validated technology that incorporates constraint effects is essential to the transfer of fracture toughness data from, for example, miniature fracture toughness surveillance specimens to RPVs. This capability could have a substantial impact on the outcome of probabilistic PTS analyses and assessments of startup/cooldown transients of aging nuclear plants. This report has provided interim results from a program to evaluate selected fracture methodologies for the quantitative assessment of crack-tip constraint effects on fracture toughness of RPV steels.

Far-field tensile out-of-plane biaxial loading and shallow-crack effects have been identified as constraint issues that influence both fracture toughness and the extent of the fracture toughness scatter band. Relevance of these issues to RPV failure predictions is supported by several observations. First, PTS loading produces biaxial stress fields in an RPV wall that have no counterpart in conventional laboratory specimens used to generate fracture toughness data. Limited data indicate that a decrease in toughness is associated with biaxial loading. Second, the probability of RPV vessel failure in PTS analyses is dominated by initiations from shallow cracks. Recent testing has demonstrated an effective increase in fracture toughness of shallow cracks compared to deep-cracked specimens. Determining the extent of the interaction between this toughness elevation associated with shallow cracks and toughness reduction due to biaxial loading effects is one of the main goals of the HSST biaxial testing program.

The focus of the studies described herein has been on evaluations of stress-based fracture methodologies (i.e., the J-Q model of O'Dowd and Shih and the D-A constraint correction model) through applications to experimental and fractographic data. These methodologies were selected for the initial evaluations because of their previously demonstrated promise as practical means for incorporating effects of crack-tip constraint into fracture assessments. Data for these assessments were obtained primarily from the HSST shallow-crack and biaxial testing programs. Shallow- and deep-crack SENB specimens and uniaxially and biaxially loaded cruciform specimens from these testing programs were analyzed using both the J-Q methodology and the D-A constraint scaling model. The SENB data set consists of 14 deep-crack and 14 shallow-crack specimens; the biaxial cruciform data set included one uniaxially loaded and three biaxially loaded specimens.

The J-Q methodology was first applied to a subset of shallow- and deep-crack SENB specimens. The J-Q analysis of the SENB specimens indicated a significant loss of constraint for the shallow-crack specimens with the Q-stress saturating at about –0.7. The deep-crack specimens had negligible constraint loss with $Q \sim 0$. Both specimens developed spatially independent Q-stress fields ahead of the crack.

The J-Q analyses of the cruciform specimens yielded results that are not as straightforward to interpret as the SENB specimens. The uniaxial cruciform specimen failed at a sufficiently high load that the far-field bending stress began to impinge on the near-tip stress field in the annulus $2 < \tilde{r} < 5$. This near-tip and far-field stress interaction produces Q-stresses that decrease linearly with distance from the crack tip. The Q' function was introduced to quantify this spatial dependence of the Q-stress field over the crack-tip annulus. The criterion $|Q'| < 0.1$ is not satisfied in the uniaxial cruciform specimen as failure is approached. However, this criterion (from O'Dowd and Shih[8]) permits a relatively large variation in Q-stress over the crack-tip annulus. In the present application, the variation in Q-stress over the annulus is greater than the difference between Q-stress values calculated for the uniform and biaxial loading cases. Biaxial loading of the cruciform specimen produces a higher stress triaxiality ahead of the crack tip at failure than the uniaxial case; also, it generates essentially a uniform hydrostatic stress field (i.e., a very low value of Q') in front of the crack tip.

The J-Q loading trajectories were computed for the uniaxial and biaxial cruciform specimens at normalized distances $\tilde{r}$ ahead of the crack tip of 2, 3, 4 and 5. At distances farther from the crack tip ($\tilde{r}$ = 4 and 5), the uniaxial and biaxial trajectories followed the same path up to relatively high load levels. The expectation was that the J-Q trajectories would exhibit this behavior at least up to intermediate loads, given the similarity of the P-CMOD responses. The J-Q trajectories at $\tilde{r}$ = 2 and 3 were not so well behaved. The trajectories for the uniaxial case exhibited a higher constraint condition (i.e., higher Q-stress) than the biaxial case for almost the entire loading path. This result conflicts with experimental results which imply that the biaxially loaded specimen is the more highly constrained specimen. However, there is no rationale for quantifying constraint at distances farther removed from the crack tip (i.e., at distances $\tilde{r}$ >2), where far-field stresses were observed to have a strong influence in the uniaxially loaded specimen. Fractographic data from the cruciform specimens showed no evidence of cleavage initiation sites in the annulus $\tilde{r} > 2$. Thus, despite the

observed inconsistencies, the cruciform specimens were interpreted in terms of J-Q trajectories computed at $\tilde{r} = 2$. From the J-Q trajectories at $\tilde{r} = 2$, critical Q-stress values of –0.69 and –0.66 were determined for the uniaxial and biaxial loading conditions, respectively. These failure points fall within the scatter of a J-Q failure locus generated from deep- and shallow-crack SENB and wide-plate results at the same normalized temperature.

Applications of the D-A scaling model to data obtained from shallow- and deep-crack SENB specimens produced very good results. The scaling model provided adjusted SSY toughness values in the transition region that were virtually identical for deep- and shallow-crack data. In addition to removing the influence of crack depth in the toughness data, the scaling model reduced the scatter associated with the shallow-crack data.

When the scaling model was applied to the cruciform data, the results were again more difficult to interpret than the SENB application. In the original formulation of the scaling model, toughness data are adjusted to SSY values based on ratios of areas (or volumes) within stress contours around the crack tip. The engineering model applied to the cruciform specimens approximates these ratios from the stress distribution directly ahead of the crack tip. Stresses very close to the crack tip ($\tilde{r} < 2$) were used to determine the J_{FB}/J_O ratios for the cruciform specimens. These ratios were found to vary ~25% over the annulus $1.5 < \tilde{r} < 4$ for both uniaxial and biaxial load cases. This difference exceeds the maximum of 10% recommended in Ref. 11 for a valid calculation of J_O. Also, the biaxial J_{FB}/J_O ratio was ~25% greater than the uniaxial ratio, which implies a greater constraint loss for the biaxial specimen than the uniaxial specimen. The latter result is inconsistent with toughness results determined from experimental data. All of the cruciform SSY toughness values determined from these ratios, however, were within the range of SSY data from the SENB specimens.

Fractographic examinations were conducted on several of the fracture surfaces from the shallow- and deep-crack SENB specimens and the cruciform specimens. Fractographic information included crack-tip blunting (which can be related to CTOD), ductile crack extension Δa, and distance to the cleavage initiation site X. The total distance to the initiation site ($\Delta a + X$) appears to increase with increasing toughness, but shallow-crack specimens seem to have lower $\Delta a + X$ values than deep-crack specimens at the same toughness level. However, additional data are necessary to confirm this trend.

Comparisons were performed between measured data describing total distance to cleavage initiation sites ($\Delta a + X$) and distance to opening-mode stress peaks in near crack-tip stress fields. The central question can be stated as follows: Are the cleavage initiation sites concentrated in a region where the computed opening-mode stress field is increasing with increasing applied J? The expectation is that cleavage initiation would occur for a condition of increasing stress at the measured initiation site. The initiation sites for the SENB shallow-crack specimens appear to fall in a region experiencing a rising stress field, and those for the cruciform specimens are located in a falling stress field. Thus, fractographic data from the SENB shallow-crack specimens tend to support the expectation for a critical-stress-based fracture criterion posed above, while data from the cruciform specimens require further study for reasons discussed previously. The preponderance of initiation sites at $\tilde{r} \sim 1$ supports crack-tip constraint methods that are based on stresses very close to the crack tip (i.e., $\tilde{r} \leq 2$). Incorporation of selected micromechanical features of the fracture process into the analytical models are planned and may provide some resolution of the issues related to representation of crack-tip stress fields in the cruciform specimen.

Toughness data for the uniaxial and biaxial cruciform specimens were reinterpreted taking into account the position of the initiation site through the thickness of the specimen. This exercise was performed because the cruciform specimens experienced a substantial decrease in crack-driving force toward the intersection of the crack and the load-diffusion control slot. This through-thickness variation is estimated to be as large as the toughness difference between biaxial and uniaxial loading conditions being determined in these studies. This decrease is more pronounced and influences a greater portion of the thickness than either deep- or shallow-crack specimens. The 3-D toughness reinterpretation lowered the average toughness of the biaxial specimens but increased the scatter of the data. This concept of taking into account the initiation site for toughness determination is unique and will require further examination.

Applications of the J-Q and D-A constraint methodologies presented herein utilized data sets generated from tests of specimen geometries that provide a contrast in analytical modeling requirements. The shallow- and deep-crack SENB specimen is modeled in terms of a 2-D plane-strain formulation, while the fully 3-D character of the uniaxially and biaxially loaded cruciform specimen must be considered. Analysis results from applications indicate that both methodologies can be used successfully to interpret experimental data from the shallow- and deep-crack SENB specimen tests. The two methodologies showed some promising features in applications to the cruciform

specimen, but also raised a number of questions concerning the interpretation of constraint conditions in the specimen from near-tip stress fields. The more successful interpretations of these methodologies applied to the SENB data are partially explained by the greater number of available data points. Crack-tip constraint analyses of the shallow-crack cruciform specimen subjected to uniaxial or biaxial loading conditions represent a significant challenge for these methodologies. Unresolved issues identified from these analyses and summarized in the foregoing discussion require resolution as part of a validation process for biaxial loading applications. Additional cruciform specimens need to be tested before any conclusion can be reached concerning the application of these methods to the cruciform data.

Some additional observations concerning applications to the cruciform specimen are presented herein. The near-tip stresses ahead of the crack are the focal point of the stress-based fracture methodologies applied in this study. The uniaxial cruciform specimen exhibited a substantial interaction of the near-tip and far-field bending stresses, which provided a contrast to a relatively uniform hydrostatic (i.e., Q-stress) field ahead of the crack tip in the SENB specimen. The biaxial specimen appears to be influenced by offsetting effects that also result in a spatially independent Q-stress field ahead of the crack. The far-field stresses, which tend to lower the near-tip stresses, are almost exactly offset by the out-of-plane stress component that increases the opening-mode stress in the biaxial specimen. This offsetting effect, however, cannot be generalized to biaxial specimens having different dimensions or load ratios. In addition, the impact of the far-field bending stress on the near-tip stresses would be reduced in specimens having larger dimensions. Testing of a limited number of larger biaxial cruciform specimens, such as currently planned within the HSST Program, would provide additional data to quantify these effects.

The primary problem with using techniques described herein to examine the influence of biaxial loading is the absence of an appropriate length scale with which to quantify constraint. Differences in out-of-plane constraint are quantified by the specimen thickness; in-plane constraint is related to crack depth, but biaxial loading cannot be related to a similar length parameter. Examination of analytical results from this study indicates that biaxial loading produces a near-tip stress pattern similar to that expected of a larger specimen under uniaxial loading (i.e., biaxial loading increases the "effective" size of the specimen). However, additional data and analyses are necessary to substantiate this observation.

References

1. T. J. Theiss et al., Martin Marietta Energy Systems, Inc., Oak Ridge Natl. Lab., "Initial Results of the Influence of Biaxial Loading on Fracture Toughness," USNRC Report NUREG/CR-6036 (ORNL/TM-12349), June 1993.*

2. R. D. Cheverton and D. G. Ball, Martin Marietta Energy Systems, Inc., Oak Ridge Natl. Lab., "Pressurized-Thermal-Shock Evaluation of the H. B. Robinson Nuclear Power Plant," pp. 263–306, USNRC Report NUREG/CR-4183 (ORNL/TM-95657/V1), September 1985.*

3. R. D. Cheverton and D. G. Ball, Martin Marietta Energy Systems, Inc., Oak Ridge Natl. Lab., "Pressurized-Thermal-Shock Evaluations of the Calvert Cliffs Nuclear Power Plant," pp. 201–244, USNRC Report NUREG/CR-4022 (ORNL/TM-9408), September 1985.*

4. R. D. Cheverton and D. G. Ball, Martin Marietta Energy Systems, Inc., Oak Ridge Natl. Lab., "Preliminary Development of an Integrated Approach to the Evaluation of Pressurized Thermal-Shock as Applied to the Oconee 1 Nuclear Power Plant," pp. 5.1–5.51, USNRC Report NUREG/CR-3770 (ORNL/TM-9176), May 1986.*

5. T. J. Theiss, D. K. M. Shum, and S. T. Rolfe, Martin Marietta Energy Systems, Inc., Oak Ridge Natl. Lab., "Experimental and Analytical Investigation of the Shallow-Flaw Effect to Reactor Pressure Vessels," USNRC Report NUREG/CR-5886 (ORNL/TM-12115), July 1992.*

6. N. P. O'Dowd and C. F. Shih, "Family of Crack-Tip Fields Characterized by a Triaxiality Parameter: Part I—Structure of Fields," *J. Mech. Phys. Solids* 39, 989–1015 (1991).†

7. N. P. O'Dowd and C. F. Shih, "Family of Crack-Tip Fields Characterized by a Triaxiality Parameter: Part II—Fracture Applications," *J. Mech. Phys. Solids* 40, 939–963 (1992).†

8. N. P. O'Dowd and C. F. Shih, Naval Surface Warfare Center, "Two Parameter Fracture Mechanics: Theory and Applications," USNRC Report NUREG/CR-5958 (CDNSWC/SME-CR-16-92), February 1993.*

9. R. H. Dodds, T. L. Anderson, and M. T. Kirk, "A Framework to Correlate a/W Ratio Effects on Elastic-Plastic Fracture Toughness (J_c)," *Int. J. Frac.* 48, 1–22 (1991).†

10. T. L. Anderson and R. H. Dodds, "Specimen Size Requirements for Fracture Toughness Testing in the Ductile-Brittle Transition Region," *J. Test. Eval.* 19, 123–134 (1991).†

11. R. H. Dodds, C. F. Shih, and T. L. Anderson, Department of Civil Engineering, University of Illinois, "Continuum and Micromechanics Treatment of Constraint in Fracture," Report UILU-ENG-92-2014, November 1992.*

12. R. O. Ritchie, J. F. Knott, and J. R. Rice, "On the Relationship Between Critical Tensile Stress and Fracture Toughness in Mild Steel," *J. Mech. Phys. Solids* 21, 395–410 (1973).†

13. D. P. Clausing, "Effect of Plastic Strain State on Ductility and Toughness," *Int. J. Frac. Mech.* 6(1), 71–85 (March 1970).†

14. J. M. Barsom, "Relationship Between Plane-Strain Ductility and K_{Ic} for Various Steels," Paper No. 71-PVP-13 presented at the First National Congress on Pressure Vessels and Piping, San Francisco, California, May 10–12, 1971.†

15. J. G. Merkle, Union Carbide Corp. Nuclear Div., Oak Ridge Natl. Lab., "An Elastic-Plastic Thick-Walled Hollow Cylinder Analogy for Analyzing the Strains in the Plastic Zone Just Ahead of a Notch Tip," ORNL-TM-4071, January 1973.*

16. D. J. Naus et al., Martin Marietta Energy Systems, Inc., Oak Ridge Natl. Lab., "Crack-Arrest Behavior in SEN Wide Plates of Quenched and Tempered A 533 Grade B Steel Tested Under Nonisothermal Conditions," USNRC Report NUREG/CR-4930 (ORNL-6388), August 1987.*

17. D. J. Naus et al., Martin Marietta Energy Systems, Inc., Oak Ridge Natl. Lab., "High-Temperature Crack-Arrest Behavior in 152-mm-Thick SEN Wide Plates of Quenched and Tempered A 533 Grade B Class 1

Steel," USNRC Report NUREG/CR-5330 (ORNL/TM-11083), April 1989.*

18. T. J. Theiss et al., Martin Marietta Energy Systems, Inc., Oak Ridge Natl. Lab., "Preliminary Results from Biaxial Shallow-Flaw Fracture Toughness Tests on Reactor Pressure Vessel Steel," ASME Pressure Vessel & Piping Conference, Denver, Colorado, July 25–29, 1993.†

19. *ABAQUS Theory Manual*, Version 4-8, Hibbitt, Karlson, and Sorensen, Inc., Providence, R.I., 1989.*

20. B. R. Bass, D. K. M. Shum, and J. Keeney-Walker, Martin Marietta Energy Systems, Inc., Oak Ridge Natl. Lab., "Constraint Effects on Fracture Toughness for Circumferentially Oriented Cracks in Reactor Pressure Vessels," USNRC Report NUREG/CR-6008 (ORNL/TM-12131), 1992.*

21. K. Wallin, "Statistical Aspects of Constraint with Emphasis on Testing and Analysis of Laboratory Specimens in the Transition Region," pp. 264–288 in *Constraint Effects in Fracture, ASTM STP 1171*, E. M. Hackett, K. H. Schwalbe, and R. H. Dodds, Eds., American Society for Testing and Materials, 1993.†

22. J. M. Barsom and S. T. Rolfe, *Fracture and Fatigue Control in Structures—Applications in Fracture Mechanics*, 2nd Ed., Prentice-Hall, Englewood Cliffs, New Jersey, 1987.†

23. D. K. M. Shum et al., Martin Marietta Energy Systems, Inc., Oak Ridge Natl. Lab., "Analytical Studies of Transverse Strain Effects on Fracture Toughness for Circumferentially Oriented Cracks," USNRC Report NUREG/CR-5592 (ORNL/TM-11581), April 1991.*

24. J. Heerens et al., "Interpretations of Fracture Toughness in the Ductile-to-Brittle Transition Region by Fractographical Observations," in *Defect Assessment in Components—Fundamentals and Applications*, ESIS/EGF9, J. G. Blauel and K.-H. Schwalbe, Eds. (Mechanical Engineering Publications, London, 1991), pp. 659–678.†

25. J.-C. Devaux et al., "Experimental and Numerical Validation of Ductile Fracture Local Criterion Based on a Simulation of Cavity Growth," pp. 7–23 in *Nonlinear Fracture Mechanics: Volume II—Elastic Plastic-Fracture, ASTM STP 995*, J. D. Landes, A. Saxena, and J. G. Merkle, Eds., American Society for Testing and Materials, Philadelphia, 1989.†

*Available for purchase from the National Technical Information Service, Springfield, VA 22161.
†Available in public technical libraries.

Appendix A

Small-Scale Yielding Solution

The SSY reference solution is determined using a boundary layer model (BLM) and a uniaxial stress-strain curve appropriate for the material under consideration. Figure A.1(*a*) depicts a semicircular finite-element model of the near-crack-tip region used in the boundary layer approach. The model incorporates a highly refined crack-tip region [Fig. A.1(*b*)] with an initial root radius at the tip 10^{-6} times the outer radius of the mesh. The mesh is defined by 1977 nodes and 624 eight-noded isoparametric plane strain elements. A linear-elastic K_I field is imposed on the model through the appropriate displacement boundary conditions. To ensure SSY conditions in the model, the maximum extent of plastic zone is limited to <10% of the outer radial dimension.

The material properties used for all calculations presented herein include Young's modulus E = 205,170 MPa, Poisson's ratio ν = 0.25, and the piecewise-linear uniaxial stress-strain curve depicted in Fig. 3.3.

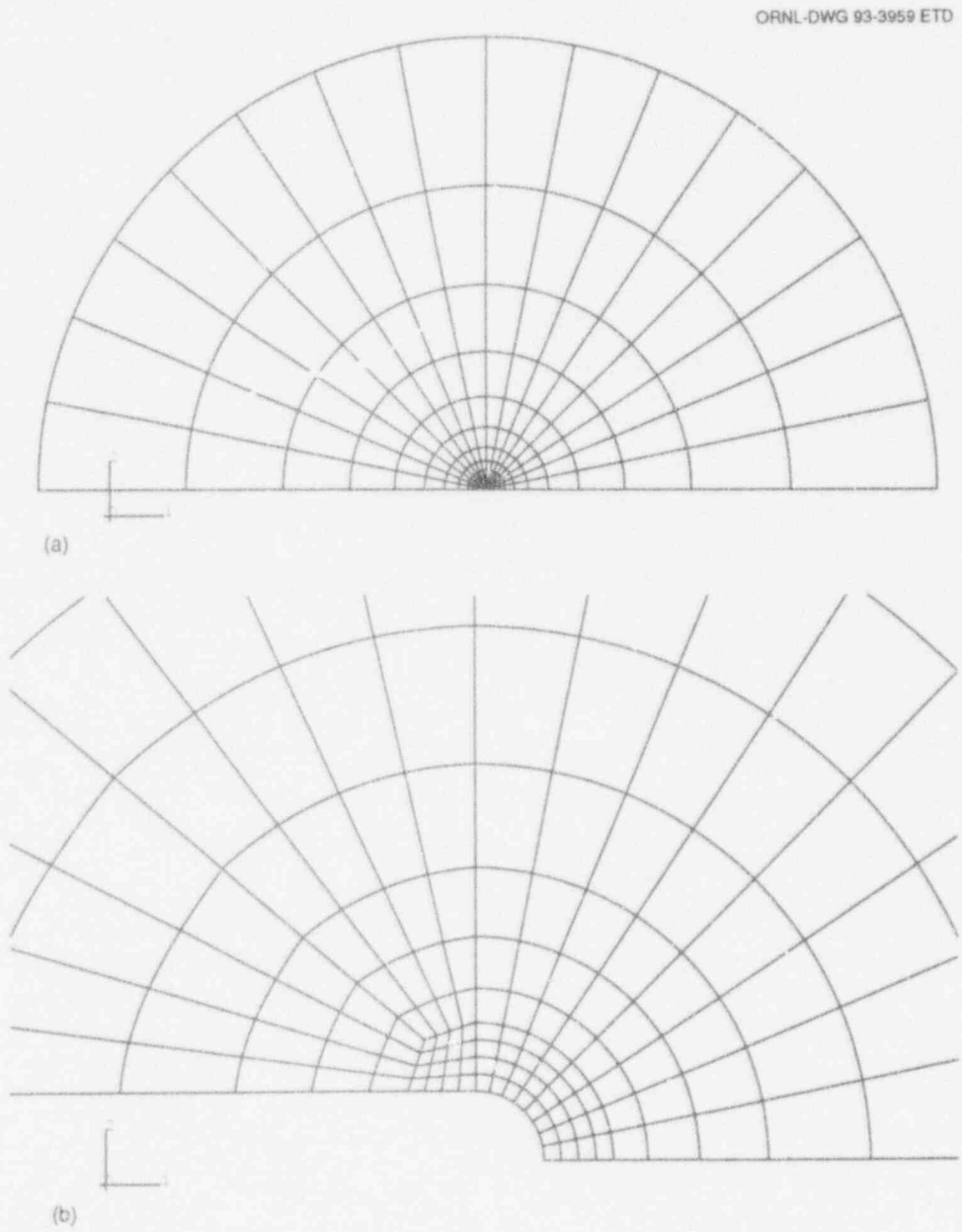

Figure A.1 (*a*) **Finite-element model employed to obtain SSY reference solution;** (*b*) **crack-tip region of SSY finite-element model**

The plane strain reference fields determined from the BLM are shown in Fig. A.2 for both finite strain and small strain formulations. In Fig. A.2, the normalized opening-mode stress is plotted vs normalized distance in front of the crack tip. A typical feature of these fields is that the finite strain and small strain solutions are essentially the same for values of $r\sigma_0/J > 2$.

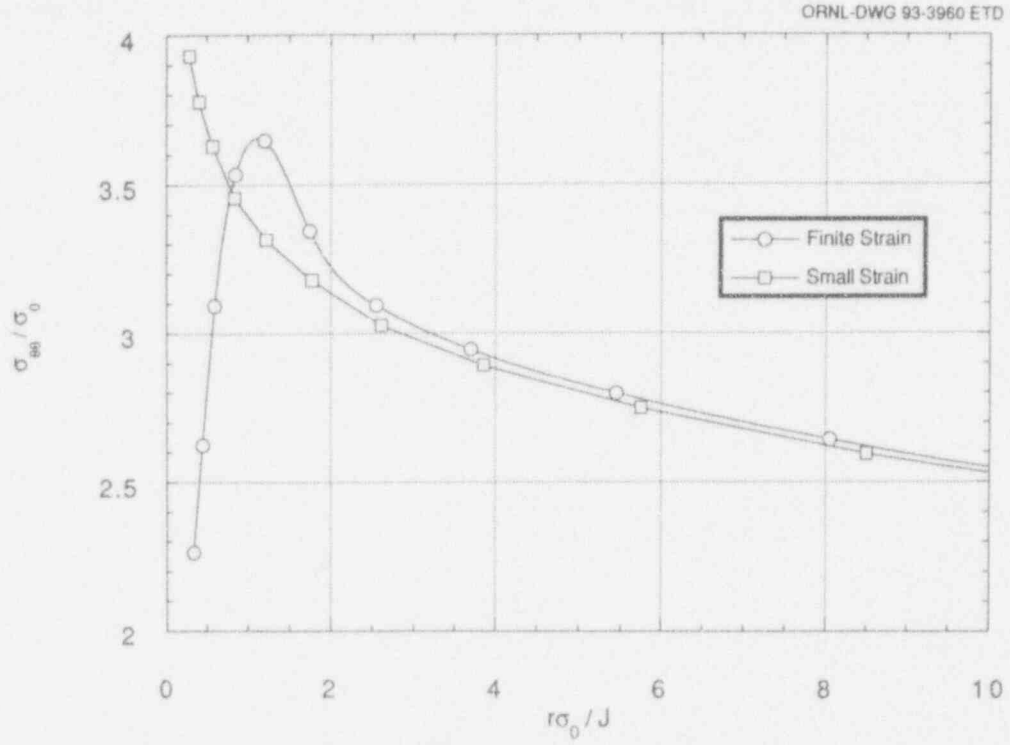

Figure A.2 SSY plane strain reference fields for cruciform bend specimen

Appendix B

Finite Strain Calculations

The crack-tip constraint analyses presented in the main body of this report were computed using a small strain, finite-element formulation. Finite strain calculations are provided here for completeness. The finite strain calculations presented in Figs. B.1–B.11 can be directly compared with the small strain calculations given in Chap. 3. Interpretations of biaxial loading effects on stress triaxiality are unchanged from those presented earlier for a small strain formulation.

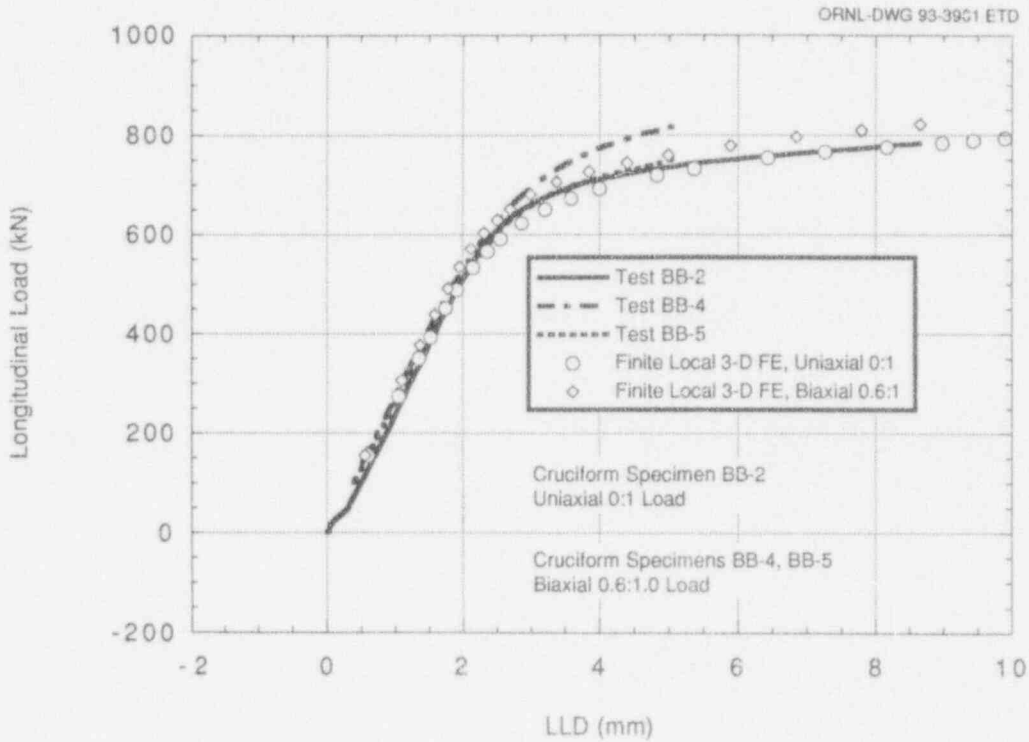

Figure B.1 Comparison of calculated (finite strain) and measured LLD for cruciform bend specimens

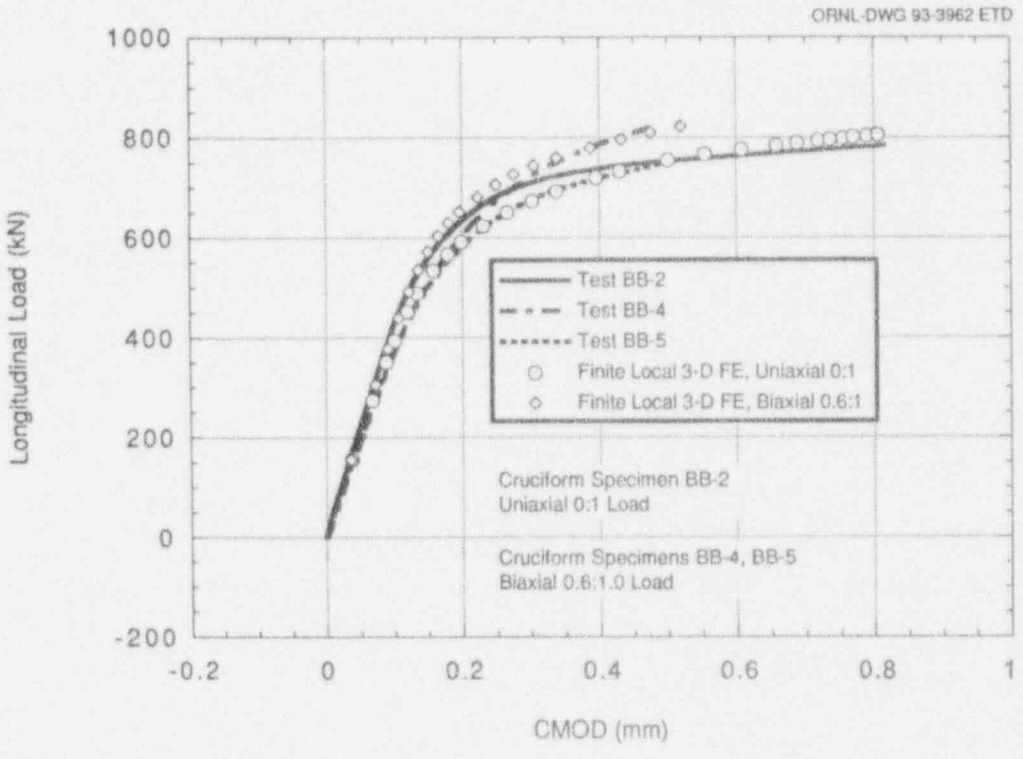

Figure B.2 Comparison of calculated (finite strain) and measured CMOD for cruciform bend specimens

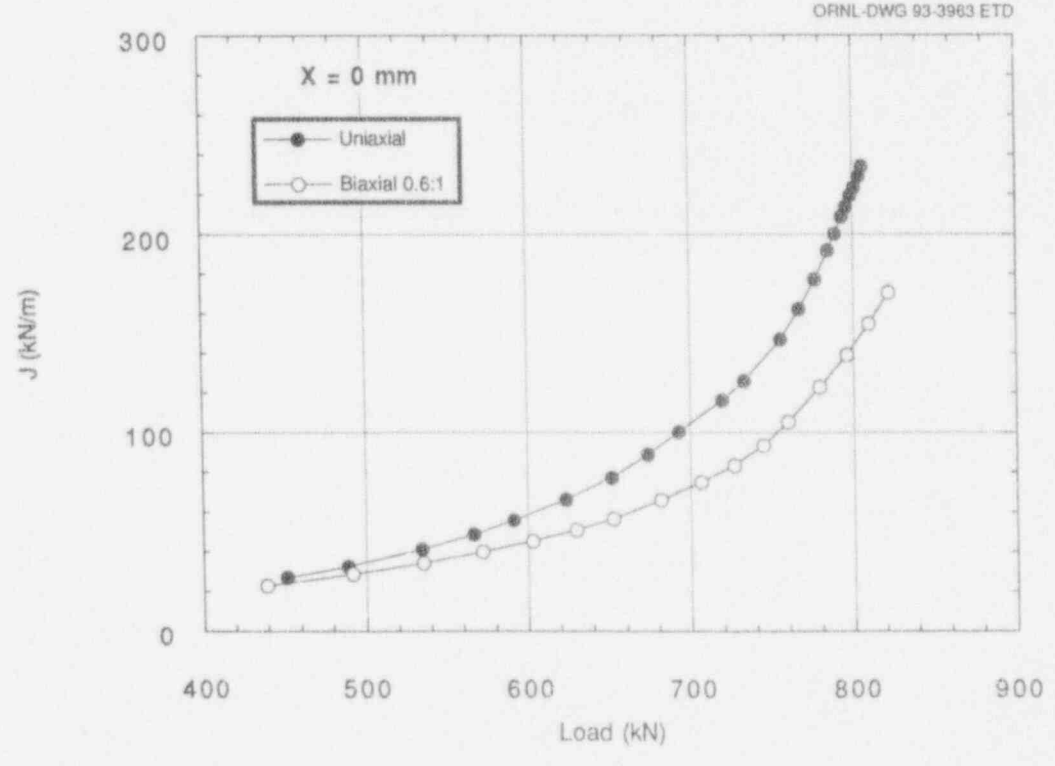

Figure B.3 Applied J at specimen midplane (X = 0 mm) (finite strain)

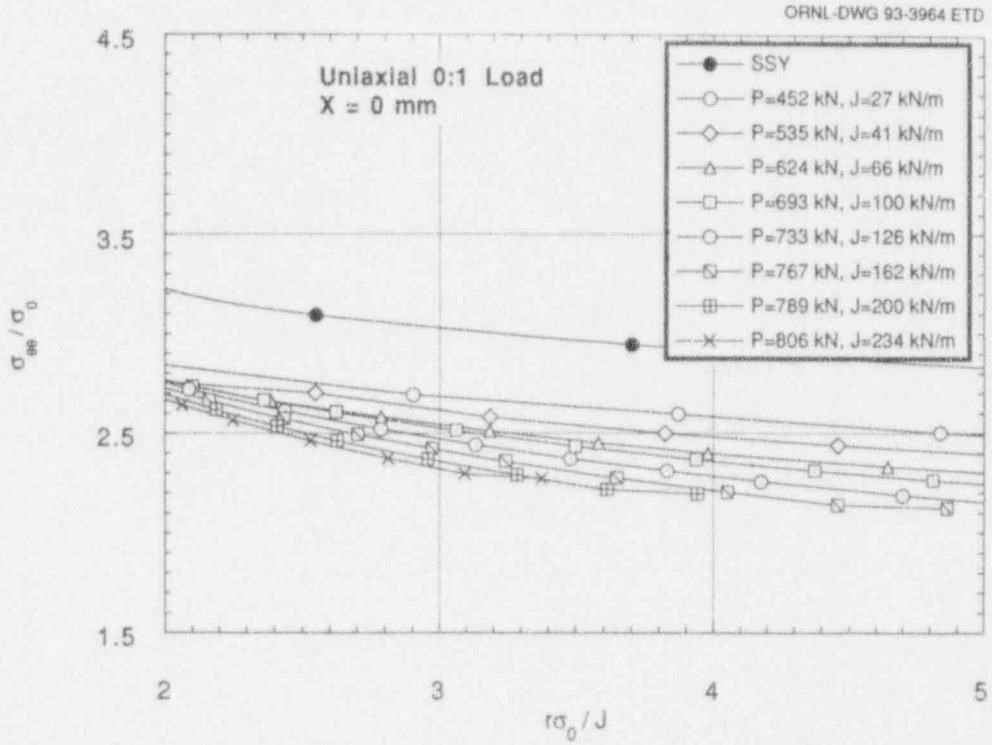

Figure B.4 Normalized opening-mode stress ahead of crack tip, X = 0 mm, uniaxial loading (finite strain)

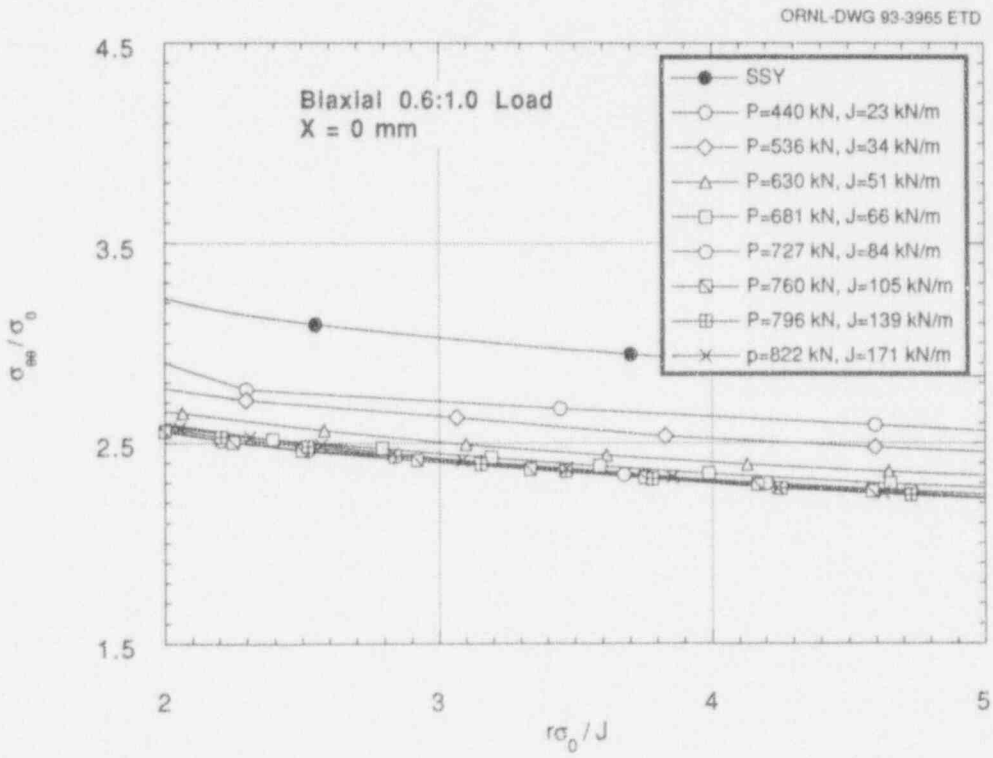

Figure B.5 Normalized opening-mode stress ahead of crack tip, X = 0 mm, biaxial 0.6:1 loading (finite strain)

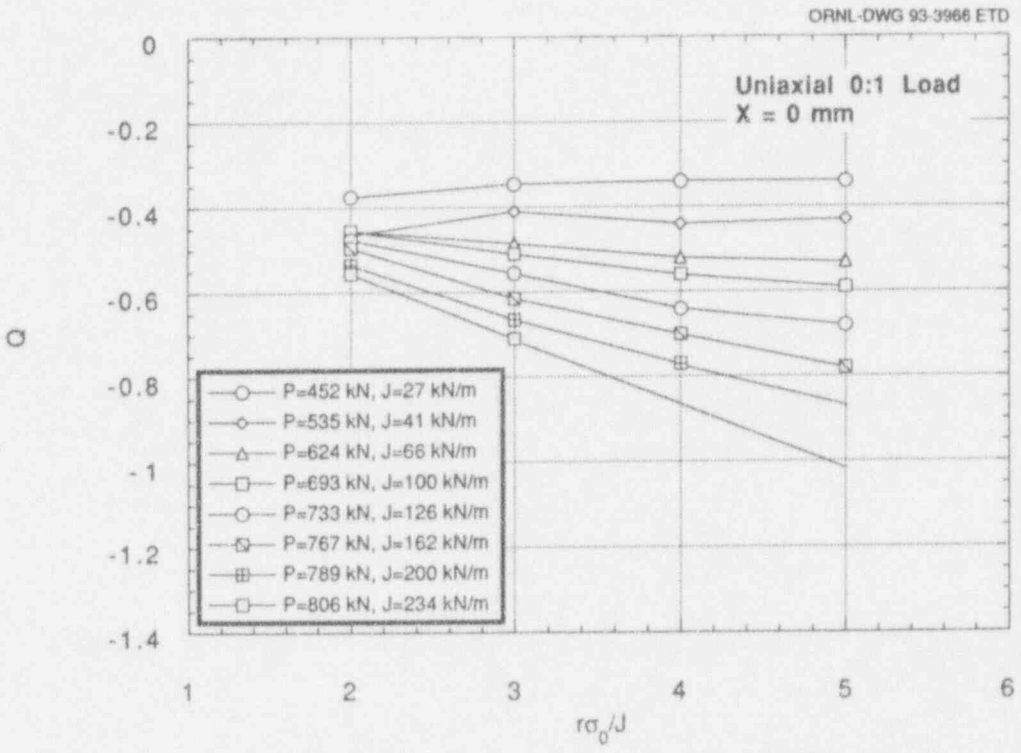

Figure B.6 Variation of Q with normalized distance ahead of crack tip, X = 0 mm, uniaxial loading (finite strain)

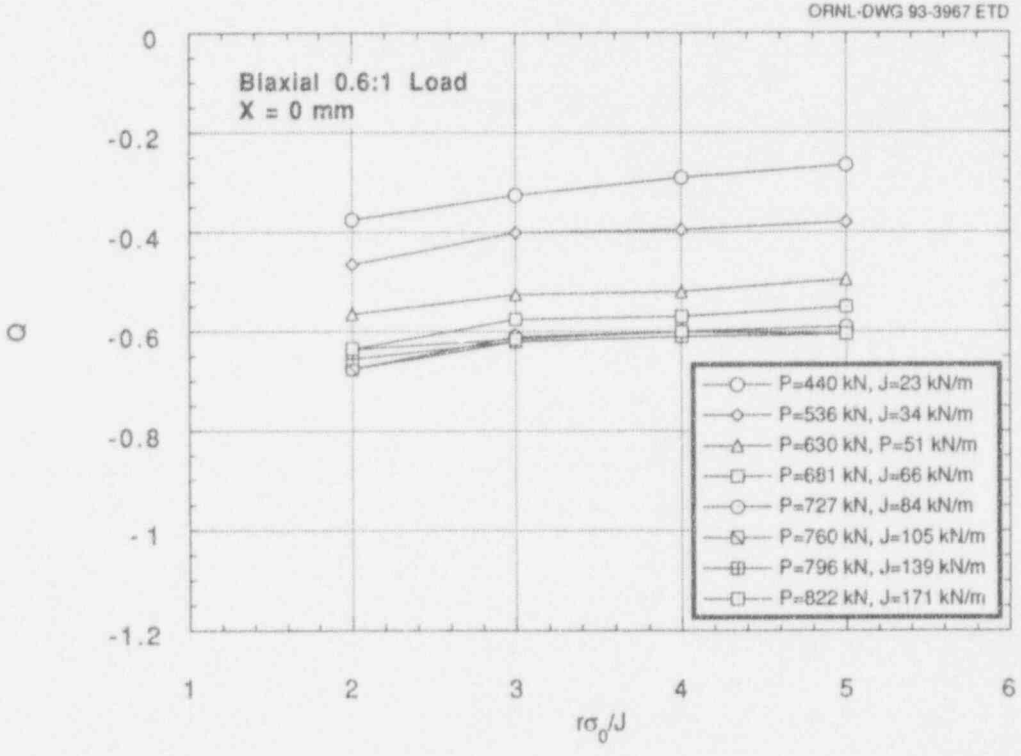

Figure B.7 Variation of Q with normalized distance ahead of crack tip, X = 0 mm, biaxial 0.6:1 loading (finite strain)

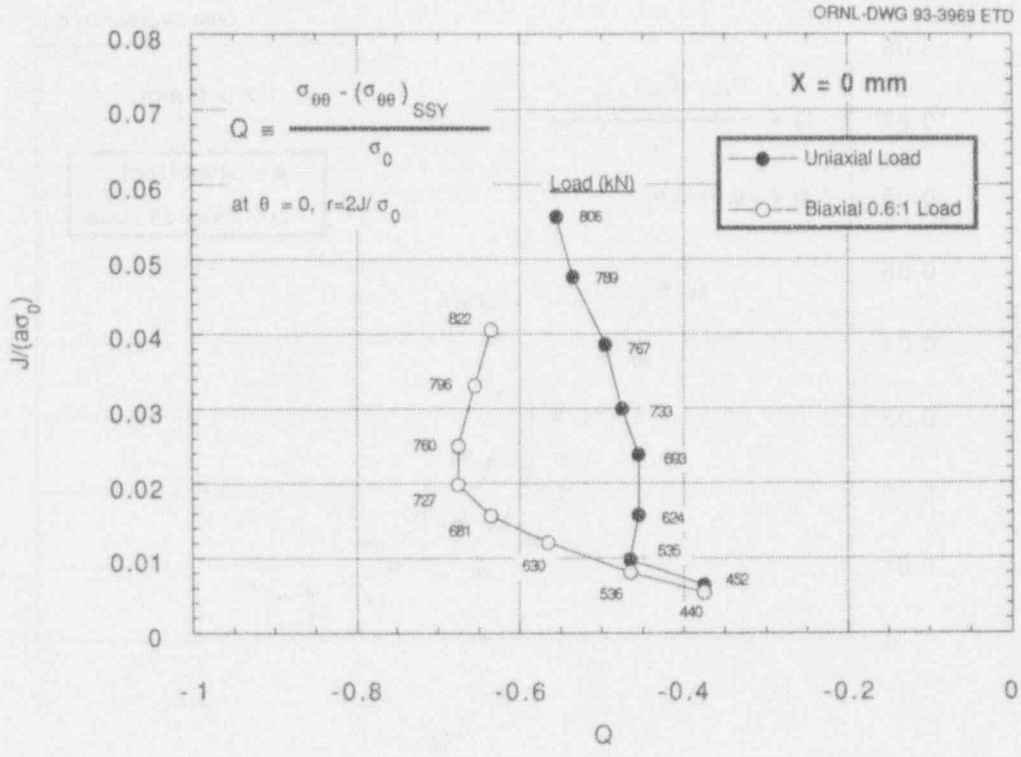

Figure B.8 J-Q trajectories at X = 0 mm for normalized distance $r\sigma_0/J = 2$ (finite strain)

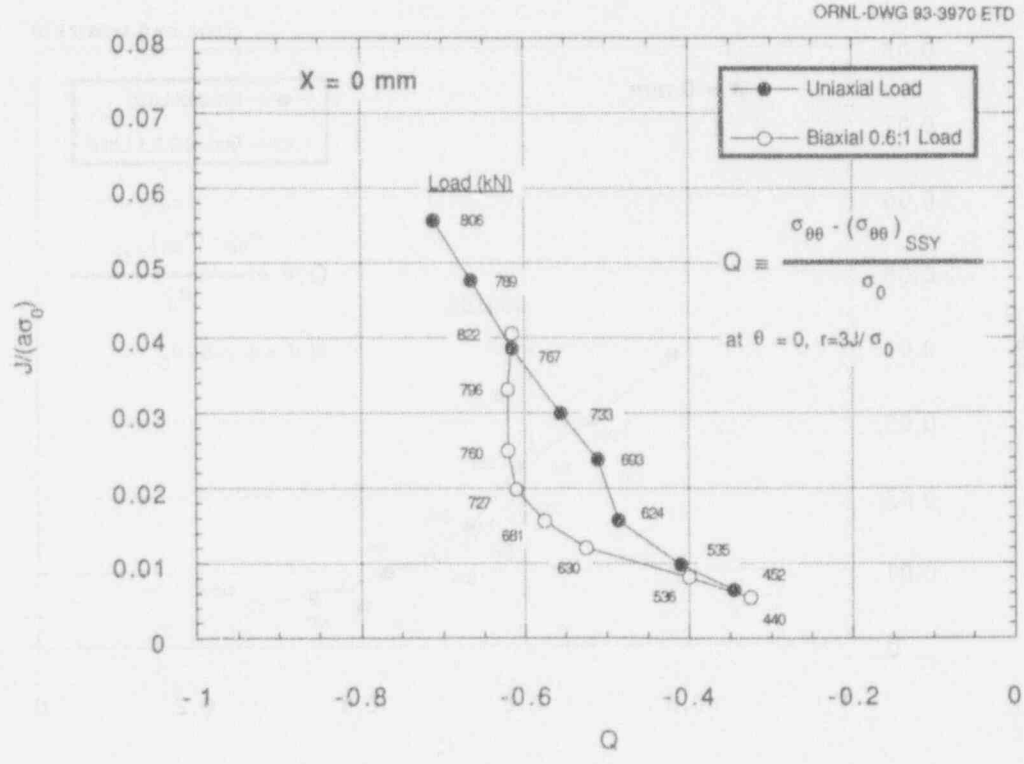

Figure B.9 J-Q trajectories at X = 0 mm for normalized distance $r\sigma_0/J = 3$ (finite strain)

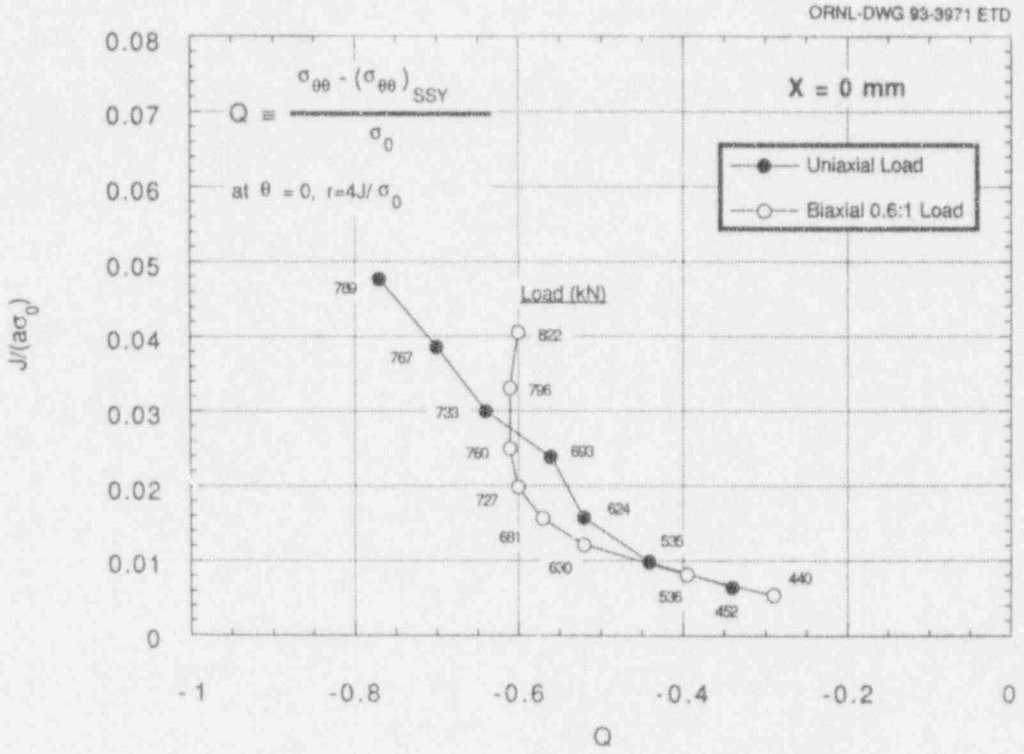

Figure B.10 J-Q trajectories at X = 0 mm for normalized distance $r\sigma_0/J = 4$ (finite strain)

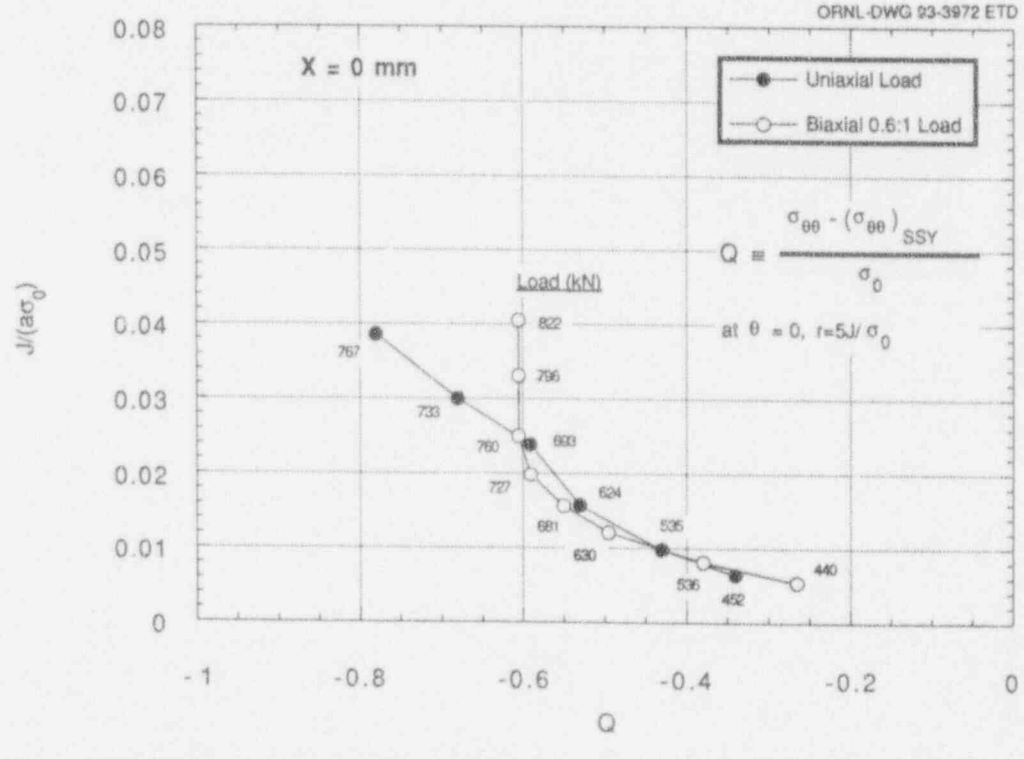

Figure B.11 J-Q trajectories at X = 0 mm for normalized distance $r\sigma_0/J = 5$ (finite strain)

Internal Distribution

1. D. J. Alexander
2–5. B. R. Bass
6. J. W. Bryson
7. R. D. Cheverton
8. J. M. Corum
9. W. R. Corwin
10. T. L. Dickson
11–12. R. G. Gilliland
13. F. M. Haggag
14. D. M. Hetrick
15. W. F. Jackson
16. S. K. Iskander
17. J. A. Keeney
18. W. J. McAfee
19. D. E. McCabe
20. J. G. Merkle
21. R. K. Nanstad
22–26. W. E. Pennell
27. C. E. Pugh
28. M. C. Rao
29. C. C. Southmayd
30–35. T. J. Theiss
36. G. E. Whitesides
37. ORNL Patent Section
38. Central Research Library
39. Document Reference Section
40–41. Laboratory Records
42. Laboratory Records (RC)

External Distribution

43. L. C. Shao, Director, Division of Engineering, RES, U.S. Nuclear Regulatory Commission, Washington, DC 20555
44. J. R. Strosnider, Materials and Chemical Engineering Branch, NRR, U.S. Nuclear Regulatory Commission, Washington, DC 20555
45–47. S. N. M. Malik, Division of Engineering, U.S. Nuclear Regulatory Commission, Washington, DC 20555
48. M. E. Mayfield, Division of Engineering, U.S. Nuclear Regulatory Commission, Washington, DC 20555
49. G. R. Irwin, Department of Mechanical Engineering, University of Maryland, College Park, MD 20742
50. L. James, Westinghouse Bettis Lab., P.O. Box 79, ZAP 13A, 814 Pittsburgh McKeesport Blvd., West Mifflin, PA 15122
51. C. F. Shih, Box D, Division of Engineering, Brown University, Providence, RI 02912
52. R. Dodds, 3140 Newmark Laboratory, 205 North Matthews, Urbana, IL 61801
53. R. Fields, National Institute of Standards and Technology, Bldg. 223, B144, Gaithersburg, MD 20899
54. W. L. Fourney, Department of Mechanical Engineering, University of Maryland, College Park, MD 20742
55. J. D. Landes, The University of Tennessee, Knoxville, TN 37996-2030
56. S. T. Rolfe, The University of Kansas, Lawrence, KS 66045-2235
57. G. M. Wilkowsky, Battelle Columbus Division, Columbus, OH 43201
58. C. W. Schwartz, Department of Civil Engineering, University of Maryland, College Park, MD 20742
59. E. T. Wessel, 312 Wolverine, Haines City, FL 33844
60. Office of Assistant Manager for Energy Research and Development, DOE–ORO, Oak Ridge, TN 37831
61. Commander and Director USAE Waterways Experiment Station, Attn: CEWES-IM-MI-R, Alfrieda S. Clark, CD Dept./#1072, 3909 Halls Ferry Road, Vicksburg, MS 39180-6199
62–63. Office of Scientific and Technical Information, P. O. Box 62, Oak Ridge, TN 37831
64. Y. J. Chao, Mechanical Engineering, The University of South Carolina, Columbia Campus, Columbia, SC 29208
65. T. L. Anderson, Department of Mechanical Engineering, Texas A&M University, College Station, TX 77843
66. J. M. Joyce, U.S. Naval Academy, Annapolis, MD 21402

NRC FORM 335 (2-89) NRCM 1102, 3201, 3202

U.S. NUCLEAR REGULATORY COMMISSION

BIBLIOGRAPHIC DATA SHEET

(See instructions on the reverse)

1. REPORT NUMBER (Assigned by NRC, Add Vol., Supp., Rev., and Addendum Numbers, if any.)

NUREG/CR-6132
ORNL/TM-12498

2. TITLE AND SUBTITLE

Biaxial Loading and Shallow-Flaw Effects on Crack-Tip Constraint and Fracture Toughness

3. DATE REPORT PUBLISHED

MONTH: January | YEAR: 1994

4. FIN OR GRANT NUMBER

B0119

5. AUTHOR(S)

B. R. Bass, J. W. Bryson, T. J. Theiss, and M. C. Rao

6. TYPE OF REPORT

B0119

7. PERIOD COVERED (Inclusive Dates)

Technical

8. PERFORMING ORGANIZATION – NAME AND ADDRESS (If NRC, provide Division, Office or Region, U.S. Nuclear Regulatory Commission, and mailing address; if contractor, provide name and mailing address.)

Oak Ridge National Laboratory
Oak Ridge, Tennessee 37831-6285

9. SPONSORING ORGANIZATION – NAME AND ADDRESS (If NRC, type "Same as above"; if contractor, provide NRC Division, Office or Region, U.S. Nuclear Regulatory Commission, and mailing address.)

Division of Engineering
Office of Nuclear Regulatory Research
U.S. Nuclear Regulatory Commission
Washington, DC 20555 -0001

10. SUPPLEMENTARY NOTES

11. ABSTRACT (200 words or less)

A program to develop and evaluate fracture methodologies for the assessment of crack-tip constraint effects on fracture toughness of reactor pressure vessel (RPV) steels has been initiated in the Heavy-Section Steel Technology (HSST) Program. Crack-tip constraint is an issue that significantly impacts fracture mechanics technologies employed in safety assessment procedures for commercially licensed nuclear RPVs. The focus of studies described herein is on the evaluation of two stressed-based methodologies for quantifying crack-tip constraint (i.e., J-Q theory and a micromechanical scaling model based on critical stressed volumes) through applications to experimental and fractographic data. Data were utilized from single-edge notch bend (SENB) specimens and HSST-developed cruciform beam specimens that were tested in HSST shallow-crack and biaxial testing programs. Results from applications indicate that both the J-Q methodology and the micromechanical scaling model can be used successfully to interpret experimental data from the shallow- and deep-crack SENB specimen tests. When applied to the uniaxially and biaxially loaded cruciform specimens, the two methodologies showed some promising features, but also raised several questions concerning the interpretation of constraint conditions in the specimen based on near-tip stress fields. Fractographic data taken from the fracture surfaces of the SENB and cruciform specimens are used to assess the relevance of stress-based fracture characterizations to conditions at cleavage initiation sites. Unresolved issues identified from these analyses require resolution as part of a validation process for biaxial loading applications. This report is designated as HSST Report No. 142.

12. KEY WORDS/DESCRIPTORS (List words or phrases that will assist researchers in locating the report.)

A533 Grade B class 1 steel
Shallow-crack beam
Constraint Analysis
Biaxial loading
Factography
Elastic-plastic fracture mechanics
Fracture toughness data
J-Q Methodology
Constraint Adjustment model
Cruciform beam

13. AVAILABILITY STATEMENT

Unlimited

14. SECURITY CLASSIFICATION

(This Page) Unclassified

(This Report) Unclassified

15. NUMBER OF PAGES

16. PRICE

NRC FORM 335 (2-89)

Federal Recycling Program

NUREG/CR–5935
EGG–2686

Summary of Work Completed Under the Environmental and Dynamic Equipment Qualification Research Program (EDQP)

Prepared by
R. Steele, Jr., D. L. Bramwell, J. C. Watkins, K. G. DeWall

Idaho National Engineering Laboratory
EG&G Idaho, Inc.

Prepared for
U.S. Nuclear Regulatory Commission

AVAILABILITY NOTICE

Availability of Reference Materials Cited in NRC Publications

Most documents cited in NRC publications will be available from one of the following sources:

1. The NRC Public Document Room, 2120 L Street, NW., Lower Level, Washington, DC 20555-0001
2. The Superintendent of Documents, U.S. Government Printing Office, Mail Stop SSOP, Washington, DC 20402-9328
3. The National Technical Information Service, Springfield, VA 22161

Although the listing that follows represents the majority of documents cited in NRC publications, it is not intended to be exhaustive.

Referenced documents available for inspection and copying for a fee from the NRC Public Document Room include NRC correspondence and internal NRC memoranda; NRC bulletins, circulars, information notices, inspection and investigation notices; licensee event reports; vendor reports and correspondence; Commission papers; and applicant and licensee documents and correspondence.

The following documents in the NUREG series are available for purchase from the GPO Sales Program: formal NRC staff and contractor reports, NRC-sponsored conference proceedings, international agreement reports, grant publications, and NRC booklets and brochures. Also available are regulatory guides, NRC regulations in the *Code of Federal Regulations*, and *Nuclear Regulatory Commission Issuances*.

Documents available from the National Technical Information Service include NUREG-series reports and technical reports prepared by other Federal agencies and reports prepared by the Atomic Energy Commission, forerunner agency to the Nuclear Regulatory Commission.

Documents available from public and special technical libraries include all open literature items, such as books, journal articles, and transactions. *Federal Register* notices, Federal and State legislation, and congressional reports can usually be obtained from these libraries.

Documents such as theses, dissertations, foreign reports and translations, and non-NRC conference proceedings are available for purchase from the organization sponsoring the publication cited.

Single copies of NRC draft reports are available free, to the extent of supply, upon written request to the Office of Administration, Distribution and Mail Services Section, U.S. Nuclear Regulatory Commission, Washington, DC 20555-0001.

Copies of industry codes and standards used in a substantive manner in the NRC regulatory process are maintained at the NRC Library, 7920 Norfolk Avenue, Bethesda, Maryland, for use by the public. Codes and standards are usually copyrighted and may be purchased from the originating organization or, if they are American National Standards, from the American National Standards Institute, 1430 Broadway, New York, NY 10018.

NUREG/CR-5935
EGG-2686

Summary of Work Completed Under the Environmental and Dynamic Equipment Qualification Research Program (EDQP)

Manuscript Completed: December 1993
Date Published: February 1994

Prepared by
R. Steele, Jr., D. L. Bramwell, J. C. Watkins, K. G. DeWall

Idaho National Laboratory
Managed by the U. S. Department of Energy

EG&G Idaho, Inc.
Idaho Falls, ID 83415

Prepared for
Division of Engineering
Office of Nuclear Regulatory Research
U.S. Nuclear Regulatory Commission
Washington, DC 20555-0001
NRC FIN A6322

ABSTRACT

This report documents the results of the main projects undertaken under the Environmental and Dynamic Equipment Qualification Research Program (EDQP) sponsored by the U.S. Nuclear Regulatory Commission (NRC) under FIN A6322. Lasting from fiscal year 1983 to 1987, the program dealt with environmental and dynamic (including seismic) equipment qualification issues for mechanical and electromechanical components and systems used in nuclear power plants. The research results have since been used by both the NRC and industry.

The program included seven major research projects that addressed the following issues: (a) containment purge and vent valves performing under design basis loss of coolant accident loads, (b) containment piping penetrations and isolation valves performing under seismic loadings and design basis and severe accident containment wall displacements, (c) shaft seals for primary coolant pumps performing under station blackout conditions, (d) electrical cabinet internals responding to in-structure generated motion (rattling), and (e) in situ piping and valves responding to seismic loadings. Another project investigating whether certain containment isolation valves will close under design basis conditions was also started under this program. This report includes eight main sections, each of which provides a brief description of one of the projects, a summary of the findings, and an overview of the application of the results. A bibliography lists the journal articles, papers, and reports that document the research.

CONTENTS

ABSTRACT iii

EXECUTIVE SUMMARY xi

ACKNOWLEDGMENTS xiii

1. INTRODUCTION 1

2. NUCLEAR CONTAINMENT PURGE AND VENT VALVE DESIGN BASIS FLOW INTERRUPTION TESTING 3

2.1 The Issue 3

2.2 Background 3

2.2.1 Torque Requirements 3
2.2.2 Background Research 3

2.3 Description of the Test Project 5

2.4 Test Results 8

2.4.1 Downstream Pressure 8
2.4.2 Valve Orientation 9
2.4.3 Upstream Piping Configuration 12

2.5 Conclusions 13

2.6 Leak Integrity Testing and Results 14

2.6.1 Testing 14
2.6.2 Test Results 14
2.6.3 Conclusions 14

2.7 Application of the Research 14

3. SEISMIC TESTING OF TYPICAL CONTAINMENT PIPING PENETRATION SYSTEMS 16

3.1 The Issue 16

3.2 Research Methods 16

3.2.1 Background Research 16
3.2.2 Description of the Test Project 17

3.3 Results 19

3.3.1 Valve Operability 19
3.3.2 Valve Leakage 19

3.3.3 Structural Integrity 19

3.4 Conclusions 19

3.5 Application of the Research 21

4. TESTING OF CONTAINMENT PENETRATION SYSTEMS AT ACCIDENT LOADINGS 22

4.1 The Issue 22

4.2 Research Methods 22

4.2.1 Background Research 22
4.2.2 Description of the Test Project 22

4.3 Results 24

4.3.1 8-in. Gate Valve System 24
4.3.2 8-in. Butterfly Valve System 25
4.3.3 2-in. Globe Valve System 26

4.4 Conclusions 26

4.5 Application of the Research 26

5. REACTOR COOLANT PUMP SHAFT SEAL PERFORMANCE DURING STATION BLACKOUT 27

5.1 The Issue 27

5.2 Assessment of Polymer Seal Performance 28

5.2.1 Evaluation of Static O-rings 28
5.2.2 Testing of Secondary Seals 28

5.3 Shaft Seal Stability 30

5.3.1 Analytical Model 30
5.3.2 Testing of Seal Stability 30

5.4 Review of Full-Scale Testing by Others 31

5.5 Conclusions 31

5.6 Application of the Research 32

6. SIGNIFICANCE OF RATTLING IN ELECTRICAL CABINETS DURING EARTHQUAKES 33

6.1 The Issue 33

6.2 Review of Qualification Tests 33
6.3 Testing of Electrical Components 34
6.4 Test Results 35
6.5 Conclusions 37
6.6 Application of the Research 39
7. SHAG TEST SERIES: IN SITU SEISMIC TESTING OF A VALVE AND A PIPING SYSTEM 40
7.1 The Issue 40
7.2 Test Description 40
7.3 Test Results 43
7.3.1 Comparison of Piping Support Systems 43
7.3.2 Performance of Piping and Snubbers 44
7.3.3 Operability of the Motor-operated Valve 44
7.3.4 High-Frequency Amplification in the Valve Assembly 44
7.4 Conclusions 46
7.5 Application of the Research 46
8. SHAM TEST SERIES: HIGH-LEVEL SIMULATED SEISMIC TESTS AT HDR 48
8.1 The Issue 48
8.2 Test Description 48
8.3 Test Results 48
8.3.1 Valve Operability 48
8.3.2 Snubber Failures 51
8.3.3 VKL Response 53
8.4 Conclusions 53
8.5 Application of the Research 54
9. EARLY RESEARCH FOR THE GENERIC SAFETY ISSUE 87 TEST PROJECTS 55
9.1 The Issue 55
9.2 Research Description 55
9.3 Research Results 55

9.4 Conclusions 56

9.5 Application of the Research 56

10. GENERAL CONCLUSIONS 57

REFERENCES 59

BIBLIOGRAPHY 61

LIST OF FIGURES

2-1. Cross section of a typical butterfly valve used in containment purge and vent applications 4

2-2. Diagram of the test section with uniform inlet flow (straight section of pipe), showing locations of instrumentation 6

2-3. Valve orientations installed in the test section with uniform inlet flow 6

2-4. Diagram of the test section with nonuniform inlet flow (upstream elbow), showing locations of instrumentation 7

2-5. Valve orientations installed in the test section with nonuniform inlet flow. The CW and CCW notations identify orientations with the disc rotating clockwise or counterclockwise relative to the figure 7

2-6. Static pressure 15 diameters downstream of valve versus valve position. Valves 1 and 2 are the 8-in. valves; Valve 3 is the 24-in. valve 8

2-7. Peak torque versus upstream static pressure, first 8-in. valve 9

2-8. Torque versus upstream pressure and angle for the second 8-in. valve, curved-side-upstream orientation, with uniform flow 10

2-9. Torque versus upstream pressure and angle for the 24-in. valve, curved-side-upstream orientation, with uniform flow 11

2-10. Torque versus upstream pressure and angle for the second 8-in. valve, flat-side-upstream orientation, with uniform flow 11

2-11. Torque versus upstream pressure and angle for the 24-in. valve, flat-side-upstream orientation, with uniform flow 12

3-1. Comparison of the measured SSE test response spectrum with the SSE required response spectrum and with the analytically predicted SSE response spectra for selected plants; horizontal response spectra for the upper half of the building 17

3-2. Sketch of the test fixture with the 8-in. gate valve assembly installed 18

3-3. Leak rates across the seat of the 2-in. globe valve 21

4-1. Sketch of the test fixture with an 8-in. gate valve system installed 23

4-2. Overhead view of the test fixture with the 8-in. gate valve assembly installed 24

5-1. Simplified diagram of a cross-section of an RCP shaft seal; this represents one of the three or four seals that constitute the entire seal assembly 27

5-2. Test cell for extrusion and friction testing of secondary seals 29

5-3. Cross-sections of the typical secondary seals subjected to testing 29

5-4. Sketch of the device used for the seal stability tests 31

6-1. Sketch of the test fixture showing where the accelerometers were mounted 34

6-2. Velocity and displacement of the GE relay during recorded chatter events. Chatter events are indicated by the voltage pulses labeled W and GE 37

7-1. A simplified cross section of the HDR facility, showing the locations of the shaker, the VKL, and the reactor pressure vessel 41

7-2. A schematic of the VKL showing the 8-in. gate valve and the U.S. stiff piping support system as configured for the SHAG tests 42

7-3. Power spectral density (PSD) plots calculated from measurements taken in the Z axis (horizontal direction parallel to flow through the valve) at three locations during two tests with a starting frequency of 8 Hz 45

8-1. A schematic of the VKL showing the 8-in. gate valve and the U.S. stiff piping support system as configured for the SHAM tests 49

LIST OF TABLES

2-1. Normalized peak torques 13

3-1. Overview of measurements during seismic testing of the three containment penetration systems 20

4-1. Summary of testing sequence 25

6-1. Test run summary 36

6-2. Waveform characterization at time of chatter 38

7-1. Type of supports used in the SHAG test series 43

8-1. Participants' support configurations for the SHAM test series 50

8-2. U.S. stiff support system test matrix 50

8-3. Snubber installation matrix for U.S. stiff support system 51

8-4. Maximum loads for struts and snubbers installed in the U.S. stiff support system 52

EXECUTIVE SUMMARY

The Environmental and Dynamic Equipment Qualification Research Program (EDQP) was sponsored by the U.S. Nuclear Regulatory Commission under FIN A6322. The program was initiated in late 1982. Activities began in FY 1983 and continued until nearly all the main issues of the program were completed. Activities then continued in FY 1988 with the Equipment Operability Program (FIN A6857). The objectives of the program were to improve the technical basis for developing qualification requirements for mechanical and electromechanical equipment in nuclear power plants. The requirements were evaluated against acceptance criteria, which included dynamic (seismic) and environmental conditions for qualification of mechanical equipment and dynamic (including seismic) conditions for qualification of electrical equipment.

The sets of equipment prioritized for research under this program were selected from a number of sources, including components and systems identified in several Nuclear Regulatory Commission (NRC) plans and research priority lists. Among these plans and priority lists are the *Nuclear Power Plant Severe Accident Research Plan* (NUREG-0900), the *NRC Action Plan as a Result of the TMI-2 Accident* (NUREG-0660), *Clarification of TMI Action Plan Requirements* (NUREG-0737), and *A Prioritization of Generic Safety Issues* (NUREG-0933).

This report formally documents the work of a major research program. The program has produced technical insights to support the NRC effort regarding Generic Safety Issue 23, "Reactor Coolant Pump Seal Failures at Station Blackout Conditions," Unresolved Safety Issue A-46, *Seismic Qualification of Equipment in Operating Nuclear Power Plants* (NUREG-1030, 1987), and the containment integrity portion of the NRC's severe accident research (NUREG-1264). The program also included preliminary work to address Generic Safety Issue 87, "Failure of the HPCI Steam Line Without Isolation." The research program included the following major research projects described in the following discussion.

1. Nuclear containment purge and vent valves were subjected to flow interruption and leak integrity tests. These were the first such tests performed with full-scale valves and piping at design basis conditions. The results of these tests contributed significantly to the nuclear industry's understanding of the torque requirements of the butterfly valves typically installed in these applications.

2. Containment penetration systems, including the penetration itself, the two isolation valves, the associated piping, and the piping supports, were subjected to seismic tests. The results confirmed that these components are resistant to earthquake loadings, in terms of the structural integrity of all the components and the leak integrity and functionality of the valves.

3. Containment penetration systems were also subjected to design basis accident and severe accident containment responses, including significant displacement of the penetration relative to the anchored piping. The results raised some minor concerns, but in general, testing showed that containment penetration systems are extremely strong.

4. Reactor coolant pump shaft seals were evaluated and some of their components tested for their resistance to station blackout conditions. This project identified some temperature concerns with the polymer materials used in the secondary seals in the seal assemblies in some designs. The project also investigated the tendency of the primary seals to pop open during station blackout conditions.

5. The significance of rattling in electrical cabinets subjected to earthquake motion was evaluated, along with the effect of the rattling on relays, switches, and other electrical

devices mounted in the cabinets. The evaluation included seismic testing of relays at conditions simulating the high-frequency effects of cabinet rattling. The results of the study showed that cabinets respond at higher frequencies during a seismic event than the frequencies for which many of these cabinet-mounted devices are qualified. Relays were also found to be sensitive to low frequencies.

6. A full-scale piping system was subjected to seismic loadings to determine the piping system's in situ response. The seismic loads were simulated by a large shaker mounted high in the containment building, a decommissioned test facility in Germany. The piping system included a naturally aged, motor-operated gate valve. The aged valve was not affected by the seismic loadings, but other anomalies in valve performance became the source of two NRC information notices, one on aging in motor operator torque springs and the other on undersized dc power cables.

7. In a follow-on test project, the piping system described in item 6 above was subjected to seismic loads simulated by two large servohydraulic shakers. In the most severe test, the magnitude of the loadings imposed by the shakers on the piping system, the valve, and the snubbers, struts, and other piping supports was approximately eight times that of a typical safe shutdown earthquake. The results provided insights on the failure loads and failure modes of snubbers subjected to high loadings. Both of these in situ test projects (items 6 and 7) provided insight on the ability of piping and valves to maintain their structural integrity when subjected to earthquake-like loadings.

8. The program also supported early research on the ability of isolation valves in the high-pressure coolant injection steam line and other high-pressure lines to close against design basis line break flows. Two full-scale test projects followed, funded as part of a subsequent research program. The results of those test projects challenged some of the equations the industry uses to size operators on motor-operated gate valves and set the operators' control devices. The results have also contributed to the industry's understanding of the behavior of motor-operated gate valves.

ACKNOWLEDGMENTS

This summary report describes eight separate research projects. Many of the researchers who did the original work in those eight projects are not listed as authors of this report. We acknowledge their effort here, and we refer the reader to the bibliography, where the reports and papers published by those researchers are listed. Specifically, we acknowledge the work of Robert C. Hill, James A. Close, Herbert S. Crapo, David B. Rhodes, Ron G. Wensel, Gary L. Thinnes, Vladimir Glozman, James G. Arendts, and Michael E. Nitzel.

We also acknowledge the following Idaho National Engineering Laboratory staff for their help in the production of this document: J. S. Isom, K. L. Lynes, C. A. Priest, D. K. Iverson, and J. L. Stoecker for text processing, G. S. Reilly and C. W. White for graphics, and D. R. Pack and J. M. Steffes for technical editing.

Summary of Work Completed Under the Environmental and Dynamic Equipment Qualification Research Program (EDQP)

1. INTRODUCTION

The Environmental and Dynamic Equipment Qualification Research Program (EDQP), conducted by the Idaho National Engineering Laboratory (INEL) and sponsored by the U.S. Nuclear Regulatory Commission (NRC) was performed because much of the safety equipment in nuclear power plants experiences very limited operation at design basis conditions. Similarly, some of the components were not tested during initial qualification phase because of the complexity and expense of performing tests at maximum design conditions. Such equipment generally was qualified through analysis and limited testing. As a result of this limited operating experience, it was difficult to answer some questions that arose concerning equipment performance. These questions, typically brought about by observed anomalous behavior in operating plants or identified by related research, challenged earlier assumptions or judgments applied in the qualification process. New research was needed to answer these questions. The program plan for the EDQP is presented in NUREG-1209.

Although the EDQP performed research on diverse equipment, there were some common threads. All research included component or system testing at design basis conditions. Thus, the research provided empirical data for comparison with the results of the analytical methods used in the earlier qualification processes. The accident load simulations were realistic, and in most cases the tested hardware was typical of that installed in nuclear plants. The research requirements, methods, and results were reviewed by representatives of the NRC and, in most cases, by the nuclear power industry, other national laboratories, and international organizations.

Research was designed by the INEL and performed at a number of sites, including the INEL, the Santa Suzanna Field Laboratory in California, Chalk River National Laboratories in Ontario, Canada, and the decommissioned Heissdampfreaktor facility located near Frankfurt, Germany.

In most cases, research on a subject was reported in more than one document. The bibliography section contains a complete list of the journal articles, meeting papers, and reports published for each major topic of the EDQP. This report summarizes the research results in a single document.

Each of the major research projects is described in a section of the report. The material is summarized but presented in sufficient detail that the reader can become reasonably familiar with the research subject.

The report covers the following major research projects:

1. Testing to determine the requirements for typical nuclear containment purge and vent valves to close against design basis flows and to maintain leak-tightness against design basis accident and severe accident pressures and temperatures

2. Testing the response of containment piping penetrations and associated piping and isolation valves to simulated earthquake loadings

3. Testing the response of containment piping penetrations and associated piping and isolation valves to the containment temperatures and pressures and the containment

wall displacements that would occur in the event of a design basis loss-of-coolant accident and a severe accident inside the containment

4. Evaluating the performance of primary coolant pump shaft seals during station blackout conditions

5. Testing the response of relays to seismic excitation typical of earthquake-induced rattling in electrical cabinets

6. Testing the response of a full-scale in situ piping system and a motor-operated gate valve to simulated earthquake loadings produced by a building shaker

7. Testing the response of the same piping system (described in item 6 above) to normal and high-level simulated earthquake loadings produced by servohydraulic shakers

8. Preliminary work preparing for full-scale testing of motor-operated gate valves at very high design basis pressures, temperatures, and flows.

2. NUCLEAR CONTAINMENT PURGE AND VENT VALVE DESIGN BASIS FLOW INTERRUPTION TESTING

2.1 The Issue

The containment purge and vent systems consist mostly of air conditioning ducting and filters. These are open loop systems where the containment atmosphere communicates directly with the atmosphere outside the containment. The only ASME code class piping in the system is the containment penetration, a short length of piping, and two isolation valves, typically butterfly valves (see Figure 2-1). The penetration and the valves are a part of the containment barrier. If a design basis loss of coolant accident (LOCA) were to occur inside the containment, failure of the isolation valves to close and seal might allow the environment inside the containment to escape to the outside.

Following the Three Mile Island (TMI) accident in 1979, NUREG-0660, *NRC Action Plan as a Result of TMI-2 Accident*, was published. Item II.E.4.2 of that document, "Containment Isolation Dependability," formalized the concern about the ability of the containment purge and vent valves to close against design basis pressure loads. NUREG-0737, *Clarification of TMI Action Plan Requirements*, was published in 1980, adding leak integrity to the purge and vent valve concerns.

The research summarized here provided information to address those concerns. Specifically, the purpose of the research was (a) to provide empirical data to determine the requirements for typical nuclear containment purge and vent valves to close during a design basis LOCA inside the containment, (b) to evaluate the methods used in the nuclear industry to estimate those requirements, (c) to determine whether the results of testing of small valves can be extrapolated to reliably predict the torque requirements of larger valves, and (d) to determine whether typical purge and vent valves will maintain their leak-tightness when subjected to design basis accident and severe accident temperatures and pressures.

2.2 Background

2.2.1 Torque Requirements. Dynamic torque requirements for a butterfly valve are typically determined by the following equation:

$$T_d = C_T \, D^3 \Delta P \qquad (1)$$

where

T_d = dynamic torque (torque required to overcome loads imposed by flow through the valve)

C_T = torque coefficient

D^3 = valve diameter cubed

ΔP = pressure drop across the valve.

The total torque requirement is the sum of the dynamic torque and the torque required to overcome bearing and packing resistance. Bearing and packing torques are easily measured and were not subject to controversy. The variable C_T (the torque coefficient) is usually developed from test results with scale model valves using the following equation:

$$C_T = \frac{T_d}{D^3 \, \Delta P} \qquad (2)$$

Industry methodologies for extrapolating torque requirements are based on the assumption that in geometrically scaled systems, when all other conditions are the same, the flow characteristics and pressure drop across the valves that have been scaled to each other will be the same. This assumption was originally based on testing using incompressible fluids.

2.2.2 Background Research. To obtain background information to support the test project, we surveyed the available literature to determine the manufacturers, types and sizes of valves used,

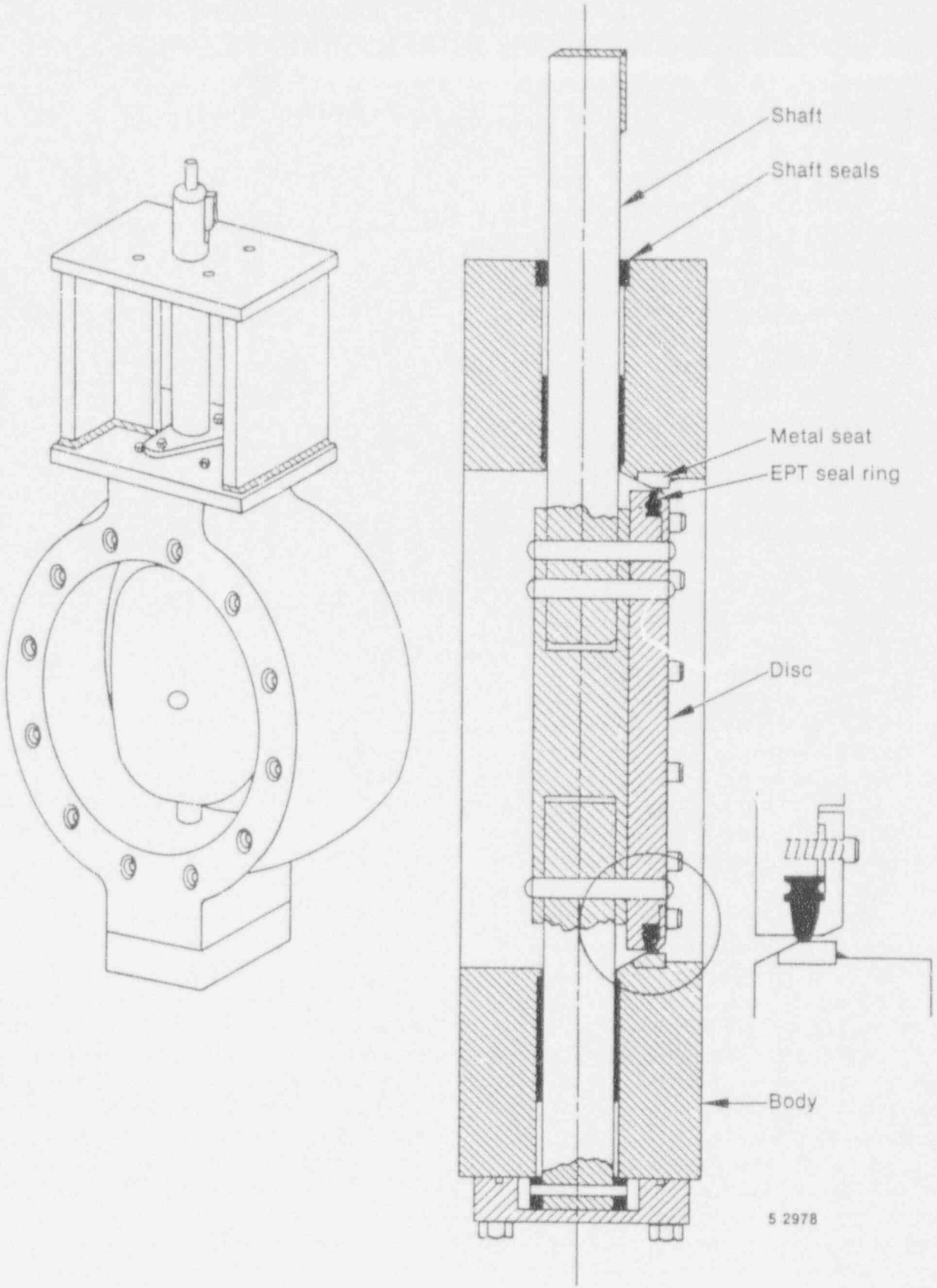

Figure 2-1. Cross section of a typical butterfly valve used in containment purge and vent applications.

and operational status of valves installed in nuclear containment purge and vent applications. In addition, we conducted a literature search to investigate related research done previously by others.

We found butterfly valves in sizes 2 to 66 in. (diameter) to be the predominant design. The valve manufacturers had done very little testing to qualify the valves for nuclear purge and vent applications, and most of that testing had used incompressible fluids. Testing performed with incompressible fluids does not necessarily validate industry equations being used for extrapolation; butterfly valves installed in purge and vent applications are expected to operate with flow of compressible fluids. Previous testing performed using compressible fluids was done at pressures too low and usually with valves too small to fully characterize valve performance at design basis LOCA conditions. The INEL butterfly valve test project described in the following discussion was the first full-scale test project performed with a gaseous flow medium at full design basis conditions and incorporating more than one valve size.

2.3 Description of the Test Project

Three butterfly valves typical of valves used in containment purge and vent applications were tested, two 8-in. (nominal pipe diameter) valves and one 24-in. valve. The valves were American National Standards Institute (ANSI) 150-lb class, elastomer sealed, offset disc, high-aspect-ratio valves. (The aspect ratio is the ratio of disc thickness to disc diameter.) High-aspect-ratio offset disc designs were chosen for testing because they are typical of most installed valves, and because their response to flow is known to be one of the most demanding of the valve designs installed in purge and vent systems. In the offset disc design, the seat or sealing surface is offset from the centerline of the valve shaft. This configuration maintains leak tightness better than the in-line seal configuration.

The two 8-in. valves, made by different manufacturers, are representative of a large population of installed valves. Their different internal designs are typical of most of the designs and sealing features of other manufacturers' offset disc designs installed in commercial power plants.

The 24-in. valve was the same design as one of the 8-in. valves; thus, testing of this valve provided insight for extrapolation methodologies. The 24-in. valve also represents the largest butterfly valve installed in purge and vent applications in operating nuclear power plants that is allowed to open to the full open position. (Larger valves installed in purge and vent applications are typically blocked, preventing them from opening more than 70%, and in many cases, 40% open.)

Testing was conducted at the Energy Technology Engineering Center (ETEC), a Department of Energy laboratory operated by Rockwell International at their Santa Suzanna Field Laboratory in California. Facility preparation and checkout started in late 1983, and testing started in early 1984.

The valves were subjected to two separate test series. Testing of valve operation with the valves closing against flow is described in the following discussion, with results and conclusions presented in Sections 2.4 and 2.5. Testing of the valves for leak integrity when subjected to accident loadings is discussed separately in Section 2.6.

In all, the three valves were subjected to 64 flow tests, with valve inlet pressures ranging from 5 to 60 psig. (The design basis pressure for most containments is between about 40 and 60 psig.) The flow medium was nitrogen at ambient temperature. The valves were tested in various orientations relative to the flow. Figure 2-2 shows the uniform flow test section (straight pipe) and Figure 2-3 shows the two valve orientations tested in that section. Figure 2-4 shows the nonuniform flow section where the valves were installed immediately downstream of an elbow, and Figure 2-5 shows the four valve orientations tested in that section.

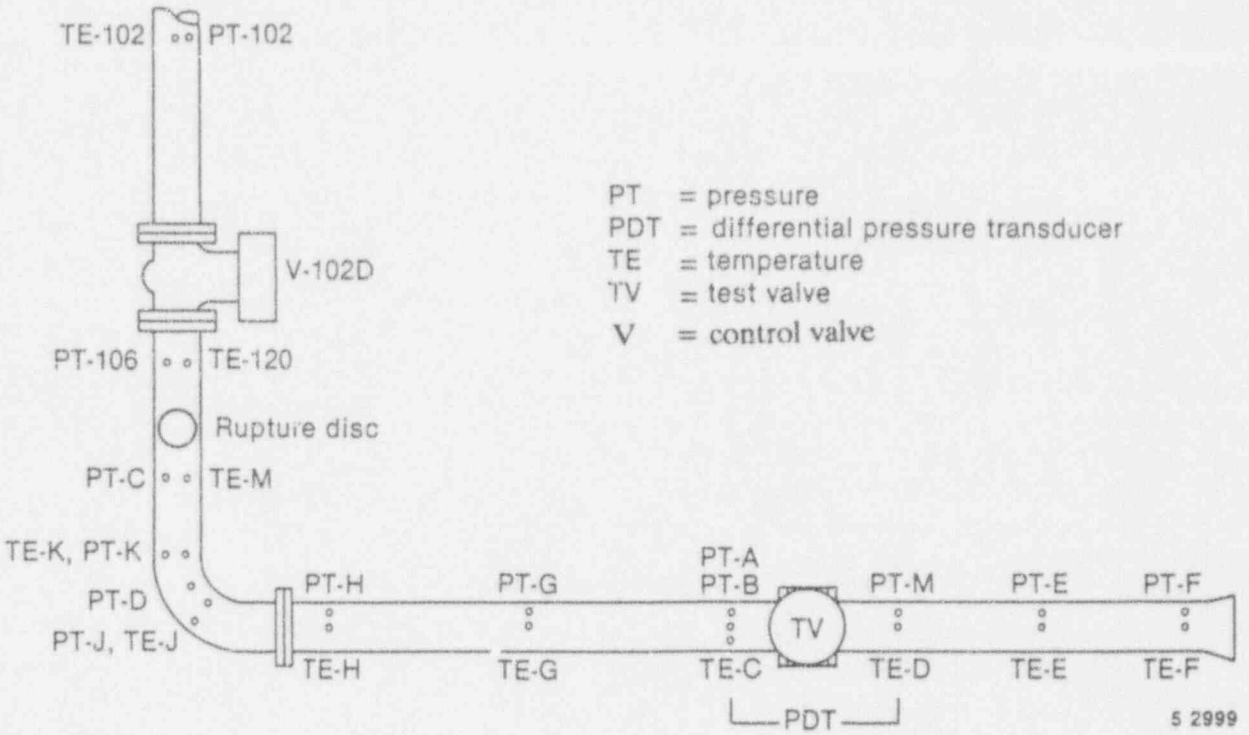

Figure 2-2. Diagram of the test section with uniform inlet flow (straight section of pipe), showing locations of instrumentation.

Figure 2-3. Valve orientations installed in the test section with uniform inlet flow.

It was necessary to flow test these numerous installation orientations and upstream piping configurations because of the wide variety of purge and vent valve installations in the plants. There was some evidence that valve orientation and upstream piping configuration have an influence on the torque loads imposed on the valve during closure against flow. When a valve is partially open, the shape of the high-aspect-ratio disc causes it to behave somewhat like an airplane wing as the fluid flows around it, with high and low pressure areas applying forces on the disc to either assist or resist closure. If the valve closes with the flat side of the disc facing upstream (FSU), these forces resist closure. If the valve closes with the curved side of the disc facing upstream (CSU), these forces assist closure.

For each test, the control valve was opened to establish the inlet pressure at the test valve at the specified value with the test valve fully open, and then the inlet pressure was maintained as constant as possible as the valve closed.

The test loop was instrumented to take up to 48 separate measurements of temperature, pressure, differential pressure, valve torque, and valve position. Figures 2-2 and 2-4 show the pressure

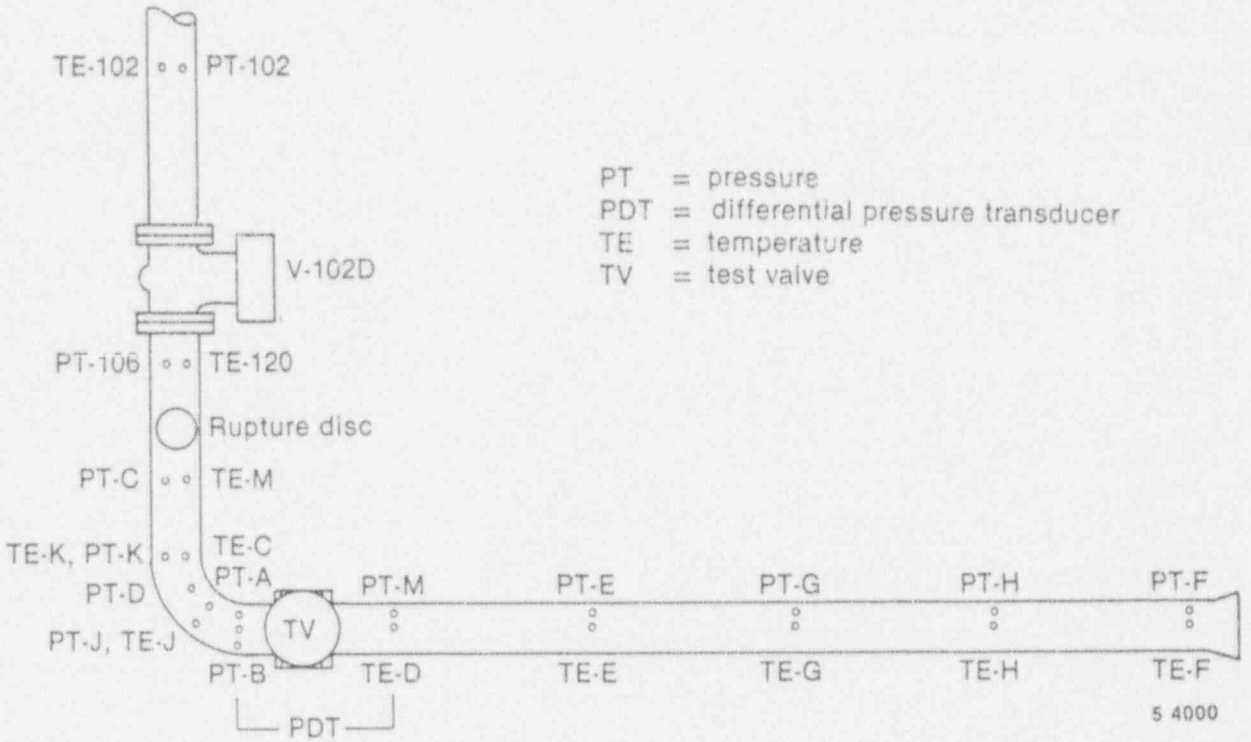

Figure 2-4. Diagram of the test section with nonuniform inlet flow (upstream elbow), showing locations of instrumentation.

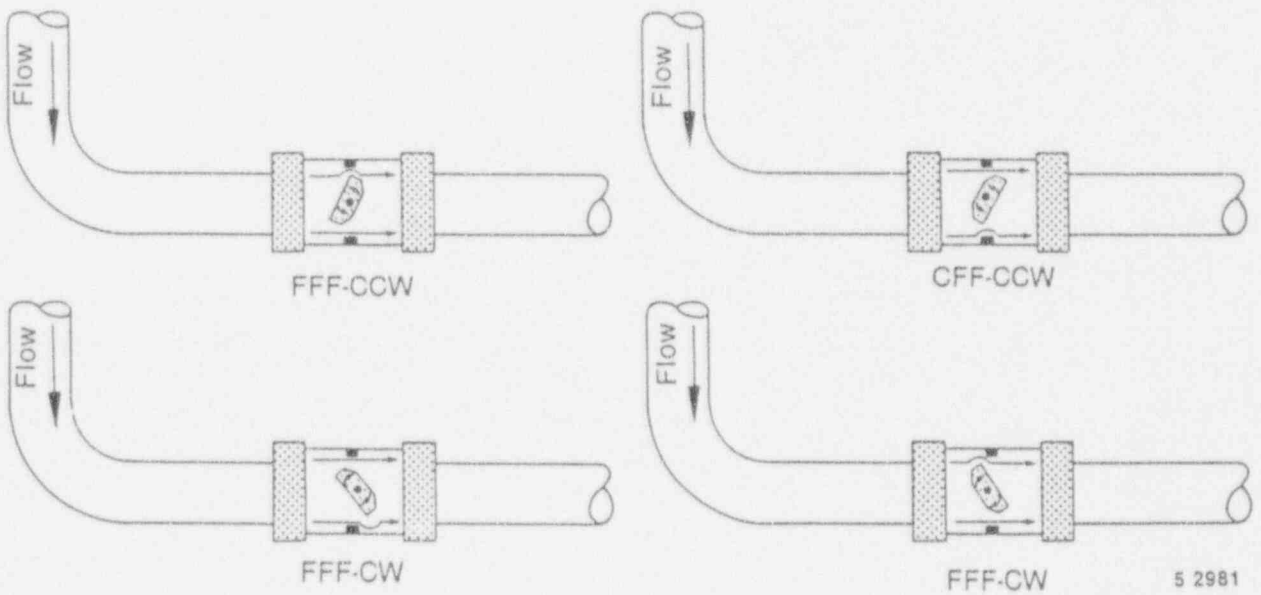

Figure 2-5. Valve orientations installed in the test section with nonuniform inlet flow. The CW and CCW notations identify orientations with the disc rotating clockwise or counterclockwise relative to the figure.

and temperature measurements made on the test sections. The direct, in-line torque cell mounted to the test valve shaft, and the rotary transformer used to monitor valve disc position, are not shown. All 48 measurements were input to a Hewlett-Packard-based data acquisition system at 155 data points per second.

2.4 Test Results

The results of the tests provided evidence that the methods typically used in the industry for determining closing torque requirements and for extrapolating small valve torques to predict large valve torques were not consistently conservative. We found that because of irregularities in the downstream pressure, the differential pressure measurement was not very helpful in characterizing valve performance at high flows. More important, we found that valve installation orientation and upstream piping geometry significantly affected the magnitude of the torque load imposed on the valve during closure.

2.4.1 Downstream Pressure. Choked and supersonic flow downstream of the disc influenced the downstream pressure measurement, thus affecting the differential pressure measurement or calculation. Figure 2-6 is a plot showing typical measurements of the static pressure 15 diameters downstream of the test valve. The downstream pressure profiles are different for each valve and are different from what one would get from measurements involving incompressible flow. We found that by using the upstream static pressure instead of the differential pressure (in Equation 1), we could more consistently characterize valve performance in these tests with compressible flow. In essence, we assumed that the downstream pressure was 0 psig.

We found the peak torque for a given valve in a given installation to be linear with upstream static pressure, regardless of valve design, size, or orientation or upstream piping configuration. Figure 2-7 is a typical plot of upstream static pressure versus peak torque. Note, however, that the slope

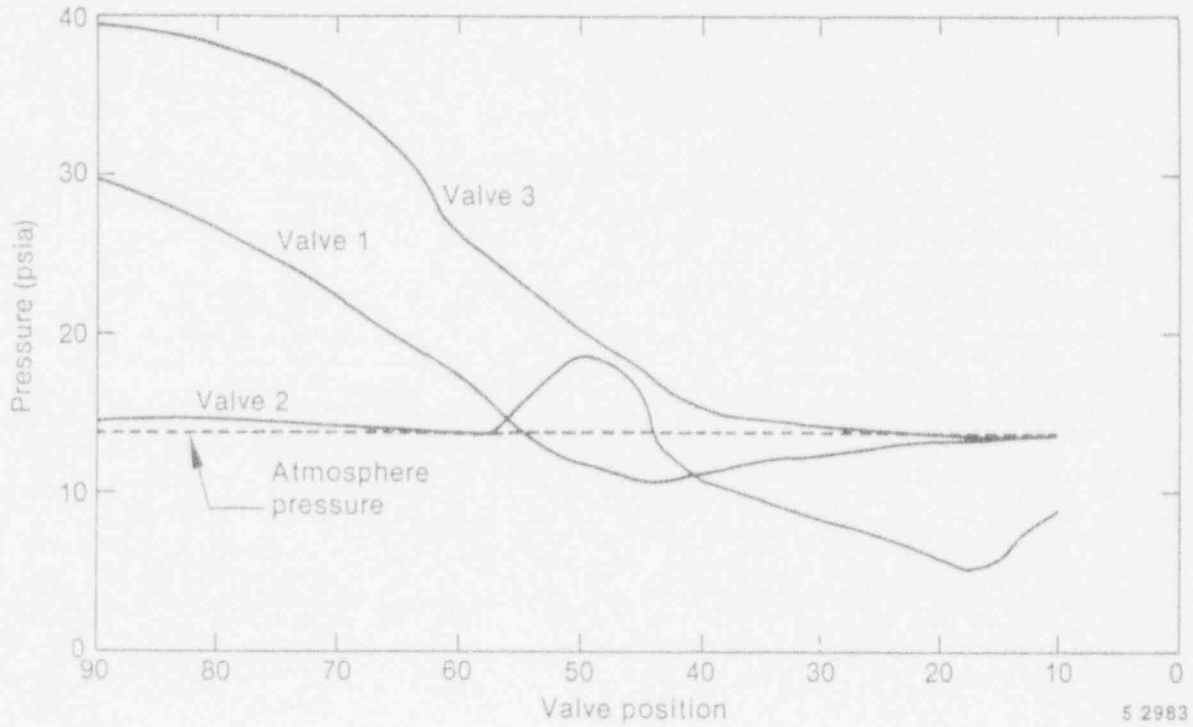

Figure 2-6. Static pressure 15 diameters downstream of valve versus valve position. Valves 1 and 2 are the 8-in. valves; Valve 3 is the 24-in. valve.

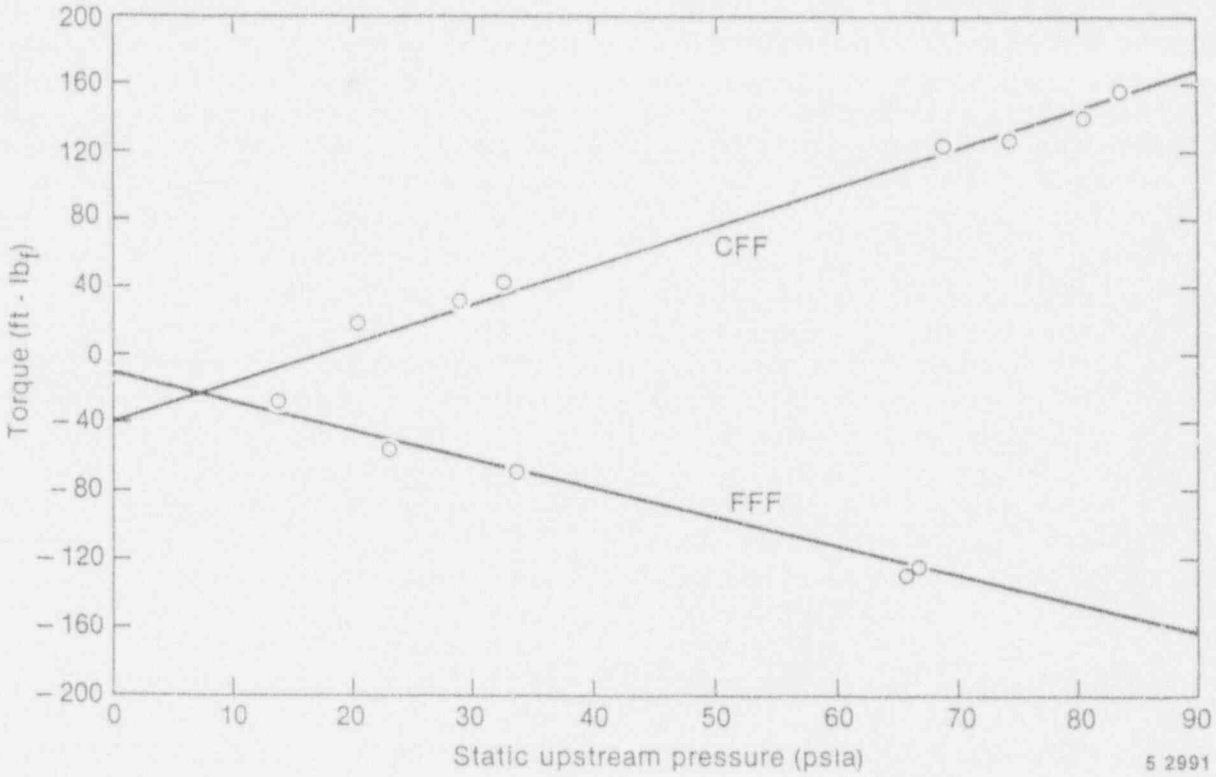

Figure 2-7. Peak torque versus upstream static pressure, first 8-in. valve.

of the linear response was not the same for different valves or for different installations. This fact prevents any universal extrapolation of valve response based on upstream pressure, but such an extrapolation of the response of a butterfly valve is possible, provided that pressure response curves are developed for each valve size and design, each orientation, and each upstream piping configuration. Note also that though the peak torque for a given valve in a given installation was linear with pressure, the disc angle at which peak torque occurred was different for different valves, different installations, and different upstream test pressures.

After our tests were performed, we used the measured results and Equation 1 to develop C_T curves for each valve, except that we used the upstream static pressure instead of the differential pressure. We also calculated large valve torque requirements from small valve C_T curves, and we evaluated the typical industry equations and assumptions by comparing the calculations to the test results.

2.4.2 Valve Orientation. Early review efforts revealed that the accepted industry method (Equation 1) for estimating butterfly valve performance was based on the symmetrical disc design used in a few nuclear plants built in the early 1960s. The symmetrical disc design is not as sensitive to the orientation of the disc relative to the flow as the offset disc design. The industry guidance did not account for the fact that valves with offset, high-aspect-ratio discs exhibit different torque performance, depending on which way the valve is installed. In addition, the industry guidance in the use of scale model test data did not account for this difference. The following discussion addresses these two issues.

We found that not only is the direction of the torque response different for the different valve orientations, but the magnitude of the peak torque and the predictability of the response are different. Generally (within reasonable tolerances allowing for data scatter), the magnitude of the peak torque measured with the valve oriented with the curved side of the disc facing upstream

was greater than that measured with the flat side upstream. This result indicates that the torque response of the valve in the curved-side-upstream orientation can be used to bound the response of the same valve in the flat-side-upstream orientation, but not vice versa.

We gained confidence in this method for bounding valve response by comparing the various valve responses as indicated by carpet plots. (Similarity among carpet plots is an indication of predictability of response from one design and one valve size to the next.) All carpet plots from tests with the curved-side-upstream orientation and were geometrically similar, even those from tests with an elbow immediately upstream of the valve. However, the plots from tests with the flat-side-upstream orientation were not geometrically similar. Figures 2-8 and 2-9 are carpet plots from an 8-in. valve and from the 24-in. valve oriented with the curved side upstream. Figures 2-10 and 2-11 are carpet plots from the same valves oriented with the flat side upstream. The geometric similarity of Figures 2-8 and 2-9 is evident.

To evaluate the relationship between scale model test data and valve orientation, we predicted the response of the 24-in. valve from the measured response of the 8-in. valve of the same design, then compared the predictions with the measured response of the 24-in. valve. We found that extrapolations based on the response of the small valve with the flat side of the disc facing upstream consistently failed to bound the response of the larger valve in either orientation. However, when the small valve was oriented with the curved side of the disc facing upstream, the resultant torques could always be extrapolated to conservatively bound the response of the large valve in either orientation, provided that the upstream pressure was not greater than 60 psig (see discussion below). (Note that we are speaking here of valve response in terms of the magnitude of the peak torque, regardless of the direction of the torque. As explained earlier, valves oriented with the flat side of the disc facing upstream respond with forces that resist closure, while valves oriented with the curved side facing upstream respond with forces that assist closure.)

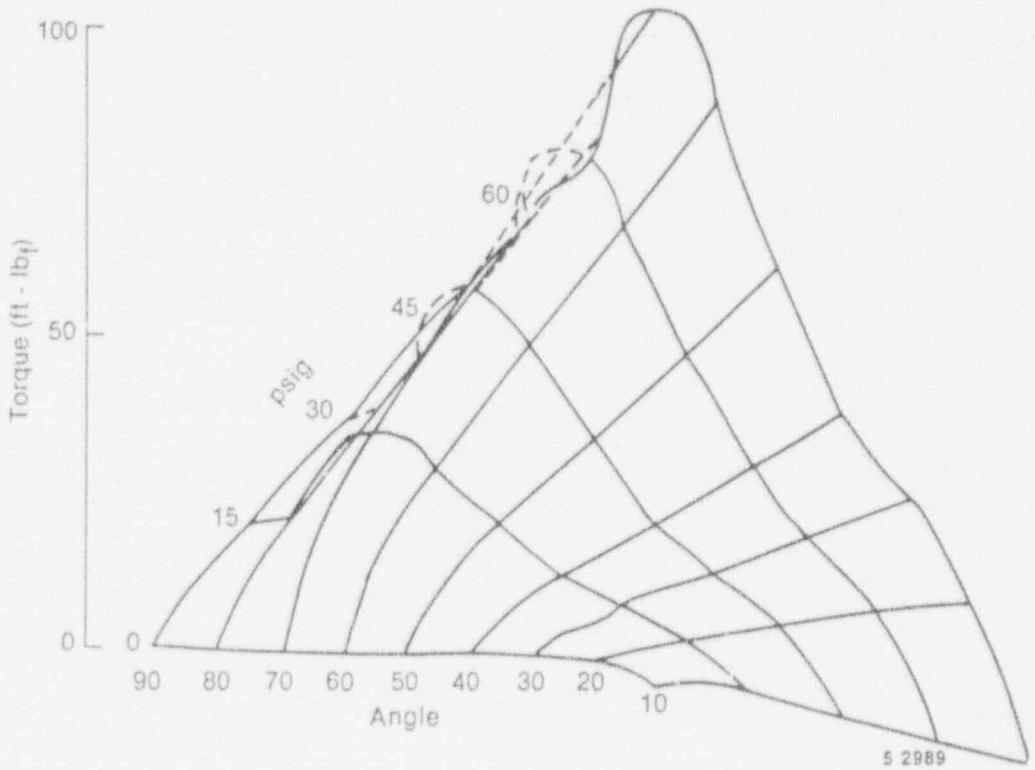

Figure 2-8. Torque versus upstream pressure and angle for the second 8-in. valve, curved-side-upstream orientation, with uniform flow.

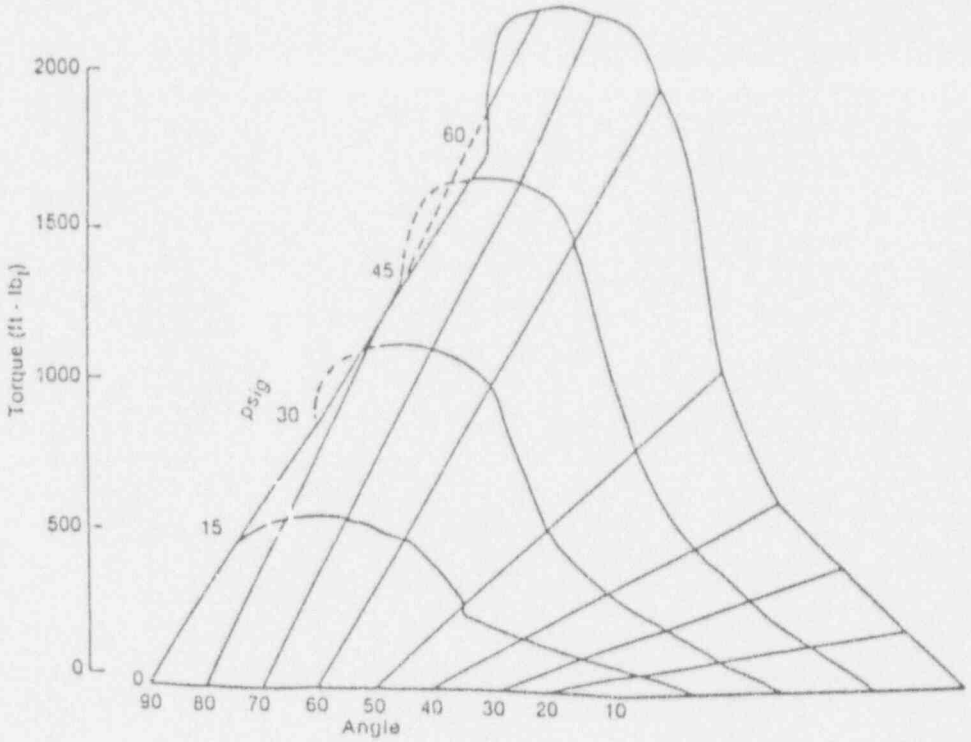

Figure 2-9. Torque versus upstream pressure and angle for the 24-in. valve, curved-side-upstream orientation, with uniform flow.

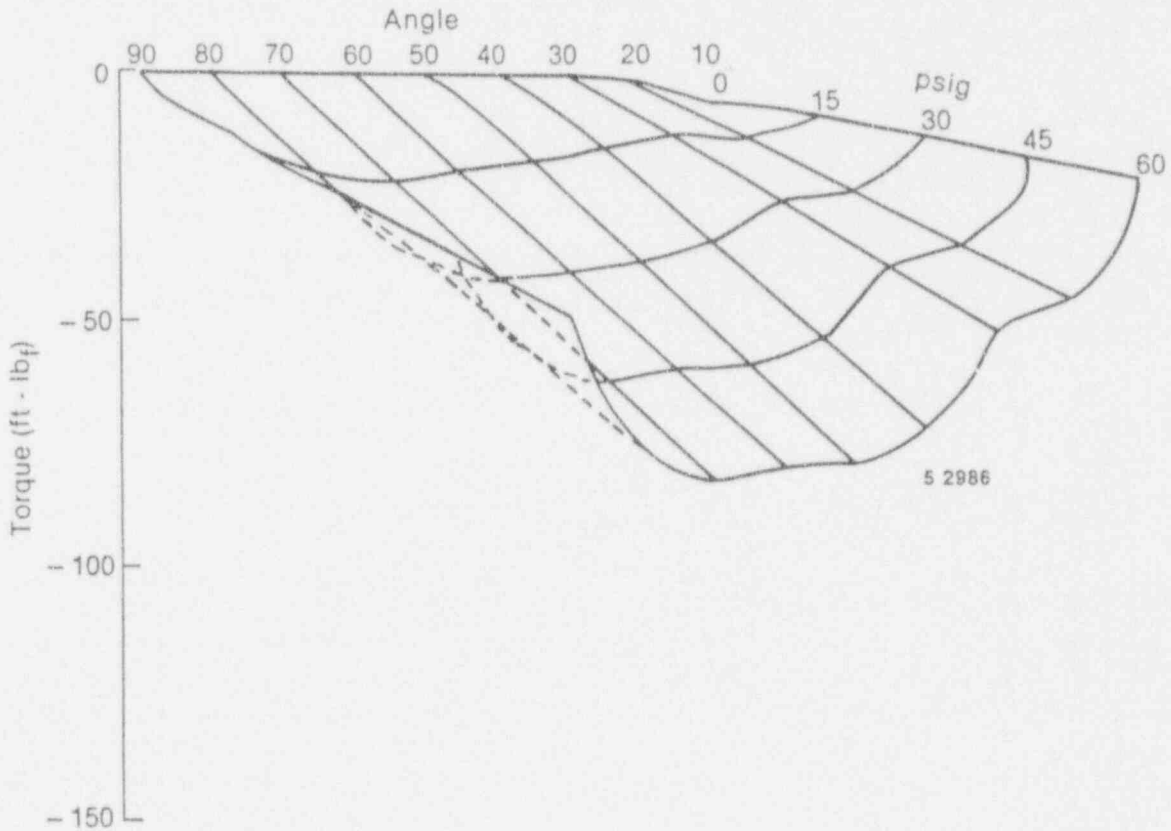

Figure 2-10. Torque versus upstream pressure and angle for the second 8-in. valve, flat-side-upstream orientation, with uniform flow.

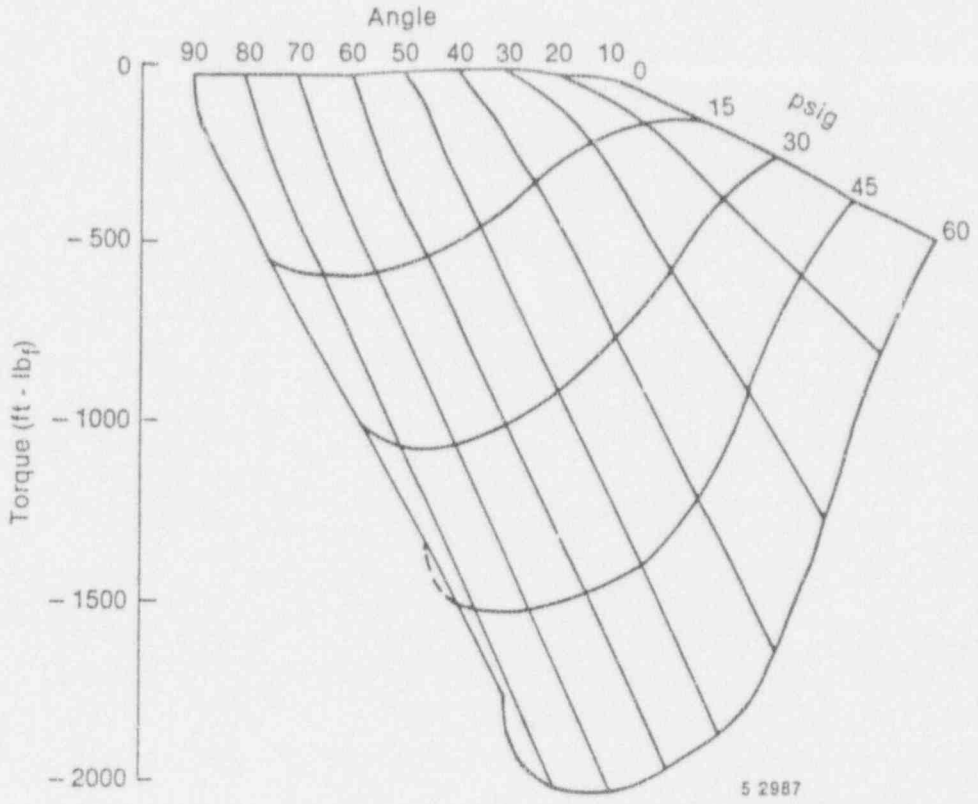

Figure 2-11. Torque versus upstream pressure and angle for the 24-in. valve, flat-side-upstream orientation, with uniform flow.

We also evaluated the validity of the diameter cubed term in Equation 1 as it is typically used to predict the response of larger valves from the response of smaller valves. (This is simply another way of looking at the issue discussed in the previous paragraph.) We found the exponent of 3 adequate for extrapolation purposes with the curved side upstream at inlet pressures up to 60 psig. At higher inlet pressures, the prediction tended to become unconservative. With the flat side upstream, the prediction tended to be unconservative regardless of the upstream pressure.

2.4.3 Upstream Piping Configuration.

Table 2-1 lists results from tests with the test valve installed in the straight section of piping for comparison with results from tests with the test valve installed downstream of an elbow. The values listed in the table are normalized peak torques measured in tests with a nominal inlet pressure of 60 psig. For each valve, the peak torque from the test with a straight section of pipe and with the valve oriented with the curved side of the disc facing upstream is assigned a value of 1.00. All other responses are compared to this value.

As stated previously, the response with the curved-side-upstream orientation with uniform flow (straight piping) generally bounds the response with the flat-side-upstream orientation with uniform flow. The exception shown in Table 2-1, where the flat-side-upstream response of the first 8-in. valve is 106% of the curved-side-upstream response, can be attributed to data scatter.

Table 2-1 shows that in some instances the presence of an elbow upstream of the test valve had a significant effect on the peak torque response of the valve. One of the curved-side-upstream orientations with an elbow had a peak torque that was 129% of the curved-side-upstream response of the same valve in a straight section of pipe, and one of the flat-side-upstream orientations with an elbow had a peak torque

Table 2-1. Normalized peak torques.

Valve orientation[a]	Upstream piping configuration	First 8-in. valve	Second 8-in. valve	24-in. valve
CSU	Straight pipe	1.00	1.00	1.00
FSU	Straight pipe	1.06	0.81	0.94
CSU-CCW	Elbow	1.29	1.00	1.04
CSU-CW	Elbow	1.14	0.95	0.92
FSU-CCW	Elbow	0.90	0.83	1.33
FSU-CW	Elbow	1.02	0.84	0.87

a. CSU indicates valve orientation with the curved side of the disc facing upstream, FSU with the flat side facing upstream. CW and CCW indicate direction of rotation relative to Figure 5.

response that was 133% of the curved-side-upstream response of the same valve in a straight section of pipe. We did not attempt to analyze for extrapolation purposes the responses of valves with upstream elbows, because there is no apparent pattern to the responses. Our best recommendation for installations downstream of an elbow is to estimate the required torque using the best available test information available, taken with the curve side upstream, and then to multiply the result by 1.5. This method should bound the worst-case response with an upstream elbow with either valve orientation.

2.5 Conclusions

In analyses involving offset-disc butterfly valves, torques for larger valves using compressible fluid can be determined using Equation (1) and torque coefficients (C_T curves) determined from realistically scaled smaller valves tested in compressible fluids, providing the following conditions are met: (a) upstream pressure is used instead of ΔP in the development of the C_T curves and in their application, (b) the torque coefficients are determined from scale model valves oriented with the curved side of the disc facing upstream, and (c) upstream flow perturbations (nonuniform flow) such as those caused by an upstream elbow are accounted for. These three issues are not subtleties; they were not widely known before this work, and their effect on the analytical determination of torque requirements can be significant. These conclusions are based on the following findings.

In our testing of three butterfly valves, the upstream static pressure served better than the differential pressure as an indicator of the torque response of offset-disc, high-aspect-ratio butterfly valves closing in compressible high-flow applications.

The torque response of these valves oriented with the curved side of the disc facing upstream was predictable, but the response with the flat-side-upstream orientation was not. However, the response with the curved-side-upstream orientation generally bounded the response with the flat-side-upstream orientation, in terms of the magnitude of the peak torque.

Nonuniform flow caused by an elbow upstream of the valve can have a significant effect on the torque response of the valve. This effect varied depending on the orientation of the valve and the direction of rotation of the disc. A multiplier of 1.5 times the curved-side-upstream response of the valve with uniform flow conservatively bounded

the worst-case response of a valve downstream of an elbow.

2.6 Leak Integrity Testing and Results

2.6.1 Testing. The leak integrity part of the test project was performed to provide information on the generic potential for purge and vent valves to leak during or after a design basis LOCA or a severe accident. The loads resulting from design basis accidents and severe accidents are radiation, pressure, and temperature. Because the elastomers used in the seals of purge and vent valves have high radiation allowables, this load was not addressed in this test project. A pressure of 60 psig was chosen to represent the design basis pressure. (The design basis pressure for most containments is between about 40 and 60 psig.) A design basis temperature was set at 280°F, the saturation temperature for the pressure. Two times the design basis pressure (120 psig) was chosen for the severe accident pressure, and 350°F was chosen for the temperature, the saturation temperature for that pressure.

Investigating the elastomer sealing material [ethylene propylene terpolymer (EPT)] used in the valves, we found that the design basis conditions were well within the specified allowables for the material. On the other hand, the severe accident temperature typically exceeded the material temperature allowables.

All three of the valves we tested had relatively new seals. Each valve was pressure tested at both the design basis accident temperature and pressure and at the severe accident temperature and pressure. Each valve was pressure tested at ambient temperature before and after each high-temperature pressure test. In each instance, pressure testing consisted of pressurizing one side of the disc while monitoring for leakage on the other side, then releasing the pressure, pressurizing the other side, and monitoring for leakage.

2.6.2 Test Resuts. The two 8-in. valves performed well during exposure to the design basis accident and severe accident temperatures and pressures, with no significant leakage detected. The 24-in. valve did not leak during exposure to the design basis accident temperature and pressure, and it leaked only a very small amount during exposure to the severe accident temperature and pressure.

Two of the valves leaked on cooldown. The first 8-in. valve, which has the elastomer seal in the valve body, leaked after exposure to the design basis temperature and after exposure to the severe accident temperature. The 24-in. valve, which has the elastomer seal on the disc, leaked after exposure to the severe accident temperature. Leakage through the 8-in. valve was as high as 470 scfh (standard cubic feet per hour), and leakage through the 24-in. valve was as high as 320 scfh. This leakage occurred because the seals experienced compression set at the elevated temperatures. Compression set was obvious in the first 8-in. valve after cooldown; one could see daylight between the disc and the seat. The second 8-in. valve, which has the seal on the disc (the design shown in Figure 2-1), did not leak on cooldown. The seal in this valve may have been less susceptible to compression set because of the seal's smaller cross section.

2.6.3 Conclusions. Containment purge and vent valves exposed to design basis conditions or severe accident conditions may leak after cooldown. These valves are installed in pairs, with one valve inside the containment and one valve outside. In most accident scenarios, the outside valve would be less likely to leak than the inside valve.

2.7 Application of the Research

The results of the research were provided to all leading manufacturers of butterfly valves. Two of them, Allis-Chalmers and Henry Pratt, actively reviewed the project from the planning through the testing and analysis.

The results provided criteria for evaluating utility submittals on containment purge and vent valves, and were used in checking utility responses to the TMI action plan (NUREG-0660).

The results are also being incorporated in the Electric Power Research Institute (EPRI) butterfly valve application guide. It is expected that this application guide will be widely used by the nuclear industry. EPRI is also expected to use the results in their MOV prediction methodology being developed to address the NRC's Generic Letter 89-10.

3. SEISMIC TESTING OF TYPICAL CONTAINMENT PIPING PENETRATION SYSTEMS

3.1 The Issue

Among the important safety-related containment features used in nuclear power plants are the containment penetrations, installed wherever piping, electrical cabling, etc. penetrate the containment structure. A typical piping penetration system consists of the penetration itself along with piping, adjacent piping supports, and two isolation valves, usually one on each side of the penetration. These containment penetration systems (CPSs) are as important as the containment structure itself in serving as the last barrier to fission product release in the event of an accident inside the containment. Because of the large number of piping penetrations (100 to 200 in plants of U.S. design), CPS valves are among the prime potential sources of local leakage through the containment.

The research summarized in this section addressed the operability and leak integrity of CPS isolation valves during and after seismic events and the structural integrity of the valves, piping, and other CPS components when subjected to seismic loads. Thus, this research served to support the NRC effort regarding Unresolved Safety Issue A-46, *Seismic Qualification of Equipment in Operating Nuclear Power Plants* (NUREG-1030). We opted to perform full-scale tests of complete systems (valve, penetration, piping, and supports) to avoid the uncertainties inherent in extrapolating results from small-scale tests or from tests of individual components. These tests, conducted in 1986, were the first full-scale, triaxial seismic tests performed on piping and valves. The purpose of the testing was to provide empirical data on the behavior of valves subjected to seismic loads and to provide results that would serve to either support or challenge the analytic assumptions used in the design of CPS piping, valves, and supports.

3.2 Research Methods

3.2.1 Background Research. A review of CPS designs used in a considerable number of plants determined that most plants are unique. However, there are some similarities in the piping layouts for CPSs, especially inside the containment. (The piping in most CPS installations makes a 90-degree bend within 15 ft of the penetration, with the inside valve either before or after the elbow.) We decided to set up three typical CPS configurations that would represent a large number of systems. We also chose to represent systems that are important to plant safety, that is, systems with a potential for leaking the containment environment directly to the outside atmosphere, and systems that would be needed to mitigate a design basis accident or an advanced severe accident.

Design basis loads vary a great deal among different plants and plant locations. Gravity, pressure, flow-induced vibration, and earthquake loads were considered.

We conducted a study of the analytically predicted acceleration response spectra for operational basis earthquakes (OBEs) and safe shutdown earthquakes (SSEs) for numerous types of containment vessel designs at varying building elevations, as reported in the appropriate NUREG reports and Final Safety Analysis Reports for 17 nuclear power plants. From that study we developed eight response spectra as specified spectra for the test project to address horizontal and vertical acceleration at two building elevations (the lower third and the upper half) for OBEs and SSEs. For an example, see Figure 3-1, which shows the specified horizontal response spectrum (labeled "test specification") for the upper half of the containment for an SSE. The analytically predicted spectra for several plants are also shown for comparison, as is the spectrum derived from the measured test input. Figure 3-1 is addressed in more detail later in this discussion.

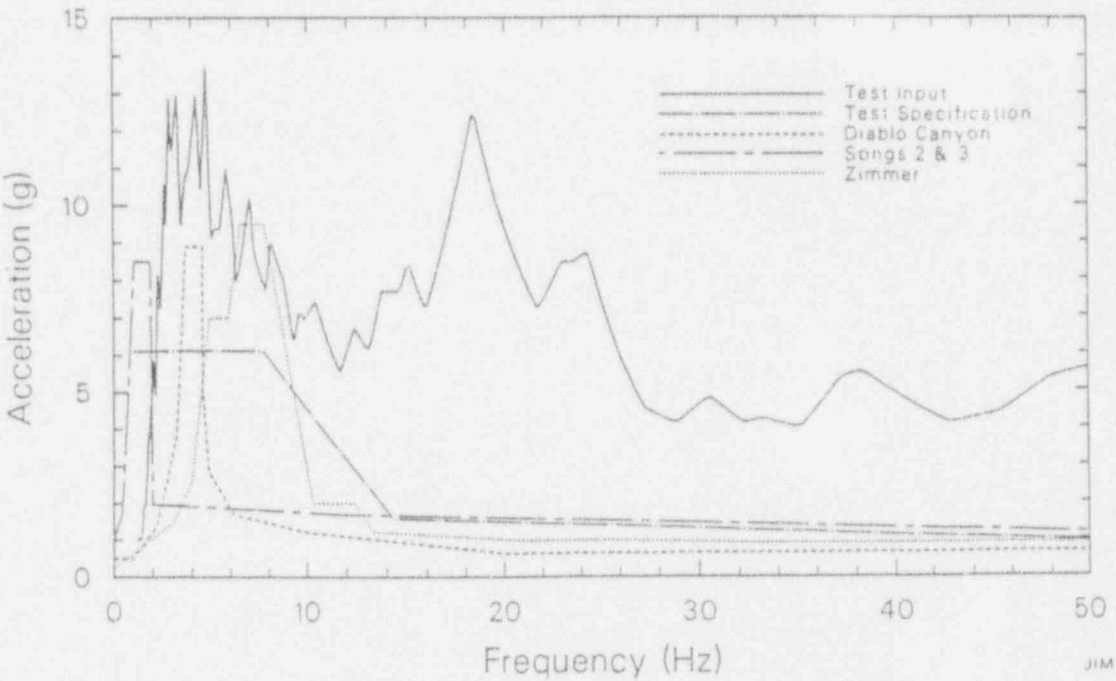

Figure 3-1. Comparison of the measured SSE test response spectrum with the SSE required response spectrum and with the analytically predicted SSE response spectra for selected plants; horizontal response spectra for the upper half of the building.

3.2.2 Description of the Test Project. One of the three configurations chosen for testing was an 8-in. gate valve system (Schedule 40 piping) modeling a containment spray system. This system was chosen because it is important to containment integrity as the final heat removal system. A containment spray system is a closed loop, liquid-filled system that requires leak integrity and valve operability for plant safety. An 8-in. butterfly valve system (Schedule 40 piping) modeling a purge and vent system was also chosen. This system is important to containment integrity because of the risk of leakage to the outside environment. The other configuration chosen for testing was a 2-in. globe valve system (Schedule 160 piping) modeling the many small bore piping systems that make up a large fraction of a power plant's CPSs. One concern with these small diameter systems is the large ratio of valve-plus-operator mass to pipe size.

We designed a test fixture that would accommodate either the 2-in. CPS or the 8-in. systems. The test fixture itself consisted of a large frame measuring 23 × 13 × 8 ft (7.6 × 4.3 × 2.6 m) constructed of 14-in. square steel tubing and mounted on pressurized air bags. Each piping system was individually installed in the test frame using nuclear grade supports, including rigid struts, spring hangers, and box beam supports. Support configurations were designed to approximate those in existing nuclear power plants. Independent triaxial motion was input into the frame by large, computer-controlled hydraulic actuators mounted to the frame. A sketch of the 8-in. gate valve system installed in the test fixture is shown in Figure 3-2.

The test fixture was designed to test only the inside half of a CPS. The connection of the piping to the containment at the penetration is stiff enough that no significant interaction between the inside piping and the outside piping would occur during an earthquake.

The piping systems were designed and fabricated in accordance with ASME Code requirements. The valves and penetrations were obtained from cancelled nuclear power plants. The piping

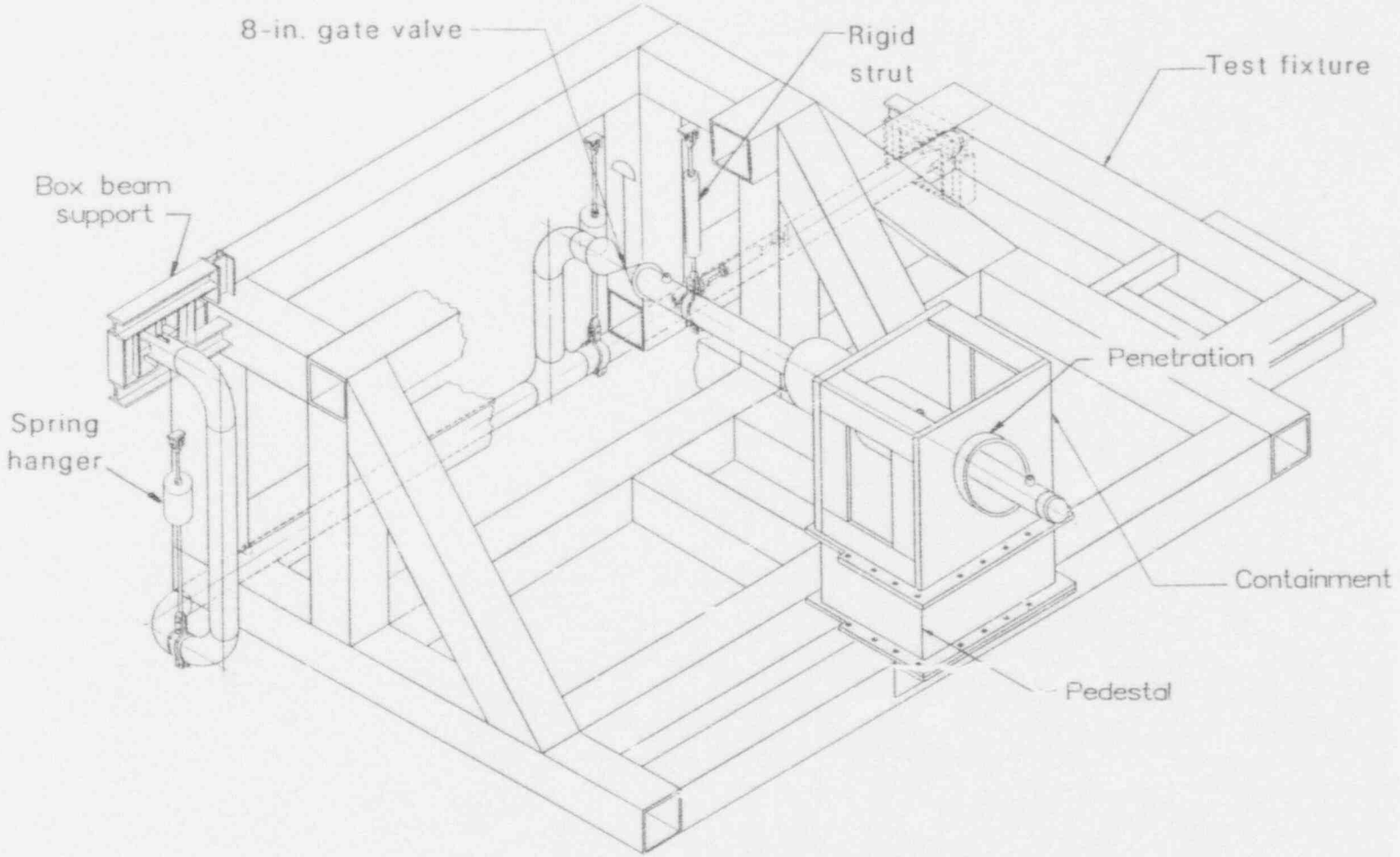

Figure 3-2. Sketch of the test fixture with the 8-in. gate valve assembly installed.

and supports were purchased from nuclear power plant suppliers.

The systems were instrumented to measure leak rates, pressures, temperatures, valve motor operator current, and valve stroke times. In addition, strain gages and accelerometers were installed on supports, valve assemblies, and piping to provide test data for comparison with predictions derived from analytical methods widely used in the industry.

Each of the three CPSs was subjected to the same test sequence, shown in Table 3-1. The fluids and pressures shown in the first column are those typical of the systems being modeled. The two low-amplitude vibration tests, conducted for 5 min each at one tenth of OBE loads, served not only to test the operability and leak integrity of the valves at those loads, but also to impose an arbitrary but reasonable amount of vibratory aging on the piping before subjecting it to the OBE and SSE loads. In the OBE and SSE tests, the 8-in. gate valve CPS and the 2-in. globe valve CPS were tested using the input response spectra for the lower third of the building, while the 8-in. butterfly valve CPS was tested using the input response spectra for the upper half of the building. After each step of testing, the acceptability of the previous test step was checked to make sure that desired load levels were achieved and that system responses were adequately measured.

3.3 Results

In general, the acceleration measured at the base of the test stand during the simulated OBEs and SSEs was equal to or considerably greater than the required response spectra specified in the test plan. In a few cases, the input spectra derived from the acceleration measurements failed to completely envelope the predicted response spectra specified in the plant reports we researched, but only at very low frequencies (2.0 to 2.5 Hz). For an example, see Figure 3-1. We judged these results to be acceptable because the lowest natural frequency for our piping systems was 3.9 Hz, so no amplification would occur at the low frequencies in question. Note also that the plant spectra shown in this figure are those that have the greatest horizontal response spectra of the 17 plants whose data we reviewed.

3.3.1 Valve Operability. The seismic loads imposed during the test sequence had no adverse effects on the operability of any of the three valves we tested. Small variations occurred in the stroke times, but these were caused not by the seismic loads, but by such factors as wear-in of new valve packing. In some cases, the measurements of motor current were slightly lower during seismic loading than after the loading ceased. Apparently, the vibration associated with the seismic loads caused a slight reduction in friction during valve operation.

3.3.2 Valve Leakage. The seismic loads did not cause any significant leakage through the valves. The 8-in. butterfly valve did not leak at all during the test sequence. The 8-in. gate valve leaked slightly during the simulated OBE (approximately 300 cm^2/h); leakage returned to zero with cycling after the simulated OBE, and remained at zero during and after the simulated SSE. Leakage through the 2-in. globe valve is shown in Figure 3-3. The valve leaked more than expected during leakage tests conducted before the simulated seismic loads. The general trend during the test sequence was for leakage to decrease with successive operation and with cumulative exposure to seismic loads.

3.3.3 Structural Integrity. The seismic loads did not cause any observable structural damage in CPS piping, valves, penetrations, or supports. No leakage occurred at any of the welds, but some very minor leakage occurred at a flange. (The 8-in. gate valve and the 2-in. globe valve were welded in place, while the 8-in. butterfly valve was welded on one side and flanged on the other.) No leakage occurred through any of the valve bonnets.

3.4 Conclusions

These tests were the first full-scale triaxial seismic tests ever performed on complete piping systems. Although the three CPSs discussed here

Table 3-1. Overview of measurements during seismic testing of the three containment penetration systems.

		Baseline measurements and conditioning					Seismic training			
System characteristics	Frequency testing	Preseismic baseline measurements	During 0.1 OBE (5 min)	After 0.1 OBE	During 0.1 OBE (5 min)	After 0.1 OBE	During OBE (30 s)	After OBE	During SSE (30 s)	After SSE
2-inch, globe valve, gas, pressure = 150 psig (1.03 MPa)	Determine first three system frequencies	Stroke[a] and seat leakage test	Stroke test[a]	Visual inspection, stroke[a] and seat leakage test[b]	Seat leakage test	Visual inspection, stroke[a] and seat leakage test	Seat leakage test	Visual inspection, stroke[a] and seat leakage test	Stroke test[a]	Visual inspection, stroke[a] and seat leakage test
8-inch, butterfly valve, gas, pressure = 60 psig (0.414 MPa)										
8-inch, gate valve, water, pressure = 100 psig (0.689 MPa)	Sequence →									

a. The stroke test consisted of measuring valve operator motor current and the stroke time as the valve moved full stroke (from closed to open or vice versa).

b. The stroke and seat leakage test consisted of at least seven stroke time and operator current measurements (two open-to-close and five close-to-open) and four leak rate measurements (two with pressure on the piping side and two with pressure on the penetration side).

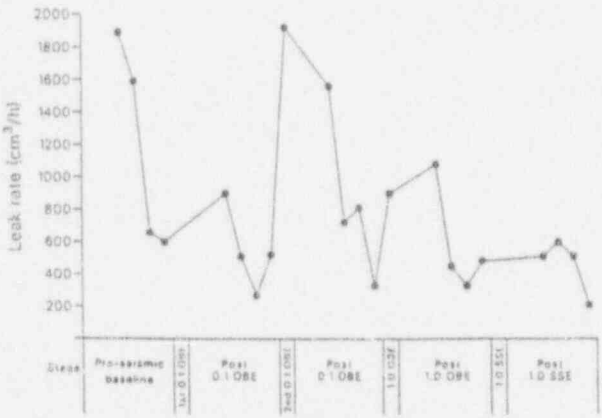

Figure 3-3. Leak rates across the seat of the 2-in. globe valve.

were not tested to failure, the applied loads were close to the most severe response spectra predicted for U.S. commercial plants. Of the changes in performance that occurred during the test sequence, any that could be attributed to the seismic loads tended to be improvements. No operational or structural failures occurred.

These results indicate that the worst case earthquakes anticipated in the design of nuclear power plants will not (a) increase the torque required for operation of CPS valves, (b) induce leaks in CPSs, or (c) cause structural failures in CPS piping, valves, penetrations, or supports.

The performance of these CPSs alleviated some concern that bench testing of individual CPS components might not be adequate. However, the test results also raised one concern. Data from accelerometers mounted on the valve and operator showed a dynamic response at frequencies higher than those for which the operator components are qualified. The implications are that vibration at these higher frequencies might cause electrical components such as relays to chatter, thus affecting the switches they control. These results concur with the results of the SHAG seismic test project, where a similar phenomenon was observed. See Section 7.3.4 of this summary report.

3.5 Application of the Research

These tests provided useful insights into the loads that piping systems might see in an earthquake environment. The results of this work, along with the results of the work reported in Sections 7 and 8 of this report, contributed to the data base that supported the NRC effort regarding Unresolved Safety Issue A-46, *Seismic Qualification of Equipment in Operating Nuclear Power Plants* (NUREG-1030). The fact was established through our work and the work of others that nuclear valves and piping will not be damaged by any credible seismic loading. The implementation plan currently in effect for addressing USI A-46 incorporates this important finding by allowing that older plants built before the modern seismic requirements were imposed can be judged by criteria less strict than a full seismic requalification.

4. TESTING OF CONTAINMENT PENETRATION SYSTEMS AT ACCIDENT LOADINGS

4.1 The Issue

A companion project to the testing described in Section 3 of this report was the testing of full-scale CPSs under design basis loadings and severe accident loadings. (For a brief description of CPSs and a discussion of their importance to plant safety, see Section 3.1.) The concern for the containment penetration, piping, and isolation valves was that the containment could grow both vertically and radially in response to a severe loss-of-coolant accident inside the containment. Because the piping is supported either from the basemat or from an internal structure that would not grow with the containment, the containment might literally pull the piping apart, causing a leak to the outside.

The tests described in this section consisted of subjecting the valves and piping to elevated temperatures and pressures and displacing the penetration relative to the piping to simulate the thermal and pressure expansion of the containment wall during design basis accidents and severe accidents. The tests were conducted in late 1987 and early 1988. During the tests, we monitored the operability and leak integrity of the valve, and we monitored the effects of the wall displacement (as much as 18 in.) on the piping and supports. The effects of radiation, steam, chemical spray, and very high temperatures (temperatures above the saturation temperature for the simulated containment pressure) were not addressed. Those loads would be better addressed in special effects testing of individual components.

4.2 Research Methods

4.2.1 Background Research. A search of the available literature and a study we conducted on thermal effects indicated that combined thermal and pressure expansion of the containment wall during a severe accident could be as great as 12 in.

4.2.2 Description of the Test Project. The three CPSs modeled and tested in the seismic test project described in Section 3 were also used for testing in this test project: an 8-in. gate valve system, an 8-in. butterfly valve system, and a 2-in. globe valve system. Some of the hardware used in the seismic testing was used again in this testing, and some new hardware was installed. The test fixture used for the seismic tests was modified and used in this test project. The 8-in. CPSs were installed in the test fixture with the penetration assembly mounted on rollers that traveled on rails to provide for a controlled displacement of the penetration relative to the piping, which was anchored to the frame of the test fixture with struts and other supports. A hydraulic ram was used to incrementally move the penetration. The rails on which the penetration rode sloped upward at 15 degrees, so that movement of the penetration would simulate both the radial and vertical displacement of the containment wall during an accident. Figure 4-1 is a diagram of the test fixture with one of the 8-in. CPSs installed. Figure 4-2 is a photograph of the 8-in. gate valve assembly installed in the test fixture.

The 8-in. containment spray test system and the 8-in. purge and vent test system modeled piping inside and outside the containment; thus each of the 8-in. systems used two valves. The two 8-in. systems were similar in design and used much of the same type of hardware.

The 2-in. system modeled only the inside piping, with the penetration end of the pipe capped to simulate the outside valve in the closed position. The configuration of the system was simpler, featuring one strut and one elbow. Containment wall displacement was modeled by anchoring the penetration and displacing the piping. At the request of NRC, the 2-in. system testing included enclosed-volume water expansion testing to determine whether overpressurization might occur in the piping between the two closed valves in a plant CPS when subjected to the high temperatures anticipated in accident conditions.

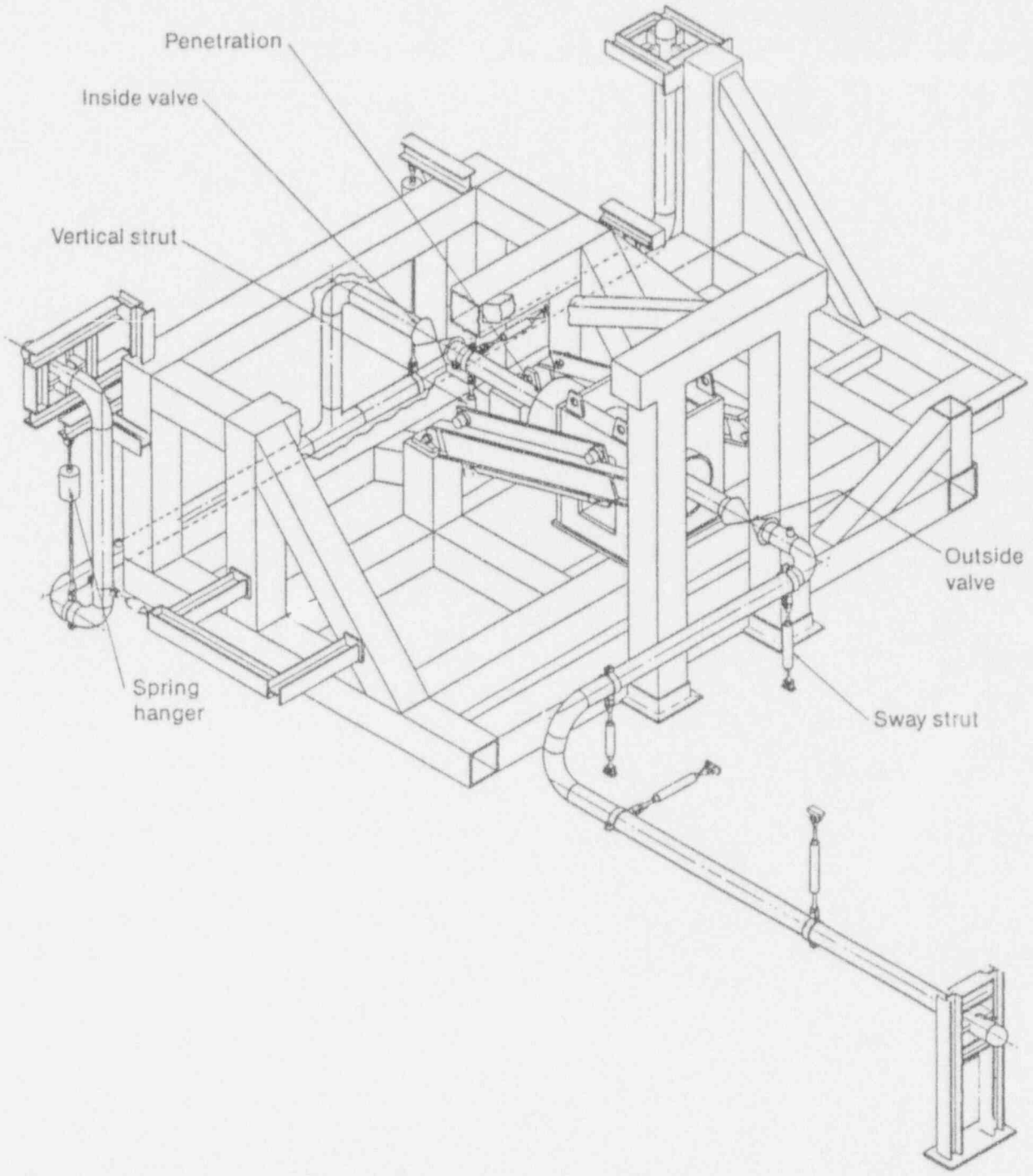

Figure 4-1. Sketch of the test fixture with an 8-in. gate valve system installed.

The piping systems were designed and fabricated in accordance with ASME Code requirements. The valves and penetrations were obtained from cancelled nuclear power plants. The piping and supports were purchased from nuclear power plant suppliers.

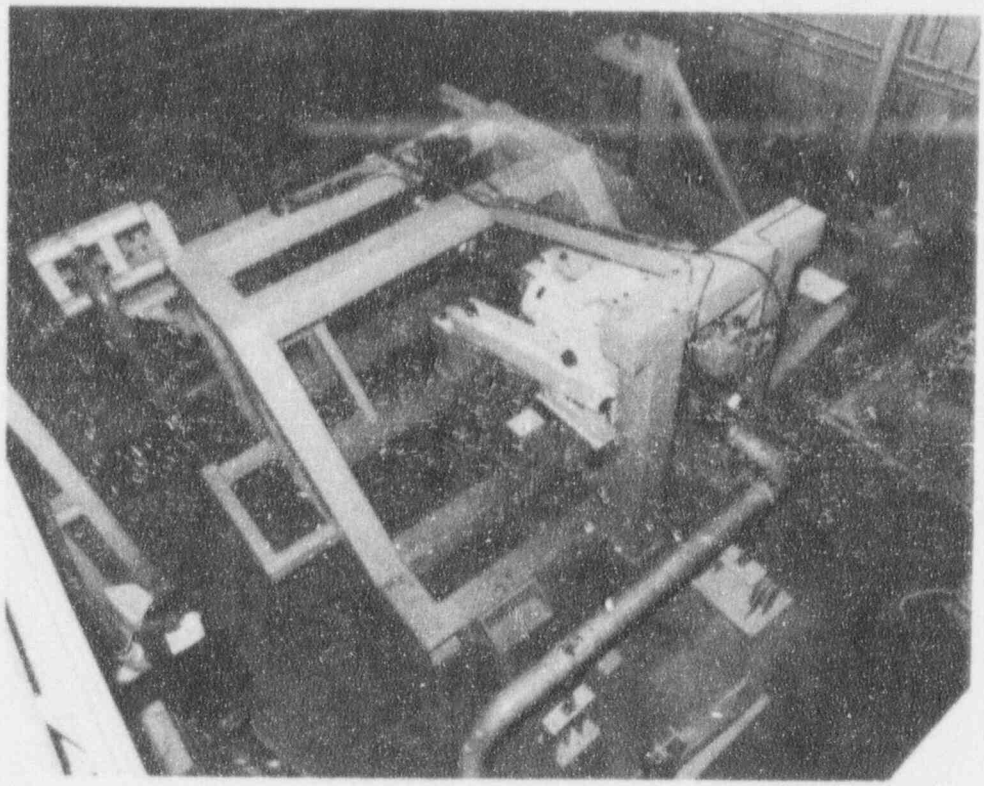

Figure 4-2. Overhead view of the test fixture with the 8-in. gate valve assembly installed.

The systems were instrumented to measure leak rates, pressures, temperatures, valve motor operator current, and valve stroke times, and strains on the valves and piping.

The basic testing sequence for each of the three CPSs consisted of (a) performing operational baseline tests on the system and (b) heating the inside valve and displacing the penetration in a stepwise fashion until reaching the desired conditions, while monitoring valve function, valve seat leakage, and strains on the piping. Table 4-1 summarizes the temperatures, pressures, and displacements imposed during the test sequence.

4.3 Results

4.3.1 8-in. Gate Valve System. The 8-in. gate valve CPS was subjected to a horizontal displacement of 13.2 in. with a corresponding vertical displacement of 3.3 in. Two of the struts were subjected to loads more than seven times their rated capacity. Some of the supports showed evidence of damage (for example, a bent end pin, a bent pipe clamp, an elongated end connection, etc.), but none of the supports in the 8-in. gate valve CPS failed.

The piping responded in a ductile manner with significant yielding but no local buckling. In addition, some minor, local deformations occurred where the piping slipped through the clamps that provide for connection to the piping supports. Ovalization occurred at one elbow, changing the external shape of the pipe from a circular cross-section with a diameter of 8.67 in. to an oval cross-section with major and minor axes of 9.16 and 8.36 in., respectively. None of the piping experienced a significant reduction in flow area.

Valve operation was not affected by the loads. However, leakage through the inside valve increased from an insignificant amount (less than 0.005 scfm) to about 0.103 scfm (standard cubic feet per minute) when the horizontal displacement reached 12.6 in. (more than twice the design basis accident specification). As the displacement increased, leakage decreased to about 0.02 to 0.04 scfm. The leakage immediately increased to

Table 4-1. Summary of testing sequence.

System integrity and pretest	Design basis accident simulation	Severe accident simulation	After severe accident simulation
8-in. systems:			
Radiography of piping welds 300 psi pneumatic test 100 psi bubble test (butterfly valves only) Baseline valve function	Heat valve to 280°F while displacing penetration 1.04 in. (horizontal) Regularly monitor leakage and valve function	Heat valve to 350°F while displacing penetration to 13.2 in. (gate valve) and 18 in. (butterfly valve) Regularly monitor leakage and valve function	Release load Check for leakage and valve function
2-in. system:			
4750 psi hydrotest Dye-penetrant exam Baseline valve function	Fill pipe with water downstream from valve Heat valve and pipe to 280°F while displacing pipe 2.0 in. (vertical) Monitor pipe for pressure buildup	Drain water from pipe Heat valve to 350°F while displacing pipe 8 in. (vertical) Regularly monitor for leakage and valve function	Apply load to flued head Displace to disfunction or failure Valve function 4750 psi hydrotest Dye-penetrant exam

0.89 scfm when, at the end of the test sequence, the load was released from the penetration and the piping returned about 4.2 in. toward its original position. A posttest examination indicated that the valve body had yielded slightly. No significant leakage occurred through the outside valve.

4.3.2 8-in. Butterfly Valve System. The 8-in. butterfly valve CPS was subjected to a horizontal displacement of 18.0 in. with a corresponding vertical displacement of 4.8 in. Two of the struts failed: a horizontal strut buckled under very high compression loads, and one rod end of a vertical strut yielded enough to allow the pin to pull through the end of the eye.

As in the gate valve testing, the piping responded in a ductile manner with significant yielding but no local buckling. Some minor, local deformations occurred at the clamps. Ovalization occurred at three elbows.

The displacement loads did not affect valve operation. Neither valve leaked during the heated portion of the test. However, the inside valve leaked at about 0.88 scfm after cooldown after the test sequence. (This same result was produced in earlier testing of butterfly valves. See Section 2.6.2.) We attributed this leak to elevated temperatures imposed on the valve with the valve in the closed position. Under those conditions, the valve's elastomeric seal is especially susceptible

to compression set, thus reducing the seal's effectiveness after cooldown. (New seals had been installed in the valves at the beginning of the testing.)

4.3.3 2-in. Globe Valve System. The enclosed-volume water expansion test of the 2-in. globe valve system (Schedule 160 piping) was performed as part of the design basis accident simulation. After the temperature reached 280°F, the pressure rose to over 4000 psig and would have continued to rise had we not shut off the heaters to prevent pipe rupture.

The globe valve CPS was tested beyond the severe accident displacement of 8 in. (vertical displacement of the end of the pipe section) to a maximum displacement of 48 in. There were no failures nor loss of function of any of the equipment. Stresses in the strut remained well within the elastic limit throughout the test. (The strut was disconnected after the displacement reached 8 in.) The piping behaved in a ductile manner with no cracking, buckling, or leakage in either the piping or the welds. Although the pipe experienced significant yielding, the cross section remained circular.

4.4 Conclusions

The pressure, temperature, and displacement loads imposed on the three CPSs we tested did not affect the operation of the valves; no noticeable changes occurred in operating current or stroke time.

No valve leakage occurred at or below design basis accident conditions. The plastic deformation of the valve body of the inside gate valve at higher displacement loadings was unexpected, but the resulting leak was small. The leak through the inside butterfly valve after cooldown raised concerns about the resistance of the elastomeric seals to high temperatures.

The CPS valves installed outside of the containment were not subjected to the high temperature loadings imposed on the inside valves. Neither of the corresponding outside valves leaked during or after our CPS testing, indicating that in an in-plant installation, both of these valve leaks we observed would have been contained by the redundant valve on the outside of the containment.

Testing showed that CPSs are extremely tough and forgiving. Damage to the piping even at severe accident displacements was minor and showed no evidence of affecting the integrity of the piping. Instances of strut failure and clamp slippage served to reduce rather than increase the stress on the piping.

Water trapped in the piping between the two valves in a CPS can build up excessive pressure at design basis temperature if no pressure relief is provided. Rupture of the pipe and possibly the valve could result. Such an occurrence would not necessarily cause a breach of containment, but it would disable the system (or at least part of the system) in which the piping and valve are installed.

4.5 Application of the Research

Part of the NRC's severe accident research was to determine the existing margins for components, systems, structures, etc. if subjected to conditions more severe than the design basis conditions. Our work, along with the work of Sandia National Laboratory (SNL), addressed the containment integrity portion of that research (NUREG-1264). The results provided many insights on the available margins of the containment and the containment penetration piping systems in accidents that progress beyond design basis loads. The results of our testing showed that the components of the containment piping penetrations (the penetrations, associated piping, and isolation valves) would not be the weak link in any credible severe accident scenario that threatened the integrity of the containment.

5. REACTOR COOLANT PUMP SHAFT SEAL PERFORMANCE DURING STATION BLACKOUT

5.1 The Issue

A typical reactor coolant pump (RCP) shaft seal assembly consists of three (or four) seals in a series. The first and intermediate seals are designed to contain a portion of the pressure while allowing some leakage through a small path toward the next seal and out through a leakoff line, while the final seal contains the remaining pressure with little or no leakage. Cooler water (100 to 160°F) is injected into the flow path ahead of the first seal to keep the seals and the leakage path cool, because typical operating temperatures of approximately 550°F in PWRs can damage certain polymer components of the seal assembly, and because otherwise the pressure drop in the leakage path might cause hot water to flash into steam between the faces of the main seal rings. One of the concerns with these seal assemblies is that during a station blackout, the pumps that supply the cooler water to the seals will be without power, allowing the hotter water to reach the vulnerable polymer components. In addition, the occurrence of flashing between the seal faces could cause one or more of the seals to pop open (seal instability), ultimately leading to a small-break loss-of-coolant accident. The research reported here addressed these concerns and thus provided information to support the NRC effort regarding Generic Safety Issue 23, "Reactor Coolant Pump Seal Failures at Station Blackout Conditions."

Figure 5-1, a sketch of a typical pump shaft seal, shows the components of interest: a static O-ring, the secondary seal, and the main seal rings. The primary hydraulic seal occurs at the main seal rings and is provided by the proximity of the rotating seal ring and the nonrotating seal ring. One of the main seal rings (in this particular design it is the nonrotating seal ring) is mounted so that limited axial motion is permitted, thus maintaining a very small, virtually constant gap between the main seal rings as the shaft moves axially relative to the housing in response to thermal and pressure-induced expansions. The

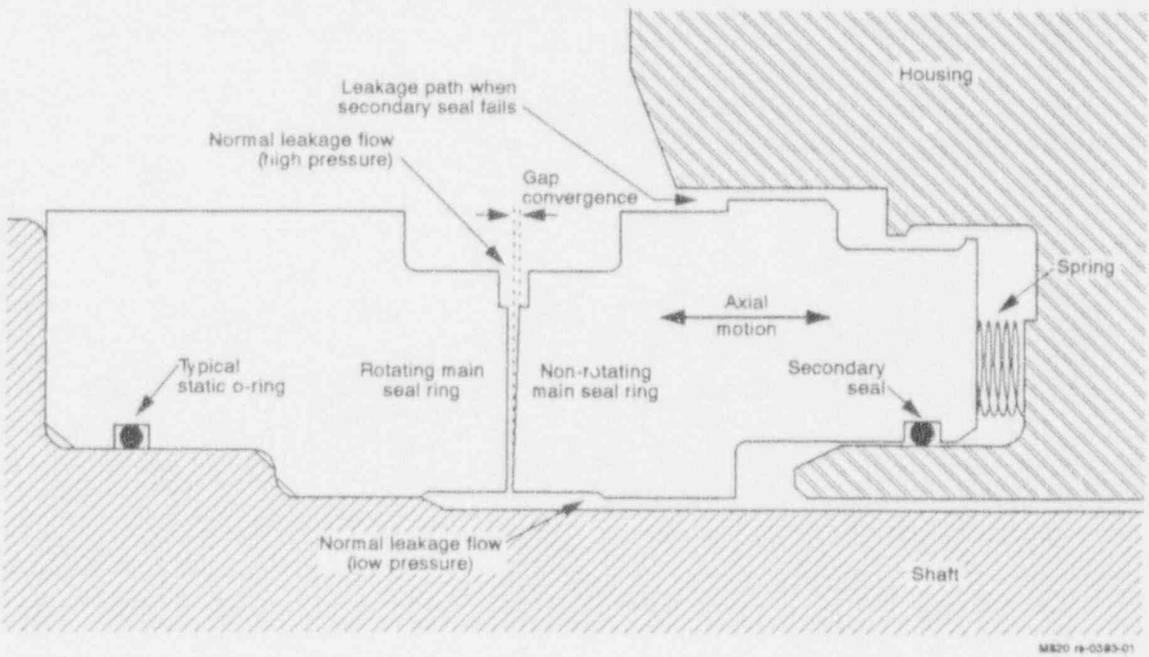

Figure 5-1. Simplified diagram of a cross-section of an RCP shaft seal; this represents one of the three or four seals that constitute the entire seal assembly.

opening between the seal faces is controlled by a balance of opening and closing forces. As the seal faces close down, the flow is reduced, and the pressure drop across the seal changes. The resulting change in opening forces causes the seal faces to open until a balance of forces is achieved. The secondary seal accommodates axial motion of the non-rotating main seal ring relative to the housing without allowing leakage between the two. These secondary seals are among the polymer components that can be damaged by high temperatures. The seal assembly includes several other polymer O-rings as static seals; one such O-ring is shown in Figure 5-1 as an example. These static O-rings seal interfaces between components that remain stationary relative to each other. Some of these static O-rings can also be damaged by station blackout temperatures and pressures.

The investigation summarized here consisted of (a) conducting a limited evaluation of the potential for static O-rings to blow out during station blackout, (b) testing the polymer seal components of the secondary seals in three different designs, with displacement of the sealing surface relative to the seal under conditions simulating the high temperatures and pressures anticipated during a station blackout, (c) conducting a computer analysis of the effects of flow, pressure, fluid condition, and seal design on the stability of the main seals (their resistance to popping open), (d) conducting limited testing of RCP shaft seals to validate the computer analysis, and (e) reviewing the available results of full-scale pump shaft seal tests conducted by others. The tests were conducted in 1986.

5.2 Assessment of Polymer Seal Performance

5.2.1 Evaluation of Static O-rings. Earlier research (reference 3) investigating the behavior of typical polymer seals used in Westinghouse RCP shaft seal assemblies showed that at some station blackout conditions, some of the static O-rings would blow out. The investigation summarized here included a limited evaluation of the potential for failure of static O-rings in Byron Jackson and Bingham International pump seal assemblies. This evaluation was based on (a) the information available on the materials used and the pressures and gaps to be sealed in these assemblies and (b) the results of the earlier testing of the Westinghouse seal assemblies. The evaluation included several assumptions on these designs that would require proprietary information to confirm, so the results are tentative. The evaluation found one static O-ring in the Bingham International seal design, namely the O-ring that seals the interface between the stationary main seal ring and its carrier, to be at risk during a station blackout.

5.2.2 Testing of Secondary Seals. The investigation summarized here included laboratory testing of secondary seals. The purpose of this testing was (a) to determine the response of the seals (whether or not they would extrude or blow out), (b) to determine the effects of relative movement of the surfaces being sealed on the extrusion behavior of the seals, and (c) to determine the friction forces developed between degraded seals and the movable main seal rings they are intended to seal. The tests were conducted by the Atomic Energy of Canada Limited Research Company (AECL) at Chalk River Nuclear Laboratories in Ontario, Canada. Three types of secondary seals were tested: Westinghouse O-rings with channel seals, Byron Jackson U-cups, and Bingham International O-rings with backup rings. See Figures 5-2 and 5-3. The Westinghouse O-rings were not the same as the O-rings typically installed in Westinghouse applications; the test project used O-rings of a different material, in anticipation of a material replacement by Westinghouse.

The test rig included a smooth cylindrical sleeve (simulating the nonrotating movable main seal ring in Figure 5-1) that was inserted into a concentric housing containing two secondary seals of the same design oriented back to back. Pressure was applied to the cavity between the two seals by distilled water supplied from a vessel pressurized by nitrogen cover gas. A linear actuator attached to the sleeve provided for axial motion of the sleeve relative to the housing. The

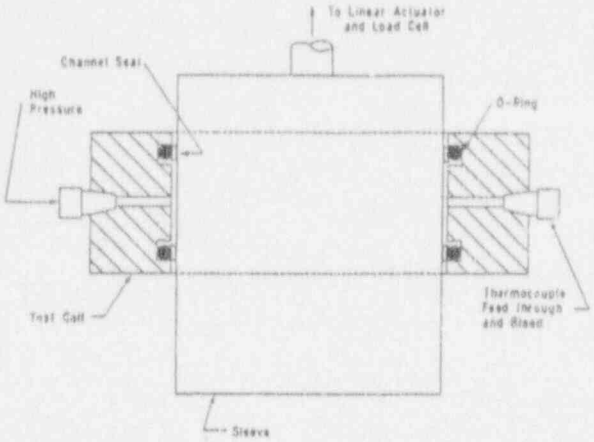

a. Westinghouse.

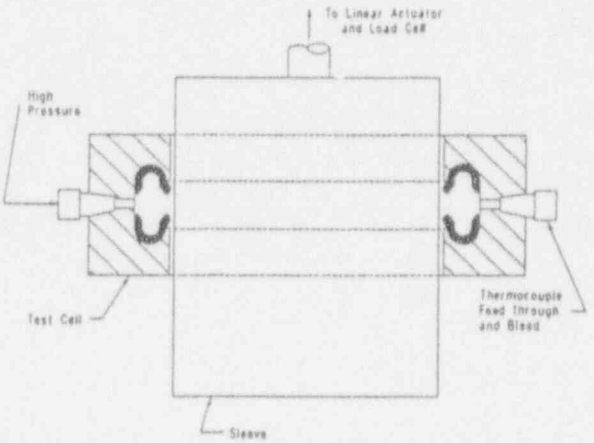

b. Byron Jackson.

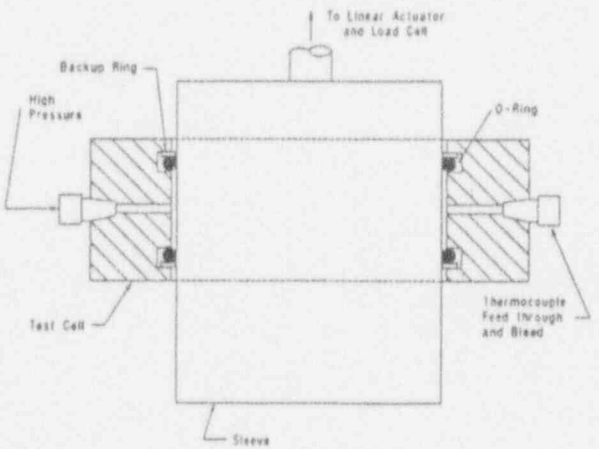

c. Bingham International.

Figure 5-2. Test cell for extrusion and friction testing of secondary seals.

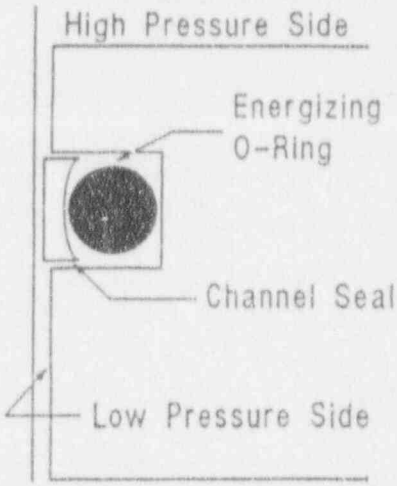

a. Westinghouse Channel Seal.

b. Byron Jackson round-back U-cup.

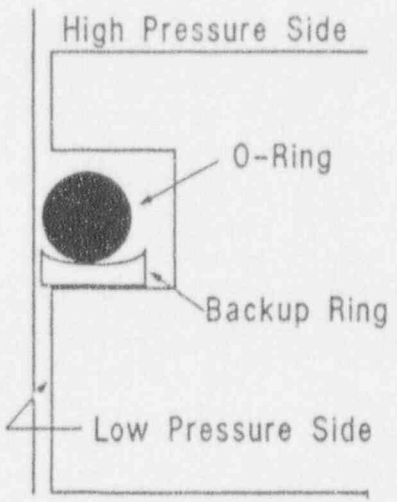

c. Bingham International O-ring with backup ring.

Figure 5-3. Cross-sections of the typical secondary seals subjected to testing.

linear actuator was instrumented with a load cell to measure the force required to slide the sleeve past the polymer seals. During testing, the housing and sleeve were heated and maintained at uniform temperature in laboratory ovens. Tests were conducted at temperatures as high as 550°F and at pressures as high as 2200 psi, with sleeve-to-housing diametrical clearances varying from 0.009 to 0.035 in.

In five tests of Westinghouse O-rings with channel seals, all the channel seals extruded. Leakage occurred in only one case; in all other cases, the O-ring took over the sealing. The force required to initiate axial movement of the sleeve at high temperature was as high as 210 lb (for two seals), almost twice that measured for the seals before exposure to high temperatures.

Seven tests using Byron Jackson U-cups were run. No significant extrusion occurred, but the U-cups did experience permanent set and severe embrittlement. Significant leakage attributable to the test conditions occurred only in the test with the most severe conditions, at 550°F and 2200 psi; the lip of the U-cup fractured. The force required to initiate axial movement of the sleeve in that test was 625 lb, the highest measured in the U-cup tests.

Nine tests using Bingham International O-rings with backup rings were run. No leakage occurred. Some extrusion of the back-up ring occurred in all the high-temperature tests (500 to 550°F). (Three tests were run at 70°F). The highest force required to initiate axial movement of the sleeve was 660 lb.

5.3 Shaft Seal Stability

Our investigation of RCP shaft seal stability, that is, the seal's resistance to popping open when flashing occurs between the seal faces, consisted of (a) a computer analysis simulating two-phase flow through the seal assemblies, and (b) limited experimental testing to validate the computer analysis.

5.3.1 Analytical Model. The computer analysis used a computer code developed by Atomic Energy of Canada Limited Research Company (AECL) of Chalk River National Laboratories. Given (a) the seal face inner and outer diameters, (b) the gap convergence or divergence (see Figure 5-1), (c) the inlet state of the fluid, and (d) the back pressure, the code calculates the leakage, the state of the fluid through the gap, and the critical balance ratio (a dimensionless value relating to the balance of opening and closing forces at which the seal becomes unstable) for a wide range of seal face separations.

The results of the computer analysis are summarized in the following discussion.

Assuming zero back pressure and 100 μin. convergence in the seal gap, unstable operation of the seal was predicted if the subcooling of the inlet fluid is less than 20°F (the seal pops open to the limit of its travel). Bistable operation (the seal opens to a larger gap and remains stable in that position) was predicted with inlet subcooling between 20 and 50°F, and stable operation was predicted with inlet subcooling above 50°F.

Assuming a seal gap convergence of 100 μin., stable operation was predicted if the back pressure is greater than about 50% of the inlet pressure, even with the inlet fluid conditions at saturation.

The effect of gap convergence depends greatly on other conditions. The computer analysis predicted that with an inlet temperature of 530°F and with zero back pressure, seals with a convergence of 100 μin. are more likely to be stable than seals with a 10 μin. convergence as fluid conditions approach saturation.

5.3.2 Testing of Seal Stability. Testing to validate the computer analysis used the test device illustrated in Figure 5-4. Most of the tests used a main seal ring with 100-μin. convergence. Representative temperatures and pressures were established and a closing load was applied to the movable main seal ring. The closing load was then gradually decreased until the seal popped

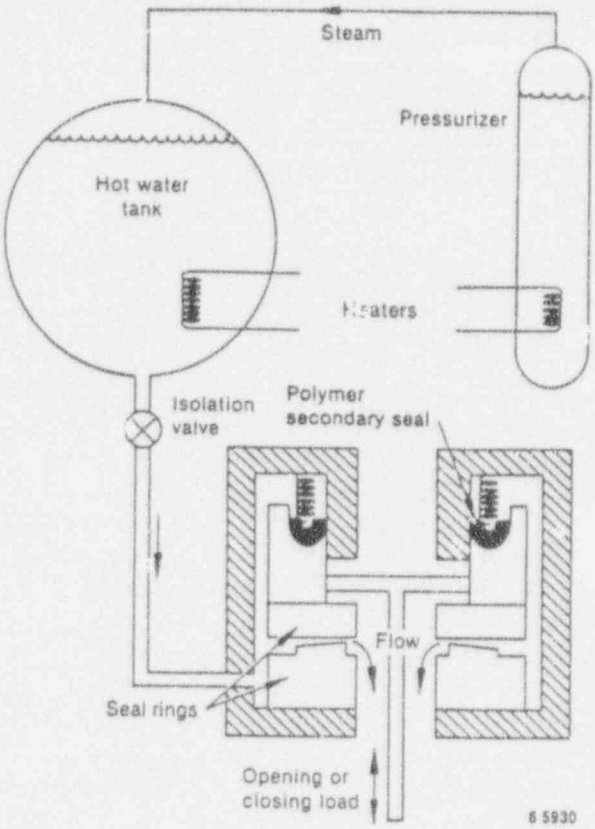

Figure 5-4. Sketch of the device used for the seal stability tests.

open. This testing allowed us to determine empirically the critical balance ratios for the conditions being tested (that is, the conditions at which seal instability occurs).

The results of the testing of convergent seal faces showed agreement within about 7% between the critical balance ratios measured during testing and the values calculated by the computer analysis. One test using a seal with the seal faces divergent by about 400 µin. (that is, the minimum gap was at the outside diameter of the seal instead of the inside) showed less agreement between calculated and measured values. The seal popped open at balance ratios at which the computer analysis predicted stability.

5.4 Review of Full-Scale Testing by Others

The results from two full-scale seal tests were made accessible to us, with restrictions on the amount of detail authorized for public disclosure, some of the information being proprietary. In a joint effort, Westinghouse Electric Corporation, the Westinghouse Owners Group, and Electricite de France (EdF) tested a 7-in. diameter seal assembly similar but not identical to the 8-in. seal assemblies used in U.S. RCPs. This full-scale test was conducted at a coal-fired plant in France in 1985. Although leakage occurred briefly through the first seal, and there were indications of brief leakage through the second seal, sustained instability of the seals did not occur. No static O-rings blew out, and there was little indication of extrusion of O-rings or channel seals. It cannot be assumed that the 8-in. seal assemblies normally used in Westinghouse plants in the U.S. will perform as well as these 7-in. seal assemblies, because there are potentially significant differences between the two.

Southern California Edison Company tested a 4-1/2-in.-diameter seal assembly in California in 1985. The tests used an operating boiler recirculation pump equipped with Bingham International seals similar to the 9-in. seals used in some U.S. nuclear applications. At some high-temperature conditions, flow fluctuations occurred consisting of brief excursions from the normal flow of 1.5 gallons per minute (gpm) to flows approaching 3 gpm. No damage to the main seal rings or the secondary seals was observed during posttest examination of the seal assembly.

The flow excursions are indication of the existence of the kind of bistable behavior predicted by the computer analysis described earlier in this summary. However, these test results consistently demonstrated lower leakage and much more stable behavior than predicted by the analysis.

5.5 Conclusions

In addition to the Westinghouse static O-rings determined by earlier testing to be susceptible to blow-out during station blackout conditions, one static O-ring in each stage of the Bingham International seal assemblies might be likewise susceptible. Certain assumptions that led to this conclusion need to be confirmed.

In general, polymer secondary seals are not expected to degrade enough to lose their sealing ability, though degradation of the seals can occur. Degraded secondary seals operate with higher friction, and the extra friction greatly increases the risk of movable seal ring popping open under conditions where seal stability is marginal.

Computer simulations indicate that RCP seals will remain stable during station blackout provided that inlet pressure is sufficiently above saturation or back pressure is sufficiently high. Seal face convergence or divergence and seal face condition can also affect the likelihood of seal stability during station blackout. In a comparison of the computer simulations with the results of laboratory testing of convergent seal faces, the critical balance ratios measured during testing agreed within about 7% with the values calculated in the simulation. Full-scale tests conducted by others indicate that the computer simulations are conservative; for example, tests showed the seals to be stable under conditions predicted by the simulations to produce unstable behavior.

5.6 Application of the Research

The results of this research were used to support the NRC effort regarding Generic Safety Issue 23, "Reactor Coolant Pump Seal Failures at Station Blackout Conditions." At the writing of this report, the resolution of this issue might include emergency provisions to provide cooling water to the seal assemblies under station blackout or other loss-of-seal-cooling conditions, or pump testing to verify seal stability under station blackout conditions.

6. SIGNIFICANCE OF RATTLING IN ELECTRICAL CABINETS DURING EARTHQUAKES

6.1 The Issue

In some instances, electrical cabinets and the components they house were not subjected to seismic qualification testing for nuclear applications. Where qualification testing was performed, the cabinets and components were generally qualified at frequencies within the normal seismic frequency range of 33 Hz or less. (Earthquakes can be expected to produce a dynamic response in the reactor building in the frequency range of 3 to 15 Hz.) If rattling occurs in an electrical cabinet during an earthquake, the rattle can produce a significant response in the cabinet at frequencies higher than 33 Hz, as well as introduce additional response at lower frequencies. In some instances, the components were qualified in tests along with the cabinets in which they were installed, so that if rattling occurs in the test, the effects of rattling on the components will have been considered by the qualification testing. In other instances, however, particularly in the earlier plants, the components were tested separately or were subjected to analyses without testing. In those cases, depending upon the component's characteristics and functional requirements, neglecting frequencies above 33 Hz raises the question of whether the component will perform its design basis function in an earthquake.

The idea of simply fixing a rattle assumes that the rattling can be detected during the qualification test, the cause of the rattling can be isolated, and some acceptable amount of rattling is known not to affect functionality of supported electrical components. Without this information, reduction of rattling to acceptable levels in cabinets is uncertain. In addition, the practical effects of the fix must be considered; for example, rattling of a cabinet door may be reduced to acceptable levels by applying screws all around, but this makes the door unacceptably difficult to open.

The purpose of the research summarized here was threefold: (a) to determine the extent to which the potential for rattling may exist in electrical cabinets, (b) to determine the effect of cabinet rattling on the electrical components mounted in the cabinet, and (c) to provide information to support the effort to determine whether current qualification testing needs to be revised to address this problem. The research consisted of (a) a review of selected qualification test reports and an analysis to determine the existence and the effects of rattling in those tests, and (b) laboratory testing of typical electrical equipment to investigate their susceptibility to vibratory response typical of that induced by rattling in electrical cabinets. The research was conducted in 1988.

6.2 Review of Qualification Tests

One hundred test reports were selected from seismic qualification programs conducted at both the Norco and the Huntsville facilities of Wyle Laboratories. The reports were reviewed for the occurrence of anomalies and the occurrence of response amplification at frequencies higher than 33 Hz.

The review identified anomalous behavior in several components. Most of the anomalies involved relays, switches, and circuit breakers. Contact chatter in relays was the most common anomaly. The review gave possible indication, but not conclusive proof, of a relationship between the occurrence of rattling and the anomalous performance of the components. Sources of rattling identified in the review were loose cabinet doors and loose device-mounting fasteners.

Of the 100 tests, six selected tests were analyzed in detail. The analyses revealed that a considerable amount of rattling occurred in five of the six cabinets. However, anomalous component behavior occurred in only two of the five. Thus, it was not possible from the available data to make a conclusive correlation between rattling and component malfunction. A serious limitation of this review was that the available data indicated only the occurrence of the anomaly, not the time

during the test at which the anomaly occurred or the corresponding component response frequency.

6.3 Testing of Electrical Components

To further investigate the possibility that rattling in cabinets subjected to earthquake excitation can cause electrical components to malfunction, we conducted tests at Wyle Laboratories. Relays were selected for testing because the review described above indicated that of the electrical components typically installed in the cabinets, relays were most susceptible to the effects of rattling. Six relays were tested: three of the Westinghouse model AR660, and three of the General Electric model CR120B. Both models are relays with normally closed contacts. Most of the tests were conducted with these relays de-energized, in the closed position (the configuration most susceptible to chatter).

The six relays were mounted on a fixture as shown in Figure 6-1, with eight accelerometers mounted at four locations as shown. The tests were performed on two test tables at Wyle Laboratories: a biaxial seismic test table, and a single axis vibration table.

Monitoring of the tests was designed to obtain data on (a) occurrence of contact chatter or change of state, (b) chatter duration and number of chatter events during each test, (c) acceleration level and frequency at which chatter occurred, and (d) the effects of contact chatter on other devices connected to the relay. To monitor item (d), each of the on-table relays was connected to an off-table relay, with the off-table relay energized by the on-table relay. The selection of off-table relays represented relays with different coil sizes, thus possibly offering different current and collapse-time sensitivities to on-table relay chatter.

The test sequence included (a) a resonance search consisting of a low level (0.2 g) sinusoidal sweep test to characterize the response of the fixture and the relays in the frequency band of 1 to 100 Hz, (b) random excitation of the relays at specified peak acceleration levels (varying from 2 to 10 g) throughout three frequency ranges: 3 to 15 Hz, 15 to 100 Hz, and 3 to 100 Hz; and (c) sine

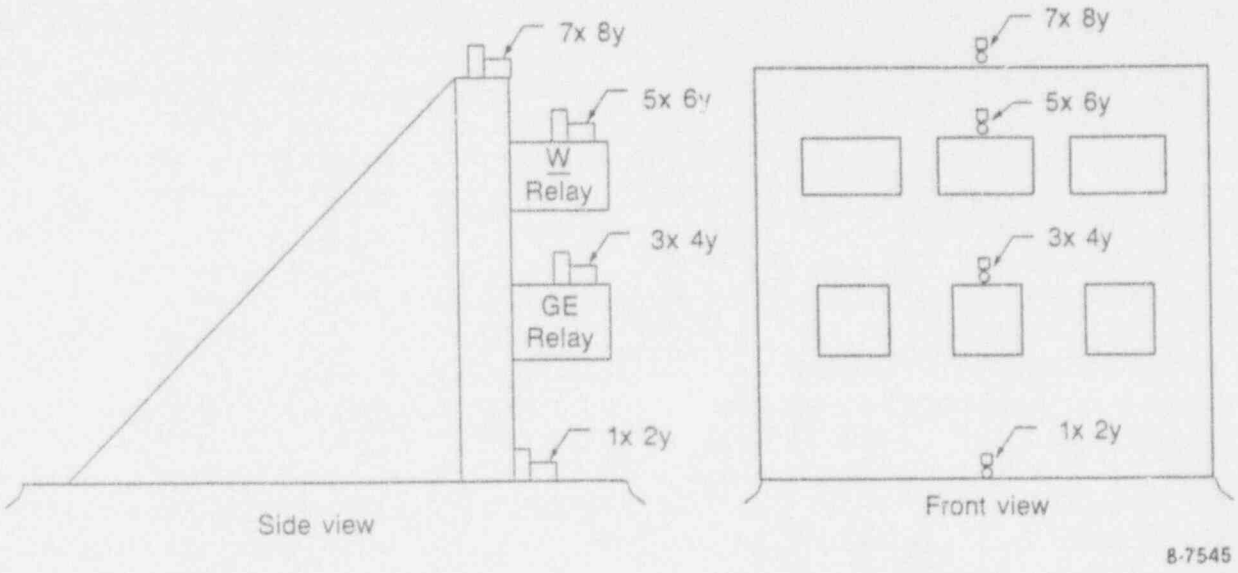

Figure 6-1. Sketch of the test fixture showing where the accelerometers were mounted.

sweep excitation in the 4 to 100 Hz frequency range at successively increasing acceleration levels. The random tests in the 3- to 100-Hz frequency band were performed to best replicate the waveforms expected during an earthquake with rattling occurring in a cabinet. The excitation was applied in the horizontal direction parallel to the relay contact line of action (the direction most likely to cause relay chatter) and in the vertical direction.

6.4 Test Results

A summary of the testing is presented in Table 6-1, with the test runs numbered from 1 to 41. Random tests in the horizontal direction in the low frequency range (3 to 15 Hz) produced relay chatter with the peak acceleration level at about 10 g, but not at lower peak accelerations. No chatter occurred in the high-frequency tests (15 to 100 Hz) even with peak acceleration as high as 15 g. In the composite frequency tests (3 to 100 Hz), chatter occurred at about 10 g (peak acceleration), but not at lower peak accelerations. No chatter occurred in any of the random tests in the vertical direction. Test runs that produced chatter were run again later with the on-table relays energized; no chatter occurred.

The occurrence of chatter in both the low-frequency and composite-frequency random tests at 10 g peak acceleration, along with the absence of chatter in the high-frequency random tests, indicates that chatter response to random motion is low-frequency sensitive. This sensitivity to low-frequency acceleration is more likely a product of contact inertia than of any resonant response.

A close examination of the data indicated that the duration of a measurement of high acceleration corresponded more closely with a chatter event than did the measurement of a peak acceleration. This phenomenon is illustrated in Figure 6-2, where chatter is closely correlated with a sustained period of relatively constant acceleration, indicated by the periods of relatively constant slope in the velocity trace in the figure. In effect, low-frequency displacements accompanied by sustained changes in velocity literally throw the contacts momentarily open. Note in Figure 6-2 that chatter in the Westinghouse relay is associated with a change in velocity in the negative direction, whereas chatter in the GE relay is associated with a change in velocity in the positive direction. This difference is due to the differences in the particular arrangement of the moving and stationary contacts in the different relays, providing further evidence that contact inertia, not resonant response, plays the important role in relay chatter.

Comparison of the responses measured at the inception of chatter (see Table 6-2) provides additional insights. Note that the instantaneous readings of acceleration on the relay case are lower at chatter events in test 16 (composite frequency) than in test 5 (low frequency). Apparently the high-frequency loads combine with the low-frequency loads in such a way as to produce chatter events at lower accelerations in the composite-frequency test than in the low-frequency test. A possible explanation for this phenomenon is that a momentary high-frequency acceleration, when superimposed upon a sustained low-frequency acceleration, adds a resonance effect to the inertial effect to trigger a chatter event at the lower instantaneous acceleration. However, note also that we are speaking here in terms of instantaneous acceleration. In terms of peak acceleration levels, the tests did not indicate a difference between the threshold levels for composite frequency tests as compared with low frequency tests. See Table 6-1. Chatter occurred at both frequency ranges at 10 Hz peak acceleration (tests 5 and 16), but in neither frequency range at 6.75 Hz, the next lowest peak acceleration tested (tests 4 and 15).

In an effort to more clearly characterize the frequency dependence of the relay chatter, we performed uniaxial swept sine tests in the 4- to 100-Hz range, as summarized in Table 6-1. The peak acceleration levels indicated in the table for each of the swept sine test runs are the control limits that were supplied to the shake table controller and were intended to be maintained throughout each sweep. The sweep function used

Table 6-1. Test run summary.

Test description	Peak acceleration level[a] (g)	Relay[b] status	Horizontal direction excitation frequency range (Hz)					Vertical direction excitation frequency range (Hz)			
			3 to 15	15 to 100	3 to 100	4 to 100	15 to 70	3 to 15	15 to 100	3 to 100	4 to 100
Random	2.0	De-energized	1,1-1	7	12	—	—	18	21	24	—
Random	3.0	De-energized	2	8	13	—	—	19	22	25	—
Random	4.5	De-energized	3	9	14	—	—	20	23,23-1	26	—
Random	6.75	De-energized	4	10	15	—	—	—	—	—	—
Random	10.0	De-energized	5[c]	11,11-1,11-2	16[c]	—	—	—	—	—	—
Random	12.0	De-energized	—	27	—	—	—	—	—	—	—
Random	15.0	De-energized	—	28	—	—	—	—	—	—	—
Random	10.0	Energized	6	—	17	—	—	—	—	—	—
Swept sine	1.0	De-energized	—	—	—	33	—	—	—	—	—
Swept sine	1.5	De-energized	—	—	—	32[c]	—	—	—	—	—
Swept sine	2.0	De-energized	—	—	—	31[c]	—	—	—	—	40
Swept sine	2.5	De-energized	—	—	—	30[c]	—	—	—	—	39[c]
Swept sine	3.0	De-energized	—	—	—	29[c]	—	—	—	—	38[c]
Swept sine	3.5	De-energized	—	—	—	34[c]	—	—	—	—	37[c]
Swept sine	4.0	De-energized	—	—	—	—	35[c]	—	—	—	—
Swept sine	3.5	Energized	—	—	—	36	—	—	—	—	41

a. Peak g definitions: Random—Amplified portion of the response spectra of the table acceleration measured at the control accelerometer.
Swept sine—Approximate peak table input motion.

b. Refers to both GE and W relays.

c. Chatter occurred on at least one on-table relay during this test.

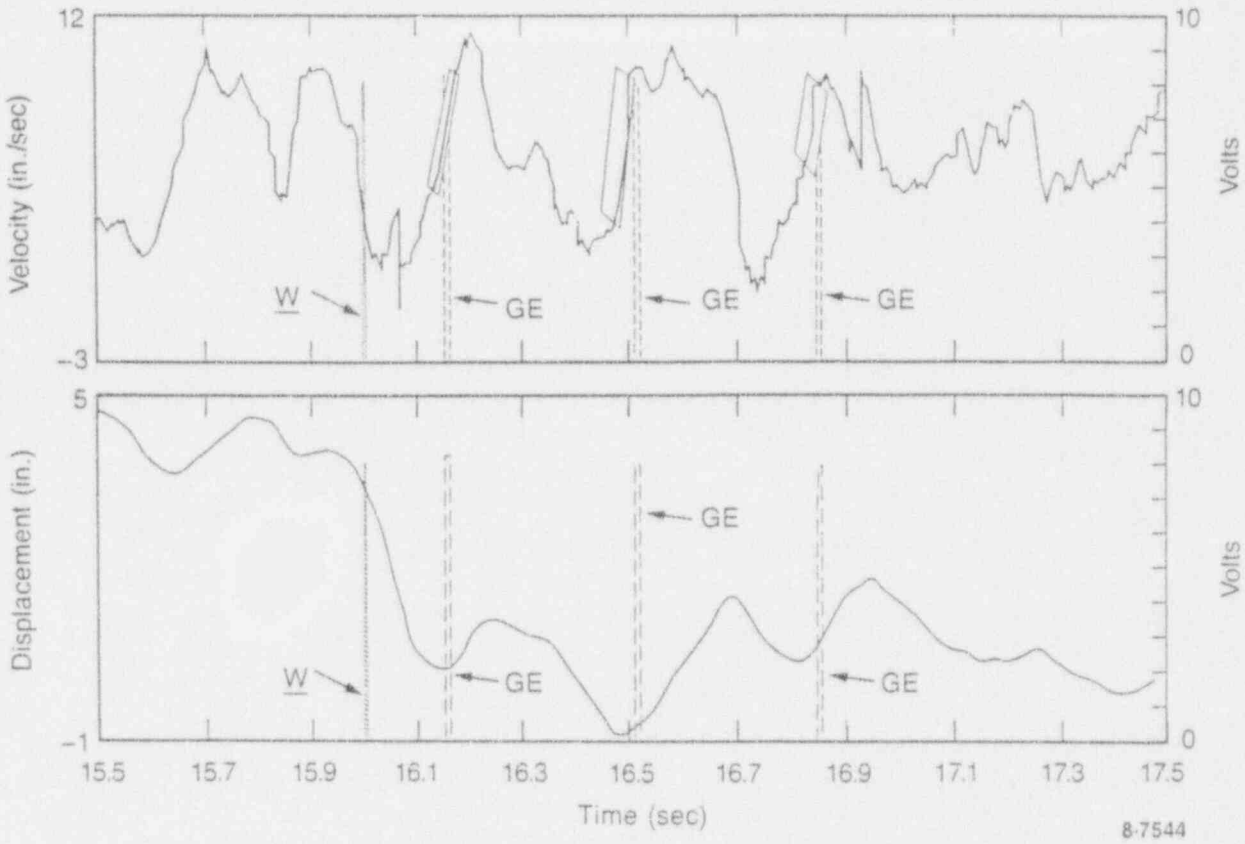

Figure 6-2. Velocity and displacement of the GE relay during recorded chatter events. Chatter events are indicated by the voltage pulses labeled W and GE.

in each of the test runs was plotted against time to determine the excitation frequency at the recorded time of chatter on the relays. Chatter occurred in horizontal test runs with peak acceleration levels of 1.5 g or greater. The data indicated sensitivity to chatter in the Westinghouse relays in the 45- to 85-Hz range and in the GE relays in the 60- to 85-Hz range. Both types of relays were sensitive to chatter in the low frequency range less than 15 Hz.

On-table relay chatter event durations ranged from 23 to 20 ms, with 30 to 50% of the events having a duration of 5 to 10 ms. Almost all of the off-table relays that were energized by the on-table relays chattered at some time during the testing in response to the chatter of the corresponding on-table relay. The causality between on-table chatter duration and off-table chatter duration could not be clearly defined from the data, but it was clear that the off-table relays exhibited longer chatter durations than the corresponding on-table relays.

6.5 Conclusions

The rattling environment is indeed real, as evidenced by the results of some equipment qualification tests of cabinets. However, the existence of rattling does not necessarily mean that a cabinet-supported device is going to malfunction. Malfunction depends not only on the existence of rattling in the cabinet but also on the characteristics of the device and the characteristics of the vibrations induced in the cabinet and component.

There may be dynamic characteristics that better reflect operability than the commonly used (IEEE 344) peak acceleration parameter, inferred from the comparison of test response spectra to required response spectra. For the relays tested in

Table 6-2. Waveform characterization at time of chatter.

Test run number	Chattering relay type	Test time at chatter (sec)	Instantaneous measurement of dynamic response at the relay at chatter						Chattering relay sustained average acceleration (g)
			General electric relay			Westinghouse			
			Acceleration (g)	Velocity (in./sec)	Displacement (in.)	Acceleration (g)	Velocity (in./sec)	Displacement (in.)	
5	GE	8.232	4.2	20	0.4	5.9	23	0.4	2.7
5	W	10.068	–5	–30	4.6	–6	–25	5.1	–2.9
5	W	14.919	–6.8	–22	5.2	–8.2	–20	5.2	–3.6
5	W	17.065	–5.5	–18	3.8	–6.0	–18	3.6	–3.3
16	GE	13.483	1.6	11	–0.6	2.1	–9	–1.4	1.4
16	GE	16.151	2.0	8	0.4	2.5	8	1	1.5
16	GE	16.508	3.0	10	–0.6	3.6	16	0.6	1.6
16	GE	16.842	3.2	9	0.7	3.5	8	1.4	1.7
16	W	11.152	–1.1	–22	–1	–2	–22	–1	–1.2
16	W	15.996	–0.8	3	3.4	–1	0	3.0	–2.1

this study, levels of sustained acceleration correlated better with anomalous operation (chatter) than did peak acceleration response.

It appears that high-frequency loads combined with low-frequency loads reduce the acceleration level at which chatter occurs, compared to low-frequency loads alone. Thus, the frequency content of the input spectra used in qualification testing may be more important than previously assumed.

Relay chatter and its effects on interfacing electrical equipment requires some consideration beyond the present seismic qualification test procedures. IEEE 344 presently requires the recording of only those chatter durations that are greater than 2 ms. The effect on secondary relays of chatter in primary relays, as observed in this study, indicates that time intervals between chatter incidents and the response characteristics of the interfacing equipment should also be considered.

These results may also have implications for seismic probabilistic risk assessments (PRAs), which presently ignore the effects of relay chatter on interfacing electrical equipment. The concern here is the possibility that increased chatter duration in secondary relays could cause failure of a safety system. This, coupled with the fact that some safety-related circuits with auxiliary relays are not easily reset if chatter should cause them to trip out, highlights the need for more research in this area of concern.

6.6 Application of the Research

The information was made available to the IEEE Standards Committee for seismic qualification.

7. SHAG TEST SERIES: IN SITU SEISMIC TESTING OF A VALVE AND A PIPING SYSTEM

The SHAG (Shakergebäude—building shaker) test series was an international project conducted by Kernforschungzentrum Karlsruhe (KfK). Researchers from the INEL joined researchers from the Argonne National Laboratory (ANL), the Electric Power Research Institute (EPRI), Kraftwerk Union (KWU), and the Staatliche Materialprüfungsanstalt (MPA) in participating with KfK in the test series. The tests were conducted in 1986 at HDR (Heissdampfreaktor), a decommissioned experimental facility located near Frankfurt, Germany.

7.1 The Issue

Seismic qualification of nuclear equipment is typically performed to industry standards, some of which are justified by only an analytical or extrapolated basis. This is especially true of qualification standards for valves and line-mounted equipment (transducers and other equipment mounted on the piping), for which seismic input is always analytically determined. SHAG testing provided an opportunity to measure actual, three-dimensional loads and actual responses to a simulated earthquake, thus providing empirical data to either confirm or challenge the analytical methods used in equipment qualification standards. The tests also provided an opportunity to evaluate the performance of an aged, motor-operated valve when operated during simulated earthquakes. The results served to contribute to the technical data base supporting the NRC effort regarding Unresolved Safety Issue A-46, *Seismic Qualification of Equipment in Operating Nuclear Power Plants* (NUREG-1030). These tests were the first in situ experiments subjecting an entire containment building and its components, including a full-scale piping system, to simulated earthquake loadings.

7.2 Test Description

Earthquake loadings were simulated in the HDR building by means of a large, eccentric mass, coastdown shaker installed on the upper floor of the HDR. See Figure 7-1. For each test, the shaker was weighted with a specified amount of weight bolted to the two shaker arms. With the weighted arms opposite each other, the shaker was spun up to a specified speed corresponding to the starting frequency for that test (varying from 1.6 to 8 Hz). The arms were then allowed to swing together, creating a revolving eccentric mass that shook the building as the shaker coasted down. The building and the equipment installed in the building responded in much the same way they would respond to an earthquake imparting dynamic energy to the building from the ground.

Our testing focused on the VKL (Versuchskreislauf—experimental piping loop), an existing stainless steel piping system located between the 18 and 24 m elevations in the HDR building. We modified the VKL by installing an aged 8-in. dc-powered motor-operated gate valve and by installing snubbers, spring hangers, and struts to create a piping support system designed to be typical of U.S. nuclear installations. The configuration of the U.S. stiff support system was based on a computer analysis of the VKL and on acceptance criteria specified in the ASME Code. The 8-in. gate valve was a 25-year-old valve from the decommissioned Shippingport Atomic Power Station. Figure 7-2 is a drawing of the modified VKL.

We installed 103 instruments on the VKL and on the HDU (Heissdampfumformer—steam generator), a large vessel to which the VKL is attached. The instruments measured acceleration, displacement, strain, force, temperature, pressure, differential pressure, valve position, valve motor amperage, and motor voltage.

The simulated earthquake tests were conducted with hot and cold pressurized water at pump flow in the piping. We monitored the operability of the valve by opening and closing the valve during and after the simulated earthquakes, with flow, pressure, and temperature loads imposed on the valve.

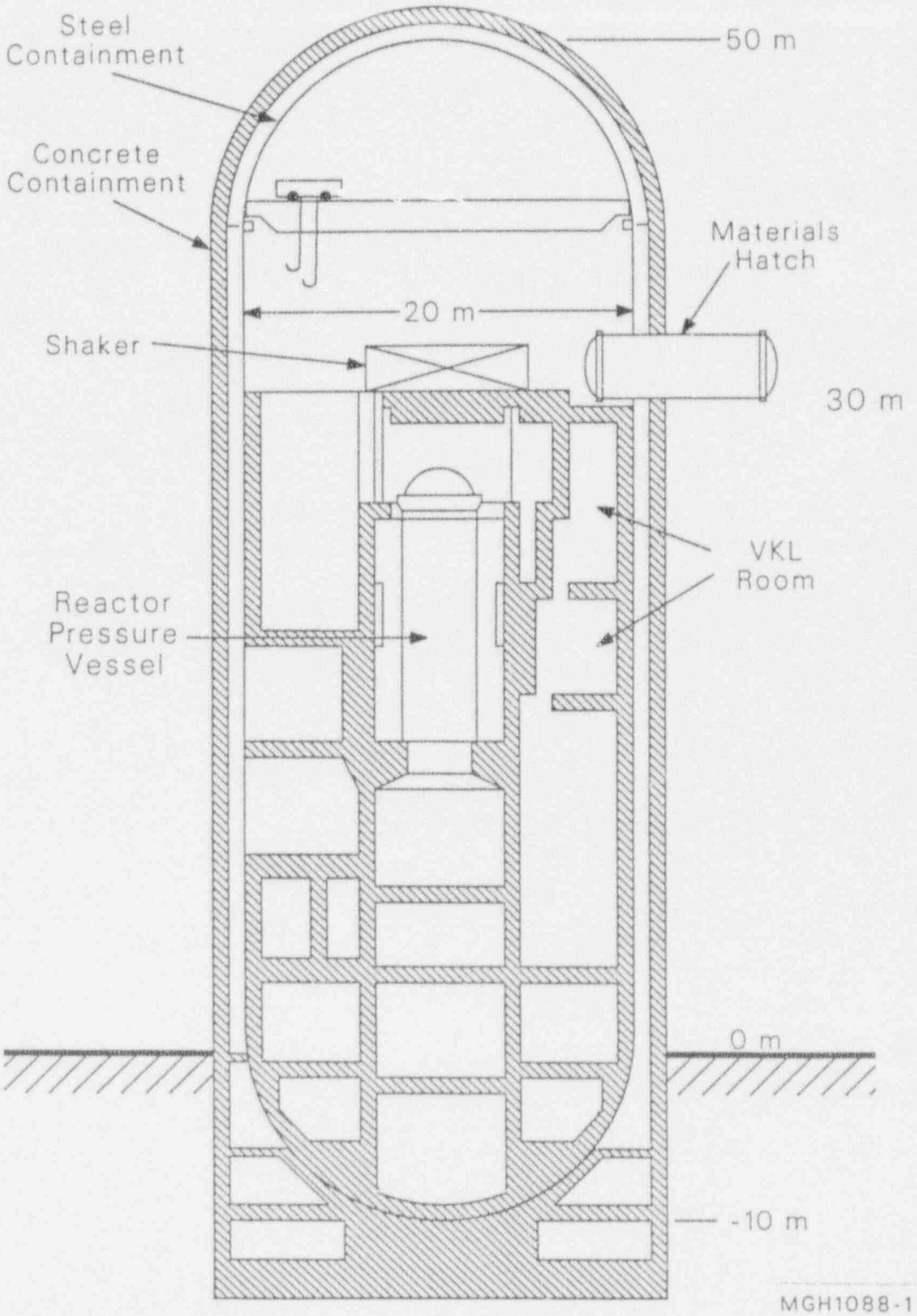

Figure 7-1. A simplified cross section of the HDR facility, showing the locations of the shaker, the VKL, and the reactor pressure vessel.

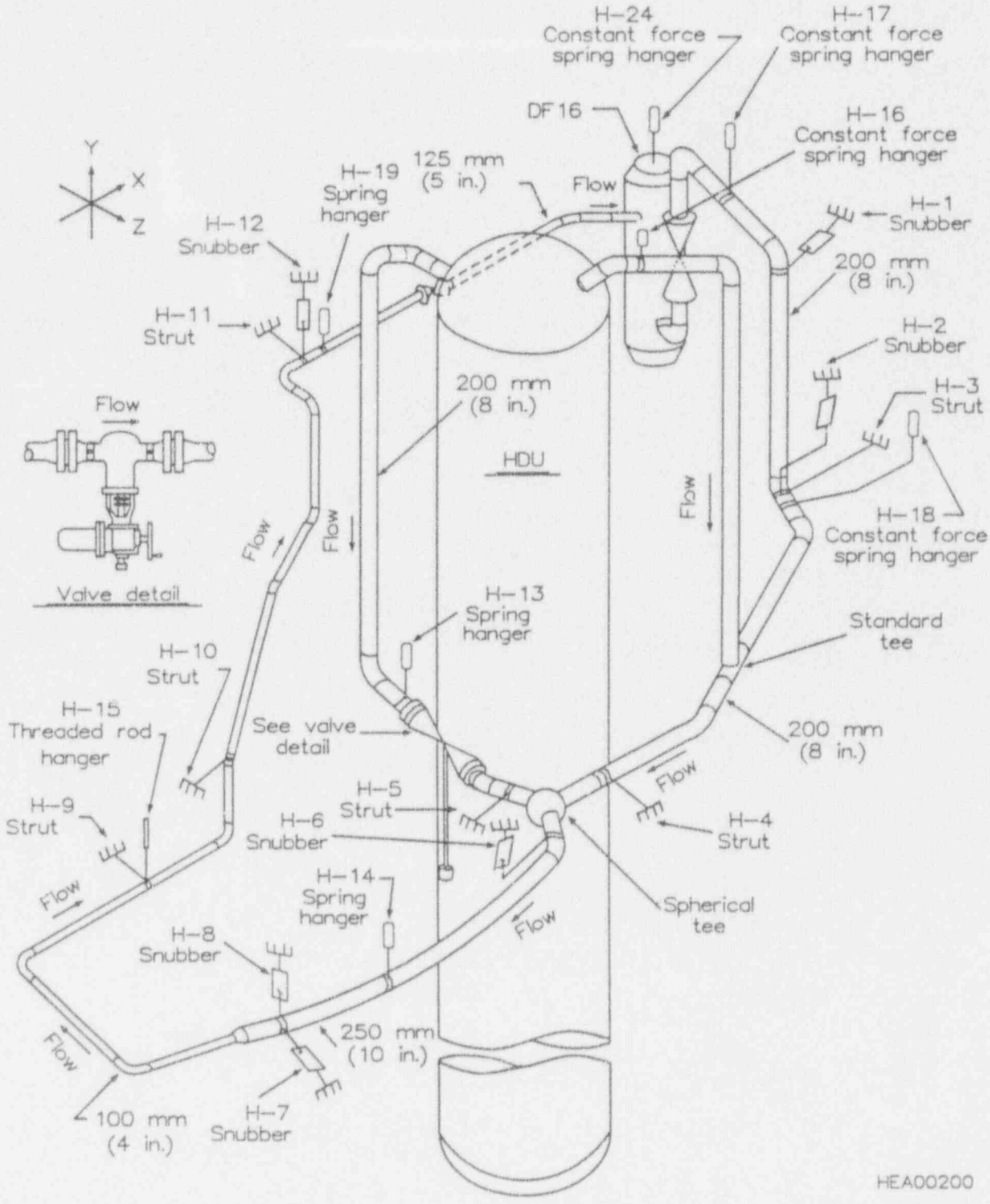

Figure 7-2. A schematic of the VKL showing the 8-in. gate valve and the U.S. stiff piping support system as configured for the SHAG tests.

The piping support configuration described above was designated the U.S. stiff system. Six other piping support systems sponsored by other participants were also installed at various times during the testing (see Table 7-1). The seven piping support systems used different combinations of

Table 7-1. Type of supports used in the SHAG test series.

Support system	System number[a]	Struts	Snubbers	Viscous mass supports	Impact supports	Flexure supports
U.S. stiff	3	6	6[b]	0	0	0
KfK very flexible	1	2	0	0	0	0
KWU flexible	2	5	0	0	0	0
EPRI/Cloud impacting	5	6	0	0	6	0
EPRI/Bechtel energy-absorbing	4	6	0	0	0	4
GERB energy-absorbing	6	5	0	2	0	0
ANCO energy-absorbing	7	6	0	6	0	0

a. We have retained the numbers chosen by KfK in order to facilitate cross-referencing among reports.

b. Five mechanical snubbers and one hydraulic snubber.

various kinds of supports to represent piping systems ranging from stiff to very flexible. The VKL's dynamic response to simulated earthquakes was monitored with each of the support systems installed so that the results could be compared. In all, 25 tests were run, with eight tests at 8 Hz, six tests at 6 Hz, and the others at lower starting frequencies. Seven of the 25 tests were conducted with the U.S. stiff support system installed.

7.3 Test Results

The actual forces applied to the building in the frequencies of interest for piping and valve research (6- and 8-Hz tests) met the requirements of the SHAG test project. Input spectra of 0.3 g ZPA (zero period acceleration) were measured at the HDU vessel and the piping system supports. The VKL responded not only to input from the building through the supports, but also intensities to even greater input from the HDU vessel through the piping connected to the top of the vessel. Input to the VKL exceeded the inputs typically calculated for U.S. East Coast safe shutdown earthquakes (SSEs) and West Coast operational basis earthquakes (OBEs). The acceleration responses of the piping averaged 1 to 3 g throughout the VKL. Some of the snubbers experienced loads approaching their ASME Code Level C allowables. Struts experienced loads of up to 11,000 lb force.

7.3.1 Comparison of Piping Support Systems. The philosophy reflected in the stiffness of the U.S. stiff system is to avoid amplification and reduce resonant response by using snubbers and struts to stiffen the piping system so that the natural frequencies in the piping are higher than the frequencies at which the building responds to an earthquake. The U.S. stiff system performed as designed, raising the resonant frequency of the piping system. In general, the U.S. stiff system and the KfK very flexible system enveloped the response of the VKL. As expected, the stresses in the stiff system were lower than in the KfK very flexible system, but the differences were not as great as we expected. The moderately flexible KWU support system, with only half as many supports as the U.S. stiff design, responded with

fewer high-peak responses and a smaller total system stress than any of the other systems.

7.3.2 Performance of Piping and Snubbers. The structural integrity of the valve and piping was not compromised by the seismic loads. None of the seven piping support systems' responses resulted in piping strain measurements that reached 50% of yield.

Snubbers are designed as either a hydraulic or a mechanical device to allow the low velocity motion typical of thermal expansion yet resist the high velocity motion typical of seismic events. Thus, snubbers can fail in two different ways: either by locking up when they should allow motion, or by allowing motion when they should lock up. The U.S. stiff system used five Pacific Scientific mechanical snubbers and one Bergen-Patterson hydraulic snubber. All of these snubbers functioned properly except for one brief instance (3 to 4 sec) with one mechanical snubber. The low force measurements in the snubber pin and the high acceleration measurements at the adjacent pipe indicated that the snubber temporarily failed to lock up. The anomaly was self correcting.

7.3.3 Operability of the Motor-operated Valve. Operability of the motor-operated valve was not adversely affected by the seismic loadings. However, analysis of the data revealed anomalous performance not related to the seismic loadings. During several of the tests, the torque switch in the motor operator failed to trip at the end of the closing stroke. The result was motor stall.

An extensive investigation ensued to discover the cause of the anomalous performance. The investigation included additional in situ testing at HDR (more than 50 tests with various torque switch settings and various flow and pressure loads), dynamometer testing of the Limitorque motor operator at Limitorque Laboratories, inspection of the torque spring, dynamometer testing of the motor (without the operator) at Peerless Winsmith (the motor manufacturer), and an analysis of the HDR circuit that supplied power to the motor operator during the tests. The investigation produced three findings, one that relates to motor-operated valves in general, and two that relate to dc-powered motor-operated valves:

1. The aged torque switch spring in the operator had taken a permanent set at about 1/2 in. shorter than its specified original length. Thus, it was necessary to change the torque switch from the nominal setting of 3 to a higher setting of 3.75 to achieve the specified torque at torque switch trip.

2. Resistance caused by heating in the dc motor degraded the motor's performance, especially at the high currents that occur at higher loads. Heating incurred during a given test run affected the motor's performance in subsequent test runs if the motor windings did not have a chance to cool between runs.

3. Resistance in the external circuit (the circuit supplying power to the motor operator at HDR) likewise degraded the performance of the motor at high currents. Even though the circuit at HDR was typical of circuits for this application in U.S. nuclear power plants, and even though the cables were sized according to conventional methods, the circuit was not adequate when the motor drew higher currents at higher loads. The configuration of the circuit was such that four long cable runs contributed to the resistance, not two. The circuit configuration also made it difficult to measure voltage drops across all four cable runs. Thus, one of the main causes of the motor operator's anomalous performance, undersized cables in the external circuit, was difficult to diagnose.

7.3.4 High-Frequency Amplification in the Valve Assembly. HDR test results indicated an unexpectedly large high-frequency response in the valve assembly. High-frequency accelerations were significantly amplified from the valve body to the valve operator. Figure 7-3 shows power spectral density (a mathematical representation of

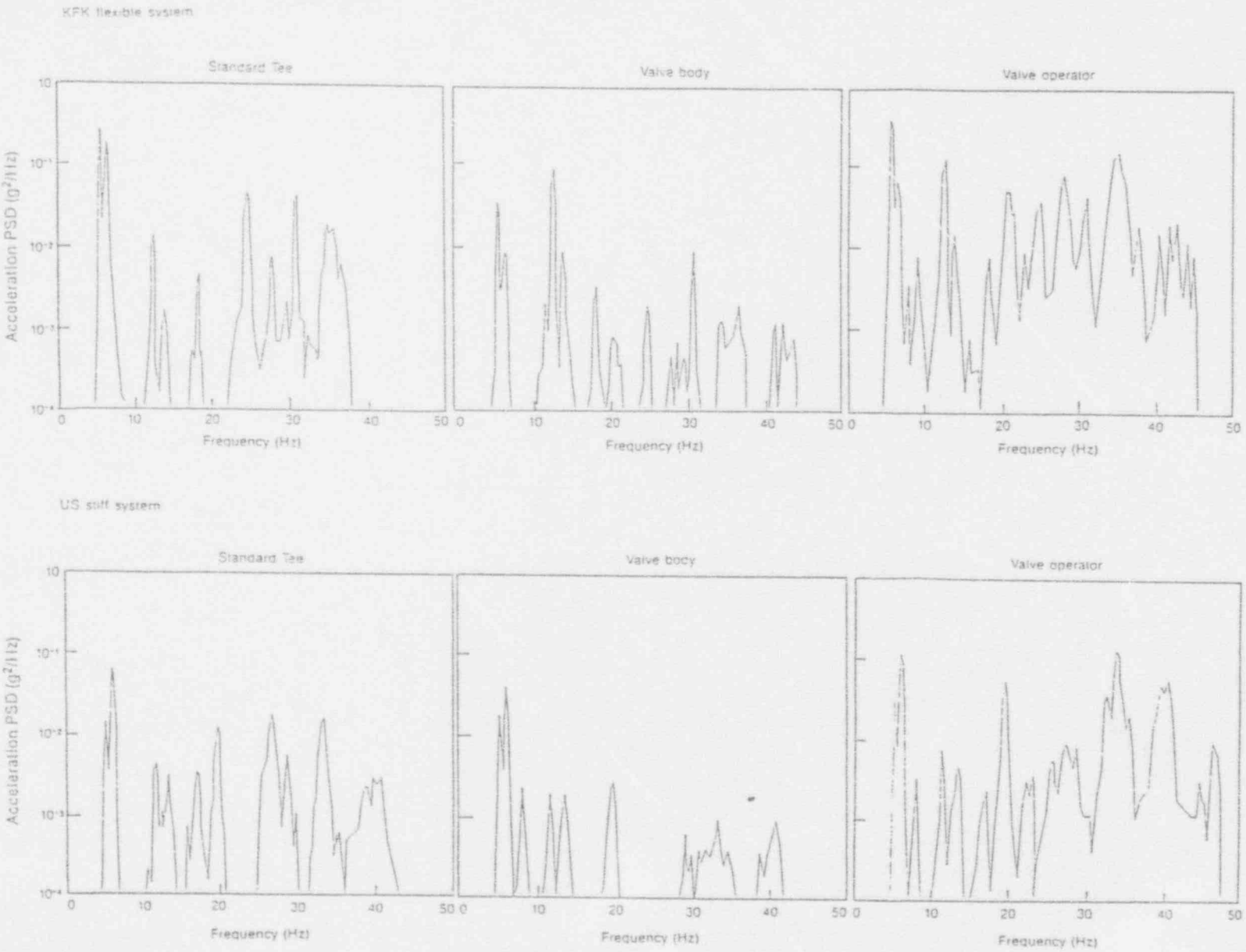

Figure 7-3. Power spectral density (PSD) plots calculated from measurements taken in the Z axis (horizontal direction parallel to flow through the valve) at three locations during two tests with a starting frequency of 8 Hz.

acceleration) calculated from measurements taken in the Z axis at three locations: the standard tee (see Figure 7-2), the valve body, and the valve operator. The results presented in the figure are from two tests, one with the KfK flexible support system installed and one with the U.S. stiff support system installed, both with a starting frequency of 8 Hz. Amplification at the valve operator in the high-frequency range (33 to 50 Hz) is evident.

This high-frequency response is not peculiar to the SHAG test series. A similar response was observed in an earlier test project, discussed in Section 3 of this summary report. Results from that test project were compared with the results from the SHAG tests to confirm the occurrence of this high-frequency response.

7.4 Conclusions

The stiff piping support systems typical of U.S. nuclear designs have disadvantages. The relative movement of the anchors in a stiff support system can actually add stress to a piping system during an earthquake or a water hammer event, and stresses caused by thermal expansion during normal operation may be large if snubbers malfunction by locking up when they should not. In general, the stresses measured with the KfK very flexible support system installed were indeed higher than those measured with the U.S. stiff system installed, but the differences were not great. Overall, stresses were lowest with the KWU moderately flexible system. These results support current thinking in the United States that the best design lies somewhere between stiff and flexible.

SHAG testing at HDR verifies that structurally, valves and piping are inherently tough. Earthquakes of credible magnitude are not likely to cause structural failure of valves or piping in piping systems designed according to methods commonly used in the U.S. nuclear industry.

Torque spring aging, motor heating, and undersized power cables can adversely affect the performance of dc-powered motor-operated valves in nuclear power plants. If the spring has taken a permanent set, and the switch is not set at a higher-than-nominal setting to compensate, the switch might trip too soon and leave the valve in a partially open position. Motor heating in a dc-powered operator can degrade the valve's performance if the valve is opened or closed more than once without time for the motor windings to cool. Undersized cables in the external circuit can present sufficient resistance to reduce the performance of the motor at high loads, when the motor demands high current. This problem (undersized cables) has appeared in several U.S. nuclear power plants. If power to the valve is marginal, whether because of motor heating or undersized cables, and the marginally powered valve is subjected to high loads on closing, the motor might stall, possibly with the valve in a partially open position. Motor stall can cause the thermal overload switches to open and render the motor operator temporarily unavailable for use. If the thermal overload switches have been bypassed or set too high, or if they malfunction, the motor will burn out. Conventional in-plant testing with no loads or with static pressure loads alone cannot detect potential deficiencies caused by motor heating or undersized cables.

The appearance of the high-frequency dynamic response in the valve operator is important because frequencies higher than 33 Hz are generally not accounted for in valve qualification procedures. It is not expected that response in this frequency range will affect the valve structurally. However, high-frequency response may affect valve operation by causing switches, relays, and other valve control devices to chatter.

7.5 Application of the Research

The results from seismic testing at HDR, as reported both by the INEL and by ANL, were included in the technical data base supporting the NRC effort regarding Unresolved Safety Issue A-46, *Seismic Qualification of Equipment in Operating Nuclear Power Plants* (NUREG-1030).

The valve test results formed part of the basis for Generic Letter 89-10, "Safety-Related Motor-

Operated Valve Testing and Surveillance." The cabling issue that surfaced during HDR testing provided insights that helped resolve a problem with a dc-powered valve at a U.S. utility and contributed to NRC Information Notice 89-11, "Failure of dc Motor-Operated Valve to Develop Rated Torque Because of Improper Cable Sizing." The torque spring issue provided information that contributed to Information Notice 89-43, "Permanent Deformation of Torque Switch Helical Springs in Limitorque SMA-Type Motor Operators."

8. SHAM TEST SERIES: HIGH-LEVEL SIMULATED SEISMIC TESTS AT HDR

Following the SHAG seismic tests described in Section 7 of this report, another international seismic research project, the SHAM (Servohydraulische Anregung Maschinetechnik) test series, was conducted in 1988 at HDR. Joining KfK in this effort were researchers from INEL, ANL, EPRI, KWU, the Fraunhofer Institut für Betriebsfestigkeit (LBF), and the Central Electricity Generating Board of the United Kingdom (CEGB).

8.1 The Issue

The SHAM test series provided additional information on the issues addressed by the SHAG test series. Specifically, the SHAM tests were designed to impose even higher earthquake-like loads on the aged, motor-operated valve (MOV) and on the VKL (experimental piping loop), with the following objectives: (a) determine the effects on valve operability and valve and piping structural integrity, (b) determine safety margins and failure modes of piping supports (snubbers, struts, etc.), (c) determine the effects of single and multiple support failures on the response of the piping system, (d) provide data so that the performance of the various piping support systems could be compared, and (e) provide additional data for the NRC effort regarding Unresolved Safety Issue A-46, *Seismic Qualification of Equipment in Operating Nuclear Power Plants* (NUREG-1030).

8.2 Test Description

The SHAM test project used two large 40-ton servohydraulic shakers, each mounted with one end attached to the structure of the HDR building and the other end attached to the VKL. The shakers provided dynamic input to the VKL at locations H-5 and H-25, as shown in Figure 8-1. Earthquake-like displacement histories were input to the shakers to produce input spectra intensities ranging from 0.6 g ZPA in the 100% SSE (nominal) tests to 4.8 g ZPA in the 800% SSE (nominal) tests. The simulated earthquake tests were conducted with pressurized water in the piping at ambient temperature with no flow. In all, 51 experiments were conducted, with six different piping support systems varying from stiff to very flexible installed on the VKL during different segments of the test series. Table 8-1 lists the supports used in each of the six support systems. Nine of the tests were conducted with the U.S. stiff support system installed. Table 8-2 presents the test matrix for those nine tests and three pretest runs. Figure 8-1 shows the locations of the supports installed on the VKL for the U.S. stiff system.

The U.S. stiff support system used earlier in the SHAG test series was modified for the SHAM testing to accommodate the hydraulic shakers. As in the SHAG tests, the U.S. support system for the SHAM tests was based on a pretest analysis of the VKL piping system using the NUPIPE-II computer code, commonly accepted industry practices, and ASME Code criteria.

The instrumentation system included over 300 instruments to measure acceleration, displacement, strain, force, fluid pressure, valve stem position, valve motor current and voltage, and other parameters. As in the earlier SHAG testing, the performance of the valve was monitored with the valve operating during the simulated earthquakes. For the SHAM tests, however, the valve's motor operator was powered by an ac motor instead of the dc motor used in the SHAG testing.

8.3 Test Results

8.3.1 Valve Operability. The ac-powered motor-operated gate valve performed smoothly during all the SHAM seismic tests. The valve body sustained accelerations as high as 7 g in the 800% SSE test, and the valve operator sustained accelerations as high as 12 g, without adverse effect. As in the CPS seismic testing and the SHAG seismic testing discussed in Sections 3 and 7 of this report, an amplified response was measured in the valve operator at frequencies higher

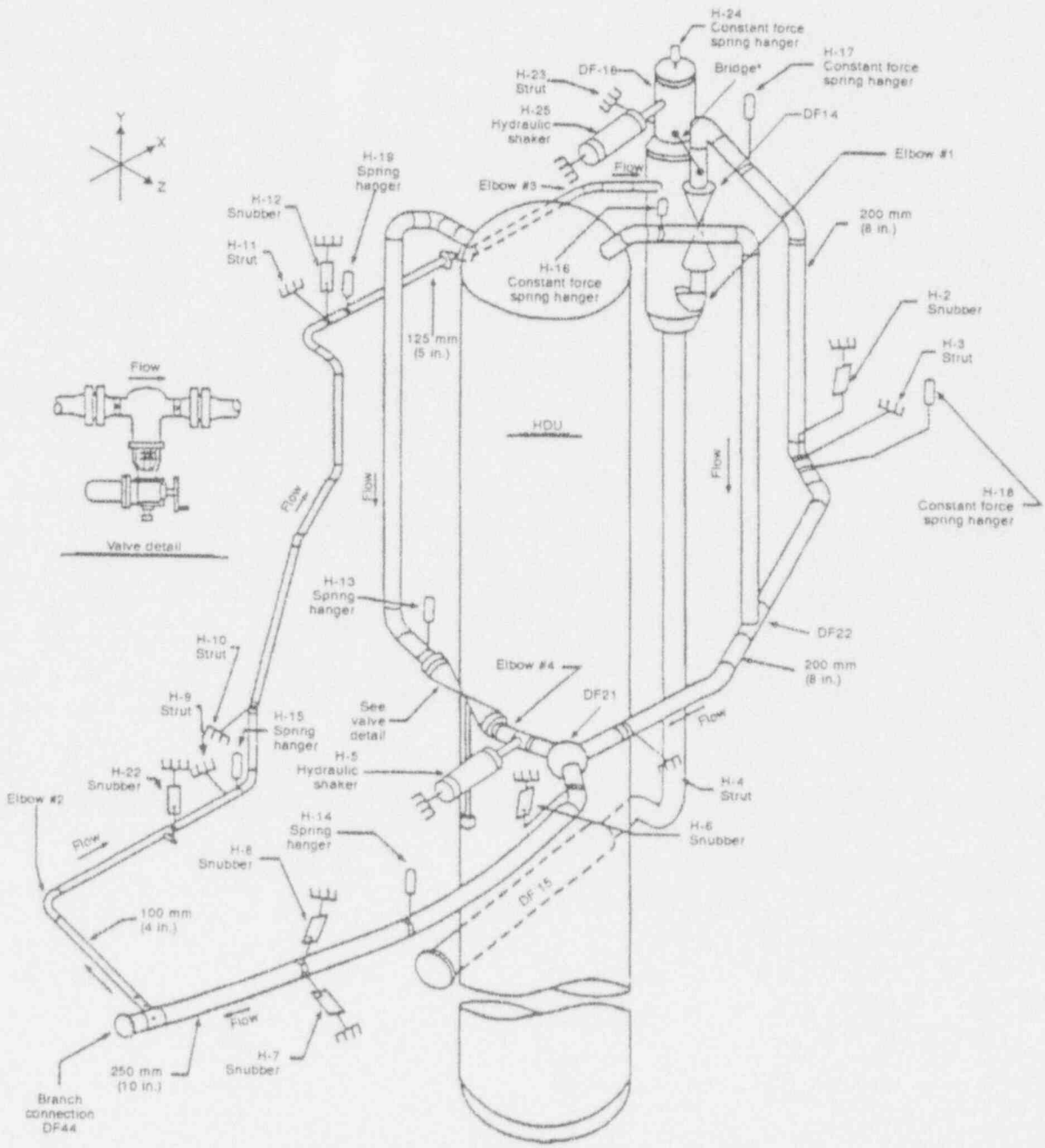

* Bridge between DF16 and DF14 installed for NRC high level tests only

M638 rs-0692-01

Figure 8-1. A schematic of the VKL showing the 8-in. gate valve and the U.S. stiff piping support system as configured for the SHAM tests.

Table 8-1. Participants' support configurations for the SHAM test series.[a]

Support number	KfK	KWU	U.S.	EPRI/ Bechtel	EPRI/ Cloud	CEGB
H-2	—	—	S	—	SS	—
H-3	—	—	RS	RS	RS	—
H-4	RS	RS	RS	RS	RS	RS
H-5	HS	HS	HS	HS	HS	HS
H-6	—	—	S	—	SS	—
H-7	—	—	S	EA	SS	RS
H-8	—	—	S	EA	SS	RS
H-9	—	RS	RS	RS	RS	RS
H-10	—	RS	RS	RS	RS	—
H-11	—	RS	RS	RS	RS	—
H-12	—	—	S	—	SS	RS
H-22	—	—	S	EA	SS	—
H-23	RS	RS	RS	RS	RS	RS
H-25	HS	HS	HS	HS	HS	HS

a. S = snubber, RS = rigid strut, HS = hydraulic shaker, EA = energy absorber, SS = seismic stop.

Table 8-2. U.S. stiff support system test matrix.

Test number	Load type	Load level
T41.35.2	Checkout	0.2g
T41.30.2	Random	0.3g
T41.30.1	Random	0.3g
T41.31.0	SSE	100% SSE[a]
T41.31.1	SSE	100% SSE
T41.31.2	SSE	100% SSE
T41.31.3	SSE	200% SSE
T41.31.4	SSE	300% SSE[b]
T41.31.5	SSE	300% SSE
T41.81.1	SSE	200% SSE
T41.81.2	SSE	600% SSE
T41.81.3	SSE	800% SSE

a. 100% SSE = 0.6 g ZPA input.

b. Incomplete test, malfunction of test equipment.

than those at which typical valve assemblies are qualified. Some contact chatter occurred in the switches in the motor operator, but operation of the motor was not affected. No visible structural damage occurred to the valve or the operator.

8.3.2 Snubber Failures. One of the objectives of the SHAM testing was to determine the loads at which snubbers and other dynamic piping supports would fail. The investigation also considered some of the more common devices for attaching piping supports to the building structure and to the piping. Among these were piping trunnion attachments and concrete anchors. None of the trunnion attachments failed. Some concrete anchors loosened somewhat, but no failures occurred. Even with loads as high as five times their rated loadings, no rigid struts failed.

Several snubbers failed. In most instances, the snubber failures occurred at loads well above their rated loadings. However, the snubber at location H-7 failed in test T41.35.2 at a loading lower than its rated loading. A replacement snubber of the same manufacturer and model likewise failed in a subsequent test at a loading lower than its rated loading. Table 8-3 lists the snubbers installed at the six snubber locations during the twelve test runs and provides information on snubber failures.

Table 8-3. Snubber installation matrix for U.S. stiff support system.

	Snubber installed[a]					
Test No.	H-2	H-6	H-7	H-8	H-22	H-12
T41.35.2	PSA-1	PSA-1/2	A/D 150[b]	A/D 70	PSA-1/4	A/D 40
T41.30.2	PSA-1	PSA-1/2	A/D 150[c]	A/D 70	PSA-1/4	A/D 40
T41.30.1	PSA-1	PSA-1/2	A/D 150[c]	A/D 70	PSA-1/4	A/D 40
T41.31.0	PSA-1	PSA-1/2	A/D 150[d]	A/D 70	PSA-1/4	A/D 40
T41.31.1	PSA-1	PSA-1/2	A/D 150[c]	A/D 70[b]	PSA-1/4[b]	A/D 40
T41.31.2	PSA-1	PSA-1/2[b]	PSA-1	PSA-1/2	PSA-1/4[c]	PSA-1/4
T41.31.3	PSA-1	PSA-1/2[c]	PSA-1	PSA-1/2[b]	PSA-1/4[c]	PSA-1/4
T41.31.4	PSA-1	PSA-1/2[c]	PSA-1	PSA-1/2[c]	PSA-1/4[c]	PSA-1/4
T41.31.5	PSA-1	PSA-1/2[c]	PSA-1	PSA-1/2[c]	PSA-1/4[c]	PSA-1/4
T41.81.1	PSA-1	PSA-1	PSA-1	PSA-1	PSA-1	PSA-1
T41.81.2	PSA-1	PSA-1	PSA-1	A/D 70[b]	PSA-1/4[b]	A/D 40[b]
T41.81.3	PSA-1	PSA-1	PSA-1[b]	A/D 70[c]	—[e]	A/D 40[c]

a. PSA denotes a snubber provided by the Pacific Scientific Corporation, whereas while A/D denotes a snubber provided by Anchor/Darling Industries.

b. Snubber failed during this test.

c. Snubber was left in place but failed during a previous test.

d. Snubber was replaced for this test and failed during this test.

e. Snubber was removed; it failed during the previous test.

One snubber, the PSA-1/4 snubber installed at H-22 during test T41.81.2, experienced a "rigid mode" failure; though it allowed excessive motion, it also resisted some force. The other snubber failures consisted of internal damage that allowed excessive motion without resistive behavior.

Where snubber failures did not occur, snubbers successfully performed their design function, keeping displacements to a minimum. In some cases, snubbers resisted loads several times their rated loadings without failure. Table 8-4 provides information on some of the loads successfully resisted by some of the snubbers.

Table 8-4. Maximum loads for struts and snubbers installed in the U.S. stiff support system.

		Predicted vs measured loads (KIP)[a]		Rated vs measured loads (KIP)[a]		
Support location	Support type[b]	Predicted for 200% SSE test[c]	Measured in test 81.1[g] (200 SSE test)	Rated[d]	Measured in test 81.2[g] (600 SSE test)	Measured in test 81.3[g] (800 SSE test)
H-2	S	2.61	–1.69	2.10	5.04	4.73
H-3	RS	3.05	3.47	2.10	10.3	13.5
H-4	RS	3.57	NA	24.73	NA	NA
H-6	S	1.27	1.36	2.10	5.64	9.17
H-7	S	1.80	4.19	2.10	9.75	–26.4[e]
H-8	S	0.85	–1.32	0.87	1.87[e]	NA[f]
H-9	RS	1.28	–0.62	0.87	2.12	4.02
H-10	RS	0.77	–0.94	0.87	–2.97	4.85
H-11	RS	1.78	–1.27	0.87	–3.23	–4.36
H-12	S	0.71	–0.55	0.52	1.07[e]	NA[f]
H-22	S	0.52	–0.47	0.52	–1.75[e]	NA[f]
H-23	RS	9.09	NA	49.5	NA	NA

a. To calculate loads in KN, multiply by 4.448.

b. S = Snubber RS = Rigid strut.

c. Predictions based on analysis of the VKL in its modified, as-tested configuration.

d. Service Level C maximum rated loadings for the snubbers and struts that were installed in tests 81.2 and 81.3.

e. Snubber failed during this test.

f. Snubber failed during previous test.

g. Negative signs denote compressive loads.

NA = Not applicable.

8.3.3 VKL Response.

Predicted versus Measured Loads. Before testing began, we conducted a typical design analysis of the VKL to configure the support system and to predict the loads that would be imposed on the various support system components (snubbers, struts, etc.) so that the components could be sized. The VKL underwent modest modifications after that pretest analysis was conducted, so we conducted another analysis of the VKL in its as-tested configuration. We then compared the response of the VKL as predicted by the analysis with the response measured during testing.

The comparison showed fairly good agreement in most instances. The analysis predicted maximum stresses in the piping at the same locations where maximum strains were measured during the tests. Measured piping responses (displacements and accelerations) were generally in the same frequency bands as predicted by the analysis. Of the loads imposed on the struts and snubbers during the tests, half were underpredicted by the analysis, and half overpredicted, in most cases by not too large a margin. Table 8-4 compares the support loads predicted for a 200% SSE test with the loads measured in test T41.81.1.

The most significant underprediction was for the snubber at location H-7. This underprediction may have been influenced by the sensitivity of the model to the support location and stiffness. The project scope did not include a posttest sensitivity study, so the exact cause of the underprediction was not determined. (Note that sensitivity studies are not usually performed in the design of piping systems in nuclear power plants.) In any case, the conservatism in the support design usually provides functional margin at all credible loads. The Pacific Scientific snubber installed at the H-7 location during the later tests in the series successfully resisted the loads it experienced in the 600% SSE test and failed only at severe overloads during the 800% SSE test.

Zipper Effect. One of the concerns addressed in seismic probabilistic risk assessments (PRAs) is the possibility that failure of a support during an earthquake would cause higher loads to be imposed on a nearby support, causing it, too, to fail. Failure of a second support would, in turn, cause a third support to fail, and so on. This phenomenon, known as the zipper effect, occurred during the 600% SSE test, during which three snubbers failed, one after the other. A fourth snubber failed during the 800% SSE test that followed. With several of its supports out of service, the VKL became more flexible and responded at lower frequencies, especially in the Y (vertical) direction of the section that runs from the spherical tee DF21 through branch connection DF44 to the DF16 component (see Figure 8-1). As expected, the test data indicated that displacements and strains increased with the failures of the snubbers. Strains were measured in excess of the 0.3% value used to define yield in stainless steel, with the highest strains measured at Elbows 1 and 2. Some plastic deformation occurred at these elbows, but no other structural damage occurred and no leakage occurred in any of the piping.

8.4 Conclusions

SHAM test results indicate that earthquake loadings will not have a significant adverse effect on valve operation, unless contact chatter in relays or switches in the motor operator consists of chatter events of sufficient duration to cause the motor controller to shut off power to the motor. This did not occur during the SHAM tests. Further investigation of this issue was outside the scope of the SHAM test project.

In most instances, the measurements taken on the VKL during the tests agreed reasonably well with analytical predictions, but they did not exactly match. In particular, there was some disagreement between predicted support loads and measured loads. Generally speaking, piping system analyses using the ASME Code rules and procedures that we followed provide assurance that the piping system will perform its function with an adequate safety margin. This was the case with the analysis of the VKL piping system at HDR. Sensitivity studies could have improved the correlation between predicted and measured

support loads, but such studies are typically not performed unless the ASME Code rules cannot be met.

The rigid struts used in the SHAM test project performed very well, resisting loads several times greater than their rated loadings without failure. Likewise, many of the snubbers performed without failure while resisting loads well above their rated loadings. All snubber results were supplied to the manufacturers for their information.

Most of the snubbers that failed did so at loads well above their rated loadings. One snubber resisted loads more than eight times its rated loading before it failed. Two snubbers of the same model failed at loads lower than their rated loadings. All snubber results were supplied to the manufacturers for their information.

Test results from the SHAM test series reaffirm the structural toughness of valves and piping. Tests conducted with multiple snubber failures show that piping can successfully withstand earthquake-type loadings when allowed more flexibility than is typical of piping support systems installed in U.S. plants. The results of other SHAM tests conducted at HDR by KfK and KWU using more flexible support systems (fewer piping supports) concur with this finding. This finding agrees with some of the current thinking in the U.S. that design practices could be revised to allow a less stiff support configuration and that such revision would not reduce the structural safety margins of piping to an unacceptable level. The tests also indicate that the zipper effect may be less of a concern than many people in the U.S. nuclear industry have supposed. No significant structural damage occurred to the piping even at very high simulated earthquake loadings with several supports disabled.

Most important, the results from the SHAM tests show that when commonly accepted design methods are applied, piping systems will likely maintain their pressure boundary during a credible earthquake; sufficient safety margins were shown to exist even with severe earthquake loadings and the loss of multiple supports.

8.5 Application of the Research

The results from seismic testing at HDR, as reported both by the INEL and by ANL, were included in the technical data base supporting the NRC effort regarding Unresolved Safety Issue A-46, *Seismic Qualification of Equipment in Operating Nuclear Power Plants* (NUREG-1030).

ANL used the test results in their effort to verify the Seismic Methodology Analysis Chain with Statistics (SMACS) computer code.

9. EARLY RESEARCH FOR THE GENERIC SAFETY ISSUE 87 TEST PROJECTS

9.1 The Issue

The turbine steam supply line of the high pressure coolant injection (HPCI) pump communicates directly with the reactor vessel and runs outside the containment to the auxiliary building, where the HPCI turbine is located. The containment isolation valves in this line are normally open. The concern with these isolation valves is whether or not they would close against the large pressure and flow loads that would occur in the event of a guillotine break in this steam line outside the containment. In such an event, their failure to close could result in common-cause failures of other equipment in the auxiliary building that were not qualified for a harsh environment. This concern is the substance of Generic Safety Issue 87 (GSI 87), "Failure of the HPCI Steam Line Without Isolation."

Our early GSI 87 research, performed as part of the Environmental and Dynamic Equipment Qualification Research Program (EDQP) that is the subject of this summary report, included efforts to determine which systems are applicable to the GSI 87 concern, determine the type and qualification of the installed valves, and develop a research plan that outlined the work necessary to provide the technical basis for the NRC effort regarding GSI 87.

9.2 Research Description

Our work included a review of available industry and research information. That review determined that two additional reactor systems are applicable to the GSI 87 concern: the reactor core isolation cooling (RCIC) turbine steam supply line and the reactor water cleanup (RWCU) system supply line. (In some early plants the system is designated by another name, but the function is the same.)

At the time we performed this preliminary study, the qualification of containment isolation gate valves for flow interruption was not well understood. The only full-scale flow interruption testing that had been performed up to that time was the testing of 3- and 4-in. power-operated relief valves (PORVs) and PORV block valves in a test program performed by the Electric Power Research Institute (EPRI) at the Duke Power, Marshall facility in 1980, after the accident at Three Mile Island. (The results of that testing are available in EPRI NP-2514-LD, 1982). The tests were of the go/no-go variety, and several of the block valves initially failed to close at their design basis load. The EPRI tests, even after thorough review, had only marginal applicability to the smallest of the GSI 87 systems.

We surveyed industry data bases to determine the type and sizes of the valves used in the three GSI 87 systems. We contacted valve manufacturers to determine the extent of hardware qualification and to determine the methods used to calculate the valve forces necessary for closing against high energy flows. The results of the earlier valve testing were studied, sizing methods used by the motor operator manufacturers were determined, and a limited study of utility methods was conducted.

9.3 Research Results

We found that the flexible-wedge motor-operated gate valve was the predominant valve design used for containment isolation in all three systems. The predominant valve size was 4 in. for the RCIC system, 6 in. for the RWCU system, and 10 in. for the HPCI system. In addition, we found that none of the valve designs installed in the systems of interest had been qualified for their respective design basis flow interruption loads. (An exception might be the Velan valves installed in RCIC systems. They were tested in the EPRI block valve tests.)

The valve manufacturers and utilities all used basically the same equations to determine a valve's operator torque and stem force requirements. (These calculations make it possible to size the operator for the valve and set the operator

control switches.) However, there were inconsistencies in how some of the important variables in the equations were determined. For the operator torque equation (which calculates the operator torque needed to achieve a given stem force), some utilities used the stem nut friction coefficients specified by Limitorque, the operator manufacturer, while others used different stem nut friction coefficients specified by the valve manufacturer.

Similar inconsistencies were evident in the use of the stem force equation (which calculates stem force for a given set of valve dimensions, fluid pressures, etc.). The disc load portion of the stem force equation is basically the disc area multiplied by the differential pressure across the disc multiplied by a disc factor, typically 0.3. We found that there were no standards on either the disc area term or the disc factor. Everything from the valve orifice area to the nominal pipe size was used to define the disc area. This difference alone made comparisons of one piece of work to another difficult. The biggest problem we found in the stem force equation was that the disc factor was analytically based and loosely associated with a friction factor. We could find no record of full-scale flow interruption testing having been performed to support the use of a disc factor of 0.3 to determine the stem force requirements of valves installed in GSI 87 applications.

9.4 Conclusions

We concluded that although some additional study would be helpful, full-scale flow interruption testing of typical gate valves would be necessary to provide the information needed to address the GSI 87 concerns. Our conclusions as to the state of the industry with regard to GSI 87, along with a plan for the proposed test project, were submitted to the NRC in July 1987. The report, *Generic Issue Number 87 Research Plan* (EGG-REQ-7676), is listed in the bibliography.

9.5 Application of the Research

The rest of the GSI 87 research was performed under NRC FINs A6857 and B5529. For the sake of continuity, we will briefly discuss the results of those research projects. Two 6-in. RWCU valves were subjected to testing at design basis conditions at the Wyle Test Laboratories in Huntsville, Alabama. The test results showed that the industry stem force equation was in fact not conservative. We also found that one of the two valve designs tested was susceptible to internal damage when closing against the design basis load. This internal plastic deformation and shearing of metal could not be predicted by any linear friction equation. The nuclear industry was reluctant to accept the results, because the two-valve sample was too small to form a basis for such important decisions.

A second full-scale test project followed, with three 6-in. valves subjected to flow interruption tests with both high energy water and high energy steam (to cover the RWCU and the RCIC concerns), and with three 10-in. valves subjected to flow interruption tests with high energy steam (to cover the HPCI concerns). These tests were performed at the Kraftwerk Union (KWU) facilities near Frankfurt Germany. The results of this test project confirmed the results of the first test project and established once and for all that the industry stem force equation did not adequately characterize valve behavior and did not conservatively bound valve requirements. Several reports on the results of these tests have been published. These are listed in the Bibliography for the reader's information.

The NRC issued a number of information notices as the research results were being analyzed, and later, because of the results of these GSI 87 test projects and because of other regulatory initiatives, the NRC issued Generic Letter 89-10, "Safety-Related Motor-Operated Valve Testing and Surveillance." The generic letter recommends that the utilities reanalyze the design basis conditions for each safety-related motor-operated valve, ensure that the operator control switches are set high enough to perform the design basis function, and, where possible, test the valve at design basis conditions to assure operability. The GSI 87 test results, along with other research results, also supported supplements to Generic Letter 89-10 that were issued to provide clarification for its implementation.

10. GENERAL CONCLUSIONS

The results of the Environmental and Dynamic Equipment Qualification Research Program (EDQP), funded under FIN A6322, contributed to the technical basis for the NRC's effort involving several generic safety issues, one unresolved safety issue, and several other NRC initiatives. The work has already been implemented in some industry consensus standards and is being reviewed for implementation in others. The valve qualification standard ANSI B16.41 is an example; it is being superseded by a new ANSI/ASME valve qualification standard that incorporates some of the early results of this work. The seismic testing performed in this program is expected to contribute significantly toward a new ASME standard on snubber qualification.

The work also identified a number of areas where further research was needed. That work is being performed in the Equipment Operability Research Program (FIN A6857) and the Nuclear Plant Aging Research Program (FIN A6389). The EPRI is also working on a valve research program to address research needs identified by the results of the EDQP and its follow-on work.

REFERENCES

EPRI NP-2514-LD, 1982, *Marshall Electric Motor Operated Valve (Block Valve) Interim Test Data Report.*

NUREG-1264, 1987, U.S. Nuclear Regulatory Commission, *Containment Integrity Research Program Plan.*

NUREG-1030, 1987, U.S. Nuclear Regulatory Commission, Unresolved Safety Issue A-46, *Seismic Qualification of Equipment in Operating Nuclear Power Plants.*

NUREG-1209, 1986, U.S. Nuclear Regulatory Commission, *Program Plan for Environmental Qualification of Mechanical and Dynamic (Including Seismic) Qualification of Mechanical and Electrical Equipment Program.*

NUREG-0900, 1986, U.S. Nuclear Regulatory Commission, *Nuclear Power Plant Severe Accident Research Plan.*

NUREG-0737, 1980, U.S. Nuclear Regulatory Commission, *Clarification of TMI Action Plan Requirements.*

NUREG-0660, 1980, U.S. Nuclear Regulatory Commission, *NRC Action Plan as a Result of the TMI-2 Accident.*

U.S. Nuclear Regulatory Commission, 1989, Information Notice 89-11, "Failure of dc Motor-Operated Valve to Develop Rated Torque Because of Improper Cable Sizing."

U.S. Nuclear Regulatory Commission, 1989, Generic Letter 89-10, "Safety-Related Motor-Operated Valve Testing and Surveillance."

U.S. Nuclear Regulatory Commission, Generic Safety Issue 23, "Reactor Coolant Pump Seal Failures at Station Blackout Conditions," NUREG-0933, 1983 (with supplements to 1992), *Prioritization of Generic Safety Issues.*

U.S. Nuclear Regulatory Commission, Generic Safety Issue 87, "Failure of the HPCI Steam Line Without Isolation," NUREG-0933, 1983 (with supplements to 1992), *Prioritization of Generic Safety Issues.*

BIBLIOGRAPHY

The research described in this summary report was reported in the documents listed here. The documents are listed in groups that correspond with the sections of this summary report, as indicated.

CONTAINMENT PURGE AND VENT VALVES (Section 2)

MEETING PAPER

J. A. Hunter, R. Steele, Jr., J. C. Watkins, "Reactor Containment Purge and Vent Valve Performance Experiments," *ANS Topical Meeting*, 1984.

NUREG/CR REPORTS

J. C. Watkins, R. Steele, Jr., R. C. Hill, K. G. DeWall, *A Study of Typical Nuclear Containment Purge Valves in an Accident Environment*, NUREG/CR-4648, EGG-2459, August 1986.

R. Steele, Jr., J. C. Watkins, *Containment Purge and Vent Valve Test Program Final Report*, NUREG/CR-4141, EGG-2374, September 1985.

R. Steele, Jr., J. C. Watkins, K. G. DeWall, and M. J. Russell, *Motor Operated Valve Research Update*, NUREG/CR-5720, EGG-2643, June 1992.

CONTAINMENT PIPING AND PENETRATIONS (Sections 3 and 4)

REFEREED JOURNAL ARTICLES

H. S. Crapo, "Containment Penetration System (CPS) Valve Tests Under Accident Loads," *Nuclear Engineering and Design, 115*, 1989, pp. 331–338.

R. Steele, Jr., R. C. Hill, J. A. Close, "Functionality and Leak Integrity of Containment Penetration Systems Subjected to Design Basis Dynamic Loads," *Nuclear Engineering and Design, 108*, 1988, pp. 7–13.

MEETING PAPERS

H. S. Crapo, "Containment Penetration System (CPS) Valve Tests Under Accident Loads," *Proceedings of the 15th Water Reactor Safety Meeting, Gaithersburg, Maryland, October 26–30, 1987.*

R. Steele, Jr., R. C. Hill, J. A. Close, "Functionality and Leak Integrity of Containment Systems Subjected to Design Basis Dynamic Loads," *Proceedings of the 14th Water Reactor Safety Meeting, Gaithersburg, Maryland, October 27–31, 1986.*

NUREG/CR REPORTS

H. S. Crapo, R. Steele, Jr., *Containment Penetration System (CPS) Tests Under Accident Loads*, NUREG/CR-5043, EGG-2524, June 1988.

J. A. Close, R. C. Hill, R. Steele, Jr., *Seismic Testing of Typical Containment Penetration Systems*, NUREG/CR-4734, EGG-2470, December 1986.

NRC TECHNICAL REPORTS (Informal Reports)

K. G. DeWall, D. K. Morton, R. Steele, Jr., *Development, Identification and Quantification of Issues Relating to the Containment Isolation System Valve Integrity Test Program*, EGG-RST-6978, August 1985.

SHAFT SEALS FOR PRIMARY COOLANT PUMPS (Section 5)

NUREG/CR REPORT

D. B. Rhodes, R. C. Hill, R. G. Wensel, *Reactor Coolant Pump Shaft Seal Stability During Station Blackout*, NUREG/CR-4821, EGG-2492, AECL-9342, May 1987.

RATTLING IN ELECTRICAL CABINETS (Section 6)

NUREG/CR REPORTS

G. Thinnes and V. Glozmaa, *Significance of In-Structure Generated Motion in Seismic Qualification Tests of Cabinet Mounted Electrical Devices*, NUREG/CR-5031, EGG-2523, June 1988.

D. D. Kana and D. J. Pomerening, *Similarity Principles for Equipment Qualification by Experience*, NUREG/CR-5012, EGG-2521, July 1988.

PIPING AND VALVE RESPONSE TO IN SITU SEISMIC TESTS AT HDR (Sections 7 and 8)

REFEREED JOURNAL ARTICLES

R. Steele, Jr., and J. G. Arendts, "Performance of a Piping System and Equipment in the HDR Simulated Seismic Experiments," *Nuclear Engineering and Design, 115*, 1989, pp. 339–347.

R. Steele, Jr., P. E. MacDonald, J. G. Arendts, "Dynamic Load Effects on Gate Valve Operability and Snubber Performance," *Nuclear Engineering and Design, 108, 1988, pp. 15–21.*

MEETING PAPERS

R. Steele, Jr., "Valve and Piping System Test Results and Effects on Regulatory Standards," *Proceedings of the 10th International Conference on Structural Mechanics in Reactor Technology, Anaheim, California, August 14–18, 1989.*

R. Steele, Jr., "Piping Support and Gate Valve Behavior During High Level HDR Simulated Seismic Tests," *Proceedings of the 16th Water Reactor Safety Meeting, Gaithersburg, Maryland, October 24–27, 1988.*

R. Steele, Jr., J. G. Arendts, "Performance of a Piping System and Equipment in the HDR Simulated Seismic Experiments," *Proceedings of the 15th Water Reactor Safety Meeting, Gaithersburg, Maryland, October 26–30, 1987.*

NUREG/CR REPORTS

R. Steele, Jr., and M. E. Nitzel, *Piping System Response During High-Level Simulated Seismic Tests at the Heissdampfreaktor Facility (SHAM Test Series)*, NUREG/CR-5646, EGG-2655, June 1992.

R. Steele, Jr., J. G. Arendts, A. G. Ware, *SHAG Test Series Seismic Research on an Aged U.S. Gate Valve and on Piping System Responses of the Decommissioned Heissdampfreaktor (HDR), Volumes 1 and 2*, NUREG/CR-4977, EGG-2505, July 1989.

M. G. Srinivasan, C. A. Kot, B. J. Hsieh, *Verification of Piping Response Calculations of SMACS Code with Data from Seismic Tests of an Inplant Piping System*, NUREG/CR-5757, September 1991.

M. G. Srinivasan, M. Mojtahed, C. A. Kot, *Verification of Nonlinear Piping Response Calculations with Data from Seismic Testing of an Inplant Piping System*, NUREG/CR-5841, March 1992.

NRC TECHNICAL REPORTS (Informal Reports)

A. G. Ware, *Evaluation of Snubber Response Data During Selected HDR SHAG Tests—Quick Look Report*, EGG-REQ-7710, May 1987.

C. A. Seaquist, *Shippingport Valves Aging Assessment, Refurbishment and Requalification*, EGG-REQ-7276, June 1986.

Valve Research, HDR/VKL Phase II SHAG Testing Requirements, EGG-REQ-7148, Rev. 0, 1, and 2, May 1986.

GENERIC ISSUE 87

NUREG/CR REPORTS

K. G. DeWall and R. Steele, Jr., *BWR Reactor Water Cleanup System Flexible Wedge Gate Isolation Valve Qualification and High Energy Flow Interruption Test*, Volumes 1, 2, and 3, NUREG/CR-5406, EGG-2569, October 1989.

R. Steele, Jr., K. G. DeWall, J. C. Watkins, *Generic Issue 87: Flexible Wedge Gate Valve Test Program, Phase II Results and Analysis*, NUREG/CR-5558, EGG-2600, July 1990.

R. Steele, Jr., J. C. Watkins, K. G. DeWall, M. J. Russell, *Motor-Operated Valve Research Update*, NUREG/CR-5720, EGG-2643, October 1991.

NRC TECHNICAL REPORT (Informal Reports)

K. G. DeWall, *Generic Issue Number 87 Research Plan*, EGG-REQ-7676, July 1987.

MISCELLANEOUS

NUREG/CR REPORTS

H. W. Heiselmann, *Identification of Equipment and Components Predicted as Significant Contributors to Severe Core Damage*, NUREG/CR-3762, EGG-2311, May 1984.

NRC TECHNICAL REPORTS (Informal Reports)

K. G. DeWall, *Generic Issue Number 87 Research Plan*, EGG-REQ-7676, July 1987.

K. G. DeWall, *Qualification of Valve Assemblies in High Energy BWR Systems Penetrating Containment*, EGG-REQ-7387, September 1986.

K. G. DeWall, *Summary of Valve Assemblies in High Energy BWR Systems Outside of Containment—Interim Report*, EGG-REQ-7297, June 1986.

NRC FORM 335 (2-89) NRCM 1102, 3201, 3202

U.S. NUCLEAR REGULATORY COMMISSION

BIBLIOGRAPHIC DATA SHEET

(See instructions on the reverse)

1. REPORT NUMBER (Assigned by NRC, Add Vol., Supp., Rev., and Addendum Numbers, if any.)

NUREG/CR-5935
EGG-2686

2. TITLE AND SUBTITLE

Summary of Work Completed Under the Environmental and Dynamic Equipment Qualification Research Program (EDQP)

3. DATE REPORT PUBLISHED

MONTH	YEAR
February	1994

4. FIN OR GRANT NUMBER

A6322

5. AUTHOR(S)

Robert Steele, Jr.
Donovan L. Bramwell
John C. Watkins
Kevin G. DeWall

6. TYPE OF REPORT

Technical

7. PERIOD COVERED (Inclusive Dates)

1983 to 1993

8. PERFORMING ORGANIZATION – NAME AND ADDRESS (If NRC, provide Division, Office or Region, U.S. Nuclear Regulatory Commission, and mailing address; if contractor, provide name and mailing address.)

Idaho National Engineering Laboratory
EG&G Idaho, Inc.
P.O. Box 1625
Idaho Falls, Idaho 83415

9. SPONSORING ORGANIZATION – NAME AND ADDRESS (If NRC, type "Same as above"; if contractor, provide NRC Division, Office or Region, U.S. Nuclear Regulatory Commission, and mailing address.)

Division of Engineering
Office of Nuclear Regulatory Research
U.S. Nuclear Regulatory Commission
Washington, D.C. 20555

10. SUPPLEMENTARY NOTES

11. ABSTRACT (200 words or less)

This report documents the results of the main projects undertaken under the Environmental and Dynamic Equipment Qualification Research Program (EDQP) sponsored by the U.S. Nuclear Regulatory Commission (NRC) under FIN A6322. Lasting from fiscal year 1983 to 1987, the program dealt with environmental and dynamic (including seismic) equipment qualification issues for mechanical and electromechanical components and systems used in nuclear power plants. The research results have since been used by both the NRC and industry.The program included seven major research projects that addressed the following issues: (a) containment purge and vent valves performing under design basis loss of coolant accident loads, (b) containment piping penetrations and isolation valves performing under seismic loadings and design basis and severe accident containment wall displacements, (c) shaft seals for primary coolant pumps performing under station blackout conditions, (d) electrical cabinet internals responding to in-structure generated motion (rattling), and (e) in situ piping and valves responding to seismic loadings. Another project investigating whether certain containment isolation valves will close under design basis conditions was also started under this program. This report includes eight main sections, each of which provides a brief description of one of the projects, a summary of the findings, and an overview of the application of the results. A bibliography lists the journal articles, papers, and reports that document the research.

12. KEY WORDS/DESCRIPTORS (List words or phrases that will assist researchers in locating the report.)

Dynamic qualification of equipment
Environmental qualification of equipment
Seismic testing
Valves
Piping

13. AVAILABILITY STATEMENT

Unlimited

14. SECURITY CLASSIFICATION

(This Page)
Unclassified

(This Report)
Unclassified

15. NUMBER OF PAGES

16. PRICE

Federal Recycling Program

NUREG/CR-5935

SUMMARY OF WORK COMPLETED UNDER THE ENVIRONMENTAL AND DYNAMIC EQUIPMENT QUALIFICATION RESEARCH PROGRAM (EDQP)

FEBRUARY 1994

UNITED STATES
NUCLEAR REGULATORY COMMISSION
WASHINGTON, D.C. 20555-0001

OFFICIAL BUSINESS
PENALTY FOR PRIVATE USE, $300

120555139531 1 1AN1RM1P111S
US NRC-OADM
DIV FOIA & PUBLICATIONS SVCS
TPS-PDR-NUREG
P-211
WASHINGTON DC 20555

SPECIAL FOURTH-CLASS RATE
POSTAGE AND FEES PAID
USNRC
PERMIT NO. G-67